

---

# The Seismic Signature of Mantle Plumes

---

Dissertation  
der Fakultät für Geowissenschaften  
der Ludwig-Maximilians-Universität München

vorgelegt von  
Markus Treml  
am 30.03.2006

Erstgutachter: Prof. Dr. Heiner Igel  
Zweitgutachter: Prof. Dr. Hans-Peter Bunge

# Widmung

**Gustav Tremel**

1940-2002

und der mensch heißt mensch  
weil er vergisst, weil er verdrängt  
und weil er schwärmt und stählt  
weil er wärmt, wenn er erzählt  
und weil er träumt und glaubt  
sich anlehnt und vertraut

oh, es ist schon ok  
es tut gleichmäßig weh  
es heilt die zeit  
ohne plan, ohne geleit

und der mensch heißt mensch  
weil er erinnert, weil er kämpft  
und weil er hofft und liebt  
weil er mitfühlt und vergibt  
und weil er lacht,  
und weil er lebt,  
du fehlst

(nach HERBERT GRÖNEMEYER, "Mensch", 2002)



# Zusammenfassung

Die Existenz von kleinräumigen säulenförmigen Aufströmen heißen Mantelgesteins von der Kern-Mantel-Grenze (KMG) wurde 1971 von MORGAN postuliert. Für sie hat sich auch im deutschen Sprachbereich der Begriff des „Plumes“ eingebürgert, der im Englischen für jegliche Form von Materialbewegung durch Auftrieb steht (ein adäquater deutscher Begriff existiert nur für den Spezialfall der *Rauchfahne*). Plumes lieferten eine Erklärung für „Hotspots“ – Stellen ungewöhnlichen Vulkanismus, der in keinem offensichtlichen Zusammenhang mit der Plattentektonik steht und durch sie nicht erklärbar ist. Hotspots erscheinen im Vergleich zur Plattenbewegung als ortsfest (WILSON [1965]) und lieferten so ein Bezugssystem für deren Bewegung.

Experimentelle und numerische Studien haben in den letzten Jahrzehnten dazu beigetragen, unsere Vorstellung von Plumes weiter zu entwickeln. Als Standard-Plume Modell hat sich das pilzförmige Kopf-Kanal-Modell (z.B. WHITEHEAD AND LUTHER [1975]) etabliert. Beim Aufstieg bildet sich ein Kopf mit großem Volumen, gefolgt von einem relativ dünnen Versorgungskanal. Erreicht der Kopf die Lithosphäre kommt es zu starkem epochalem Vulkanismus, bei denen große Flut-Basalt-Regionen entstehen. Die nachfolgende aus dem Kanal gespeiste vulkanische Tätigkeit bildet (z.T. unterseeische) Insel-Ketten mit Hawaii als klassischem Beispiel.

Nun sind alle Elemente des beschriebenen Erscheinungsbildes des Standard-Plumes auf der Erde nur selten an einem Plume zu beobachten (COURTILLOT *et al.* [2003]). Jüngere Studien verzichten zunehmend auf vereinfachende Annahmen und kommen so zu einer Vielfalt von Erscheinungsformen von Plumes. Diese scheinbare Beliebigkeit wird von einigen Wissenschaftlern ausgenutzt, um die Plume-Hypothese anzugreifen (z.B. ANDERSON [2000]), weil sie letztere untestbar macht. Sie schlagen alternative Ursachen für den ungewöhnlichen Vulkanismus von Hotspots vor, zum Teil mit erheblichen Implikationen für den Zustand des Mantels.

Die Kenntnis der wirklichen Form und Größe von Plumes und des Volumenstroms aber könnten ein Schlüssel zu zahlreichen geodynamischen Fragen sein und den Parameterraum der Mantelkonvektion und den Wärmehaushalt der Erde deutlich einschränken.

Deswegen hat die Geophysik und die Geochemie versucht, ein Bild von Plumes im Mantel zu erhalten. Seismologische Verfahren haben die beste räumliche Auflösung und werden daher verstärkt eingesetzt. Der seismischen Tomographie kommt hier als direktes bildgebendes Verfahren die größte Bedeutung zu. Zwei Arten der Tomographie werden unterschieden, die regionale teleseismische und die globale Tomographie. Beide basieren auf dem Prinzip, dass die Laufzeit der Wellen zwischen einem Hypozentrums-Seismometer-Paar von den Materialeigenschaften des zwischen ihnen liegenden Gesteins abhängt. Da der Großteil der Variationen in den seismischen Geschwindigkeiten und der Dichte in der Erde mit der Tiefe stattfindet, kann ein rein tiefenabhängiges (1-D) Modell bereits den überwiegenden Teil der Laufzeiten erklären. Die lateralen Variationen können demnach als Abweichungen von einem Standard

1-D Erdmodell beschrieben werden. Werden viele verschiedene Hypozentrums-Seismometer Kombinationen verwendet, dann ist die Vieldeutigkeit, wo auf dem Laufweg die Materialeigenschaften variieren, zumindest zum Teil auflösbar und die räumliche Verteilung der seismischen Geschwindigkeiten bestimmbar. Die Verteilung der Erdbebenherde auf der Erde ist im wesentlichen konzentriert an den Plattengrenzen, und Seismometer konnten bis vor wenigen Jahren nur an Land aufgestellt werden. Diese Beschränkung in Erdbebenlokationen und Seismometerstandorten führt dazu, dass die Erde nicht überall gleich gut und nicht dicht genug von aufgezeichneten seismischen Wellen durchstrahlt wird. Geschwindigkeitsunterschiede sind also nicht überall gut auflösbar, was insbesondere für Plumes mit ihren kleinräumigen Kanälen Schwierigkeiten bereitet. Plumes haben durch ihre hohe Temperatur niedrige seismische Geschwindigkeiten und sind daher prinzipiell mit tomographischen Methoden nachweisbar. Bisher basierten die verwendeten Methoden überwiegend auf der Strahlentheorie. Diese ist eine Näherung der Wellentheorie für unendliche Frequenzen. Analog zur Optik ist diese Näherung überall dort erlaubt, wo die Wellenlängen klein gegenüber der Größe des durchstrahlten Objekts sind. Für Plume-Kanäle mit Durchmessern von etwa 120–200 km ist dies jedoch für mittel- bis langperiodische seismische Wellen nicht der Fall. Wie in dieser Arbeit gezeigt, treten Wellenfeldeffekte als Abweichung von der Strahlentheorie auf und führen zu einem „Verheilen“ der Wellenfront, also einer Abnahme des durch eine kleinräumige Niedriggeschwindigkeitszone (Plume) verursachten Laufzeitverzögerung mit steigender Entfernung nach der Anomalie. Da bis in die letzten Jahre überwiegend Strahlen-Tomographie für die Abbildung von Plumes benutzt wurde, führte das zu einer Unterschätzung der Geschwindigkeitsanomalien der Plumes und somit vermutlich zu einem zu niedrigen Wert für den Wärmefluss in Plumes. Letzterer ist zusammen mit der Frage nach dem Entstehungsort von Plumes aber ein wichtiger geodynamischer Parameter.

Daher wurde in den vergangenen Jahren eine Tomographie-Methode entwickelt (MONTELLI *et al.* [2004b]), welche nicht mehr auf Strahlentheorie beruht, sondern die Wellennatur der seismischen Wellen berücksichtigt. Diese sogenannte „Finite-Frequenzen“-Methode wurde zur Abbildung von Plumes eingesetzt und konnte eine Verbesserung der Plume-Abbilder bewirken.

Eine systematische Untersuchung des Einflusses von Plumes auf teleseismische Wellen in Abhängigkeit der wichtigsten Plume-Parameter in Form einer Vorwärtsmodellierung gab es bislang noch nicht.

Die sich für eine solche Studie für diese Arbeit ergebenden Fragestellungen lauten:

- Welches sind die Auswirkungen von Plume-artigen Niedriggeschwindigkeitszonen auf seismische Wellen und wie unterscheiden sich diese von bisherigen strahlentheoretischen Vorstellungen?
- Wie hängen diese Wellenfeldeffekte von den wichtigsten Plume-Parametern, d.h. der Ursprungstiefe, dem Durchmesser, der Stärke und dem lateralen Verlauf der Anomalie ab?
- Lassen sich daraus Empfehlungen für die Konfiguration und Auswertung zukünftiger seismologischer Plume-Experimente ableiten?
- Gibt es besonders geeignete seismische Phasen für die Untersuchung von Plumes, und wie kann man diese bestimmen?

Um diese Fragen zu beantworten, wurden 3D-Simulationen von globaler Wellenausbreitung durch einfache Plume-Modelle (vertikale Zylinder erniedrigter seismischer Geschwindigkeiten)

in drei Epizentralabständen ( $45^\circ$ ,  $90^\circ$  und  $135^\circ$ ) durchgeführt. Hierfür wurde das Spektralelemente Programm SPECFEM3D von KOMATITSCH AND TROMP [2002a,b] verwendet, welches derzeit das ausgereifteste Programm für diese Aufgabe ist. Allerdings erfordert dessen Benutzung erhebliche Rechenleistung und Zeit, was bei vorhandenen Ressourcen der benötigten Supercomputer zu einer Beschränkung auf mittlere bis lange Perioden der Wellenfelder führt.

Als Alternative zu den aufwändigen 3D-Rechnungen für die ganze Erde wurde in dieser Arbeit parallel zu den Rechnungen mit der Spektralen-Elemente Methode ein hybrider Finite-Differenzen Ansatz entwickelt, der es erlaubt, einen Teil der Rechnungen in 2D auszuführen. Hierbei wurden zwei existierende Algorithmen kombiniert, die sich auf bestimmte Spezialfälle beschränken und dadurch Rechenzeit und Speicherplatz sparen.

Es ist dies zum einen der Ansatz von IGEL AND WEBER [1995, 1996], bei dem ein achsensymmetrischer Aufbau der Erde angenommen wird, weswegen die Berechnungen lediglich in zwei Dimensionen erfolgen. Das erhaltene Ergebnis kann aufgrund der Achsensymmetrie um die Achse gedreht werden und ist so auch für drei Dimensionen gültig. Durch die Verwendung der achsensymmetrischen Gleichungen wird das geometrische Abklingen der Amplituden der Welle durch die Ausbreitung richtig wiedergegeben, außerdem sind im achsensymmetrischen Fall horizontale Scherwellen (SH) von den vertikalen Scherwellen (SV) und den Kompressionswellen (P) entkoppelt, was deren getrennte Rechnung ermöglicht. Der andere Ansatz (NISSEN-MEYER [2001]) führt die Rechnungen zwar in 3-D aus, beschränkt aber den Bereich auf eine Kugelsektion. Dies vermeidet erstens die Singularitäten im Gitter bei der Verwendung von Kugelkoordinaten, zum anderen sinkt dadurch der Rechenaufwand und Speicherplatzbedarf, so dass hohe Frequenzen gerechnet werden können.

Beide Verfahren haben Schwächen: der achsensymmetrische Ansatz ist nur für achsensymmetrische (wie z.B. 1D-) Erdmodelle benutzbar, also für lokalisierte 3-D Strukturen wie Plumes nicht brauchbar. Die Beschränkung der 3-D Wellenausbreitungssimulation auf Kugelsektionen führt dazu, dass Wellen von Beben aus großer Entfernung, wie sie typischerweise für die Tomographie verwendet werden, nicht modelliert werden können.

Um dennoch die Vorteile der beiden Methoden für Plume-Studien nutzen zu können, kam im Rahmen dieser Arbeit die Idee auf, beide Ansätze zu kombinieren, indem die Wellenausbreitung über lange Distanzen im 1D Hintergrundmodell mit der achsensymmetrischen Methode und die Berechnung der 3-D Wellenfeldeffekte im Bereich des Plumes mit der Kugelsektionsmethode durchgeführt wird. Dies führt zu einer Konzentration der Rechenleistung auf den Bereich, wo sie nötig ist und zu einer effizienten Berechnung des Wellenfeldes dort, wo es sich durch ein Modell bewegt, das nur Änderungen in einer Dimension (der Tiefe) aufweist.

Ein Vorteil der Methode ist die Möglichkeit der Einspeisung nur eines Teils des Wellenfeldes, weil für den achsensymmetrischen Fall PSV- und SH-Wellen entkoppelt sind. Wird das eine oder andere Wellenfeld in den Kugelsektionscode eingespeist, sind auf der/den nicht eingespeisten Seismogrammkomponente(n) die durch den Plume verursachten Konversionen in den jeweils anderen Wellentyp beobachtbar. Ein weiterer Vorteil bei Verwendung des Programms in seiner seriellen Version ist, dass der 3-D Teil erst dann eingeschaltet werden kann, wenn Energie diesen Bereich erreicht. Dadurch wird erhebliche Rechenzeit gespart.

Es wurde auch ein Konzept für die Parallelisierung des Algorithmus entwickelt, welches darauf beruht, die Kommunikation innerhalb der einzelnen Programme in einer eigenen Kommunikationsumgebung stattfinden zu lassen, während die Kommunikation zwischen den Unterprogrammen in der globalen Umgebung stattfindet. Aufgrund der frei wählbaren, beliebigen Modellgrößen und Prozessorenzahlen ist diese Lösung aber nur für bestimmte Spezialfälle realisiert. Abschließend wird ein Beispiel für die Anwendbarkeit des hybriden Konzepts an Hand

von Rechnungen mit einem einfachen Plume-Modell gegeben.

Wie bereits erwähnt, wurden die systematischen Untersuchungen der Plume-Effekte mit dem Spektrale-Elemente Programm SPECFEM3D durchgeführt, welches zu diesem Zwecke erweitert wurde, um geeignete Plume-Modelle implementieren zu können. Es wurde eine Reihe von Rechnungen mit verschiedenen Plume-Modellen durchgeführt, die sich jeweils in einem Parameter unterschieden. Die Seismogramme wurden mit denen, die sich für das verwendete Hintergrundmodell (PREM) allein ergeben, verglichen. Es wurden im wesentlichen nur Unterschiede in der Ankunftszeit und Amplitude der einzelnen seismischen Phasen festgestellt, Änderungen der Wellenform waren nicht auffallend, sofern sie nicht durch Überlagerung zweier unterschiedlich stark verzögerter Phasen zustande kamen. Daher wurden Auswerteroutinen zur Gewinnung von Laufzeitverzögerung (mittels Kreuzkorellation) und Amplitude entwickelt und auf die Daten angewendet.

Die Laufzeitverzögerungen wurden exemplarisch für verschiedene Phasen in Kartenform dargestellt und deren räumliche Verteilung in Abhängigkeit von der Plume-Position untersucht. Hierbei traten z.T. deutliche Abweichungen von strahlentheoretisch erwartetem Verhalten auf: zum einen ein starker Rückgang der Verzögerungen unmittelbar hinter dem Plume, und zum anderen negative Verzögerungen, also im Vergleich zum ungestörten PREM-Modell verfrühte Ankunftszeiten. Letztere Beobachtung ist gegen jegliche Intuition (die meist auf strahlentheoretischen Vorstellungen beruhen), man würde nicht erwarten, dass eine Zone niedriger Geschwindigkeit Wellen gewissermaßen beschleunigt. Dennoch sind die verfrühten Ankunftszeiten völlig konform mit der Wellentheorie, sie werden durch die zweite Fresnelsche Zone verursacht. Zahlreiche jüngere Abhandlungen (z.B. HUNG *et al.* [2000]; ZHOU *et al.* [2004]) über die Empfindlichkeit von seismischen Wellen gegenüber Geschwindigkeitsänderungen illustrieren dies: im Gegensatz zum seismischen Strahl, dessen Empfindlichkeit auf eine Linie (eben den Strahl) beschränkt ist, wird die Laufzeit der Wellen von Geschwindigkeiten in einem ausgedehnten Bereich beeinflusst, genau auf dem Strahl und in einem Bereich um ihn herum jedoch nicht. Für einfache direkte Phasen mit Epizentralentfernungen bis ca.  $70^\circ$  sehen diese „Sensitivity Kernels“ genannten Empfindlichkeitsverteilungen in der Längsausdehnung aus wie Bananen und erinnern im Querschnitt an Schmalzkringel, weshalb sie in der Literatur häufig „Banana-Doughnut Kernels“ (MARQUERING *et al.* [1999]) genannt werden. Bei größerer Entfernung passen die Fresnelschen Zonen der direkten Phasen nicht mehr in den Mantel und ihre Empfindlichkeitsverteilung verkompliziert sich in oft wenig anschaulicher Weise. Gleiches trifft auf komplexere Phasen wie Kernphasen oder Kernreflexionen zu.

Das rasche Abklingen der Verzögerungen hinter dem Plume ist im wesentlichen Folge der bereits beschriebenen Verheilung der Wellenfront und somit auch frequenzabhängig. Hinzu kommen weitere geometrische Effekte, etwa, dass sich der Laufweg der Welle durch den Plume – und somit die Möglichkeit durch ihn eine Verzögerung zu erleiden – mit der Tiefe ändert. In der Summe können diese Effekte ein komplettes Verschwinden der Laufzeitverzögerung bei großen Entfernungen hinter dem Plume möglich machen.

Abgesehen von diesen allgemeinen Beobachtungen, treten folgende Unterschiede in den Laufzeitverzögerungen der Plume-Modelle in Abhängigkeit von den variierten Parametern auf. Der Radius des Plumes bestimmt zum einen die Größe der von Laufzeitverzögerungen und Amplitudenänderungen der Phasen betroffenen Fläche. Zum anderen ändert sich bei Variation des Radius auch das Verhältnis von Plumegröße zur Wellenlänge, welches ein Maß für die Bedeutung der Finiten-Frequenzen-Effekte ist. Für den in dieser Arbeit untersuchten Frequenzbereich von 0.05 Hz–0.01 Hz und die modellierten Plume-Radien von 60–300 km ergeben sich



je nach verwendeten Frequenzen und Plumegrößen starke Finite-Frequenzen-Effekte, während andere Kombinationen diese nur schwach aufweisen.

Die Stärke der Anomalie sollte eigentlich lediglich linear die Laufzeitverzögerungen beeinflussen, es wurden aber hiervon abweichende Beobachtungen gemacht, beispielsweise zeigen die Laufzeitverzögerungen eines Plumes mit 12,4% S-Wellengeschwindigkeitserniedrigung ein Wiederansteigen in größerer Entfernung hinter dem Plume. Die Interpretation zu dieser Beobachtung ist, dass der Plume selbst durch die hohen, von ihm verursachten Geschwindigkeitsstörungen den Weg der Wellen und somit die Empfindlichkeitsbereiche signifikant beeinflusst. Dies ist insbesondere dann von Interesse, wenn zukünftige Finite-Frequenzen-Tomographien zeigen sollten, dass Plume-Perturbationen höher sind als bisher angenommen.

Für die räumliche Verteilung der Geschwindigkeitsanomalie als Funktion des Abstands zur Plume-Achse wurden drei Modelle verwendet: ein sprunghafter Verlauf, einer, der einer Gaußschen Funktion folgt und ein physikalisch realistischeres Modell, welches den Effekt des thermischen Halos beinhaltet. Dabei ist die Anomalie im Inneren des (sehr schmalen) eigentlichen Plume-Kanals konstant und fällt dann einer logarithmischen Funktion folgend nach außen hin ab, wie man es von den Temperaturen um den Plume herum infolge von Wärmeleitung erwarten würde. Die Ergebnisse der Rechnung mit den drei Perturbationsfunktionen zeigen, dass Unterschiede in den Perturbationsfunktionen wenig Einfluss auf die Laufzeitverzögerungen bei den betrachteten Frequenzen haben. Lediglich die maximale Verzögerung ist beim Plume mit dem sprunghaften Perturbationsverlauf kleinräumig leicht erhöht, was dadurch zu erklären ist, dass dort Wellen eine größere Verzögerung akkumulieren können, ohne dass diese durch Verheilung der Wellenfront wieder zurückgehen.

Wie bereits erwähnt, kommt der Ursprungstiefe von Plumes eine große Bedeutung in der Diskussion um die Existenz von Plumes zu. In der Arbeit wurden die zwei Tiefen modelliert, welche physikalisch ausgezeichnet für die Entstehung von Plumes sind: die KMG und die Grenze zwischen oberem und unterem Mantel in 660 km Tiefe. Die Unterschiede zwischen den beiden Modellen treten in den Laufzeitverzögerungskarten erst in größerer Entfernung hinter dem Plume auf – dort kommen Wellen an, welche beim 660 km-Plume diesen „unterlaufen“. Dies ist im Einklang mit der Strahlentheorie, jedoch ist der beobachtete „Laufzeitschatten“ länger als strahlentheoretisch erwartet, was auf die Ausdehnung der Wellenempfindlichkeit im Vergleich zum Strahl zurückzuführen ist.

Die Amplituden werden durch den Plume, der als Zone erniedrigter Geschwindigkeiten wie eine Linse wirkt, hinter dem Plume-Zentrum erhöht. Dieser Fokussierungseffekt ist auch frequenzabhängig, kann aber bei den modellierten Frequenzen nicht dazu benutzt werden, verschiedene Perturbationsfunktionen mit einem effektiven Durchmesser von 200 km zu unterscheiden. Ansonsten zeigt die räumliche Verteilung der Amplituden eine ähnliche Charakteristik wie die der Laufzeitverzögerungen, was sich aus der Ähnlichkeit der Sensitivity-Kernels erklärt, die sich lediglich durch den Bereich um den Strahlweg, welcher für die Laufzeiten keine Empfindlichkeit aufweist, unterscheiden. Dieser Bereich ist bei den Amplituden nicht vorhanden. In der Praxis sind die (geringen) Amplitudenunterschiede weniger genau zu bestimmen als die Laufzeitverzögerungen, weshalb letztere wohl die relevantere Signatur des Plume tragen.

Beim Vergleich der räumlichen Verteilung der Plume-Effekte wurde deutlich, dass strahlentheoretische Überlegungen bezüglich des Effekts des Plumes auf eine bestimmte Phase zu völlig falschen Ergebnissen bei den verwendeten Frequenzen führen können. Steil einfallende Phasen wie z.B. die Kern-reflektierte S-Phase ScS sind aus strahlentheoretischer Sicht ideale Kandidaten, um Plume zu untersuchen, da deren Strahl eine lange Zeit im Plume läuft und somit

hohe Laufzeitverzögerungen oder Amplitudenveränderungen erleiden kann. Gerade für diese Phase wurde gezeigt, dass der Laufzeiteffekt nicht wie erwartet fokussiert in der Nähe des Plumes auftritt. Bei der flach einfallenden sS-Phase, wo man dies nicht erwarten würde, ist es jedoch der Fall. Dahingegen erfüllt die steil einfallende SKS-Phase bei einer Entfernung von  $90^\circ$  die Erwartungen, welche aus der Strahlentheorie resultieren und eignet sich hervorragend für Plume-Studien. All dies macht deutlich, dass die eindimensionale Verteilung der Empfindlichkeit entlang des Strahls keine Rückschlüsse auf die wirkliche Empfindlichkeit mittel- und langperiodischer Wellen zulässt. Letztere müsste für jede Phase und Epizentraldistanz mit hohem Aufwand für die jeweilige Frequenz dreidimensional berechnet werden, was jedoch an die Grenzen der Machbarkeit stößt. Zumindest für achsensymmetrische Erdmodelle stellt die von NISSEN-MEYER *et al.* [2005] vorgeschlagene Methode aber eine Möglichkeit dar, Empfindlichkeitsverteilungen effizient zu berechnen. Nur wenn der Plume selber, etwa durch seine hohe Perturbation, die Empfindlichkeitsverteilung der Welle beeinflusst (worauf es Hinweise in der Arbeit gibt), ist es erforderlich, Berechnungen für dreidimensionale Modelle durchzuführen.

In der in dieser Arbeit gezeigten Existenz von Finiten-Frequenzen Effekten liegt aber nicht nur der Nachteil, dass aufwändigere Berechnungen der Empfindlichkeit der Wellen durchgeführt werden müssen, um geeignete Phasen für die Untersuchung von Plumes in bestimmten Tiefen bei gegebener Epizentraldistanz zu ermitteln. Ein Vorteil dieser heterogenen Empfindlichkeitsverteilung im Vergleich zur gleichförmigen Verteilung entlang des Strahls liegt darin, dass mit der Finiten-Frequenzen Theorie genauer bestimmt werden kann, wo die Welle von etwaigen Heterogenitäten beeinflusst wird. Somit lassen sich anhand der Empfindlichkeiten der Wellen Phasen finden, die genau den zu untersuchenden Bereich beproben. Dies in Zukunft gezielt auszunutzen, stellt eine mögliche Verbesserung der seismischen Methoden dar.

Im letzten Teil der Arbeit werden die Ergebnisse der Modellierungen im Hinblick auf den Island-Plume interpretiert. Dieser ist das Paradebeispiel für einen Hotspot der mit einem Mittelozeanischen Rücken zusammenfällt und mit ihm interagiert. Die Anomalie unter Island ist derzeit der best-erforschtete Plume der Welt. Er wurde mit zahlreichen Experimenten untersucht, von denen die in diesem Zusammenhang interessantesten das ICEMELT und das HOTSPOT Tomographie Experiment sind. Beide haben relativ dichte ( $\approx 75$  km Stationsabstand) Seismometernetze verwendet, welche aber in ihrer Apertur auf die Landmasse von Island beschränkt geblieben sind. Einer Faustformel folgend, ist die Apertur eines Tomographienetzes in etwa der maximalen Tiefenaufösung gleich. Demnach können beide Datensätze keine Aussagen darüber machen, ob die Island-Anomalie an der 660 km Diskontinuität (oder noch höher) endet, oder ob sie bis zur KMG reicht. Globale Tomographie-Studien haben zwar versucht, die Anomalie bis in die Tiefe zu verfolgen, sind aber aufgrund ihrer beschränkten Auflösung dazu nicht in der Lage und widersprechen sich daher auch.

Ein Vergleich der Realdaten des Peru-Erdbebens mit synthetischen Daten dieser Arbeit zeigte, dass die nicht modellierten starken Effekte der variablen Krustenmächtigkeit unter Island die Laufzeiten z.T. stärker beeinflussen als der Plume selbst und außerdem von Station zu Station variieren, was einen Vergleich zwischen den Stationen wenig Aussagekraft gibt. Weiterhin wurden Amplitudenunterschiede sichtbar, die durch die nicht in die Modellierung eingebaute Wellenabdämpfung verursacht werden.

Die zwei Hauptfragen bezüglich des Island-Plumes wurden mit den synthetischen Verzögerungsverteilungen der Modellrechnungen untersucht. Hierfür wurden die Laufzeitschatten in vier verschiedene Erdbebeneinfallrichtungen gedreht und lediglich der Teil dargestellt, der auf der Landfläche von Island beobachtbar wäre. Es zeigt sich, dass die Frage, ob der Island-Plume eine große Ausdehnung und dafür eine geringe Anomalie hat oder eine geringe Ausdehnung

und eine starke Anomalie (groß-warm oder klein-heiß) mit nur auf Island aufgezeichneten Daten deutlich unterschieden werden kann. In einer parallelen Arbeit mit der gleichen Art von Modellierung haben ALLEN AND TROMP [2005] mittlerweile auch gezeigt, dass die Daten einen dünnen und heißen Plume plausibel machen und dessen mögliche Größenausdehnung eingegrenzt. Bei der Frage nach der Tiefenausdehnung der Island Anomalie wurde untersucht, ob eine Unterscheidung der Fälle Plume-Ursprungsort an der KMG und in 660 km Tiefe mit langperiodischen Daten auf Island zu beantworten ist. Zwar existiert die bereits erwähnte Faustformel für den Strahlenfall, welche nahelegt, dass dies nicht möglich ist, aber es wurden in der Arbeit auch Unterschiede zwischen Strahlentheorie und Welleneffekten bezüglich dieser Frage festgestellt. Dennoch ergab sich, dass die Daten, die auf der Landfläche Islands aufgezeichnet werden können, eine Unterscheidung nicht erlauben. Hierfür wäre die Aufstellung von speziellen Seismometern die auf dem Meeresboden betrieben werden können („Ocean Bottom Seismometers“, OBS) erforderlich.

Das führt uns zu der Frage der Konfiguration zukünftiger Plume-Experimente. Hierfür lassen sich aus den Erkenntnissen dieser Arbeit folgende Schlussfolgerungen ziehen. Der Verheilungseffekt der Wellenfront reduziert die Laufzeitverzögerungen bereits in unmittelbarer Nähe des Plume sehr stark – die stärksten Gradienten treten innerhalb weniger Plume-Radien von der Plume-Achse entfernt auf. Deshalb sollten dort die Stationsabstände gegenüber heute üblichen Werten verringert werden, etwa auf unter 50 km, um beispielsweise das Maximum des Laufzeiteinflusses zu erfassen.

In größerer Entfernung vom Plume sind die Variationen gering, hier reichen die üblichen Abstände zwischen den Seismometern aus. Ab etwa 500 km von der Plume-Achse werden die Laufzeitverzögerungen sehr klein, so dass sie je nach den Umständen nicht mehr aufgelöst werden können. Es ist aber genau der Bereich von 500–800 km Entfernung von der Plume-Achse, in dem die Unterschiede zwischen einem Plume, der auf den oberen Mantel beschränkt ist, und einem, der von der Kern-Mantel-Grenze kommt, auftreten. Um diese wichtige Frage in der Plume-Debatte zu beantworten, werden deshalb dort Stationen gebraucht. Deren Standorte sollten aber sehr sorgfältig ausgewählt werden, um die schwachen Effekte detektieren zu können. Die Qualität geht hier vor der Quantität, wobei eine gute azimutale Abdeckung dennoch nicht vernachlässigt werden darf. Hierbei kann als Hilfe für die Bestimmung sinnvoller Standorte die globale Seismizitätsverteilung dienen, die es erlaubt, Richtungen zu bestimmen, aus denen in der begrenzten Laufzeit eines Experiments mit hoher Wahrscheinlichkeit Aufzeichnungen von Erdbeben zu erwarten sind. Dies wurde am Beispiel von Island gezeigt. Solche Standorte sind gegebenenfalls nur mit Meeresbodeninstrumenten zu erreichen, es können aber – wie ebenfalls am Beispiel Island erläutert – auch weiter entfernte, existierende Permanentstationen dazu verwendet werden.

Ein entsprechendes Groß-Experiment zur Erforschung des Hawaii-Plumes wird gerade durchgeführt; in dessen Rahmen werden 72 Unterwasser-Instrumente auf dem Boden des Pazifiks im Abstand bis über 1000 km vom Plume aufgestellt. Durch die bestehende Meeresmikroseismik dort werden deren Aufzeichnungen insbesondere im langperiodischen Bereich brauchbar sein. Genau dieser aber ist von den Finiten-Frequenzen Effekten betroffen. Die Studie dieser Effekte in der vorliegenden Arbeit leistet einen Beitrag zur Interpretation der in diesem und zukünftigen Plume-Experimenten gewonnenen Daten.



# Contents

<b>Deutsche Zusammenfassung</b>	<b>i</b>
<b>Contents</b>	<b>ix</b>
<b>List of Figures</b>	<b>xi</b>
<b>List of Tables</b>	<b>xiv</b>
<b>Introduction</b>	<b>1</b>
<b>1 Mantle plumes and their seismic effects</b>	<b>5</b>
1.1 Plumes in the Earth's mantle . . . . .	5
1.1.1 The standard plume model . . . . .	6
1.1.2 Plume types: what else could plumes look like? . . . . .	10
1.1.3 Thermal Halo . . . . .	11
1.2 Seismological techniques for plume imaging . . . . .	12
1.2.1 General seismic effects of plumes . . . . .	13
1.2.2 Seismic Tomography . . . . .	14
1.2.3 Finite-frequency phenomena . . . . .	17
1.2.4 Finite-frequency tomography . . . . .	21
1.2.5 Other seismological techniques . . . . .	23
1.2.6 Plume projects and experiments . . . . .	26
1.3 Plumes – a key to geodynamic questions . . . . .	29
1.3.1 Whole or layered mantle convection . . . . .	30
1.3.2 Plumes and the Earth's heat budget . . . . .	31
1.3.3 Do plumes exist at all? – plume criticism . . . . .	33
1.4 Summary and Conclusion . . . . .	34
<b>2 A hybrid finite-difference method for global waveform modeling</b>	<b>35</b>
2.1 Introduction . . . . .	35
2.2 The finite-difference method . . . . .	36
2.2.1 Theory . . . . .	36
2.2.2 Finite difference methods for spherical media . . . . .	37
2.3 The hybrid finite-difference method . . . . .	39
2.3.1 Hybrid methods for global wave-propagation . . . . .	39
2.3.2 The hybrid axisymmetric / spherical section approach . . . . .	40
2.3.3 Verification . . . . .	44

2.3.4	Application of the hybrid approach . . . . .	45
2.3.5	Parallelization . . . . .	49
2.4	Discussion . . . . .	49
<b>3</b>	<b>Forward modeling of wave propagation through mantle plumes</b>	<b>53</b>
3.1	The Spectral Element method . . . . .	53
3.1.1	Basic principles . . . . .	54
3.1.2	Program SPECSEM3D for global wave propagation . . . . .	55
3.1.3	Seismogram format and data processing . . . . .	56
3.1.4	Plume models in SPECSEM3D . . . . .	57
3.2	Experiment configuration and data processing . . . . .	64
3.2.1	Modeled earthquake and epicentral distances . . . . .	67
3.2.2	Computation of the wavefield and processing of results . . . . .	69
3.2.3	Tools for seismogram analysis . . . . .	72
3.3	Results . . . . .	76
3.3.1	Travel-time delay shadows . . . . .	76
3.3.2	Evolution of travel-time delay along the great circle . . . . .	90
3.3.3	Evolution of amplitudes behind the plume . . . . .	103
3.4	Discussion and conclusions . . . . .	108
<b>4</b>	<b>Application to Iceland</b>	<b>111</b>
4.1	Iceland – the best studied plume on Earth . . . . .	111
4.2	The Iceland hotspot – state of the art . . . . .	113
4.2.1	General information, evolution, Geology . . . . .	113
4.2.2	Seismological and geophysical studies, plume parameters . . . . .	114
4.2.3	Iceland plume properties: summary and appraisalment . . . . .	130
4.3	The 1995 Peru earthquake and its records on Iceland . . . . .	130
4.3.1	The earthquake . . . . .	130
4.3.2	Data at Icelandic stations . . . . .	131
4.4	Synthetic data for the Peru earthquake . . . . .	132
4.4.1	Processing and comparison of seismograms . . . . .	132
4.4.2	Fk analysis . . . . .	133
4.4.3	Interpretation of synthetic results with respect to Iceland . . . . .	138
4.5	Summary . . . . .	142
	<b>Summary and Conclusion</b>	<b>145</b>
	<b>Bibliography</b>	<b>149</b>
	<b>Acknowledgements</b>	<b>163</b>
	<b>Curriculum vitae</b>	<b>165</b>

# List of Figures

1.1	Map showing the locations of hotspots/plumes on the globe . . . . .	6
1.2	Two possible plumes in the Earth . . . . .	7
1.3	Schematic illustration of a mantle plume, its possible effects and seismological techniques applied to explore them . . . . .	13
1.4	Illustration of the region sampled by regional teleseismic tomography experiments	15
1.5	Sketch illustrating wavefront healing . . . . .	18
1.6	Modeled wavefront healing for two anomaly magnitudes . . . . .	19
1.7	Finite-frequency sensitivity kernels for a P wave at a distance of 60°. . . . .	20
1.8	Conversions of teleseismic P waves at the upper mantle discontinuities . . . . .	24
1.9	Comparison of the Hawaiian island chain to Iceland . . . . .	27
1.10	Seismometer and OBS locations of the PLUME experiment . . . . .	28
2.1	Illustration of axisymmetry . . . . .	39
2.2	Illustration of the hybrid axisymmetric/3D-approach . . . . .	41
2.3	Flowchart of the hybrid code . . . . .	42
2.4	The hybrid grid (example for the SH case) . . . . .	43
2.5	Seismograms calculated with the hybrid code . . . . .	45
2.6	Legend to the snapshot figures of the hybrid code . . . . .	46
2.7	Snapshots of the wavefield as calculated with the hybrid code . . . . .	47
2.8	SH to PSV conversions . . . . .	48
2.9	The parallelization scheme for the hybrid code (axisymmetric SH, PSV and 3D)	50
2.10	The hybrid communication concept . . . . .	51
3.1	The meshing and mapping of the Spectral Element Method . . . . .	55
3.2	Simulated global seismograms – transverse component . . . . .	58
3.3	Simulated global seismograms – radial component . . . . .	59
3.4	Simulated global seismograms – vertical component . . . . .	60
3.5	Plume model created with the plume model subroutine of SPEC3D . . . . .	61
3.6	Velocity perturbation functions . . . . .	63
3.7	Array of virtual seismometers of this study . . . . .	66
3.8	Receiver rings around the plume center . . . . .	67
3.9	Location of epicenters of modeled earthquakes with respect to Iceland . . . . .	69
3.10	Ratio of plume diameter to wavelength as a function of depth for 20 s and 100 s	70
3.11	Seismograms for the P-wave for all plume models with radius=100 km . . . . .	71
3.12	Maximum cross-correlation coefficients for the P-phase, plume model P6 . . . . .	72
3.13	Ray-paths of phases used for deriving travel-time delays . . . . .	73
3.14	Travel time delay shadow perturbed by interference with another phase . . . . .	75

3.15	P-phase travel-time delay for a plume with a radius of 100 km and a sharp perturbation function . . . . .	77
3.16	Delay maps for the P-phase, $\Delta=90^\circ$ : comparison of the perturbation function . . . . .	78
3.17	Delay maps for the SS-phase, $\Delta=90^\circ$ : comparison of weak vs. strong plume . . . . .	79
3.18	Delay maps for the S- phase, $\Delta=90^\circ$ : comparison of origin depths . . . . .	80
3.19	Delay maps for $\Delta=90^\circ$ : comparison of SP and SKKS phases . . . . .	81
3.20	Delay maps for the SKS-phase, $\Delta=90^\circ$ , for several plume models . . . . .	83
3.21	Delay maps for $\Delta= 45^\circ$ and $135^\circ$ . . . . .	85
3.22	Delay maps for $\Delta= 45^\circ$ : comparison sS and ScS . . . . .	86
3.23	Frequency-dependent delay shadows for a sharp CMB plume at $\Delta=90^\circ$ . . . . .	88
3.24	P-phase travel-time delay as a function of epicentral distance: sharp r=100 km radius plume . . . . .	90
3.25	Ray paths of the P/P <sub>diff</sub> -phases for several epicentral distances . . . . .	92
3.26	Length of the P/P <sub>diff</sub> -phase path behind the plume and its depth at the plume location . . . . .	93
3.27	Frequency-dependent analysis of the P-phase delay time evolution with distance from the plume center (sharp CMB plume at $\Delta=90^\circ$ ). . . . .	94
3.28	P-phase travel-time delay as a function of epicentral distance and perturbation magnitude: sharp r=100 km-radius CMB-plume. . . . .	95
3.29	P-phase travel-time delay as a function of distance from the plume center: comparison of two origin depths . . . . .	96
3.30	P-phase travel-time delay as a function of epicentral distance: sharp vs. Gaussian r=100 km-radius plume. . . . .	97
3.31	P-phase travel-time delay as function of epicentral distance: Comparison between sharp and Gaussian perturbation function for two plume radii . . . . .	98
3.32	Wavelengths as a function of depth for several periods . . . . .	99
3.33	P-phase travel-time delay as a function of epicentral distance: comparison of CMB-plume models with r=60, 100 and 300 km radius, but the same integral perturbation. . . . .	100
3.34	P-phase travel-time delay as a function of distance for a plume from the CMB at $45^\circ$ epicentral distance. . . . .	101
3.35	P-phase travel-time delay as a function of distance behind the plume center, comparison of different epicentral distances . . . . .	102
3.36	Spatial distribution of P-phase amplitude ratios (PREM+Plume)/PREM for different plume models . . . . .	104
3.37	Frequency-dependent amplitude ratios (PREM+Plume)/PREM . . . . .	106
3.38	P-phase amplitude ratios of (PREM+plume)/PREM for three plume models with radii equivalent to 100 km . . . . .	107
4.1	Iceland and its surrounding with main geotectonic features . . . . .	112
4.2	Position of the Iceland plume with time (from LAWVER AND MÜLLER [1994]). . . . .	113
4.3	Azimuthal equidistant map of global seismicity centered on Iceland . . . . .	116
4.4	Histogram of number of earthquakes per epicentral distance for Iceland . . . . .	118
4.5	Histogram of number of earthquakes per back-azimuth from the Iceland plume . . . . .	118
4.6	Tomographic image by WOLFE <i>et al.</i> [1996]. . . . .	120
4.7	Horizontal slices through a finite-frequency tomography model of Iceland . . . . .	125
4.8	Bouguer anomaly map of Iceland from DARBYSHIRE <i>et al.</i> [2000] . . . . .	127



4.9	Map of Moho depth by DARBYSHIRE <i>et al.</i> [2000]. . . . .	127
4.10	Source-time function of the November 12, 1996 Peru earthquake . . . . .	131
4.11	Map of stations installed in and around Iceland . . . . .	132
4.12	Comparison of synthetic with real data for station BORG . . . . .	133
4.13	Illustration of the fk-analysis . . . . .	135
4.14	fk-analysis of the P phase window of the 1996 Peru event using HOTSPOT stations . . . . .	137
4.15	Delay distribution in Iceland for several back-azimuths (ScS phase at $90^\circ$ ) . . .	140
4.16	Delay distribution in Iceland for the PP and SKKS phase at $\Delta=90^\circ$ . . . . .	141
4.17	Delay distribution in Iceland for the SKS phase at $90^\circ$ : influence of the head . .	143

# List of Tables

3.1	Parameters of the plume models . . . . .	62
3.2	parameters of the modeled earthquakes . . . . .	68
3.3	phases picked for the three components and the different epicentral distances . . . . .	74
3.4	Maximum delay times of the SKS phase . . . . .	82
3.5	Parameters of the P-phase hitting a plume at $45^\circ$ from the epicenter . . . . .	103
4.1	Studies on the Iceland plume over time . . . . .	115
4.2	Summary of plume parameters as derived by Iceland studies . . . . .	129

# Introduction

“Au matin du départ il mit sa planète bien en ordre. Il ramona soigneusement ses volcans en activité. Il possédait deux volcans en activité. Et c'était bien commode pour faire chauffer le petit déjeuner du matin. Il possédait aussi un volcan éteint. Mais, comme il disait, ‘On ne sais jamais!’. Il ramona donc également le volcan éteint. S'ils sont bien ramonés, les volcans brûlent doucement et régulièrement, sans éruptions. Les éruptions volcaniques sont comme des feux de cheminée. Evidemment sur notre terre nous sommes beaucoup trop petits pour ramoner nos volcans. C'est pourquoi ils nous causent tant d'ennuis.”

ANTOINE DE S<sup>T</sup> EXUPÉRY, *Le Petit Prince*

The focus of this thesis is the application of seismic waves to study the origin and structure of hotspot volcanoes. With increasing computation power and the availability of computer codes for modeling three-dimensional wave-propagation at a global scale it is now possible to carry out a full-wavefield parameter study of the seismic effect of plumes at teleseismic distances. The goal is to overcome ray-theoretical deficiencies and to study the wave-effects of mantle plumes, the hypothesized cause of unusual hotspot volcanism.

In general, both volcanism and earthquakes are closely related to plate tectonics – volcanoes and epicenters mostly concentrate at plate boundaries. An exception is ocean island volcanism: so-called “Hotspots” with no obvious link to plates. On the contrary, they seem to be stationary in time while plates are moving across them, with Hawaii being the classic textbook example. WILSON [1963, 1965] realized the importance of hotspots for constraining plate motions, he found that hotspots seem to be fixed in space over time relative to each other, thus providing a reference frame for the motion of plates throughout Earth's history.

However, the reasons for this “hotspot fixity” remained elusive, until MORGAN [1971] came up with his mantle plume hypothesis, suggesting columnar upwellings from the lowermost mantle as the *underlying* mechanism for hotspots. The plume model became very popular and well accepted, able to explain several features within the Earth. Only a proof, in terms of pictures of mantle plumes that could reveal their dimensions and their origin, has yet to be provided, though answers to these questions would give important constraints on key geodynamic parameters, such as the total heat flow from the core. Moreover, a decision upon the classic conflict between geophysics and geochemistry whether mantle convection takes place as whole mantle convection or has to be layered for preserving geochemical reservoirs could possibly be found by showing either that plumes come from the lower mantle (i.e., the core mantle boundary region, as originally suggested by MORGAN) or that they originate at the bottom of the transition zone.

Seismic tomography offers the highest-resolution imaging technique for delivering pictures of the Earth's mantle. Waves of larger earthquakes are travelling through the entire body of the Earth and are recorded as seismograms at hundreds of stations of the Global Seismic

Network (GSN) and several high density regional networks (e.g., the German Regional Seismic Network, GRSN). The information contained in these seismograms is used to invert for the seismic velocities in regions of the Earth that have been sampled by the waves, just like in a computer tomography scan of a human's body in medicine. In seismic tomography, the underlying principle is that waves travelling through a low-velocity zone, such as a plume, take a longer time to arrive at the seismometer than waves running through an established average Earth model with a velocity distribution that is only depth-dependent. These travel-time delays (or early arrivals for high-velocity objects) are used to mathematically infer the object's seismic velocity perturbation.

However, unlike in medicine where artificial sources are used and can be moved around the patient's body, the locations where earthquakes occur are predetermined by nature and are concentrated at plate boundaries. Additionally, seismometers could — up to some years ago — only be operated on land. Possible locations of seismometers are therefore restricted by the uneven land distribution on planet Earth. Thus, due to the reduced combinations of earthquake and seismometer locations it is likely that certain points of the Earth's interior are less sampled by recorded waves, making it more difficult to retrieve their properties.

Therefore, global mantle tomography studies suffered from a relatively low resolution, corresponding to wavelengths of less than 1000 km, in some places possibly 500 km (ROMANOWICZ [2003]). Nevertheless, this resolution was sufficient to provide the first pictures of subducting slabs which showed that they indeed penetrate the lower mantle. This seemed to confirm the idea of whole mantle convection. However, such observations were sparse and the images of plumes remained a key to this question. Unfortunately, contrary to slabs, plumes are expected to be smaller in size and as low-velocity bodies they are subject to diffraction or specifically to healing effects, making them harder to detect with seismic travel-time delays.

As an alternative, local tomography studies with dense arrays above the plumes have been carried out with large and expensive dedicated experiments. Examples relevant for this work are the ICEMELT (1993-1996) and HOTSPOT (1996-1998) experiments on Iceland and the largest seismic experiment in Germany ever, focussing on the Eifel plume region (1997-2001).

Apart from the latter mentioned continental example, local or regional plume tomography studies have always been difficult due to oceanic seismic noise since most of the classic plumes lie beneath ocean islands (e.g. Hawaii, Iceland, the Azores). The advent of broadband seismometry made it possible to also record and use longer periods that are not as much affected by oceanic noise than the classically used period range of 1–5 seconds. The emergent onsets of phases on low-period seismograms were harder to pick, thus, the measurement of arrival times was more and more carried out using cross-correlation techniques.

However, despite an early warning by WIELANDT [1987] and long-standing knowledge in optics that ray theory is no longer valid for these relatively low frequencies, mantle tomography was still based on the ray (i.e. infinite-frequency) approximation. The problem with plumes being low-velocity objects is that waves that are running around them at normal, i.e., faster, velocity are diffracted into the region behind the object (following Huygens principle (1690)), thus arriving earlier than the delayed waves running through it. This “wavefront healing” masks and thus eliminates the travel-time delay of the plume which makes it difficult to image plumes and leads to an underestimation of their velocity perturbation.

MARQUERING *et al.* [1998] quantitatively introduced wave theory to this problem and came up with pictures of the spatial distribution of the sensitivity of waves, so called “sensitivity kernels”. These showed that — in contrast to ray theory — the sensitivity of a wave with a finite (i.e. low) frequency content is zero right at the position of the classic ray. The seis-

mological community began to realize that ray tomography, violating its assumptions under the circumstances of how it was used at that time, is no longer suitable for some questions in global seismology. In the following years finite-frequency theory was developed (e.g. DAHLEN *et al.* [2000]), overcoming the limitations of ray-theory by taking into account wavefield effects, and leading finally to the realization of the first global finite-frequency tomography study (MONTELLI *et al.* [2004b]).

Apart from the direct imaging of plumes using tomography, many attempts have been made to find seismic evidence for plumes. In the mid 80's the region that MORGAN postulated to be the source of plume, i.e., the lowermost mantle and especially the core mantle boundary (CMB) region, attracted more and more interest. The 200–250 km above the CMB at 2900 km depth, called D" layer after the old nomenclature of Bullen, turned out to be laterally highly heterogeneous (e.g. GARNERO AND HELMBERGER [1986]), comparable to the other thermal boundary layer of the Earth, the lithosphere. Ultra-low velocity zones (ULVZ) were detected and identified as plume sources, a global correlation between these zones and the current hotspot distribution was shown (e.g. THORNE *et al.* [2004]).

At the same time, using a technique called “receiver functions”, seismologists started to map the depth of the two major seismic discontinuities that form the boundaries of the transition zone between the upper and lower mantle. Since these discontinuities are thought to be caused by phase transitions, their depths should change upon the passage of a plume due to its effect on the pressure and temperature conditions. In fact, the expected resulting thinning of the transition zone could be found at plume locations (e.g. SHEN *et al.* [1998]). What was still missing, was the convincing image of the connection between all those features in the form of a continuous plume-like low-velocity anomaly.

This fact was taken advantage of in the late 90's when, under the leadership of reputable geophysicist DON ANDERSON, some scientists began to put the plume hypothesis into question. With results of the Iceland plume tomography studies, in which some of the plume opponents were involved, they tried to disprove the core-mantle boundary origin of one of the two classic textbook plumes. However, due to the extent of the used seismometer arrays that were restricted to the land mass of Iceland it was not possible to get resolution below about 450 km and all the arguments for an origin at the 660 km discontinuity were thus speculation. To extend the aperture of the array to look deeper beneath Iceland and to answer the question of the origin depth of the Iceland plume, seismometers on the seafloor would be necessary. The development of such instruments (ocean bottom hydrophones (OBH) or seismometers (OBS)) led to the first usable, yet very expensive instruments in the mid nineties. The question of the optimal array configuration therefore became more important.

It was at the beginning of this thesis work that the following questions were raised: Do plumes in Morgan's sense exist? Where does the Iceland plume originate? Is there a continuous low-velocity anomaly connecting ULVZ at the CMB through the thinned transition zone and further up to the hotspot location, the surface expressions of plumes? Can we proceed with ray-theory tomography to image plumes? Do we have to extend land-based experiments to the seafloor using expensive ocean-bottom seismometers? Where to put these instruments best to capture the piece of information missing? And finally: can we afford to only use the first-onset travel-time information rather than the entire information about the plume that might be given over the full length of the seismograms – not only in the timing of onsets but also in the waveform?

This thesis focuses on the whole-wavefield aspect of the plume's seismic signature which takes into account finite-frequency effects that have been neglected in plume studies for a long

time. In this work a study of the sensitivity of the wavefield parameters such as travel time and amplitudes on plume parameters is carried out in order to derive appropriate seismic phases and seismometer locations for imaging plumes with seismic data. Such a study requires 3D calculations of global wave propagation.

The first chapter reviews the current idea held by Earth scientists concerning the state of the mantle and more specifically of plumes. The simple head-tail model is presented as well as current more sophisticated ideas of what plumes may look like. The effects of plume-like vertical low-velocity zones on the seismic wavefield are discussed and an overview about seismological techniques and their limitations for imaging plumes is given. The importance of taking into account wavefield effects for seismic investigations of plumes is emphasized by illustration of wavefront healing. Projects for imaging plumes are presented, with the current PLUME project targeting Hawaii being an example for the importance of long-period information for oceanic plume studies. The chapter is concluded with a demonstration of the role of plumes as a key to geodynamic questions.

In the second chapter a new method for forward modeling of global seismic wave propagation through confined 3D structures is presented. It is a hybrid approach combining existing finite-difference method algorithms in order to eliminate their respective drawbacks for studying localized 3D mantle features. The used algorithms and their coupling are described, the method is verified and an application with a plume model is shown.

Chapter 3 begins with the description of a 3D spectral-element method program for global wave-propagation modeling and its extension for incorporating plume models.

Thereafter, results of numerical modeling of three-dimensional wave propagation through mantle plume models at teleseismic distances are presented and discussed. The effects of the presence of a plume is examined in terms of travel-time delay maps, the evolution of the delay along the great-circle through epicenter and plume, and amplitude changes due to focussing caused by the plume. The focus of this part lies in the wavefield effects and the differences to what is expected from ray-theory.

Iceland, the surface expression of the textbook example of a ridge-centered plume, is subject of Chapter 4. Iceland has the advantage of being an oceanic hotspot yet has a large land-mass to install seismometers on. It has therefore been the target of numerous recent studies the most important of which are reviewed. The usefulness of applying a seismic array technique to the Iceland plume is explored and the results of Chapter 3 are interpreted with respect to the Iceland plume.

# Chapter 1

## Mantle plumes and their seismic effects

In the following we introduce the concept of mantle plumes and review plume studies – going from the simple traditional model to recent more sophisticated ideas with the goal of learning what reasonable bounds for plume parameters are in terms of shape, width, perturbation and depth extent. This information is used in the second part of this thesis for setting up plume models for a numerical wave-propagation study. Moreover, the models suggested for plumes provide open questions about the properties of actual plumes. One of the aims of this thesis is to explore, whether we can distinguish the suggested parameters of plume properties in seismic data.

In the second part of the chapter seismic effects of plumes and the resulting seismological techniques to image plumes are discussed. The focus lies on tomographic methods, currently providing the highest resolution for plume imaging, and especially on the wavefield aspect – in contrast to the ray-theoretical approximation – and its importance for seismological plume studies.

The chapter ends with motivating why we should care about plumes: they may be a key to a couple of geodynamic questions.

### 1.1 Plumes in the Earth’s mantle

JASON MORGAN suggested in 1971 that about 20 plumes from the lower mantle bring heat and primordial material up under the asthenosphere. There, it spreads out radially and is the major driving force for plate motion. He claimed that mid-oceanic rises are passive features of convection and that the pull of the sinking plates (slabs) does not provide the major tectonic stress. With this “plume hypothesis” MORGAN has given a dynamically consistent model for the occurrence of hotspots (WILSON [1963, 1965]) – volcanic centers with no obvious link to subduction – and their relative fixity with respect to plate motion.

The plume/hotspot concept has attracted a lot of interest, especially in the last two decades. Several new hotspots with assumed underlying plumes have been suggested; hotspot lists today range from the originally proposed 20 to more than 100, while the number of plumes varies between nine (COURTILLOT *et al.* [2003]) up to an estimate of about 5 200 plumes in total (MALAMUD AND TURCOTTE [1999]). Figure 1.1 shows the location and heat flux of the 20 most researched hotspots.

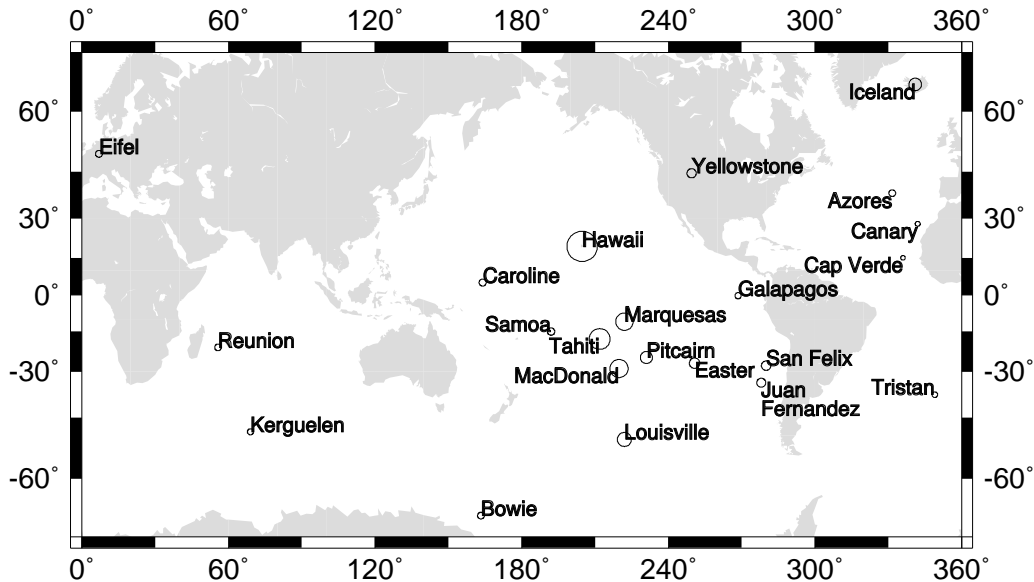


Figure 1.1: Map of hotspot location or of occurrence of volcanism without obvious link to plate tectonics that might be related to an underlying plume. The size of the circles reflects the estimated plume flux, as given in SLEEP [1990].

The term “plume”, in its general meaning, refers to any kind of localized flow of material due to buoyancy. Buoyancy is caused by a density difference which can be of thermal or compositional origin: on the one hand hotter matter has less density than colder material, due to thermal expansion. On the other hand, there might also be a density difference between materials with the same temperature but with a chemically different composition. In both cases the lighter material tends to flow against the direction of gravity, unless resistant forces such as viscosity inhibit the flow.

Although it is clear that there are compositional differences in the Earth, and probably also within the mantle, the theory of plumes has been developed mostly for thermal buoyancy. In the next subsection, a summary of important aspects of the thermal plume concept is given, while deviations or sophistications of this simple model will be discussed in the subsequent subsection.

### 1.1.1 The standard plume model

For the generation of thermal plumes a thermal boundary layer is required. In the Earth, even if there is some uncertainty in the geotherm, the major boundary layer is the core-mantle boundary. Since MORGAN [1971] suggested plumes come from the lower mantle the core-mantle boundary origin is also consistent with the original idea of mantle plumes. The term plume is not very well defined (a considerable source for misunderstanding in the “plume



debate” of recent years), thus, it might be helpful to define plumes coming from the lowermost mantle as “Morganian plumes” (see COURTILOTT *et al.* [2003]).

In the following, we will follow such a “Morganian plume” from the CMB all its way up to the surface and discuss the main associated effects which might be detectable with geophysical and especially seismological techniques that are reviewed in the next section.

As already mentioned, the core-mantle boundary is the primary candidate for a thermal boundary layer (TBL) that might (literally) give rise to a thermal plume. Another candidate is an important seismic discontinuity at a depth of 660 km (referred to as the “660-discontinuity”, see Fig. 1.2) contradicts the lowermost mantle origin and is discussed later.

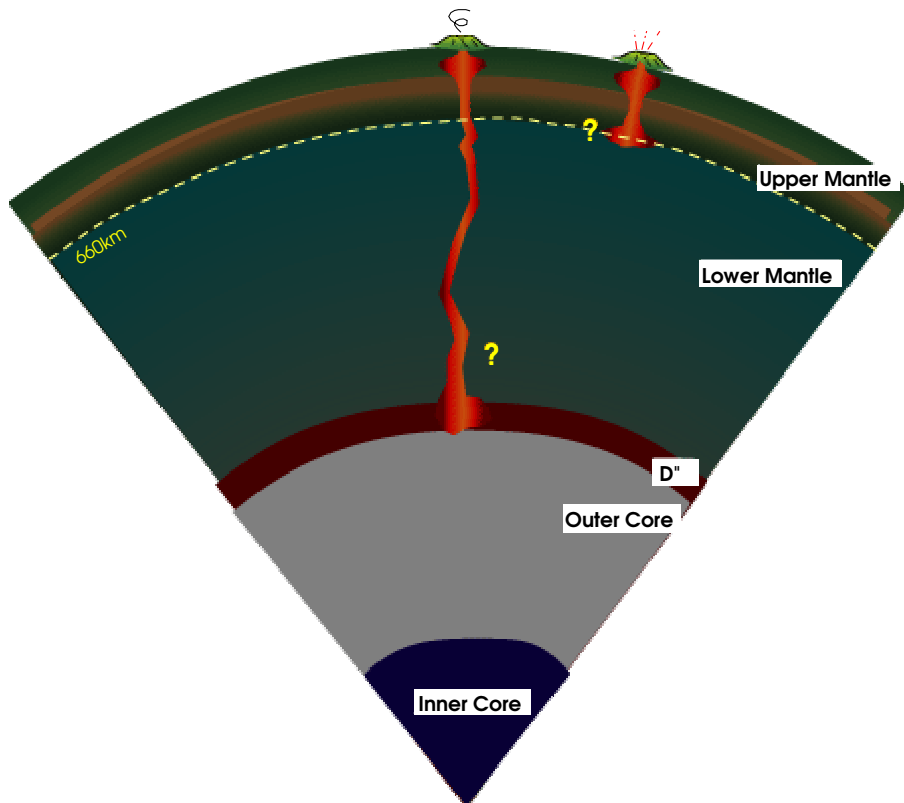


*Figure 1.2: Illustration of plumes in the Earth, generating hotspot volcanism. Two possible plume-origin locations are shown, the core-mantle boundary and the 660-discontinuity. MORGAN [1971] in his original paper suggested a source in the lower mantle. Nowadays it is commonly assumed that plumes tap the so called D''-layer at the bottom of the mantle. Figure modified after <http://mahi.ucsd.edu/Gabi/plume.dir/mantle-slice.gif>.*

From the discontinuity of adiabatic temperature curves between the core and the lower mantle the temperature jump across the CMB is estimated to be 800–1000° (JEANLOZ AND MORRIS [1986]). Others give values of 840° (STACEY AND LOPER [1983]) or more than 1300° (BÖHLER *et al.* [1995]). If plumes originate in the CMB region their buoyancy should be driven by this temperature contrast. The estimated excess temperature of plumes in the upper mantle as derived by seismic studies, however, is only 200–300°. Cooling of the plume by heat conduction or entrainment of mantle material (described later) can not explain this discrepancy. A possible explanation is the existence of a compositionally denser layer at the

bottom of the the lowermost mantle (the “D” region”). Another reason for the difference in plume excess temperature values is the usage of ray-tomography, that probably underestimates the actual seismic velocity effect and thus temperature excess of a plume. This is one of the main issued treated in this thesis and will be explained in detail later in this chapter. Moreover, the conversion between seismic velocities and temperature relies upon relatively simple assumptions.

Lower mantle seismic anomalies in the CMB region show an anticorrelation between shear wave velocity anomalies and bulk sound speed (FARNETANI AND SAMUEL [2005]) which also suggest a thermo-chemical origin of plumes. However, in the following we will still assume a thermal plume and discuss possible effects of compositional buoyancy when necessary. Apart from a TBL plumes need a lateral variation of temperature in order for an initial instability to form. Today there is seismic evidence that the D" region is very heterogeneous, probably as much as the crust, which is the upper TBL. For example subducting slabs after sinking down to the core-mantle boundary (“graveyard of slabs”, e.g., GREEN [2001]) could modulate heat flow from the core, thus – among other mechanisms – providing lateral variations of temperature across the TBL. With the discovery of pronounced ultra-low velocity zones (ULVZ) at the base of the mantle (GARNERO *et al.* [1993]), there is also evidence for partially molten material at this depth.

Consequently, seismologists looked for a spatial correlation between ULVZ locations in the lowermost mantle and hotspot locations. Such a correlation could be found (e.g. WILLIAMS *et al.* [1998]), however with a tendency that the locations of hotspots lie near edges of low-velocity regions. THORNE *et al.* [2004] showed a geographic correlation between hot spots and lateral shear wave *gradients* in the lowermost mantle. So there is evidence for a CMB origin of plumes and associated lateral temperature variations.

A locally elevated temperature makes the material there buoyant with respect to the surrounding region. It therefore rises in the form of a dome structure and finally evolves into a large diapir, the leading “plume head”. The head is followed by a tail (e.g., WHITEHEAD AND LUTHER [1975]), which is smaller in diameter, maybe only about 20 km (LOPER AND STACEY [1983]), acting as a conduit. When rising towards the surface, the plume reaches the 660-discontinuity. The reason for a jump in seismic velocities at the depth of 660 km is thought to be a phase transition from Perovskite, the dominant lower-mantle mineral, to Ringwoodtite (Gamma-Spinel). Such a phase transition has been observed in laboratory measurements under pressure (P) and temperature (T) conditions realistic for the mantle at this depth. The phase transition has a negative slope in the P/T-curve (Claudius-Clapeyron-slope, or “Clapeyron slope”) of about  $-2$  MPa/K (CONDIE [2001]).

The passage of hot material, such as a plume, from beneath would lift the phase transition to occur at shallower depth, thus reducing its lateral density deficit. In case the density increase caused by the phase transition balances or even exceeds the density contrast of the plume there would be no negative net density difference anymore and thus no driving buoyancy force for the plume to rise: the plume would be stuck under the 660-discontinuity and would not be able to penetrate the upper mantle (a mechanism that would explain layered convection, discussed later in this chapter). Though this might be the case for plumes with low buoyancy flux, there is evidence that some plumes do cross this discontinuity and continue to rise. Even for plumes that are strong enough to pass this barrier, the resistance to penetration of the upper mantle exerted by the 660-discontinuity is likely to bulge the plume conduit below it. However, after passage of the discontinuity the viscosity will likely be lower in the upper mantle which reduces its resistance against plume flow and is leading to a higher speed of rising material in the plume

conduit and thus to a smaller radius. Thus, around the 660-discontinuity a modulation of the width of the plume conduit is likely.

The next major seismic discontinuity lies at about 410 km depth (the “410 discontinuity”). The sudden change in seismic velocities and density there is commonly explained by the fact that Olivine, the major upper mantle mineral transforms to Wadsleyite, a much denser phase of the same chemical composition. In this case, the Clapeyron slope is positive and thus enhances buoyant flow across the discontinuity.

Under the lithosphere the plume material is spreading radially outward and might be taken away by the drag of the overlying plate (SLEEP [1990]). The flow of material against the lithosphere creates a dynamic force that produces a swell (typically 1 000–2 000 km in diameter, elevation of 1 000 m or more) of the plate.

The swell has a large gravitational effect, it causes a geoid high. The bathymetric effect of the swell dominates over the influence of the density reduction in the plume (e.g. KEAREY AND VINE [1996]) leading to a net high in gravity. Only after its correction the influence of the mass deficit in the plume is visible as a low in the Bouguer gravity map (see Fig. 4.8 for the Iceland case).

By decompression upon rise, a part of the plume material melts, rises further and creates hotspot volcanism. This volcanism is distinct in its origin and chemistry from arc volcanism where at convergent plate boundaries (subduction zones) slabs with water saturated sediments penetrate the mantle and heat up. Here as well partially molten material rises, however, with a different chemical composition.

Due to the head-tail structure, there are two stages of volcanism created by plumes (MORGAN [1981], RICHARDS *et al.* [1989]). The head, when reaching the surface, creates large igneous provinces (LIPs). LIP is the collective term for large volumes of dominantly igneous mafic rock (e.g. ANTRETTTER [2001]) emplaced in relatively short time periods (episodic: less than 1 My, RITSEMA AND ALLEN [2003]) with no obvious relation to plate tectonics. LIPs may exist as oceanic plateaus, continental flood basalts, ocean basin flood basalts, passive margin volcanics, or submarine ridges (e.g. ANTRETTTER [2001]).

When the head is exhausted or dragged away by motion of the overlying plate, the plate continues to move over the stationary plume source. As a consequence of ongoing volcanism a track of seamounts or, if reaching the water surface, a chain of volcanic islands is created, consisting of Ocean Island Basalts (OIB). The origin of the chemical composition that defines OIB is thought to be the plume conduits. Due to continuous motion of the overlying plate there is an age progression of the volcanic activity from the LIPs to and along the hotspot track.

A prominent example for this sequence is the Réunion hotspot. The Deccan traps, a region of flood basalts covering large parts of India is considered the remnants of its head (e.g. SLEEP [1990]). It is connected to the Cagos-Laccadive Ridge, and, with an interruption around the Central Indian Ridge, with the Mascarene Plateaux, and finally with the island of Réunion, a volcanically active ocean island. The interruption of a hotspot track when passing a spreading center (ridge) is typical, the hotspot activity jumps from one plate to the other (SCHUBERT *et al.* [2001]). In other cases, such as Iceland, the plume is capturing a segment of the ridge, leading to ridge jumps (see Chapter 4).

Until now, we looked at plumes as features independent of the rest of the mantle, ignoring its large scale Rayleigh-Bénard convection. To a first order this is justified, since plumes rise much faster ( $10^5$ - $10^6$  yrs) than the time scale of convective overturn ( $10^9$  yrs) of the mantle, what explains that plumes seem to be relatively stationary sources for hotspot volcanism.

STEINBERGER AND O'CONNELL [1998] and STEINBERGER [2000] studied the fate of plumes in a convecting mantle, and examined the deflection of plumes by “mantle wind”, an allusion to what happens with a smoke plume in the atmosphere. Using several mantle models and two plume origin depths (D" for plumes with head and 660 km for plumes without) they obtain tilted plume conduits and moving hotspots that explain observations mostly as good as, or even better than, fixed hotspot models.

For example in Iceland, SHEN *et al.* [2002] find that the signature of the plume in terms of a thinned transition zone is shifted with respect to the plume anomaly in the upper mantle, as mapped by seismic tomography. They infer a tilt of the conduit of at least  $9^\circ$  to the south.

In summary, plumes are considered the active upwellings from a heated basal boundary layer (i.e., the CMB), while sinking slabs are the active downwellings. Mid-Ocean ridges, in contrast, are passive upwellings, closing the gaps left by the plates pulled down at subduction zones (MORGAN [1971]).

### 1.1.2 Plume types: what else could plumes look like?

Apart from the likely oversimplified classical ‘large head – vertical tail’ structure there are many other models that were suggested when scientists skipped zero-order approximations and moved on to more complex models, both experimental and numerical ones.

In the following, some of these studies are briefly reviewed in order to illustrate the bandwidth of possible manifestations of plumes and the associated unsolved questions about their actual shape, structure and dimension. On the one hand, this helps constraining parameters for the forward-modeling study, on the other hand it will become evident that it is not possible to sample the entire parameter space spanned by these studies and that it is necessary to concentrate on the basic properties.

COURTILLOT *et al.* [2003] try to classify plumes into three different categories using a ranking scheme defined on the fulfillment of a list of plume criteria. This list consists of the existence of a chain of volcanic centers with monotonous age progression, flood basalts at its origin, a high buoyancy flux, a high ratio of the Helium isotopes  $^3\text{He}/^4\text{He}$ , and a low-velocity anomaly for shear waves.. They find only nine plumes fulfilling at least three of the criteria which are considered “primary” plumes by the authors: Afar, Caroline, Easter, Hawaii, Iceland, Louisville, Réunion, Samoa and Tristan. These plumes are thought to be consistent with Morgans’s theory and thus rise from the lowermost mantle. The plumes – with the exception of Iceland – are located at the margins of the two, likely compositional, superplumes beneath western Africa and French Polynesia. A second type of plume in their model originates from the top of the superplumes, which themselves are stuck below the transition zone. The lack of flood basalts of these transition-zone plumes is explained by the fact that production of LIPs would require melting  $10^8 \text{ km}^3$  of mantle material, which would fill large parts of the upper mantle. The criterion for primary plumes, i.e., LIPs and long-lived plume conduits can thus only be produced at depths much deeper than the transition zone.

The approximately 20 hotspots that are neither primary plumes nor have their surface signature on top of the large superplumes are considered “Andersonian” type (named after the plume opponent ANDERSON, see below), i.e., of asthenospheric origin.

CSEREPES AND YUEN [2000] suggest a partially penetratable 660-discontinuity with what they call a second asthenosphere beneath it. Fed from this low-viscosity zone, plumes rise through the 660-discontinuity to the surface. These plumes represent the counterparts of slabs passing the 660 from the upper mantle in form of avalanches after accumulating above

the 660-discontinuity for some time. Cerepes and Yuen show – using numerical modeling – that such plumes can exist, would be vigorous, rise fast, and develop large plume heads, as would be necessary to create flood basalts.

MALAMUD AND TURCOTTE [1999] set up a heat budget for the Earth and assume that the entire heat from the core comes from plumes. They extrapolate the frequency-size distribution of known plumes to find the number of smaller plumes that are not recognized since they lack a clear hotspot characteristic. The authors settle on a total number of 5 200 plumes. They suggest the many small-scale seamounts, e.g., in the Pacific, as being the signature of these plumes.

The studies of COURTILOT *et al.* [2003] with nine “real” plumes and MALAMUD AND TURCOTTE [1999] represent end-members concerning the number of plumes in the mantle.

FARNETANI AND SAMUEL [2005] question the head-tail structure of plumes. They find – using numerical modeling of thermo-chemical convection – that a head-tail structure is not required for deep seated plumes and thus that the absence of a head is not a sign for a non-deep origin of the plume. Moreover, plume conduits might be laterally heterogeneous due to chemical heterogeneities in the lower mantle. Furthermore, the narrow conduit model for purely thermal plumes is replaced by a variety of possible shapes and sizes of plumes, when considering thermo-chemical convection. Indeed, their plume models look much like the images from finite-frequency tomography (example see Fig. 4.7) rather than the symmetric idealized looking plumes from conventional models.

DAVILLE AND VATTEVILLE [2005] remind us of the transient nature of plumes. They carry out experiments for demonstrating the life cycle of a plume. Plumes develop and if their reservoir is exhausted they die from bottom to top and then fade away by thermal diffusion. The authors warn to interpret the snapshots of the current state of mantle convection delivered by seismic tomography in terms of depth of origin of plumes, since it is not clear at which state of their lives we see plumes today. For example, plumes may seem to originate in the mid-mantle while they are only disconnected from their source at greater depth. Moreover, they find in their experiments that textbook plumes with head and tail are only a short transient feature in the life time of a plume and not deriving this picture by tomography should not be interpreted in terms of non-existence of deep plumes. They suggest that the variety of plumes we “see” today may just be varieties of stages in plume evolution rather than a variety of plume types.

### 1.1.3 Thermal Halo

Up to now we only considered the thermal properties a plumes insofar as their temperature excess with respect to the surrounding mantle provides the driving force for their upward motion. In the following the lateral thermal structure of a plume with time is discussed since it influences the spatial distribution of seismic wave-speeds. In turn, seismic studies might be able to tell something about the temperature distribution and thus age of a plume. The question as to whether seismic methods can resolve the lateral perturbation function and thereby separate the contribution of the conduit from its halo is investigated in Chapter 3.

The upward flow of hot plume material leads to conduction of heat out of the plume. Since the rise speed of the material ( $\approx 1.6\text{--}4.8$  m/yr, LOPER AND STACEY [1983], 1.7 m/yr (TRYGGVASON *et al.* [1983], extreme values of up to 20 m/yr (LARSEN *et al.* [1999]) is much faster than the progress of the temperature front due to heat conduction, no significant cooling of the plume conduit takes place.

Nevertheless, on the long term the surrounding material is heated and the plume develops a “thermal halo” with time. Since seismic methods – via the seismic velocities – are sensitive to the temperature, they also sample the halo, not only the small conduits. The latter would lie below the resolution of any seismic method, if values for the conduit radius of only about 10 km, as given by LOPER AND STACEY [1983] are realistic.

For typical heatflow values for a weak, an intermediate and a strong plume (3, 30, 300 GW) SCHUBERT *et al.* [2001] give radii for thermal halos of 54, 96, and 170 km, respectively. It is therefore reasonable to not directly compare plume diameters from numerical simulations of flow with diameters from seismic images.

The halo effectively insulates the plume conduit and prevents a major loss of temperature of the plume material in the conduit upon rise (GRIFFITHS AND CAMPBELL [1991]). This ensures that the thermal signature of the plume is not lost at depths that are probed by the regional tomographic experiments described later. However, due to the lower pressure in the plume stem, colder mantle material is driven towards the plume, thus reducing the width of the halo again (LOPER AND STACEY [1983]; SLEEP [2004]).

The idea of axisymmetric plumes resulting from the thermal halo concept has recently been questioned by FARNETANI AND SAMUEL [2005] who show that in case of a thermo-chemical plume that would rise from a heterogeneous D" source region the conduit itself may be laterally heterogeneous.

The material surrounding thermal plume *heads* (which – in contrast to tails – are limited in their vertical extension) is heated by the head, becomes buoyant and rises with, and is eventually entrained into it. For purely chemical plumes, there would be no entrainment, which is a thermal effect, thus they would have smaller heads (GRIFFITHS AND CAMPBELL [1991]). Compositional buoyancy is also not subject to thermal diffusion (GRIFFITHS AND CAMPBELL [1991]), in contrast to thermal buoyancy where thermal conduction takes place. For mixed compositional and thermal plumes, the compositional and thermal effect would be decoupled (FITTON *et al.* [1997]).

## 1.2 Seismological techniques for plume imaging

“Seismic imaging of mantle plumes is still in its infancy but should soon become a turbulent teenager”

JEAN-CLAUDE NATAF, 2000

In this section the seismic effects of plumes are discussed with a focus on the wave aspect – in contrast to considering the approximation of infinite-frequency rays. Seismological techniques that explore these effects for imaging plumes are described and two examples of seismic experiments targeting at plumes are presented. This is done in order to provide a basis for understanding the plume wavefield effects modeled in Chapter 3 and for judging their relevance with respect to the usability for real experiments and existing techniques.

### 1.2.1 General seismic effects of plumes

All the properties of mantle plumes described in the last section, lead to physical effects that can be assessed with geophysical measurements. Thus, for obtaining an image of the Earth's interior several geophysical methods exist with seismic tomography having the highest resolution. High resolution is required for imaging plumes, since the thermal anomaly of the plume conduits are expected to have a diameter on the order of 200 km or even less. Apart from seismic tomography for the imaging of plumes there are several other seismological techniques providing information about the possible structure of a plume. An overview of these methods and their target regions is given in Fig. 1.3.

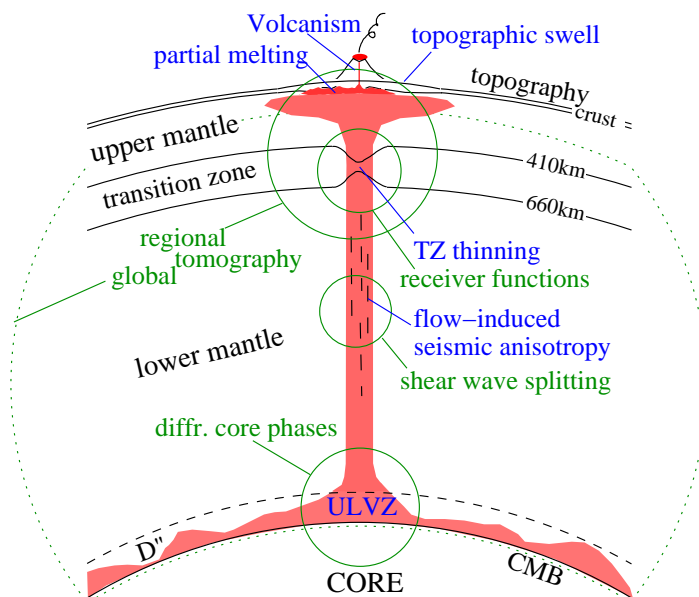


Figure 1.3: Schematic illustration of a mantle plume (red), its possible effects (blue annotations) and seismological techniques applied to explore them (green annotations).

The thermal effect of a plume lowers the seismic wave speeds by about 1% and 1.7% per  $100^\circ\text{K}$  for compressional ( $v_P$ ) and shear waves ( $v_S$ ), respectively. Furthermore, it deflects the discontinuities of the transition zone, with the 410 discontinuity becoming 8 km per  $100^\circ\text{K}$  deeper and the 660 discontinuity being elevated by 5 km per  $100^\circ\text{K}$  (JULIAN AND FOULGER [2003]). The resulting travel-time perturbations of direct or converted waves are used by tomographic methods, precursor studies or the “receiver function” technique to derive the plume location and size. Flow of material into the plume conduit, in the conduit itself and away from it into the plume head is expected to result in direction dependence of seismic wave-speed. This seismic anisotropy causes shear waves to split up in a faster and a slower wave, with a measureable difference in arrival time between the two phases in a seismogram. Analysis of this data helps to constrain the flow regime in the mantle and in a plume. Waves diffracting around the core are very sensitive to the structure of the core-mantle boundary region. Since this is likely to be the location of plume origin, studying core-diffracted waves might shed light on the sources of plumes. Partial melting due to the hot material affects the wave speeds for shear waves and compressional waves to a different amount. The same is true for compositional buoyancy. Thus, looking for a correlation or anti-correlation of the two wave speeds gives hints

about the state of the plume material. The importance of this is exemplified by residuum (melt extracted) mantle – peridotite – which is buoyant, but has *higher* wave speed than its parent fertile peridotite (JULIAN AND FOULGER [2003]). This corrupts the general assumption for the interpretation of tomographic results that seismically slower material reflects hotter material. Thus, it is useful to monitor any possible compositional heterogeneities to prevent misinterpretation.

The seismological methods for exploring the effects are described in the following sections.

### 1.2.2 Seismic Tomography

We start with a basic introduction to seismic tomography in order to provide a basis for a more detailed and also critical discussion of this key technique for imaging plumes – also for the non-seismologists.

Tomographic inversion – generally spoken – is deriving the distribution function of some material property from integral values measured outside the object under study (e.g. AKI AND RICHARDS [2002]; a detailed introduction is given by BLEIBINHAUS [2003]). In seismic tomography the object of interest is the Earth (in its entirety or parts of it) the integral values are the travel times or the derived travel-time perturbations from earthquakes measured with seismometers at or close to the Earth’s surface.

In the following, the ray-theoretical description is used. In this theory, strictly only valid for the infinite-frequency limit of waves, a wave is described as a ray, directed perpendicular of the wavefront. If a ray travels through a low-velocity body, such as a plume, it acquires a travel-time delay with respect to a neighboring ray traveling in the unperturbed medium. Of course, when measuring this travel-time delay from a seismogram one does not know where the delay is acquired since it is in principle an integral effect over the entire path of the ray. If other rays travel through the same low-velocity object (and again others do not) this ambiguity can be resolved by back-projection, and the location, size and velocity perturbation can theoretically be obtained. However, in the real world the ideal conditions necessary are not met for seismic tomography. A high density of crossing rays necessary for inversion is lacking and the method described above assumes infinite frequency of the waves.

Apart from seismology, tomographic methods for imaging a body is used in medicine where much better conditions are met. This leads to high-resolution pictures of the human body not achieved for the body of the Earth. Apart from the limited ray coverage of the Earth (see below), other differences between seismic and medical tomography are that the ray approximation is entirely valid for medical tomography, and that rays in medical tomography can be regarded as being straight lines, and thus have known paths. This is not the case for the Earth due to uneven distribution of earthquake and seismometer locations and because of the ratio of the size of the Earth’s heterogeneities to the wavelengths of the seismic waves used.

Several tomography methods have been developed and are used for imaging the Earth, coping with the problems of seismic tomography in different ways. These are described in the following, starting with regional and global ray-tomography for body waves. These two techniques are somewhat complementary, however, the first one is limited to the upper mantle, the latter suffers from a low resolution in the lower mantle. This illustrates why (ray-)tomography studies were not yet able to provide a clear answer to the question about the origin depth of plumes. Knowledge about these techniques is needed for the interpretation of the modeling results in this thesis, i.e., to be able to judge, how (finite-frequency) wavefield effects of a



plume are resolved with (infinite-frequency) ray-tomography. This is especially true for the first technique, regional teleseismic tomography.

### Regional Experiments for Teleseismic Tomography

Regional tomography experiments are carried out to study the region under a particular area. An array of seismometers is deployed over the region of interest for a time span that is sufficiently long enough to acquire teleseismic recordings from a broad range of azimuths. The typical runtime of such experiments is several months to 2 years, recent experiments had inter-station spacings of typically 75 km (e.g., the HOTSPOT network on Iceland, see Chapter 4). When using body-waves (surface wave tomography will be described later), such a setup provides a good resolution in the intermediate depth range. At shallow depth, there is a lack of crossing rays since the incidence angles of the rays become steeper when approaching the surface due to lower velocities there (see Fig. 1.4). The crust finally is unresolved, since the rays there run almost parallel. If a special model for the crust, for example from a refraction seismic experiment, is not available, station corrections have to be applied to the travel times because lateral crustal heterogeneities can distort the travel times significantly (ALLEN *et al.* [2002b]). These crustal influences would be mapped into heterogeneities at greater depth and would thus distort the obtained image. When approaching depths of about the size of the

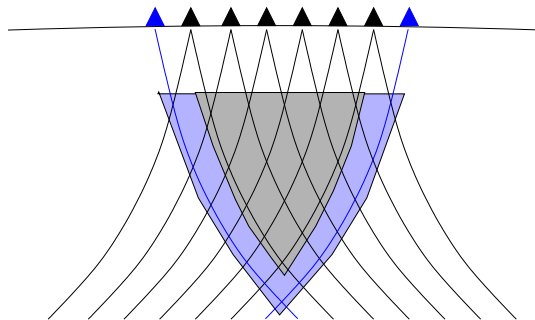


*Figure 1.4: Illustration of the region sampled by regional teleseismic tomography experiments. Black triangles represent seismic stations, black curved lines are rays from teleseismic earthquakes. The grey shaded area is the region that can be resolved with that configuration. The region directly under the stations is not resolved due to a lack of crossing rays. From a depth on that is comparable to the aperture of the array there are also no crossing rays, thus no information about the Earth below this depth can be obtained. The maximum depth of resolution can be increased by adding stations (blue triangles) that extend the aperture of the array. This results in a resolved region that is extended in both the vertical and horizontal direction (light blue area). However, there is no improvement for the uppermost region. Note the diamond shape of the cells that become even more stretched when the rays turn to a steeper incidence at shallow depth. This leads to vertical smearing of the resolved structure (KELLER *et al.* [2000]). This sketch assumes ray theory and is thus only valid for high frequencies.*

array aperture crossing rays are again becoming sparse since teleseismic waves have incidence angles of about  $30^\circ$ . Since there are no horizontal rays there is a tendency to vertical smearing in the obtained images (KELLER *et al.* [2000], a good example of this is the reconstruction test in RITTER *et al.* [2001]). Carrying out resolution tests, this smearing can be quantitatively

assessed and by that an overinterpretation of the images can be avoided. Regional tomography is currently the tool with the highest resolution in the depth range of about 100–400 km. Going deeper would require larger array apertures while keeping the inter-station spacing small. The operation of such a large network is an enormous financial and logistic effort and can only be carried out in cooperative projects, such as the Eifel plume project or the large scale US initiative USArray. However, for plumes, mostly located underneath ocean islands, the restriction of using land-based seismometers makes it impossible to operate large arrays. The development of Ocean Bottom Seismometers (OBS) is therefore an important extension of the seismometer technology. In the beginning, these instruments were very expensive and deployment and data recovery still is very challenging. A careful choice of the site, with a focus on the location of the expected plume effects is therefore necessary. This is one of the main issues of this thesis and the simulations presented in Chapter 3 will reveal the spatial distribution of plume effects on the seismic wavefield for frequencies typically used for OBS studies. At the time of writing this thesis, the first large-scale deployment of OBS for studying plumes is underway, with the first stations already deployed around Hawaii (PLUME experiment, see <http://mahi.ucsd.edu/Gabi/plume.html>).

## Global Whole-Mantle Tomography

A very large array is obtained and resolution is extended down to the core-mantle boundary when using data of all the stations available around the globe. Because of the large inter-station spacings and the limitation to a land location of the instruments the resolution is limited and worse compared to regional teleseismic tomography. Moreover, earthquake locations concentrate mostly on plate boundaries and thus cover only a small amount of the total surface of the Earth. This leads to poor sampling of parts of the Earth, especially in the southern hemisphere and particularly in the Indian Ocean. Resolution also decreases in the lower mantle. The uneven sampling of the Earth by seismic waves may also lead to a smearing-like distortion that has to be taken into account. Several resolution test approaches are applied and provide an estimate of the resolution power of the models in different parts of the Earth.

The resolution limit of current tomography models is about 500 km (ROMANOWICZ [2003]). However, small scale features such as plumes seem to differ significantly between the models, if they are seen at all. Instead, most whole-mantle models agree with respect to large-scale anomalies (BECKER AND BOSCHI [2002]).

Several techniques for parameterization of tomographic models are used, e.g., spherical harmonics expansion, partitioning into blocks or discretization on grids. Moreover, to solve the generally ill-posed problem of tomographic inversion, regularization is necessary to transform the problem into a well-posed one. This process selects one of the many possible solutions (TRAMPERT [1998]). Thus, different choices of regularization may lead to different solutions for the same problem, which all seem unique once the choice is made.

Since the beginning of seismic instrumentation a lot of observations have been gathered and delivered to and collected by international agencies. Travel times are published in bulletins, for example by the International Seismic Commission (ISC). The problem with these travel times is that they are measured by a lot of people, presumably in many different ways, ranging from picking of arrival times in seismograms by hand to sophisticated cross-correlation methods with synthetic pulses. Especially picking of arrivals times is often rather subjective. Thus, there might be large and partly systematic observational errors. For example, the frequency for

which the travel-time measurements are carried out is generally unknown. For the ISC dataset it is estimated to be in the 1 Hz range. As we will see later travel-time delays are frequency dependent and thus the information at what frequency they are measured may be crucial. Timing problems due to unsynchronized clocks or software problems of the data loggers have been discovered by careful inspection of the data, and have probably biased several studies in the past.

Quality improvements in the future are to be expected due to the use of only digital high-quality data sets and travel-time measurements using objective and consistent ways, e.g., by cross-correlation at a defined frequency. The study by MONTELLI *et al.* [2004b] is a recent example for this direction. Although the locations of earthquakes and seismometers will not change considerably in the future one can expect that global tomography will still ameliorate.

However, concerning mantle plumes and their conduits one has to keep in mind that the resolution of today's global tomography methods is not yet suited for imaging the narrow conduits even though several studies claim to resolve them.

## Surface-wave Tomography

Although we focus on body-wave effects resulting from plumes, a short description of surface-wave tomography is given because this technique is able to resolve the uppermost part of the Earth (especially the upper 100 km that are unresolved by the body-wave methods just presented) and to detect plume heads. The latter is possible because surface waves methods give absolute perturbations in contrast to regional tomography methods that use relative travel times.

Surface waves, such as Rayleigh and Love waves, are low-frequency waves traveling along the Earth's surface and are affected by depths corresponding to their wavelength. Surface waves with longer period/wavelength reach deeper into the Earth and are therefore affected by the higher velocities there. This leads to different velocities for different periods of surface waves and thus to dispersion. When measuring surface-wave dispersion in a region and comparing it to numerically calculated dispersion curves, the velocity structure of the subsurface can be derived (e.g. ALLEN *et al.* [2002a]).

Surface-wave and body-wave tomography might be combined in a complementary way, as done by RITSEMA *et al.* [1999] for global tomography and ALLEN *et al.* [2002a] for regional tomography.

Concerning plumes, it is not expected that the narrow tails are influencing surface waves. However, surface waves should be sensitive to the plume-head material pending under the lithosphere and creating the topographic swells. Rayleigh waves of about 75 s period are sensitive to depth just below the Moho and should therefore be suitable for the detection of plume heads (NATAF [2000]).

### 1.2.3 Finite-frequency phenomena

The above mentioned limitations and shortcomings, i.e., the assumption of high, or actually infinite frequencies became more and more significant when seismologists started looking for plumes. Already WIELANDT [1987] pointed out that diffraction effects, leading to a "healing" of the wavefront perturbation caused by a low-velocity body (Figs. 1.5, 1.6), may bias or falsify the results of ray tomography. Though this effect is well known from optics, and even though

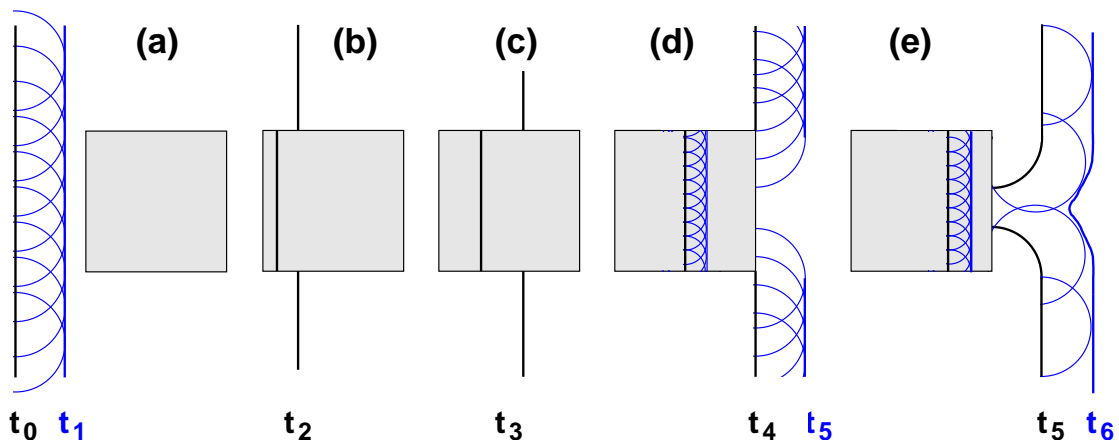
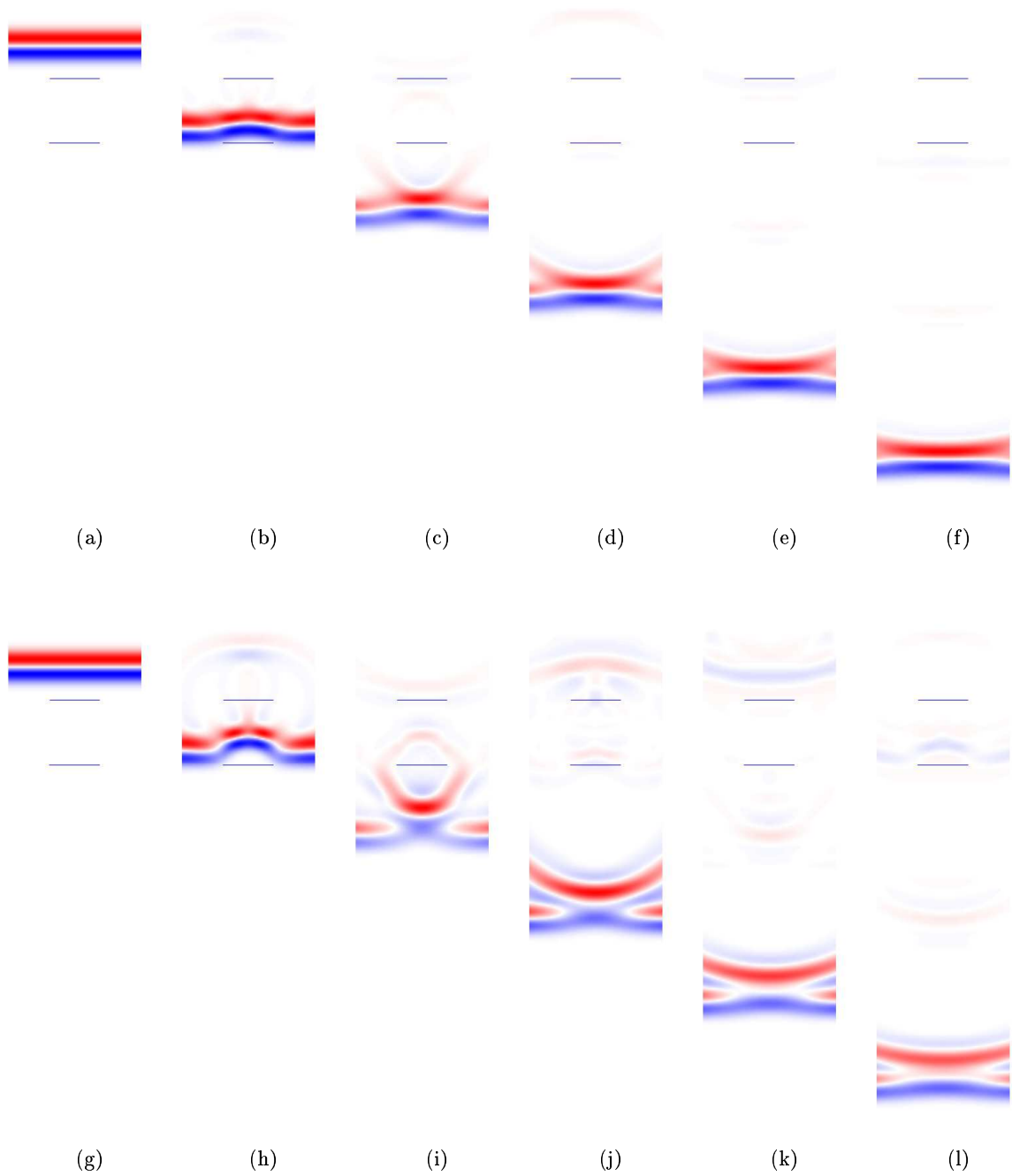


Figure 1.5: Illustration of wavefront healing. Sketch **a**) shows a plain wavefront, running from the left to the right side, before it reaches a low-velocity object (50% velocity contrast; grey square). After HUYGENS, each point of the wavefront (black line, timestep  $t_0$ ) can be considered a source emitting secondary waves (blue circles) itself. These interfere coherently to form the resulting wavefront of the next timestep  $t_1$  (thick blue line). **b**) the wave is now passing the low-velocity body while a part of it is running through it, with a delayed wavefront. The two wavefronts could have been constructed in the same way as in **a**) **c**) same as **b**), but for later timestep ( $t_3$ ), **d**) same situation as in **c**), but now the wavefront traveling outside the low-velocity body reach its back edge. Again, every point of the wavefront can be thought of as acting as a source, leading to the circular waves in blue. These enter the zone behind the low-velocity box and add coherently again (thick blue line is then the wavefront for time step  $t_5$ ) **e**) construction of the wavefront for time step  $t_6$ . Only four secondary waves are shown, for the sake of simplicity. Now the secondary waves emitted from the curved wavefront of time step  $t_5$  (black line) add to fill the gap previously left by the low-velocity body (blue wavefront of time step  $t_6$ ). The wavefront “healed”. The wave running through the low-velocity body will arrive later, in the coda of the first one and is thus hidden by it. This is a simplified schematical illustration. Details like reflections from the low-velocity body or head waves at the interface are neglected for the sake of simplicity.

WIELANDT and GUDMUNDSSON [1996] reminded seismologists of the fact that this technique might underestimate perturbations, tomographers have long ignored this limitation.

Diffraction tomographic approaches, such as migration, has been used for seismic exploration already for a long time, but only DOORNBOS [1992] introduced diffraction tomography into earthquake seismology. JI AND NATAF [1998a,b] improved this method for vertical structures, such as plumes, and applied it to Hawaii. MARQUERING *et al.* [1998] then computed the first 3D waveform sensitivity kernel for long-period waves that showed that the sensitivity right on the position of the classical ray is zero (see Fig. 1.7). This contradicted the basis of ray-theory tomography which assumes that waves sample the Earth only right at the position of their rays. It has been known, that a finite-frequency wave would also sample a region around it, the “Fresnel zone” whose diameter is about  $\sqrt{\lambda L}$  (e.g. MONTELLI *et al.* [2003a]), with  $\lambda$  being the wavelength and  $L$  the length of the ray. The (first) Fresnel zone is the region, where a wave reflected at a scatterer within that zone has only up to half a wavelength phase



*Figure 1.6: Wavefront healing for two velocity-anomaly magnitudes. Figures a)-f) show the evolution of a wavefront passing a low-velocity zone (the lines represent its front and back end) of 10% velocity difference. Wavefront healing can be clearly observed, in Fig. f) the wavefront is almost undisturbed again. Figures g)-j) shows the same sequence but for a stronger (25%) low-velocity anomaly. Here, due to the higher velocity contrast healing takes longer and is not completed at the end of the sequence. The snapshots are results of 2D acoustic FD modeling.*

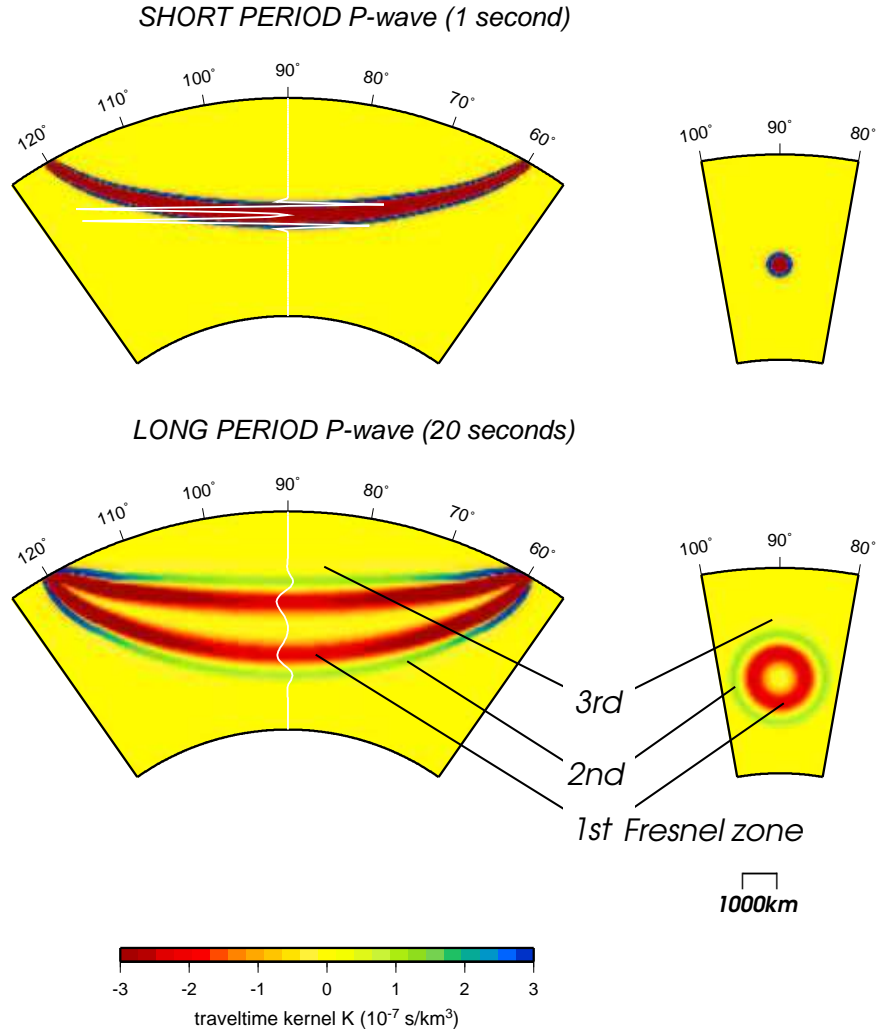


Figure 1.7: Finite-frequency sensitivity kernels for a  $P$  wave at a distance of  $60^\circ$ . For a 1 Hz-wave the kernel looks like a “fat ray” (top). On the limit to infinite frequencies it would collapse to an infinitesimal small line, the ray. However, even for a 1 Hz-wave, the sensitivity right on the ray is zero, as revealed by the white line which represents the sensitivity function at the central cross-section. For lower frequencies, as shown at the bottom for a period of 20 s, the hole in the sensitivity becomes large and the sensitivity is distributed over a broader region around it, referred to as the (first) Fresnel zone. It is surrounded by the second Fresnel zone (green/blue region), where the sensitivity is positive, resulting in earlier arrivals caused by a low-velocity body in this zone. Examples for this counter-intuitive effect will be given in Chapter 3. With increasing order the Fresnel zones become weaker and smaller; the third Fresnel zone is hardly visible in light red (negative sensitivity). Figure modified after MONTELLI *et al.* [2003b].

difference to the initial wavefield and thus interferes constructively with it at the receiver.

It is surrounded by higher-order Fresnel zones with alternating signs in which the phase difference is  $\frac{(n-1)\lambda}{2} \dots \frac{n\lambda}{2}$ . Consequently, within Fresnel zones with odd numbers – such as the first Fresnel zone – constructive interference takes place, leading to a negative value in the sensitivity kernel, i.e., a low-velocity anomaly increases the travel time. For Fresnel zones with even orders the inverse is true. They have *positive* sensitivity, i.e., a low-velocity body such as a plume leads to earlier arrivals and thus seems to speed up a seismic wave. This completely counter-intuitive effect is examined in this thesis and its existence for long-period waves is shown in Chapter 3. The size of the Fresnel zones decreases with increasing order, moreover the amplitude of the sensitivity decreases strongly with the order. Therefore, mostly only the first and second Fresnel zones are considered, since the effects of higher-order zones cannot be resolved.

Other tomographers as well computed sensitivity kernels and tried to take the broader sensitivity of waves into account by using “fat rays” (e.g., KATZMAN *et al.* [1998]), while still ignoring the zero-sensitivity right on the ray. However, the computed sensitivity kernels showed that at a period of 20s (which is, e.g., the dominant period of the frequently used data set of the Scripps Institution of Oceanography, California) the hole in the middle of the sensitivity kernel is as large as 700 km (Fig. 1.7, bottom), thus easily missing smaller objects, such as plume conduits. These finite-frequency sensitivity kernels attracted a lot of attention and became known as “Banana-doughnut”-kernels (MARQUERING *et al.* [1999]), a name that reflects their shapes in longitudinal and perpendicular cross-sections.

NOLET AND DAHLEN [2000] then studied the effect of these finite-frequency kernels on the evolution of travel-time delays and showed that wavefront healing follows a diffusion equation and that the conservation of energy is violated, leading to a loss of information due to diffraction.

More papers on finite-frequency kernels (ZHAO *et al.* [2000]) and their effects on travel times (DAHLEN *et al.* [2000]; HUNG *et al.* [2000]) as well as the shortcomings of conventional ray tomography (DAHLEN [2004]) appeared, but it took some time until the first tomography study appeared that took finite-frequency effects into account by using these kernels.

#### 1.2.4 Finite-frequency tomography

MONTELLI *et al.* [2003a, 2004b] focused on mantle plumes to demonstrate the advantages of their new finite-frequency tomography method and attracted a lot of attention (AGU fall meeting, 2003; KERR [2003]). They applied the method to P-wave tomography and developed unprecedented images of plumes. They imaged six plumes extending into the lower mantle to or close to the core-mantle boundary: Ascension, Azores, Canary, Easter, Samoa and Tahiti. Moreover, they found plumes that terminate in 1 000–1 900 km depth (e.g. Bouvet, Galápagos, Réunion, and Bowie), or even shallower, such as Afar or Etna/Eifel. Among the plumes that have no continuation to the lower mantle was Iceland, a fact that produced some turbulence in the discussion surrounding the origin and existence of the Iceland plume (see Chapter 4).

It should be noted that apart from the introduction of finite-frequency tomography, two other major differences to previous tomography studies exist. First, care was taken with the timing information. The timing bug in the software of the Quanterra data logger used at many global networks has been corrected, and data where there was doubt as to whether the external timing synchronization worked, was removed. Second, a new, adapted irregular parameterization was used together with a depth dependent grid spacing of about 200 km in

the upper and 600 km in the lower mantle. GUUST NOLET (personal communication), one of the authors of the study, attributes only about half of the improvements of the study to the finite-frequency technique, while about one fourth is due to parameterization, and timing error removal, respectively.

Moreover, the long-period data set is used together with a short-period data set, which is inverted using classical ray theory. Thus, in the results the full effects of the finite-frequency technique may not be very dominant; the authors say in the supplementary online material that using only the long-period data set with finite-frequency theory would produce higher anomalies by as much as 50% and that all imaged structures also show up in the short-period dataset alone, only weaker. This is a sign that careful data selection and timing control might be as important as finite-frequency effects, but also indicates that for obtaining the correct amplitudes of the perturbations the finite-frequency aspect of waves might have to be taken into account.

However, this first approach to incorporate finite-frequency kernels in tomography studies showed that a sharper and more pronounced image of plumes can be obtained. To date, no other global study using the technique has been carried out. HUNG *et al.* [2004] applied the method on regional tomography data for the Iceland plume (see Chapter 4) and at the time of writing the thesis reports on similar studies for the Tanzania anomaly and the Azores plume are given at the AGU Chapman Conference.

## Critical review of the presentation of tomographic results

After having discussed tomographic techniques and their limitations we take a critical look at how tomographic results are presented in publications. Especially concerning plumes, we are confronted with absolute statements in the titles of tomography papers, e.g., “The seismic anomaly beneath Iceland extends down to the mantle transition zone and no deeper” (FOULGER *et al.* [2000]) or “Tomographic evidence for a narrow whole mantle plume below Iceland” (BIJWAARD AND SPAKMAN [1999]). These – totally contradictory – statements do not result from a major improvement in tomographic techniques – the papers appeared in two successive years. This leads to confusion of the (non-specialist) reader, unless he very carefully and critically studies the publications. Concerning the two papers just mentioned, we will see in Chapter 4 that the conclusions of some studies are not well founded. But how is it possible and what are the reasons that a paper can claim a tomographic finding and show it in a convincing way, while the next one states the opposite?

Apart from differences in the choice of the regularization (TRAMPERT [1998]), as already mentioned, the graphical presentation, i.e., the tomographic *images* themselves are somewhat problematic, because they leave the interpretation to the individual reader of the study. A variety of graphical features often used and the use of different colorscales inhibit a fair comparison of the different studies. An early (i.e., too early) saturation of the colorscale (cf. BIJWAARD AND SPAKMAN [1999]) translates a broad range of values to the color representing the maximum, thus leading to a sharp impressive image that sometimes ignores strong relative variations. By adjusting the level of saturation, several different impressions can be generated, depending on the intention of the author. Also highly nonlinear colorscales (e.g. RITTER *et al.* [2001]) and isosurface bodies with specific choice of the isovalue are used to pronounce (desired?) structures. These techniques, however, all represent pre-interpretations of the data (and often even reduces the information content of the data displayed) and prevents the reader from an objective comparison of different studies. An illustrative example is



given by FOULGER *et al.* [2001]. They compare different tomographic images of Iceland. Only in two cases (their own study and the first tomographic study by TRYGGVASON *et al.* [1983]) they were able to get the original data and thus to use the same color-scaling. This indicates that the (competing) authors of different tomographic studies may not wish to allow for an objective comparison and that the graphical pre-interpretation of the data is intentional (and thus, in a way, unscientific).

It would also be useful to include resolution information in the global tomography images, e.g., by a coding of saturation values, such that best resolved anomalies would appear in full saturated colors, while spots with no or little resolution are shown in white or pale colors, respectively (therefore, white should not be part of such a colorscale). This would prevent the reader from overinterpreting parts of the results with insufficient resolution and would be a much more honest presentation of the data.

The usage of alternative display techniques, such as isoline maps, also suppresses information. These also provide some freedom for pre-interpretation, e.g., in the choice of the isovalue-steps used. A sad example again is BIJWAARD AND SPAKMAN [1999] who show a 0.25% isoline to help the readers eye to see a plume – a value that is usually considered being “noise” in tomography studies.

This behavior of tomography scientists will probably prevent the establishment of a standardized and thus comparable way of displaying tomographic data. It would therefore be desirable that the original data of all studies are downloadable to enable researchers exploring and comparing the data.

A promising initiative is the “Reference Earth Model” (REM) project coordinated by LASKE, DZIEWONSKI AND MASTERS (see <http://mahi.ucsd.edu/Gabi/REM>). It tries to coordinate and integrate the efforts of global tomographers towards a 3D Earth model that can be used as a reference. As for constructing the PREM, it is planned to also include information independent from seismology, such as from mineral physics, geochemistry and geodynamics, to obtain a consistent model. However, according to LASKE [2005] also this attempt suffers from missing will to share data.

In summary, seismic tomography is currently the only means for globally imaging the Earth’s interior and especially the mantle. It is a powerful tool, however, results should be treated carefully and should not be overinterpreted, keeping in mind the resolution, the restrictions and assumptions of this method. The development of finite-frequency theory for tomography, as well as the growing global dataset that includes data from ocean-bottom instruments raises hope that better and more detailed images of the mantle will be possible in the next years. Eventually, full-wavefield inversion by adjoint-methods or “time-reversal-imaging” (e.g. TROMP *et al.* [2005]) will become standard methods for tomography one day and could represent the next large step towards a better understanding of Earth’s interior.

### 1.2.5 Other seismological techniques

Apart from tomographic methods seismologists use other techniques to obtain information about the mantle, the most important of which are presented briefly in the following, for the sake of completeness. We start with two techniques for mapping the influence of plumes on seismic discontinuities.

On their way to the upper mantle plumes from the lowermost mantle have to cross two

primary discontinuities at 660 and 410 km depth that bind the transition zone. Due to the fact that plumes are hotter than the surrounding mantle the transition zone, and thus the seismically detectable discontinuities are deflected upwards or downwards since the Clapeyron-slope of the discontinuity is positive (660) or negative (410), respectively.

Thus, the mapping of depths of these discontinuities provides a means for detection of plume conduits in the mid-mantle, which are tomographically difficult to image because of their small diameters. In addition, the advantageous fact that the depth deviations of the two discontinuities caused by plumes have an opposite sign (uplift of the 660-, depression of the 410-discontinuity) leads to a high relevance of transition-zone thinning studies.

It should be stated here that recent studies suggest that the phase transitions in garnet and ilmenite have an important influence on the transition zone discontinuities as well (e.g. DEUSS AND WOODHOUSE [2001]), which might change the predicted behavior of the transition zone discontinuities. However, currently most studies assume the classical model for phase transitions.

### Receiver functions

Among others (see “precursor techniques” below), one technique for the task of mapping the depth of discontinuities has turned out to be especially useful. It is called the receiver functions method and takes advantage of the fact that at every discontinuity compressional waves (P) are converted to vertical shear waves (SV) (and vice versa).

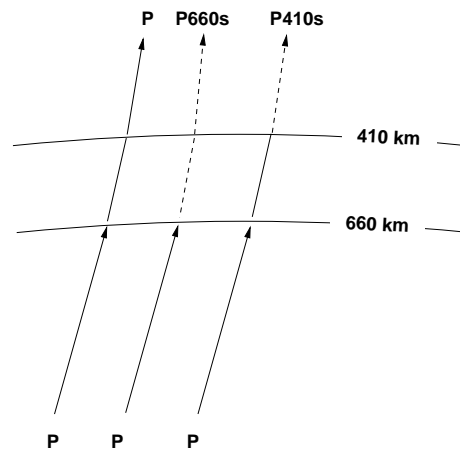


*Figure 1.8: Conversions of teleseismic P-waves at the upper-mantle discontinuities forming the transition zone. Incoming P-waves (solid lines) are transmitted as P-waves and converted to upgoing SV-waves (dashed lines) at 660 and 410 km depth. Complications such as multiples or reflections are omitted.*

With three-component seismograms the component axes (usually North, East and vertical) can be rotated to the “ray system” such that the different wave types separate and are isolated on one component. If the component carrying the SV-wave is deconvolved with the one carrying the P-wave, one obtains the so-called “receiver function”, a seismogram with spikes at times where there is a correlation between the converted wave and the P-wave. This deconvolution removes the source time function and sharpens the signature of the conversion in time, and – given a velocity model – in depth.

Receiver function studies can be carried out to study Moho, 410 and 660 depth variations with only one high-quality station. That is why this technique has been very popular and used extensively in the 90s. Since it is able to see a signature of a plume in the transition zone, it could serve to prove a plume's extension to the lower mantle. For this reason receiver functions have been used to map transition zone thickness beneath several hotspots (e.g., BUDWEG [2002] and GRUNEWALD *et al.* [2001] for the Eifel, LI *et al.* [2000] for Hawaii, and LI *et al.* [2003] for several ocean islands). The receiver function studies of SHEN *et al.* [1996, 1998, 2002, 2003] targeting the transition zone beneath the Eifel plume will be discussed in Chapter 4 on Iceland.

For completeness, it has to be stated that the receiver-function is implicitly based on ray theory. However, most authors take the finite sensitivity of waves (Fresnel zone) into account.

### **Precursor studies**

Another technique to map the depth of seismic discontinuities of the transition zone is the observation of precursors. Precursor studies are frequently carried out to investigate lateral changes in seismic properties or topography of seismic discontinuities (e.g. ESTABROOK AND KIND [1996]; FLANAGAN AND SHEARER [1998]). Precursors are signals that arrive earlier than a certain phase, in most cases due to a reflection of that phase that shortens its actual path. Precursors are used because they are easy to identify, contrary to "post-cursors", i.e., phases coming later than a strong phase and thus being hidden in the coda. For instance, the receiver-function method described above uses P-to-S conversions, which reach the surface after the main P-phase, in its coda, and therefore needs sophisticated processing to retrieve the converted phase. Precursor phases often used are PP- or SS-precursors. While the PP-phase is the underside reflection off the surface, part of the P-wave is already reflected off (or converted to a S-wave at) a deeper discontinuity and thus arrives earlier at the receiver. This leads to the term PP-precursor. Precursory phases for mapping the depths of the bottom and top of the transition zone are P410P, P660P, P410S, P660S, S410S, S410P, S660S, and S660P. In practice differential travel-times between the surface underside reflection and its precursor are used. This method along with numerical simulations has been applied to the Hawaii plume with a high amount of data and data quality (SCHMERR *et al.* [2004]) in the framework of a collaboration with the ASU seismology group within this project. Preliminary results (N. SCHMERR, personal communication) do not reveal any influence of a plume beneath Hawaii on the discontinuities that form the transition zone.

### **Study of the CMB region**

Even though the core-mantle boundary region and the D" layer and their interaction with plumes is not included in the plume models of the modeling part later in this thesis we briefly look at this region. First, since the most commonly assumed source for plumes is the D" layer at the core-mantle boundary, techniques to examine this layer are also appropriate for plume studies. The D" layer is an extremely laterally heterogeneous region with partly strong anisotropy and with high-velocity zones, assumed to consist of ancient subducted slabs and ultra-low velocity zones (ULVZ), the supposed source of plumes. Thus, the seismic behavior of this region belongs to the issue of the seismic signature of plumes.

Second, a lot of these investigations were carried out by members of the seismology group at Arizona State University to which a strong collaboration within this project exists. For

example, the thesis by THORNE [2005] deals with numerical modeling of wave propagation of structures in the lowermost mantle (using modeling techniques developed by the group in Munich that are described in the next chapter). This is why this special aspect of a plume's influence on the seismic wavefield will not be treated further in the modeling part of this thesis.

Many seismological studies have been carried out to investigate the D" region (e.g., FARNETANI [1997], RUSSELL *et al.* [1998], FOUCH *et al.* [2001], ROST *et al.* [2005]), also for looking for possible roots of mantle plumes (WOLFE [1998]). Some used precursors to core reflected phases such as ScP and PcP, others studied scattered core phases, e.g. PKP or SKS, or looked at travel times and waveform anomalies of a variety of phases (SPdKS, S,  $S_{diff}$ , PKP, ScS, SKS) (THORNE AND GARNERO [2004]).

A recent study suggests another phase transition in the lowermost mantle, from perovskite to a denser mineral phase, preliminary called "post-perovskite" (MURAKAMI *et al.* [2004]). This new phase has attracted a lot of interest, because it is strongly anisotropic and can thus explain the abrupt onset of anisotropy at the D" (GARNERO [2004]). Whether this phase transition is the actual boundary layer between lower mantle and D" is not yet clear.

## Shear wave splitting - Anisotropy studies

Upward flow in the plume conduit, radial entrainment of ambient material into the conduit and radial outward flow into the plume head or the asthenosphere are supposed to cause seismic anisotropy by flow alignment of the crystals. Thus, all the regions of a plume, the foot, the conduit and the head may be subject to anisotropy. Therefore, numerous experimental studies have been carried out (GARNERO [2004]; RUSSELL *et al.* [1998], and FOUCH *et al.* [2001] for Hawaii, BJARNASON *et al.* [2002] and SCHLINDWEIN [2001] for Iceland, and LI AND DETRICK [2003] for constraining plume-ridge interaction for Iceland).

Comprehensive numerical shear-wave splitting studies for constraining anisotropy have been carried out for all aspects we focus on in this work, i.e., for plume-like structures (RÜMPKER AND SILVER [2000]), taking into account frequency dependence (RÜMPKER *et al.* [1999]), and by using array techniques (RYBERG *et al.* [2005]). Therefore, anisotropy is not included in the plume models for this work, since the approach taken in this thesis is to start with simple models and to study first-order seismic effects of plumes in a systematic way. Anyway, it should be kept in mind that anisotropy might play an important role for plumes.

### 1.2.6 Plume projects and experiments

In the following, two major seismological studies of plumes are described in order to give an idea about the effort currently undertaken and realizable with experiments dedicated to a specific plume. The focus is on the experiment setup, i.e., the number, spacing, position and type (land/sea) of the stations and the spatial extend of the array. This information will be used to later design a realistic setup for the numerical study.

The seismologically best studied plume is the Iceland plume, the case example of a ridge-centered plume. Since Iceland is the target area of a later application (see Chapter 4), the Iceland experiments and studies will be treated in detail in Chapter 4.

The other classic example of a hotspot as the surface expression of a plume is Hawaii. Due to its isolated position in the Pacific and its impressive obvious hotspot track with clear age

progression it is a textbook intraplate plume. Interestingly, the experiences of the investigations of Iceland are currently applied to Hawaii.

### Hawaii: PLUME experiment

Hawaii is the hotspot with the strongest buoyancy flux (e.g. SLEEP [1990]) and it shows all the features that belong to the plume hypothesis. However, from a seismological point of view, Hawaii is surprisingly poorly studied. The main reason for this is the relatively small size of the islands that form Hawaii and its position far away from major earthquake centers. Moreover, only one permanent station exists on Hawaii, the GSN station Kipapa (KIP) on Oahu.

For extending the database the Dublin Institute for Advanced Studies (DIAS), the University of Hawaii, Honolulu, and the GeoForschungsZentrum (GFZ), Potsdam operated eleven mobile seismic broadband stations on the Hawaiian islands from June 1999 to May 2001. The data were mainly used for receiver function studies (LI *et al.* [2000]) and – due to the linear alignment of stations – not useable for tomography.

While several tomographic studies and experiments have been carried out on Iceland, only the development of ocean bottom seismometers (OBS) opened the way to a comparable study of the Hawaii plume. The reason becomes evident when comparing the distribution of land mass of the two hotspots. In Figure 1.9 the islands of Hawaii are plotted over a map of Iceland at the same scale. As can be seen, apart from the much smaller land mass of Hawaii, its linear

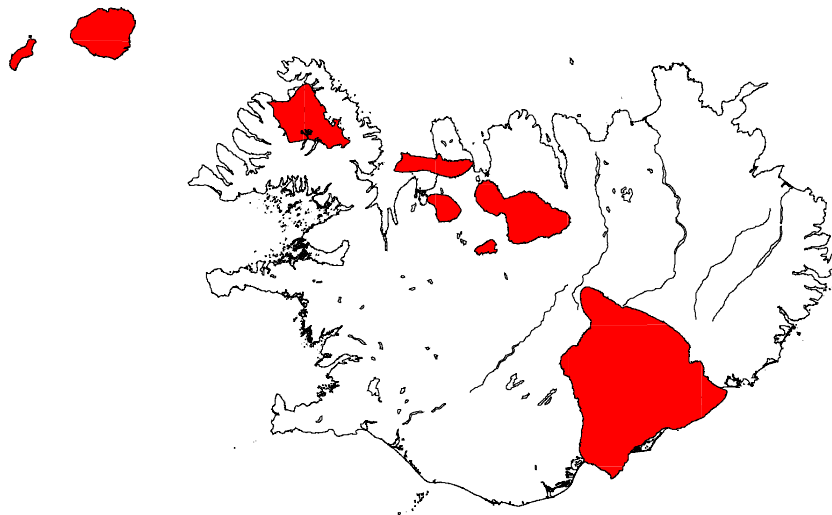


*Figure 1.9: Comparison of the Hawaiian island chain (red) to Iceland. The same scale is used along with an equal area projection.*

alignment can only lead to a small extension of a seismometer array perpendicular to the direction that the islands line up.

The large-scale experiment currently underway for Hawaii is called “Plume-Lithosphere Undersea Mantle Experiment” (PLUME). It was preceded by several studies (MELT, OS-

NPE, SWELL and PELENET) in order to prepare this effort and to test the instrumentation (LASKE *et al.* [1999]). With the installation of the US National OBS instrumentation pool (OBSIP, [www.obsip.org](http://www.obsip.org)) a sufficient number of OBS were available for a large-scale experiment. Within the PLUME project the deployment of 64 OBS and 10 portable broadband stations is being carried out at the time of writing this thesis. The experiment consists of two phases. In the first one-year phase an array of 33 broadband OBS close to Big Island is deployed with an inter-station spacing of about 75 km for body-wave tomography (Fig. 1.10). The array has an aperture of about  $400 \times 670$  km and is centered on the assumed current position of the plume conduit. Another 39 OBS are proposed to be equipped with differential pressure gauges that are intended to be used for surface-wave tomography. In the second

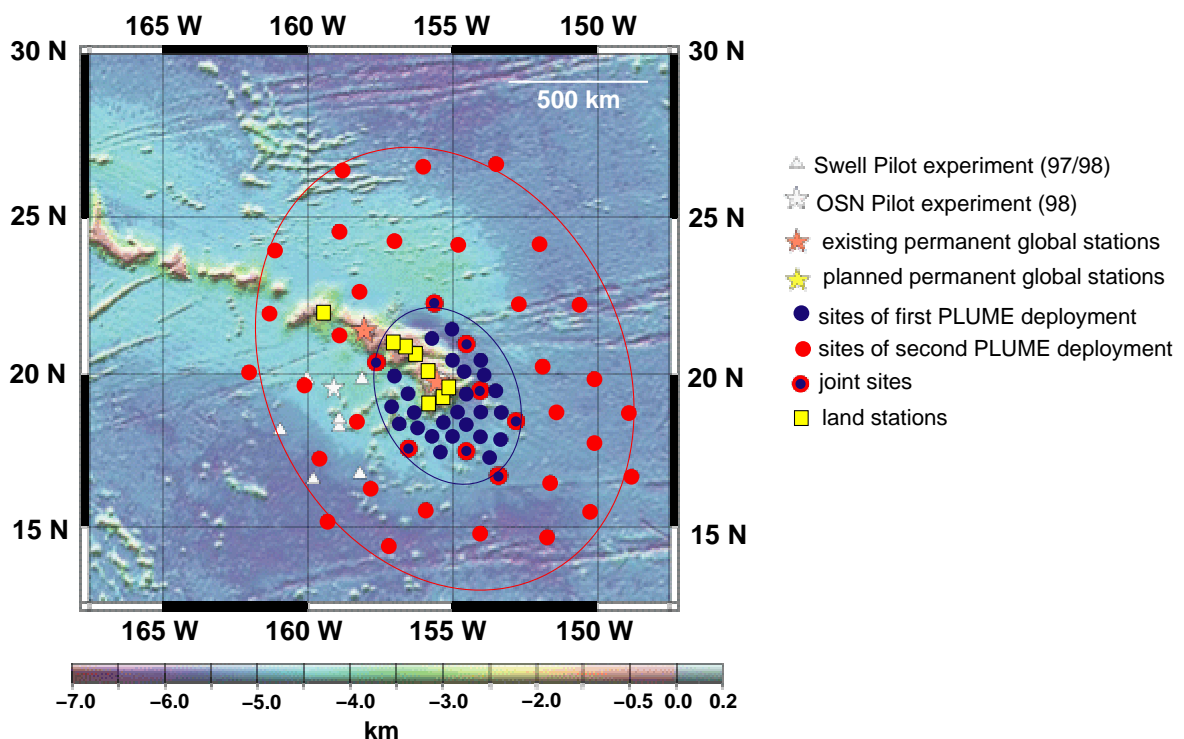


Figure 1.10: Seismometer and OBS locations of the PLUME experiment. Compare to Figs. 1.9 and 4.11. The figure is modified after a map taken from the PLUME website (<http://mahi.ucsd.edu/Gabi/plume.dir/deployment.gif>).

phase, a wider array of about  $1000 \times 1500$  km and an interstation spacing of roughly 200 km (and thus lower resolution) is operated for another year. The aim is to extend the resolvable depth in order to look for a continuation of the plume into the lower mantle. The experiment will end in 2007 with the recovery of the stations and data will be available to the public from 2009 on. The questions that are expected to be answered with the data of the experiment are basically identical with those for the Iceland experiment, i.e., the origin, the width, the position, and the magnitude of the anomaly of the plume. Since Hawaii is the plume with the largest buoyancy flux the answers to this questions provide key constraints for geodynamics.

## Eifel plume Project

The Eifel plume project (RITTER *et al.* [2000]) is an effort comparable with the experiments for imaging the Iceland plume (see Chapter 4). It focuses on the Quaternary Eifel volcanic fields on the Rhenish Massif in Germany. In a collaboration of ten European institutions geophysical, geological, volcanological and geochemical investigations are undertaken (KEYSER *et al.* [2002]) to better understand the nature of volcanism in the Eifel. The tomographic experiment is the central part of the project. 158 mobile recording stations deployed from November 1997 to June 1998 complement the 84 permanent stations in Central Europe (RITTER *et al.* [2001]). In contrast to Iceland, there are no restrictions on seismometer placements due to oceans, allowing for a larger array aperture of  $500 \times 500$  km. Moreover, oceanic seismic noise is not a critical problem in central Germany, but anthropogenic noise is more important due to high population density and industrial activity.

In a P-wave tomography study RITTER *et al.* [2001] use 7319 hand-picked P- and PKP-arrival times to invert for the structure beneath Central Europe. The anomaly images show a low-velocity body of about 100 km width south-west of the western Eifel volcanic field. Resolution tests reveal that the image is reliable from 70–410 km depth.

In a very careful study KEYSER *et al.* [2002] use data from the same experiment to derive a S wave-model for the Eifel region. They use 3773 travel-time residuals — compared to 560 travel-time measurements for the ICEMELT experiment and 1300 residuals for the HOTSPOT project both of which suffered from oceanic noise in Iceland. The difference in the amount of data comes mainly from the absence of oceanic noise and the high number of stations which was possible because there were no limitations by a coast. The S-wave tomography reveals the same anomaly as the P-wave study, however, with a hole at about 170–340 km depth.

Apart from the two projects just presented, a lot of other programs, such as the Japanese Superplume Project (ISHIDA *et al.* [1999]), the Oceanic Upper Mantle Dynamics initiative (OMD, <http://cis.who.edu/science/GG/OMD/>), and the European Ocean Plume Project targeted plumes. The latter was intended to let Europe take the leadership in the development of OBS and undersea seismic plume experiments (HOFMANN *et al.* [2000]). This was the last field in seismology where US scientists are not superior concerning the dimension of effort undertaken, as the project's proposal states. Ironically, this project did not get funded and with the installation of OBSIP, the US OBS instrumentation pool and the PLUME project, the US is also pioneering in this field.

## 1.3 Plumes – a key to geodynamic questions

After looking at mantle plumes and plume imaging techniques in detail, we now step back in order to discuss the relevance of plumes in the general geoscientific frame. Plumes are the key to several geodynamic questions, which are raised in the following and which motivate the forward-modeling study in the second part of this thesis.

For many years mantle plumes played a side-role in geosciences because their postulation in 1971 by MORGAN coincided with the major breakthrough of plate tectonics. In the light of plate tectonics plumes, or more precisely Hawaii served as a nice support for plate motion theory, since its hotspot track reflects the motion of the Pacific plate. Only in recent decades plumes have attracted more attention among geoscientists. With increasing resolution of both regional and global tomography the first images came up revealing low-velocity zones in the

upper and lower mantle, that could be interpreted and associated with mantle plumes. On the other hand experimental studies of plume generation and growth in a realistic mantle-like setting using analogue media suggested the existence and possible modes of plumes (WHITEHEAD AND LUTHER [1975]).

Moreover, in the last decade of the 20th century increasing computer power enabled scientists to carry out numerical modeling of mantle convection and thus of plumes that complemented experimental studies and overcame the restrictions of experiments.

Geodynamics, in contrast to plate tectonics, which is a kinematic model, deals with the driving forces and the processes in the mantle. Geodynamics itself is a rather young science, for several reasons. First it took WEGENER's theory of moving plates (WEGENER [1912, 1921]) more than fifty years to become accepted in geoscience. After the breakthrough of plate tectonics (WILSON [1965]) plate-motion rates could be determined, either from the past (paleo-motions) by using the magnetic patterns on the seafloor or recent motions measured using the Global Positioning System (GPS) and Very Long Baseline Interferometry (VLBI). These motion rates are important boundary values (in the word's best sense) for geodynamic modeling. The latter is becoming more and more important. By numerically modeling the processes in the Earth's interior in 3D with models that move towards reality (e.g. BUNGE *et al.* [1997]) it is now possible to produce dynamically consistent structures, including hot upwellings (plumes).

### 1.3.1 Whole or layered mantle convection

Today, there is no doubt about the existence of mantle convection. Its style, however, is not yet clear and has been the subject of discussion, especially between geochemists and geophysicists. A short overview about this classical conflict is given here to illustrate the role of plumes in answering important questions in geodynamics.

**Geochemistry** (this part is based on a paper by VAN KEKEN *et al.* [2002])  
The classical prevailing picture of the mantle for geochemists was a division into a depleted convecting upper mantle (depletion due to melt extraction upon crust formation) and a primordial undegassed lower mantle ("primitive mantle"). Both are distinct geochemical reservoirs and are separated by the 660-discontinuity, which in this model is a chemical boundary and acts as a barrier to convection. This was supported by the compressional nature of subduction zone earthquakes and the absence of hypocenters below 670 km. This layered convection assumption is necessary because otherwise the two reservoirs would be mixed. The existence of two distinct reservoirs was suggested by two fundamentally different types of rock coming from the mantle: Mid-Ocean Ridge Basalts (MORB), in this model corresponding to depleted upper mantle, and Ocean Island Basalts (OIB), which is found at hotspots and is thought to consist of primitive mantle contaminated upon rise with depleted upper mantle. One key isotope ratio, especially for plume studies, has been the one between  $^4\text{He}$  and  $^3\text{He}$ . While  $^3\text{He}$  is a Helium isotope preserved since the formation of the mantle,  $^4\text{He}$  is produced from Uran and Thorium by radioactive decay. Since the upper mantle is already mostly degassed and thus depleted in  $^3\text{He}$ , it has low  $^3\text{He}/^4\text{He}$  ratios, comparable to those in the atmosphere (i.e., for MORB 7-10 times the atmospheric ratio (COURTILLOT *et al.* [2003])). Magma erupted at hotspot volcanoes, on the contrary, shows high ratios, consistent with the lower mantle origin of OIBs, where preserved  $^3\text{He}$  is stored. Also, other noble gases support the idea of the existence of a reservoir in the lower-mantle that has preserved high concentrations of volatiles



from the time of formation of the mantle.

### Geophysics

In contrast to the ideas of geochemistry, evidence from geophysics and especially seismology suggests a whole mantle convection model. The importance of the 660-discontinuity as a barrier to mantle flow is not evident from a geophysical point of view, the discontinuity is regarded not as a chemical boundary but rather a phase transition from one mineral phase to a denser one. Earthquake hypocenters reach to depths of 720 km and thus into the lower mantle. Seismic tomography has shown slabs going through the transition zone into the lower mantle (VAN DER HILST *et al.* [1997]) and there are indications for (and meanwhile first images of) plumes from the lower mantle (MONTELLI *et al.* [2003a]), being the active upwellings reaching the surface.

Then, in the late 80s, geochemical models showed that the existing isotope database for oceanic mantle can be explained by combining five components: depleted MORB mantle (DMM), enriched mantle of two types (EM1 and EM2), a component characterized by high ratios of  $\mu = {}^{238}\text{U}/{}^{204}\text{Pb}$ , referred to as HIMU, and a depleted peridotitic component shared by all hotspots, that is distinct from MORB, called FOZO (acronym of “FOcal ZOne”). It turned out that FOZO had the observed high  ${}^3\text{He}/{}^4\text{He}$  characteristic and that its appearance is indicative for hotspots. These consist of a mixture between FOZO and an enriched component with low  ${}^3\text{He}/{}^4\text{He}$  and high  ${}^{187}\text{Os}/{}^{188}\text{Os}$  ratios that is consistent with and thus considered to be recycled mafic crust.

This five-component model loosens the layered convection constraint and even includes subduction of crust down to the origin depth of mantle plumes. Geochemical reservoirs are still needed, and these would be destroyed by mixing of whole mantle convection (VAN KEKEN *et al.* [2002]).

The task for geosciences now is to find a plausible model that takes into account both, geophysical constraints, and geochemical findings. Several solutions to this problem have already been suggested (see review and discussion of VAN KEKEN *et al.* [2002]; TACKLEY [2000]). One of the most far-reaching models is the one of PHIPPS MORGAN AND MORGAN [1999]. It basically says that all mantle material reaching the surface is coming from plumes, and that the chemical differences between MORB and OIB are the result of two stages of melting. One that occurs upon rise of plume material due to decompression – the resulting melt is feeding hotspots above the plumes. The residue of plume material (the most part) is feeding the asthenosphere where it is flowing horizontally towards the spreading center. Close to the ridges the next decompression and subsequent melting occurs to produce MORB. The authors finally come up with a flow-chart for an entire mantle material recycling scheme, solving the problem of distinct chemical reservoirs.

However, though intellectually challenging, the direct applicability of this model is limited and a testable model is yet lacking. A better image of mantle plumes is crucial to better constrain these models and rule some out.

### 1.3.2 Plumes and the Earth’s heat budget

The Earth continuously loses heat through its surface, a quantity that is measureable ( $\sim 44\text{TW}$ , e.g. SCHUBERT *et al.* [2001]). The ratio of the amount of heat of the individual sources is still

enigmatic. Apart from the heat of the core, there is also radioactive production of heat in the mantle. In a traditional model, the ratio between heat brought up to the surface through plumes and heat from mid-ocean ridges would reflect the ratio between cooling of the core and radioactive heat production in the mantle. Several studies addressed this problem.

DAVIES [1988] estimated the heat coming from plumes using the magnitudes of their swells. Hotspot swells are created by the dynamic effect of buoyant material, the buoyancy is balanced isostatically by the topography. They are thus a measure of buoyancy and heat fluxes of the underlying plumes (for purely thermal plumes buoyancy and heat flux are related to each other by the ratio of heat capacity and thermal expansivity). However, not all of the heat inferred from swell magnitudes reaches the surface and is measurable there before being re-subducted. The swell measures the heat flow to the base of the lithosphere, while only the surface heat flow can be measured directly. Therefore, a direct comparison of swell-deduced heat flow and measured heat flow is not possible.

Comparing the values obtained by the swell-method to numerical modeling of both whole-mantle and layered convection DAVIES found that most of ocean bathymetry is generated by whole-mantle plate-mode convection, followed by plume-mode upwelling.

Moreover, the largest hotspots dominate heat flux but in their sum ( $\sim 2.5$  TW) they only account for less than 10% of the surface heat flow. Since this is consistent with values suggested for the heat flow from the core, DAVIES concludes that this is evidence for plumes coming from the core-mantle boundary. SLEEP [1990] carried out a more detailed and sophisticated study of the same type and confirms the results of DAVIES [1988] by obtaining a similar global flux.

MALAMUD AND TURCOTTE [1999] take a different approach. They collect data on heat flow and find that the values for plumes by DAVIES [1988] and SLEEP [1990] do not explain the constraints of basal heating on the lithosphere, that are attributed being due to plumes. They plot a cumulative frequency-size distribution of plumes and find that a power-law explains the data for the stronger plumes, whereas for weaker ones ( $\leq 30$  GW) they find deviations that they think are due to lacking surface manifestations (swell or geoid anomaly; in agreement with SLEEP [1990]) of weak plumes. They thus extrapolate the curve up to where the total sum of heat flow is equal to the basal heating value they assume for the lithosphere. They end up with 5240 plumes, the weakest ones having only 1 GW heat flow. The authors associate these weak plumes with the large number of small seamounts that exist, e.g., in the Pacific. The sum of heat flow by plumes in their model is 15.8 TW ( $\sim 36\%$  of the surface heat flow). This is much more than the values by DAVIES [1988] ( $\sim 5\%$ ) and would give the role of plumes in the heat budget of the mantle a much higher relevance. Moreover, assuming the heat carried up by plumes comes from the core, the core cooling rate would also be higher.

In the plume-fed asthenosphere and plum-pudding models of PHIPPS MORGAN *et al.* [1995]; PHIPPS MORGAN AND MORGAN [1999] material reaching the surface from both hotspots and mid-ocean ridges comes from plumes – at different stages of melting. If this proves true, it as well increases the importance of plumes for the heat transport in the Earth.

LABROSSE [2002] remind us that there is another possibility of cooling the core – advection by cold plume, i.e., subducting slabs arriving at the CMB. Using numerical modeling he found that this is the more important mechanism in removing heat from the core. Moreover, his simulations show that many of the starting plumes that take heat from the CMB do not make it to the surface. Thus, he concludes that the heat carried up through plume measured in the way of DAVIES [1988] and SLEEP [1990] is only a lower bound for the heat flux from the core to the mantle.

Just taking these few studies we see that plumes play a crucial role for determining the heat budget of the mantle and cooling of the core. A better understanding of plumes, their origin, their possible sizes in terms of heat flux and numbers will give important constraints on the thermal history of the Earth.

### 1.3.3 Do plumes exist at all? – plume criticism

Even if the plume concept receives more and more attention and attracts further research efforts in the last decades some few scientists put into question the existence of plumes.

Especially in the first years of the new millennium, plume opponents joined forces (e.g. [www.mantleplumes.org](http://www.mantleplumes.org)). They organized conferences (Penrose conference, 2003; Chapman conference, 2005), triggered discussions on the internet (The Geological Society of London: Plumes Online Debate, [www.geolsoc.org.uk/plumesdebate](http://www.geolsoc.org.uk/plumesdebate), 2003), and in journals (Astronomy & Geophysics, Vols 43/44, 2002/2003, Science, Vol. 300, 2003), as well as at international meetings (for a review of plume debates at AGU 2002 fall meeting, see KERR [2003]).

While some of these scientists even suggest that mantle convection models are possible without plumes (and that hotspot volcanism is caused by melt generation in the upper mantle) (e.g. ANDERSON [2000]; VAN WIJK *et al.* [2001]) there is a lively discussion whether plumes are features of the upper mantle only (e.g. FOULGER *et al.* [2001]), and thus “non-Morganian plumes”, or whether plumes originate at the lower-mantle thermal boundary layer, the CMB.

The protagonists of the plume opponents are the geophysicist DON ANDERSON (e.g., ANDERSON [2000]), entitled “The thermal state of the upper mantle: No role for mantle plumes”, the geochemist HAMILTON with a radical opinion, arguing for completely different tectonics (AGU fall meeting 2001 poster title “plumes do not exist”), and seismologist GILL FOULGER.

This thesis does not question the existence of plumes. A detailed review of the standpoint of plume opponents is not given here, except in Chapter 4 for the case study of the Iceland plume where a critical review of all studies is given. It is stated that some of the opponent’s arguments are considered contradictory with current scientific evidence. However, science lives also from questioning what is thought to be well established, and thus such contributions should not be rejected beforehand without further consideration. In that sense we consider a paper by JULIAN AND FOULGER [2003] who provide a “checklist” for the existence of plumes (that they try to disprove). Two points of this checklist concerning seismological issues can be summarized as follows:

- **ScS and multiples**

An S wave that is reflected at the core-mantle boundary and observed at a close epicentral distance is propagating almost vertically. Such a wave (the ScS phase) should be very well suited for studying nearby plumes, since it travels almost exclusively through the plume and its record is not contaminated by any structural complication, as e.g., in teleseismic tomography. Especially for Iceland, which itself is the location for several strong earthquakes, this could serve as a diagnostic phase for the presence of a plume. However, it should be noted here, that NATAF [2000] stated that “there is little hope of using core-reflected (...) phases to detect plumes in the lower mantle because (...) wavefront healing (...) will be very large in this geometry”. In Chapter 3 we will come back to this issue.

- **plume guided waves or “fiber waves”**

Low-velocity bodies can act as waveguides, an effect observed from fault zone guided waves (FOHRMANN *et al.* [2004]), and fiber glass optics. Plumes, being low-velocity structures, would be natural candidates for behaving in a similar way. Since numerical studies have been used successfully to investigate fault zone guided waves, it should also be possible to investigate this effect for plumes with numerical simulations and thus to decide why such waves have never been observed.

## 1.4 Summary and Conclusion

We have seen that mantle plumes – provided they exist – may be able to put constraints on several geodynamic questions, e.g., the heat budget of the Earth or the style of mantle convection. However, today there are various different ideas about the shape, size, number, strength, and geometry of plumes in the Earth.

Seismology, providing the tools with highest resolution for imaging the Earth’s interior, has been frequently used to look for plumes, however, these studies were not yet able to provide detailed images of plumes over their full length. In the review we have shown that seismic plume studies using ray-theory due to the ignorance of the wave-effects, suffer from major problems when used for the detection and imaging of the small plume conduits. Wave phenomena – the most important one for travel-time tomography being wavefront healing – have been discussed, providing the motivation for carrying out a full-wavefield forward modeling study through plumes, while at the same time providing a basis for understanding and interpreting the resulting finite-frequency effects.

In order to carry out a systematic study of plume-like structures a reduction of the range of various suggested plumes models to the primary properties of a plume – being a buoyant upwelling – is necessary: we suggest to use a vertical cylindrical low-velocity body without a head, since the influence of the latter would be on a larger scale than that of typical experiments (examples of which were reviewed in this chapter) for plume studies.

Such a model can be described with only a few parameters such as the conduit diameter, the magnitude of perturbation, the origin depth or the lateral perturbation function. This allows a phenomenological study of the seismic effects of plumes in dependency of these properties which are crucial for constraining geodynamic parameters. With the knowledge of how a certain plume parameter of interest maps into observable seismic properties, such as the travel-time of the wave, plume experiments can be optimized.

## Chapter 2

# A hybrid finite-difference method for global waveform modeling

A new, hybrid finite-difference (FD) method for 3D global wavefield modeling is presented. It enables high-frequency studies of wavefield effects of confined 3D structures, such as plumes, on a teleseismic wavefield that has travelled through an axisymmetric background model. For such 3D wavefield studies full-3D waveform modeling methods can be used (e.g. KOMATITSCH AND TROMP [2002a]) which are however restricted to low frequencies due to still existing limitations in computer power. To overcome this problem, hybrid approaches have been developed (e.g. WEN AND HELMBERGER [1998]; WEN [2002]; CAPDEVILLE *et al.* [2002, 2003]), combining existing methods with the aim of extending the frequency range of simulations. We present a method that combines a global axisymmetric FD algorithm with one for a confined 3D spherical section. The teleseismic global wavefield through an axisymmetric, or standard 1D model can be calculated with a 2D method that takes advantage of its axisymmetry and thus nevertheless correctly takes into account 3D geometrical spreading behavior. It is passed to a 3D spherical section that can include an arbitrary, confined 3D structure implemented in the same background model as the one used for the axisymmetric domain. In this spherical section the 3D wave equation is solved allowing for studying the 3D wavefield effects of the structure.

The method is applied to a plume model that is placed in PREM at an epicentral distance of 90 degrees. The 3D effects of the plume on the SH-wave is examined including conversions to P and SV waves.

### 2.1 Introduction

Numerical modeling of global wave propagation is of eminent importance for modern seismology. Synthetic seismograms of standard 1D Earth models such as IASP91 (KENNETT AND ENGDAHL [1991]) or PREM (DZIEWONSKI AND ANDERSON [1981]) serve as references. Modeling the effects of specific structures in the Earth such as subduction zones, plumes or ultra-low velocity zones at the core-mantle boundary on the seismic wavefield and understanding how these effects can be used to image these structures is another important field for numerical modeling. Moreover, full-waveform inversion techniques are under development (adjoint method, time-reversal imaging, e.g., TROMP *et al.* [2005]) and will be feasible in the future due to increasing computer power and the existence of adequate 3D global wave-

field modeling methods. This will open up a new era in imaging the Earth’s interior and in exploiting the entire information that is delivered with seismograms.

To date, a variety of computer programs and methods are available to generate synthetic seismograms, the classical and most popular ones being the reflectivity method (FUCHS AND MÜLLER [1971]), the WKBJ-method (CHAPMAN [1978]), and normal-mode summation (e.g. CAPDEVILLE *et al.* [2000]).

Complete methods for numerical wavefield modeling can achieve arbitrary accuracy but can require enormous computational resources. They solve the partial differential equations of the full wavefield. These methods include the Finite-Difference method, the Finite-Element method, the Finite-Volume method, pseudospectral methods (such as the Fourier and the Chebychev method), and the Spectral Element method.

## 2.2 The finite-difference method

This section briefly summarizes the basics of the finite-difference method and reviews the two finite-difference approaches for simulating wave propagation in spherical media from which a hybrid method will be constructed in the next section.

### 2.2.1 Theory

Finite Differences (FD) have widely been used to numerically propagate seismic waves. Comprehensive reviews of the method and their application to seismic wave propagation have been given recently by MOCZO *et al.* [2004] in the framework of the European SPICE project or will be published in near future (MOCZO *et al.* [2006]). The major advantage of the method is its relative simplicity and the use of local operators, allowing for simple model splitting and thus easy parallelization of the algorithms.

Several FD-codes have been developed by HEINER IGEL and co-workers (e.g., IGEL [1993], IGEL AND WEBER [1995], IGEL AND WEBER [1996], IGEL AND GUDMUNDSSON [1997], THOMAS *et al.* [2000]) and served as a basis for further developments by the seismology group of the University of Munich. For example, a Cartesian 3D FD code was developed by STRASSER [2001] for applications on wave propagation through mantle plumes at regional distances. This work was promising since it showed observable effects of plumes consistent with the work by TILMANN *et al.* [1998]. It also demonstrated the need to use spherical geometry when one wants to study seismic effects of plumes at larger distances.

Most FD approaches are based on the velocity-stress formulation (VIRIEUX [1986]) combined with a staggered grid. Therefore, both will be explained in the following. The velocity-stress formulation of the seismic equation of motion for an elastic anisotropic medium with a moment tensor and single force excitation reads (e.g. MOCZO *et al.* [2006])

$$\rho \frac{\partial v_i}{\partial t} = \nabla_j (\sigma_{ij} + M_{ij}) + f_i \quad (2.1)$$

for the generalized version of Newton’s second law (action principle), and

$$\frac{\partial \sigma_{ij}}{\partial t} = c_{ijkl} \frac{\partial \varepsilon_{kl}}{\partial t} \quad (2.2)$$

for the generalized Hooke’s law that assumes that the elastic properties of the medium are constant in time and describes the elastic behavior of the material. The elasticity tensor

$c_{ijkl}$  contains 81 components, of which only 21 are independent due to the symmetry of the stress and the strain tensors and energy conservation constraints. For the case of an isotropic medium it reduces to the two elastic moduli, Lamé's second constant  $\lambda$  and the shear modulus  $\mu$ . The moment tensor  $M_{ij}$  represents the double couple forces, single sources are given by  $f_i$ .

The principle of the FD method for solving these two partial differential equations lies in the approximation of the spatial functions by truncated Taylor series. For the velocity  $v$  this reads

$$v(x + \Delta x) = v(x) + \partial_x v(x) \Delta x + \frac{\Delta x^2}{2!} \partial_x^2 v(x) + \dots \quad (2.3)$$

leading to

$$\delta_x v(x) \approx \frac{v(x + \Delta x) - v(x)}{\Delta x} \quad (2.4)$$

for the first order approximation of the first derivative. The approximation error caused by the truncated terms of Eq. 2.3 with respect to Eq. 2.4 is of the order  $\Delta x$ . In contrast to the forward-difference scheme in Eq. 2.4, a centered scheme is the second order approximation. This reduces its approximation error to the order of  $\Delta x^2$ .

To apply finite-differences to the seismic wave equation, it is necessary to discretize the stiffness tensor  $c_{ijkl}$ , the density  $\rho$  and the wavefield  $v_i$  on a spatial grid. To do so most FD methods use a "staggered grid" where the wavefield variables and the material properties are not defined on the same grid points. A staggered grid being a centered scheme with only half the grid size reduces the approximation error by a factor of four while not requiring more memory.

The time evolution is approximated using the same Taylor series truncation which leads to

$$v(t + \Delta t) \approx v(t) + \frac{\partial v(t)}{\partial t} \Delta t \quad (2.5)$$

The cycle for solving the wavefield equations consists of updating the velocity values from the neighboring ones, then updating the stress values with the new velocity values and finally extrapolating the values in time using Eq. 2.5.

Modern FD programs mostly use a 4th-order spatial approximation instead of the first-order scheme shown above for the sake of simplicity. Moreover, if not modeling the entire globe, there are unphysical model boundaries leading to artificial reflections. These are avoided using so called "absorbing boundaries", that is, a rim of grid points where the function values are multiplied with an decreasing factor  $<1$ . They continuously damp the wavefield towards the model boundaries and this weakens the wave and its reflections from the model boundary such that they have a neglectible influence on the modeled seismograms. In recent years, so called "perfectly matched layers" (PML, e.g. MARCINKOVICH AND OLSEN [2003]) became a better alternative to absorbing boundary techniques but are not elucidated here since they are not used in this thesis.

## 2.2.2 Finite difference methods for spherical media

When considering wave propagation on a global scale, it is useful to turn to spherical coordinates since the Earth is in first approximation a sphere. When expressing the elastic wave

equation (2.1) in spherical coordinates  $(r, \theta, \varphi)$  one obtains (e.g. NISSEN-MEYER [2001]):

$$\rho \frac{\partial v_r}{\partial t} = \frac{\partial \sigma_{rr}}{\partial r} + \frac{1}{r} \frac{\partial \sigma_{r\theta}}{\partial \theta} + \frac{1}{r \sin \theta} \frac{\partial \sigma_{r\varphi}}{\partial \varphi} + \frac{1}{r} (2\sigma_{rr} - \sigma_{\theta\theta} - \sigma_{\varphi\varphi} + \sigma_{r\theta} \cot \theta) + f_r \quad (2.6)$$

$$\rho \frac{\partial v_\theta}{\partial t} = \frac{\partial \sigma_{r\theta}}{\partial r} + \frac{1}{r} \frac{\partial \sigma_{\theta\theta}}{\partial \theta} + \frac{1}{r \sin \theta} \frac{\partial \sigma_{\theta\varphi}}{\partial \varphi} + \frac{1}{r} ([\sigma_{\theta\theta} - \sigma_{\varphi\varphi}] \cot \theta + 3\sigma_{r\theta}) + f_\theta \quad (2.7)$$

$$\rho \frac{\partial v_\varphi}{\partial t} = \frac{\partial \sigma_{r\varphi}}{\partial r} + \frac{1}{r} \frac{\partial \sigma_{\theta\varphi}}{\partial \theta} + \frac{1}{r \sin \theta} \frac{\partial \sigma_{\varphi\varphi}}{\partial \varphi} + \frac{1}{r} (3\sigma_{r\varphi} + 2\sigma_{\varphi\theta} \cot \theta) + f_\varphi \quad (2.8)$$

If we further assume the model to be rotationally symmetric (axisymmetric) with the  $\theta = 0$  line as symmetry axis the equations become invariant with respect to  $\varphi$ . Thus, all derivatives with respect to  $\varphi$  are vanishing. Then it reads (e.g. THOMAS *et al.* [2000]; IGEL AND WEBER [1995]):

$$\rho \frac{\partial v_r}{\partial t} = \frac{\partial \sigma_{rr}}{\partial r} + \frac{1}{r} \frac{\partial \sigma_{r\theta}}{\partial \theta} + \frac{1}{r} (2\sigma_{rr} - \sigma_{\theta\theta} + \sigma_{r\theta} \cot \theta) + f_r \quad (2.9)$$

$$\rho \frac{\partial v_\theta}{\partial t} = \frac{\partial \sigma_{r\theta}}{\partial r} + \frac{1}{r} \frac{\partial \sigma_{\theta\theta}}{\partial \theta} + \frac{1}{r} (\sigma_{\theta\theta} \cot \theta + 3\sigma_{r\theta}) + f_\theta \quad (2.10)$$

$$\rho \frac{\partial v_\varphi}{\partial t} = \frac{\partial \sigma_{r\varphi}}{\partial r} + \frac{1}{r} \frac{\partial \sigma_{\theta\varphi}}{\partial \theta} + \frac{1}{r} (3\sigma_{r\varphi}) + f_\varphi \quad (2.11)$$

Note that now the P- and the vertical S-waves (PSV, first two equations) are decoupled from the horizontally polarized S-waves (SH, last equation). Due to the decoupling of SH- and PSV-waves in the axisymmetric case, they can be treated separately and independent of each other.

On the basis of Equations 2.6–2.8 and 2.9–2.11 two main developments of finite-difference codes exist for global wave-propagation simulation, the axisymmetric, and the spherical section approach. For global wave propagation, an axisymmetric SH-wave FD code was developed by CHALJUB in the mid-nineties (CHALJUB AND TARANTOLA [1997] and CHALJUB [2000]), and extended to higher orders by IGEL AND WEBER [1995]. The concept of axisymmetry was transferred to the PSV case by IGEL AND WEBER [1996] and has been further modified by JAHNKE [2006] with the extension to higher orders and the propagation through the inner core. Since the axisymmetric computations are carried out in a 2D domain, these codes allow one to achieve a much higher resolution than with a full 3D domain. Despite the use of 2D domains, this method is capable of accurately reproducing the effects of three-dimensional geometrical spreading. Because of the axisymmetry of the problem, the results can be extended to three dimensions by simply rotating the wavefield around the axis.

The input of axisymmetric (which includes all 1D) Earth models such as PREM (DZIEWONSKI AND ANDERSON [1981]), IASP91 (KENNETT AND ENGDahl [1991]) or AK135 (KENNETT *et al.* [1995]) is adequate for many issues in global seismology and the results give helpful constraints in terms of 1D reference model solutions e.g., for tomography. However, the implementation of sources or regional structures in the Earth require these to be extended to rings (or, cylindrical volumes if including the axis) due to the axisymmetry (Figure 2.1). For example, a plume at some epicentral distance is extended to a ring structure with a radius equivalent to the epicentral distance; thus no true 3D study of wavefield effects of such an object can be carried out using the axisymmetric approach on its own.

Concerning seismic sources, this problem can be overcome by placing a point source at (or technically actually close to) the axis. The assumption of a point source still permits progress on many important studies that utilize teleseismic data at high frequencies.



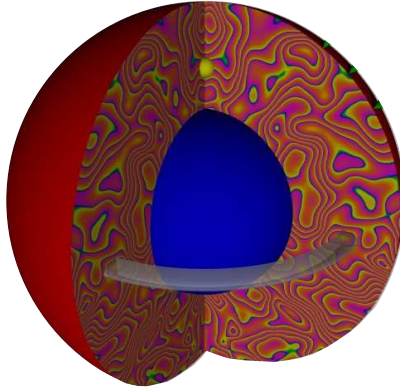


*Figure 2.1: Illustration of axisymmetry. The source (yellow point) is centered at the axis. The heterogeneous structures along a cut plane through the center are independent of  $\phi$  and therefore ring-like (grey). Figure modified after JAHNKE *et al.* [2002].*

NISSEN-MEYER [2001] developed a 3D FD method in spherical geometry, however limited to spherical sections to avoid singularities and diminishing grid spacing towards the axis and the center, and applied it to simulate wave propagation through subducting slabs (IGEL *et al.* [2002]). Reflections from the artificial model boundaries are suppressed using absorbing boundary conditions. This method is particularly useful to look at continental scale wave propagation, when the spherical nature of Earth and its effect on the wave field has to be taken into account and lateral heterogeneities have considerable strength (e.g. subduction zones, continental margins, etc.).

In summary, both the axisymmetric approaches as well as the spherical section approach suffer from severe restrictions when applied to global wave propagation through lateral structures such as plumes or subduction zones at teleseismic distances.

In general, it can be stated that for teleseismic wavefield studies of locally confined 3D structures in a radially symmetric background model, such as intended in this thesis, full 3D calculations are a computational waste since the wavefield propagates most of the distance in a radially symmetric Earth model that is more efficiently dealt with using a 2D computational domain or alternative techniques. On the other hand, with the presence of spherical section codes there are tools for computing the regional wavefield effects around 3D structures. Thus a combination of axisymmetric and spherical sections approaches towards a hybrid algorithm appears desirable.

## 2.3 The hybrid finite-difference method

### 2.3.1 Hybrid methods for global wave-propagation

At present, hybrid methods are a hot topic in computational global seismology since they are able to overcome the drawbacks of the individual methods while combining their advantages.

Earlier developed hybrid methods for teleseismic lower mantle studies (WEN AND HELMBERGER [1998], WEN [2002]) combine 1D and 2D methods (generalized ray theory, 2D-FD simulations, and Kirchhoff theory).

Another approach, closer to the hybrid idea presented and realized within this thesis is the combination of the spectral-element method for spherical geometries with normal-mode approaches (CAPDEVILLE *et al.* [2002, 2003]). It couples the normal-mode solution for the inner, radially symmetric part of the Earth (the inner and outer core and for 3D upper mantle studies also the lower mantle) with the SEM for the entire or the upper mantle, respectively. A disadvantage of the method is, that the interface between the domains has to be strictly spherically symmetric, thus precluding the incorporation of effects due to CMB topography or the ellipticity of the Earth (KOMATITSCH AND TROMP [2002a]).

### 2.3.2 The hybrid axisymmetric / spherical section approach

Coming back to the two finite-difference approaches presented in the last section – the axisymmetric and the spherical section codes – it is evident that there are obvious drawbacks with either of the approaches when attempting to model scattering effects of highly localized 3D structures (from here on, we will take a plume as an example). In order to overcome these limitations we decided to combine the approaches with the goal of exploiting the long-distance simulation capabilities of the axisymmetric approach with the complete 3D solution in a localized region, thereby considerably widening the frequency range that can be modeled with current computer hardware. The idea of this hybrid approach is to calculate the propagation of the wavefield from the source through an axisymmetric (e.g., 1D) Earth model over teleseismic distances using the axisymmetric approach. At the distance where the plume is to be modelled the axisymmetric wavefield is passed to the boundaries of the 3D spherical section (Figure 2.2) and continues to be calculated in full 3D towards the 3D plume model. Thus, within the 3D-section, true 3D wavefield effects like scattering and diffraction can be modeled using an incoming teleseismic wavefield that can up to now not be calculated in 3D for higher frequencies with a reasonable effort.

The lateral extent and position of the 3D spherical section with respect to the source (the epicentral distance of the target 3D object) can be freely chosen, keeping in mind that close to the polar axis we are approaching singularities in the grid. Thus, centering the 3D section around the equator (e.g. 65-115°) is ideal since the lateral grid spacing within the spherical section is exposed to the least variations. This is an appropriate distance range for many teleseismic studies. At closer distances, the 3D spherical section code may be used alone without excessive computational effort.

An advantage for the hybrid method presented here arises from the fact that for the axisymmetric case, the SH and the PSV components of motion are decoupled — as mentioned above. For the hybrid method that means that it is possible to combine only one of the two axisymmetric codes with the 3D spherical section code and to study the effect of one type of motion alone. This is especially interesting for studying conversions from one type of motion induced by the 3D structure to the other. An example for this will be shown in the application section.

Even if conceptually simple, care must be taken when combining the two axisymmetric and the spherical section algorithms. In order to guarantee a reliable interplay of the three codes that form the hybrid code it has to be made sure that the grid spacing and the background model are identical, and that the time step as well as the time evolution cycle are synchronized.

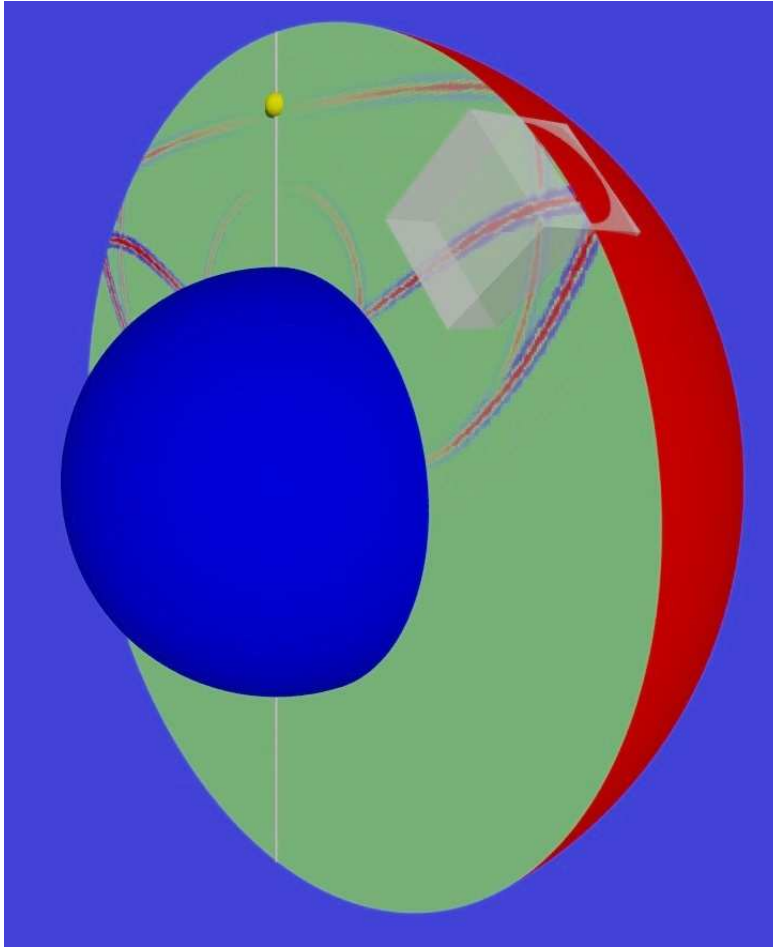


*Figure 2.2: Hybrid axisymmetric/3D-approach. The global wavefield is computed on an axisymmetric 2D-domain with the source centered on the axis. It is then passed to the regional 3D spherical section that is located at some distance and includes the 3D structure of interest.*

This is ensured by using a hybrid initialization subroutine for both sub-codes (see program flowchart in Fig. 2.3).

The calculation of wave-propagation in the 3D section only starts when energy arrives at 10 grid points around the spherical section for the first time. For the serial version of the code this saves a lot of computation time since the wave-propagation over the teleseismic distance is only computed with the fast 2D axisymmetric algorithm. This is another advantage of the hybrid concept presented here.

After the 3D section code is switched on, the codes must in each time step run either one after the other (serial execution, dashed line in Fig. 2.3) or in parallel (for a parallel algorithm, solid line) during the time-evolution loop of the velocity-stress cycle VIRIEUX [1986]. Moreover, the velocity-stress cycle of classical finite-difference codes has to be split into separate parts for velocity and stress, to enable communication between the axisymmetric and the 3D codes after each part (Fig. 2.3).

The actual heart of the hybrid code is the interface between the axisymmetric codes for

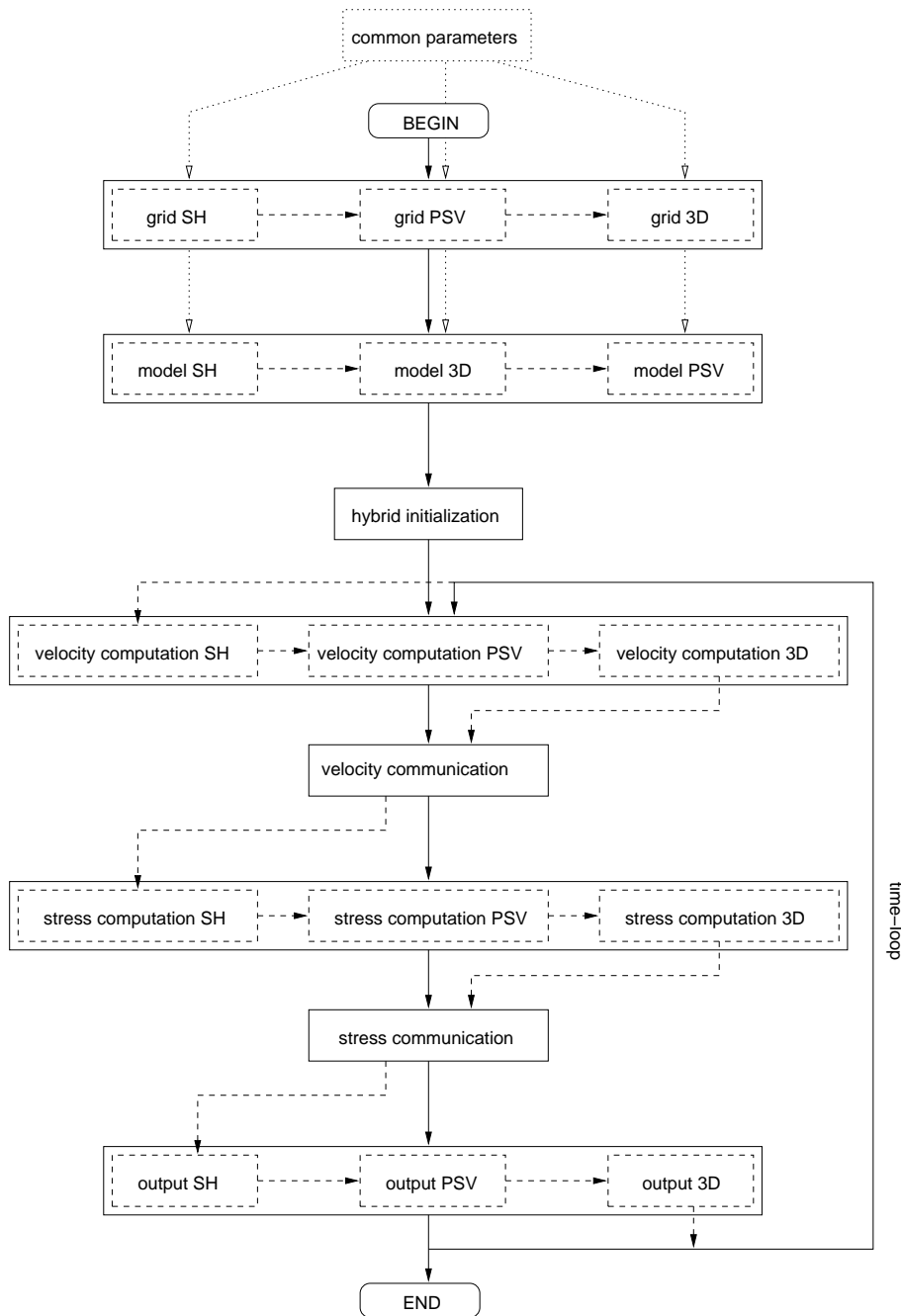


Figure 2.3: Flowchart of the hybrid code: full lines and boxes represent the program flow of a parallel algorithm, the dashed lines and boxes are for serial execution of the code. Note that not every component (SH, PSV, 3D) has to be switched on. It is possible to run the code omitting either SH or PSV, and the 3D section (and thus the communication parts) may only be switched on after the first arrival of energy at its edges in order to save computation time. The subroutines for gridding and model initialization get their parameters from a common parameter file. In the hybrid initialization part the time step is derived from the stability criterion and the model parameters of all the sub-codes.

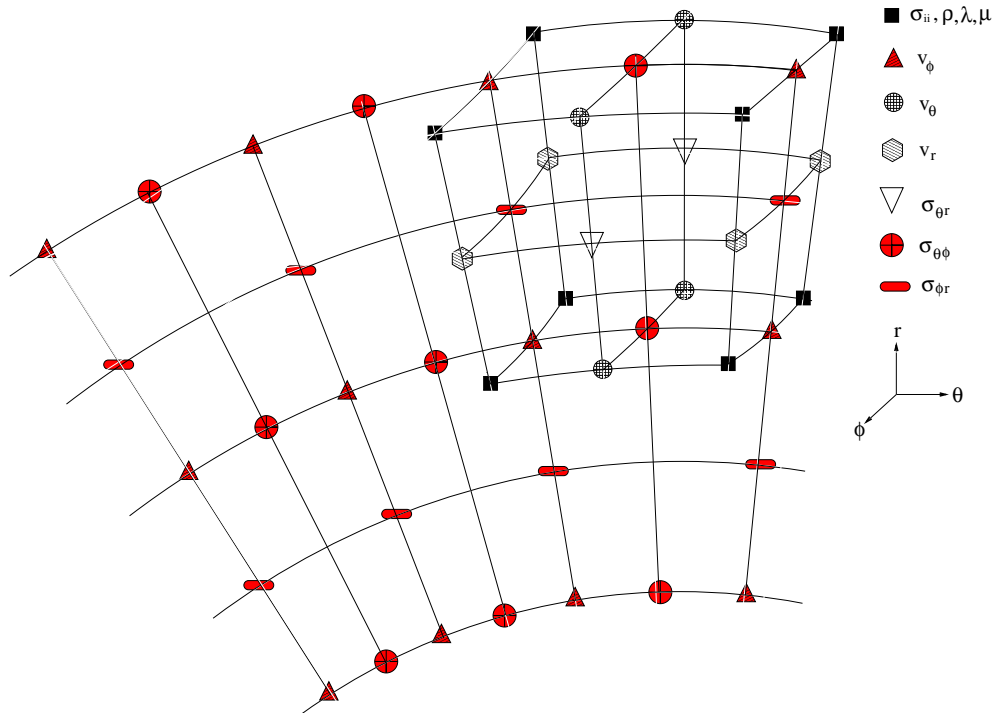


Figure 2.4: The hybrid grid (example for SH case). Several grid cells of the axisymmetric SH grid are shown together with one 3D grid cell of the spherical section grid. Different symbols represent grid points with different variable defined there. Red symbols stand for variables that are necessary to define horizontal shear waves.

global wave propagation and the regional spherical 3D section. The  $r$  and  $\theta$  coordinates of the gridpoints of the 3D section correspond to (i.e., spatially coincide with) the gridpoints of the axisymmetric grid. For illustration, Figure 2.4 shows the grid cell of the spherical section 3D-FD scheme and its position in the axisymmetric SH 2D grid. Coupling of the grids and thus of the two codes is done by communication of the wavefield information for the grid points. In order to correctly pass the global wavefield to the 3D code the first  $nop/2$  ( $nop$ =operator length) points of the front side and the bottom of the spherical section are set to the corresponding velocity and stress values of the axisymmetric code. This is done for every time step (and for velocity and stress separately) and ensures a continuous flow of the global wavefield into the 3D box.

As an alternative to the program flow just presented the global axisymmetric wavefield may also be stored once for all since it does not change for the types of studies for which the hybrid concept presented here is suited. In that case, instead of the execution of the axisymmetric code(s) the axisymmetric wavefield has to be read from disk in the communication subroutines. Depending on the actual setup and the disk access speed this might lead to a significant reduction of computation time when carrying out computations with the same configuration but many different models in the 3D section. This option can be regarded as using the spherical section code with “boundary conditions” determined by the global wavefield.

As a consequence of this way of coupling the codes the absorbing boundaries of the spherical 3D code have to be modified. When feeding the axisymmetric wavefield in the spherical section code at the front and the bottom side, no absorbing boundaries can be used at these sides.

In consequence, waves running (back) towards the front end and the bottom of the spherical 3D section are reflected at this feeding-in zone. However, since there are no sources in the spherical section model itself – as is usual for FD modeling – and since the main direction of wave propagation is towards the surface and the back end of the section (where an absorbing boundary exists) this is not a severe limitation. Only waves reflected by the plume or the surface or waves converted by the plume might run 'backward' and are thus reflected at the model end. By extending the size of the spherical section in  $\theta$ - and vertical direction the arrivals of these reflections at the receivers can be delayed such that they will not appear on the seismograms at times where phases of interest show up. Extending the section is not a significant waste of model space because the points that would have been necessary for the absorbing boundaries can be spent for this purpose. Moreover, since it takes twice the time for waves to run to the model and the reflected waves to come back every grid point spent to extend the spherical section increases the delay significantly.

The same reasoning is used to justify circular boundary conditions that are necessary to avoid refractions from the 'loose ends' of the sides of the block, where derivatives can not be calculated due to missing neighbors and absorbing boundaries can not be used either.

The general direction of energy, however, is towards the back side of the block. So from this side the strongest reflections are to be expected. These can be damped away with absorbing boundaries placed at the back-end of the block.

In addition, the restrictions on placing absorbing boundaries only apply to the components that are communicated. Take for example the SH-case. Only SH-energy reflected at the plume is reflected at the communication zone or appears on the other side due to circular boundary conditions. Conversions showing up on other components can run into the absorbing boundaries at all sides.

### 2.3.3 Verification

Comparison of seismograms produced by the spherical section part of the hybrid code with the ones of the axisymmetric part provides a simple verification of the hybrid method since the axisymmetric code is verified within the COSY project (IGEL *et al.* [1999]), while the accuracy of the spherical-section method is assessed by IGEL *et al.* [2002].

If both domains use the same model, the wavefields and thus the seismograms recorded at the surface are supposed to be identical. This comparison is shown in Fig. 2.5, where the first onsets of the SH wave for receivers in both domains are shown together. The background model used is the isotropic part of PREM without the crustal layer. For the  $105^\circ$ -extension in the  $\theta$ -direction, 2000 grid points are used, and for the vertical direction down to the core-mantle boundary 580 grid points are used. At a distance of about  $81^\circ$  (1545 grid points) the 3D spherical section grid begins. It extends 350 grid points ( $18.375^\circ$ ) in the  $\theta$ -direction (including 50 points for absorbing boundaries) and 250 points ( $13.125^\circ$ ) in the  $\varphi$ -direction. The 3D section is discretized with 180 grid points in the vertical direction which corresponds to a depth of about 900 km, thus including the entire upper mantle. Computations were carried out on a 2.8 GHz Pentium 4-processor, required 1820 MB of RAM and took about 39 hours.

A point source is used one grid point from the symmetry axis. The source time-function can be arbitrarily chosen, with the possibility to use an impulsive ( $\delta$ -) source excitation in time. This leads to seismograms that are Green's functions that can then be convolved with any desired source wavelet. For the seismograms shown, a two-pole Butterworth 20 s low-pass filter for the suppression of numerical noise was used. The slight observable differences result

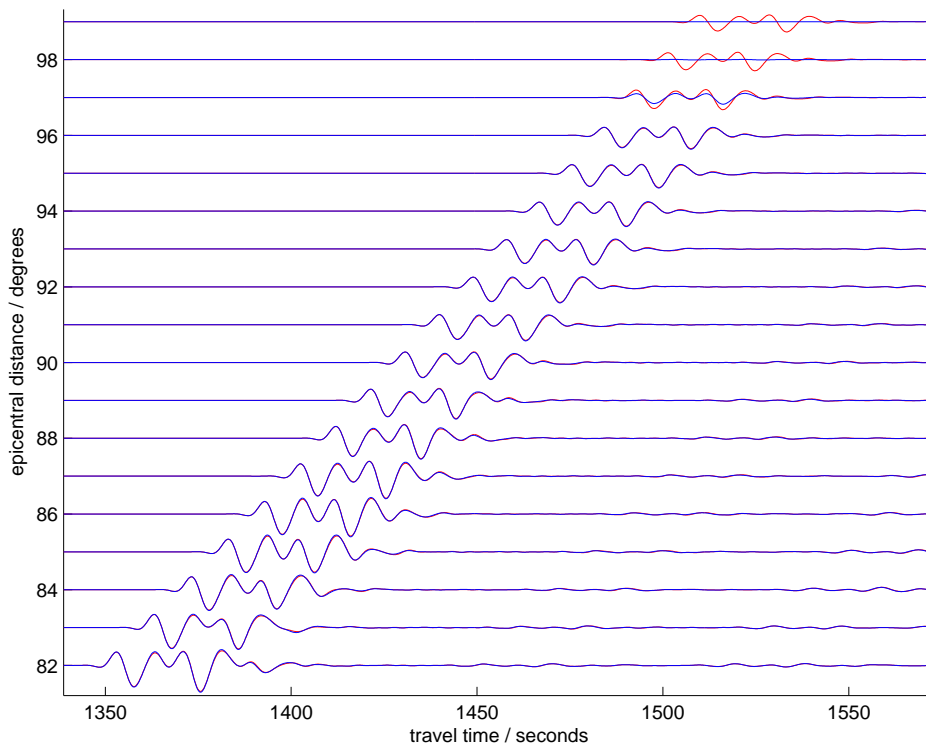


Figure 2.5: Seismograms for  $\Delta=82-99^\circ$  epicentral distance calculated with the hybrid code. Both domains, the axisymmetric (red line) and the 3D (blue line), use the PREM model. The direct  $S_H/ScS_H$ -wave is shown. Deviations between the seismogram pairs observable from  $97^\circ$  on result from absorbing boundaries that affect the 3D section from this distance on. At  $99^\circ$  on the 3D signal is effectively down at zero amplitude.

from small differences in the dispersion relation between the two- and the three-dimensional case and would thus be intrinsic to the hybrid method. Apart from that, it can be seen that at higher epicentral distances the seismograms of the spherical section diminish due to the use of absorbing boundaries at the back side of the section.

### 2.3.4 Application of the hybrid approach

For the application of the hybrid approach to the plume problem, a subroutine for implementing simple plume models was written. It is similar to the plume-model subroutine later described for the Spectral Element Code. Moreover, the subroutines for outputting the seismograms was modified to write out binary SAC (Seismic Analysis Code, GOLDSTEIN AND MINNER [1996]) format. This reduces the amount of needed disc space and eases subsequent processing of the data using SAC. As an illustration of the functionality of the hybrid method, we show an application to a plume at about  $90^\circ$  epicentral distance. Only the axisymmetric SH code is coupled with the spherical section code. This enables us to study conversions from SH to PSV waves caused by the plume.

The setup is the same as used for Fig. 2.5, only that here, in order to obtain snapshots of the wavefield, a band-limited source spectrum is required. We used 20 s as the dominant period for a Gaussian source-time function. Fig. 2.7 shows the resulting snapshots for all

components through different cross-sections through the plume, or at the surface.

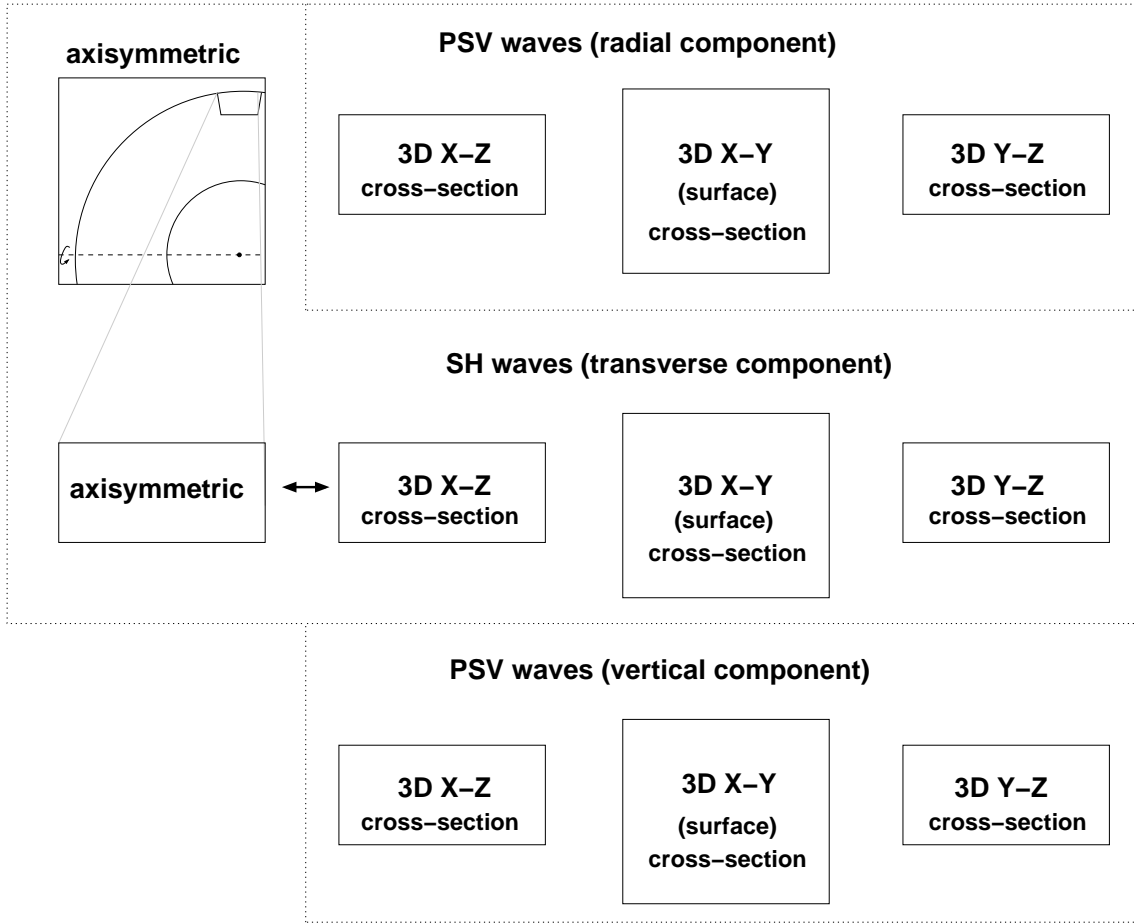


Figure 2.6: Legend to the snapshot figures of the hybrid code. In the upper left the SH wavefield of the axisymmetric domain is shown together with the symmetry axis and the position of the 3D section. Below, the axisymmetric wavefield at the position of the 3D section is enlarged. To the right of that, the wavefield at the same position, but calculated with the 3D code is shown. Differences between these wavefield should be only due to the usage of different models in the two codes (e.g. PREM in the axisymmetric and PREM+plume in the 3D domain). The other images in the middle row are other cross-sections through the model, all showing the transversal (SH) component. The upper and lower row show the radial and vertical components, respectively. Both components contain PSV waves and since no PSV energy is fed in by the axisymmetric code, these can only be generated by conversions due to lateral heterogeneities in the 3D. model. The right column shows depth cross-sections perpendicular to the direction of wave propagation, the middle column shows surface cross-section, and the left one shows depth cross-sections in the direction of wave propagation, as the leftmost column does for the axisymmetric wavefield.

The panels of Figure 2.7 show snapshots of the wavefield at different cross-sections (for a legend see Fig. 2.6) through the plume center (horizontal depth slices or at the surface) of the three components (radial, transversal and vertical). Since only SH waves are fed in from the axisymmetric code only the middle row (showing transversal, i.e. SH motion) gets a signal.



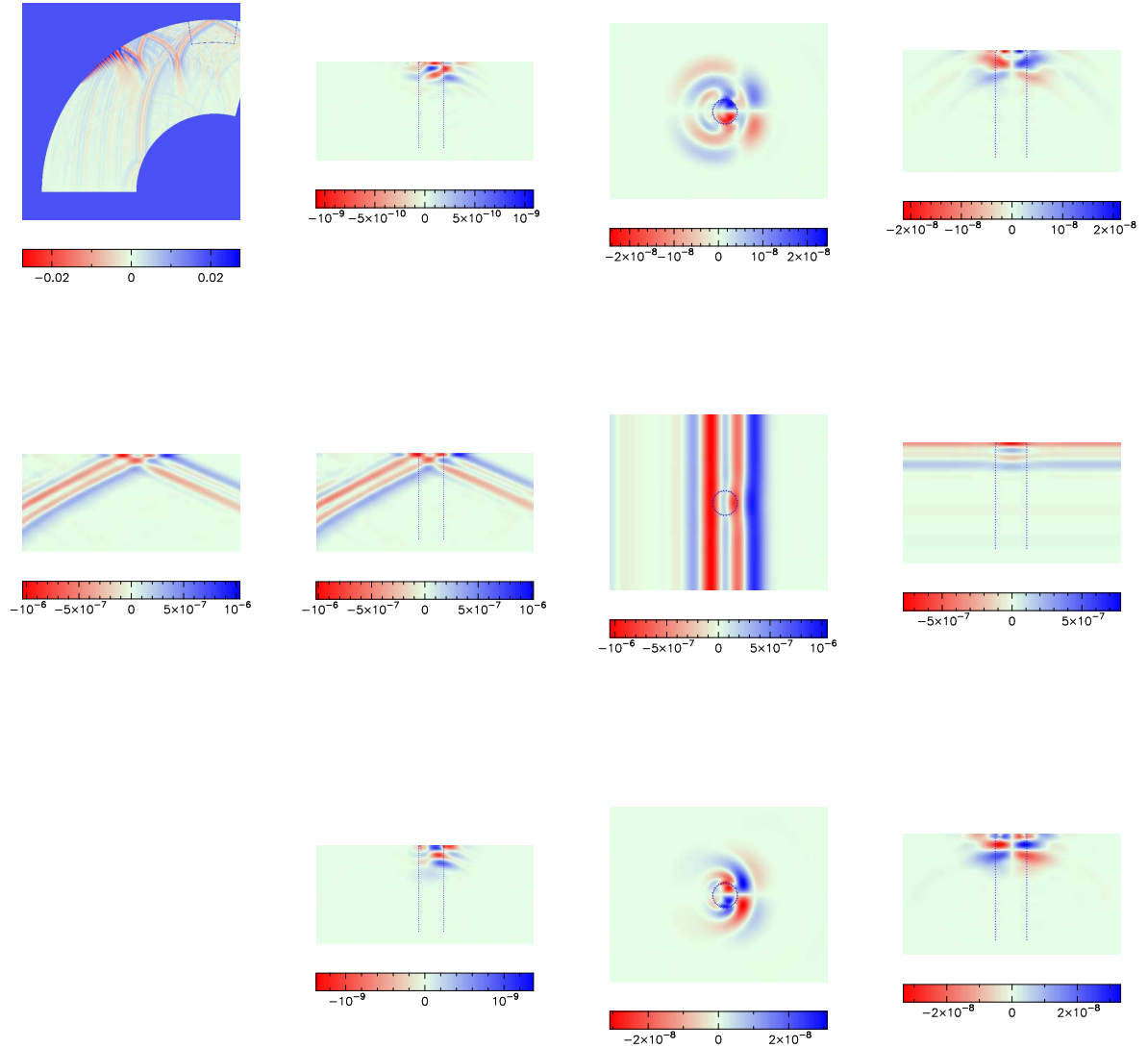
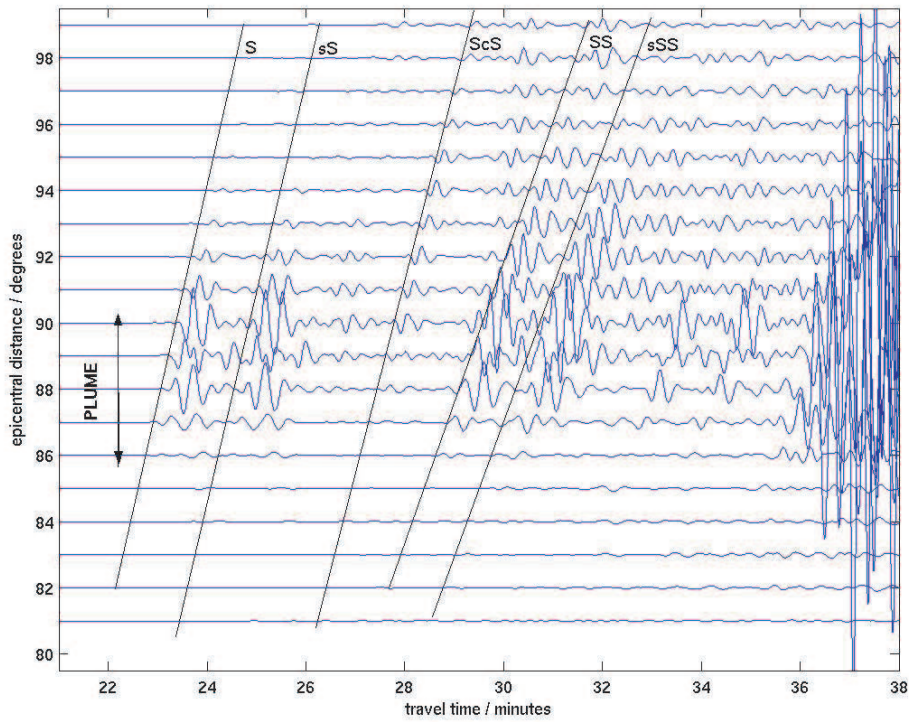
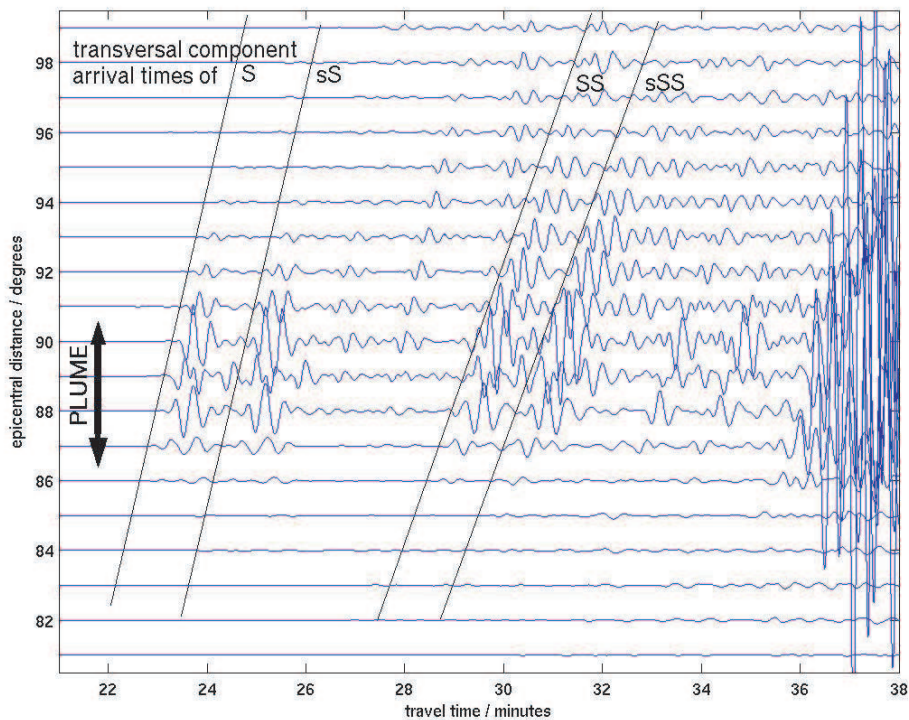


Figure 2.7: Snapshots of the wavefield as calculated with the hybrid code. A legend for this figure is given in Fig. 2.6. The upper and the lower row show conversions caused by the plume. In the middle picture (surface SH-motion) the healing behind the plume is clearly visible. Absolute amplitudes are arbitrary and serve only for comparison. Plume boundaries are given in blue.



(a) vertical component



(b) radial component

Figure 2.8: SH to PSV conversions caused by the plume. a) close up of radial component, b) vertical component. When feeding the spherical section only with SH waves, a signal appearing on the radial and vertical components can only result from conversions of SH to P-SV waves by a lateral heterogeneity, i.e. the plume. The onsets of some SH-phases are given as a black line, for reference. Note that some of the P-SV onsets here are earlier than these SH-arrivals, because P-waves travel faster after conversion than SH waves.

Motions on the other components are due to conversions at the plume. Conversion seismograms are shown in Fig. 2.8, for both the vertical (subfigure (a)) and the radial component (b). In these figures the arrival times of the SH wave are marked as black lines. The conversions concentrate in the epicentral distance range of the plume (cf. TILMANN *et al.* [1998]) and behind it. Note also some converted signals before the arrival of the original SH-wave (e.g. at  $90^\circ$ ). This is due to conversion at greater depth and subsequent faster propagation of the generated P wave.

The two leftmost panels of the middle row in Fig. 2.7 show the transversal (SH) component of the axisymmetric domain (left) and the spherical section. They differ only slightly, this is the difference in the wavefield caused by the plume.

Compared to other methods the parallel computation of the axisymmetric wavefield with the 1D model along with the wavefield in the spherical section using a 3D model has the advantage that the undisturbed solution is always provided along with the seismograms that are influenced by the 3D structure. A separate run for the background model (which is 1D) alone, needed for comparison, is an overkill to the problem, when carried out in full 3D.

### 2.3.5 Parallelization

In order to achieve high-frequency wavefield simulations, workstation clusters or supercomputers have to be used which requires parallel algorithms. The concept for parallelizing the hybrid algorithm goes beyond simple classical FD domain decomposition and is presented in the following.

Parallelization using domain decomposition and the Message Passing libraries (MPI) is currently the standard way to obtain reasonable portability and performance of numerical wave propagation codes even if the extra effort for parallelization is significant.

For the hybrid code a parallelization scheme based on MPI has been developed (Fig. 2.9).

Apart from running the parallelized subcodes in parallel inter-code communication is necessary. As a result of a long line of development and testing a scheme was developed (Fig. 2.10) that takes advantage of the possibility to define groups of processes within MPI, each with its own communicator (e.g., `MPI_COMM_SH` in Fig. 2.10).

Thus, it is possible to create a separate environment for each of the codes in a way such that there is no interference of the codes for example if the same variable names are used in the codes. This is an advantage since it allows development of the subcodes without much consideration of the other codes, as long as the variables used for inter-code communication are not affected.

Between these environments inter-code communication is possible. This is realized using the global message-passing communicator (`MPI_COMM_WORLD`). However, the routines that pass the axisymmetric wavefield to the spherical section are still restricted to special cases. Since the domain sizes of the individual codes can be chosen independently, a general scheme turned out to be difficult to realize.

## 2.4 Discussion

To study 3D wavefield effects of spatially confined structures in the mantle such as slabs or plumes an accurate modeling of 3D wave propagation is necessary. However, full 3D methods, though available and more and more used (e.g. KOMATITSCH AND TROMP [2002a])

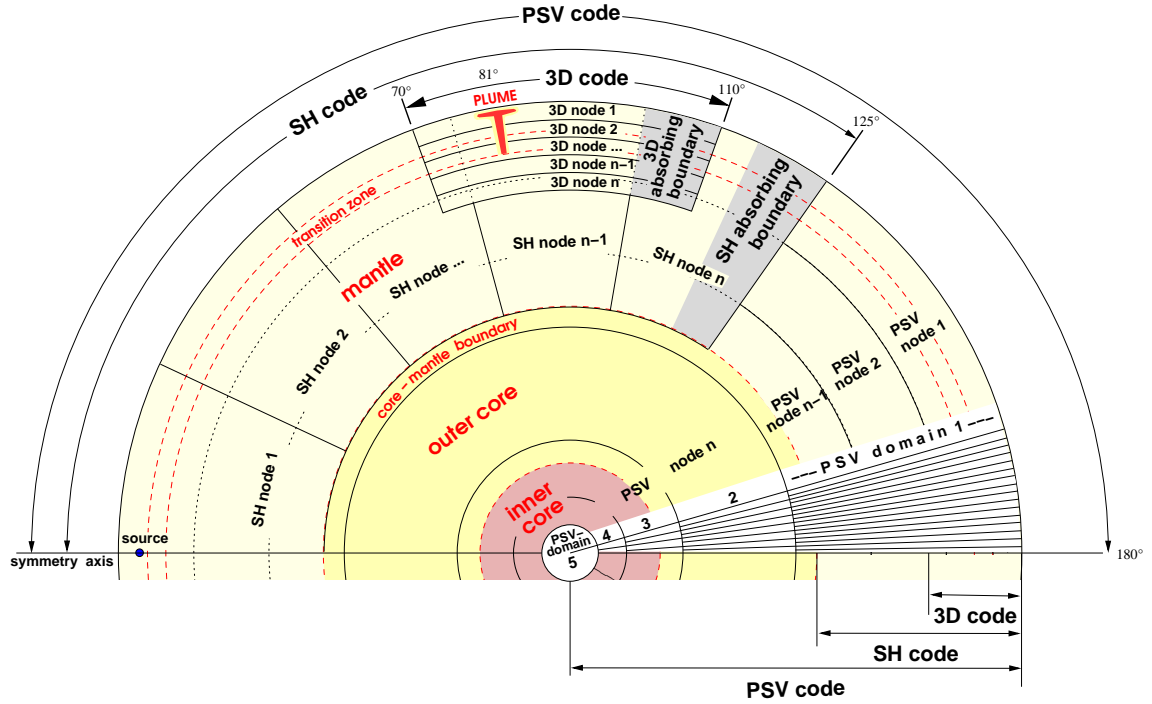


Figure 2.9: The complete parallelization scheme of the hybrid code with the axisymmetric SH- and PSV code and the 3D spherical section code. The PSV-code uses  $m$  nodes and covers the entire epicentral range ( $0-180^\circ$ ), with a vertical domain decomposition and a vertical, but different parallel distribution of nodes. The SH-code only covers an epicentral range that in this example slightly exceeds the 3D section's back end ( $0-125^\circ$ ). It is parallelized in the  $\theta$ -direction and uses  $n$  nodes. The 3D spherical section (here,  $70-110^\circ$ ) again uses vertical parallelization with  $k$  nodes. As an example, a plume coming from the '660' is implemented at an epicentral distance of  $81^\circ$ . Major discontinuities of the Earth are given in red dotted lines, node or domain boundaries in black. Grey shaded regions are the absorbing boundaries of the SH and the 3D code. At the right side at high epicentral distances the grid is shown with the domain numbers for the PSV-code.

are computationally still very expensive and are an overkill to the problem since most of the Earth structure modeled is still only 1D. Therefore, a new, hybrid method that combines an axisymmetric approach with a spherical section method has been developed which is more efficient. In this method the propagation of the wavefield over the long epicentral distance range is modeled using a 2D computational domain allowing for an efficient computation with an axisymmetric or 1D (e.g. PREM) background model. Around the structure of interest, the global wavefield is passed to a confined 3D spherical section grid, on which the full 3D wavefield including the interaction with the modelled structure is computed. An advantage is, that the expensive calculation in the 3D domain is only activated when energy approaches the 3D section, which saves computation time. This setup is suited for parameter studies with a lot of parameter combinations for confined structures and their interaction with the global wavefield at teleseismic distances. For closer distances the spherical section code can be used alone. Moreover, the hybrid method benefits from the possibility of considering only one of the independent wavefields (SH or PSV) since they are decoupled for the used axisymmetric

models. Thus, the study of conversions (SH to PSV and vice versa) is possible with the advantage to obtain the converted signals alone and not mixed with the actual arrivals on the respective component.

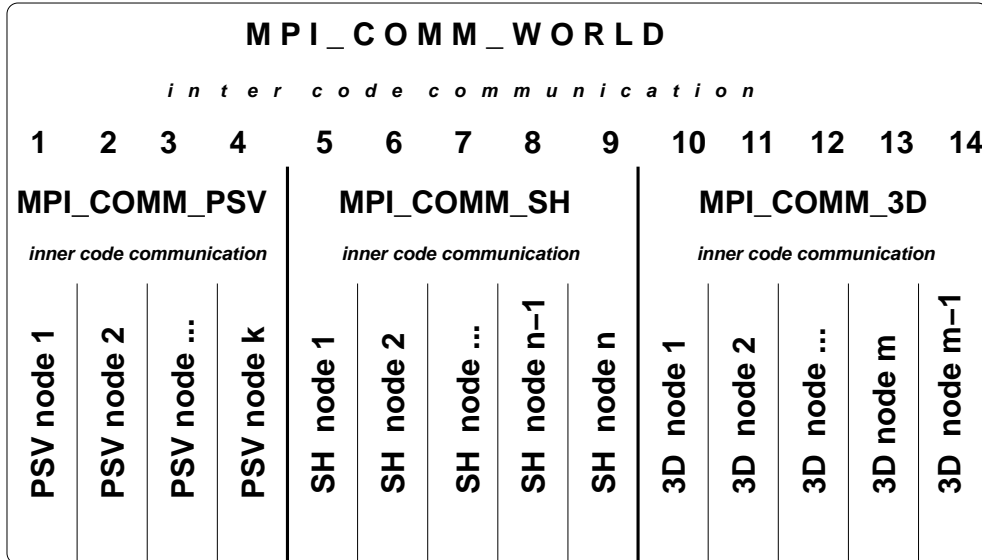


Figure 2.10: The hybrid communication concept. In this example, 12 nodes are globally available for the hybrid code (global node numbering from 0–11). The global MPI-communicator MPI-COMM-WORLD enables communication between all the nodes, and thus also inter-code communication. The nodes are distributed on the different codes. For each code a MPI sub-group for inner-code communication is set up, as well as node numbering for each code.

However, in order to run both the SH- and PSV-part together with the spherical section code parallelization is required because the memory and computation time needed for a serial execution exceeds the possibilities of a single current PCs. As already stated, the concept for parallelization is still restricted for some special cases. These do not fulfill the requirements for carrying out extensive parameter studies of whole-mantle plumes. At the time of developing the hybrid code, a code using the spectral-element method which is described in the next chapter became available which is suited for global wave propagation studies. Therefore, we decided to use this code for the following simulations for the plume parameter study. Nevertheless, the code developed here provides a useful tool for confined upper-mantle structure parameter studies and allows for an efficient computation of high frequencies with a need of computation time and memory that is far less than that of full-3D modeling programs.

and is achieves frequencies



## Chapter 3

# Forward modeling of wave propagation through mantle plumes

This chapter presents the results of modeling teleseismic wave propagation through mantle plumes using the spectral element method which is briefly summarized at the beginning. Subsequently, the spectral element program SPECFEM3D and the subroutine developed for implementing plume models is described.

Thereafter, a selection of seismic plume models will be presented that sample the parameter space of suggested plume properties such that we can investigate the influence of the perturbation magnitude, the radius of the plume conduit, its origin depth and the spatial distribution of the perturbation of seismic velocities.

With the knowledge about the dimension of the plume models we suggest a receiver configuration consisting of several geometries that is expected to capture the seismic effects caused by a plume. It covers a large area with a relatively high density since we want to answer the question where to best place seismometers with respect to a plume in order to invert seismic data for obtaining the properties of a plume.

For covering a wide range of teleseismic epicentral distances and in order to investigate the plume's influence on a variety of phases we model earthquakes in three distances to the plume. Their parameters and their location with respect to Iceland – the study case of the next chapter – are presented.

It will be motivated that for the used frequency range and plume dimensions finite-frequency effects are supposed to play a major role. We will show that the perturbation of the seismic velocities and density with a plume-like model mainly results in travel-time delays and amplitude effects. Thereafter, the routines for mass processing of the simulation data to extract these two quantities from the synthetic seismograms are described. Eventually, the seismic effects of the plume models depending on their parameters are presented on the basis of selected examples of phases and epicentral distances. The chapter ends with a discussion of the relevance of the findings for plume experiments.

### 3.1 The Spectral Element method

The Spectral-Element Method (SEM) has been a valuable tool in fluid dynamics for more than 20 years (PATERA [1984]). It was introduced to local-scale seismic wave propagation by SERIANI *et al.* [1992]. In 2000, CHALJUB applied the method to global wave propagation.

KOMATITSCH and TROMP presented a parallel spectral element code (SPECFEM3D) in two versions for both, local and global wave propagation. After briefly summarizing the principles of the spectral element method, the code is described in some detail since it is used and modified for this work. The section finishes with presenting the plume-model subroutine that has been added for the study of plumes in this work.

### 3.1.1 Basic principles

A detailed introduction and description of the SEM can be found in SCHUBERTH [2003] and in papers by KOMATITSCH AND TROMP [1999, 2002a,b]; KOMATITSCH *et al.* [2002, 2003]; CHALJUB *et al.* [2006]. The next two sections are based on these publications if not stated otherwise.

The spectral element method is a high-order variational method that combines the ability of classical finite element methods to handle complex geometries with the exponential convergence rates of spectral methods.

It is based on the integral, or “weak” form of the elastic wave equation. The latter is obtained by multiplying the wave equation (2.1) for an inhomogeneous elastic medium with a time dependent, so-called “test function”  $v$ . Applying integration by parts an integral over the boundary of the domain is obtained that vanishes by introducing free surface conditions. Finally, we obtain the weak form that reads

$$\int v \frac{\partial u_i}{\partial t^2} d^3r - \int \nabla v \sigma d^3r = \int v f d^3r \quad (3.1)$$

The main steps used in the spectral element method to solved this equation are briefly summarized as follows:

- Decomposition of the domain into elements by meshing which take into account inhomogeneities and discontinuities to avoid oversampling. The integral form of the elastic wave equation now has to be solved for every element separately
- Mapping of each element onto a reference cube  $[-1, 1]^3$ . This way, all further calculations for the elements can be carried out in the same manner
- Element-wise Lagrange-type interpolation of the functions under the integrals on the standard interval
- Integration of the functions using a special scheme, the so-called Gauss–Lobatto–Legendre quadrature
- Choosing the interpolation points to be the same as the integration points of the GLL quadrature leads to an exactly diagonal “mass matrix” (first term on the left hand side of Eq. 3.1. The second term is the so-called “stiffness matrix”)
- Assembly of the elemental mass- and stiffness matrices leads to a global linear system of equations that can be written in the following matrix form:

$$\mathbf{M}\vec{U} + \mathbf{K}\vec{U} = \vec{F} \quad (3.2)$$

with  $\vec{F}$  being the vector of the external forces acting on the system

- Integration of this system in time. Due to the diagonality of the mass matrix an explicit time-stepping scheme can be used, usually a FD scheme



### 3.1.2 Program SPEC-FEM3D for global wave propagation

The spectral element method, as described above, was implemented in the 3D global wave-propagation code by KOMATITSCH and TROMP. Through the years a couple of options have been implemented, including anisotropy, attenuation, topography and bathymetry, extended sources, and the possibility of accounting for the effects of self-gravitation and rotation of the Earth. Thus, to date, SPEC-FEM3D is the only program for 3D wave propagation simulation for the entire globe which allows calculation of realistic teleseismic seismograms. It supports parallelization using MPI for application on workstation clusters or large super-computers. The program consists of two parts, the so-called “mesher” (`meshfem3D`) and the “solver” (`specfem3D`) along with some routines for post-processing of the output data, e.g., for combining the graphical output of the different processors.

The mesher creates a mesh for the globe (Fig. 3.1), based upon the concept of the quasi-uniform projection, or cubed sphere (SADOURNY [1972], RONCHI *et al.* [1996]) which was introduced to global wave propagation problems by TAYLOR *et al.* [1997] and CHALJUB [2000].

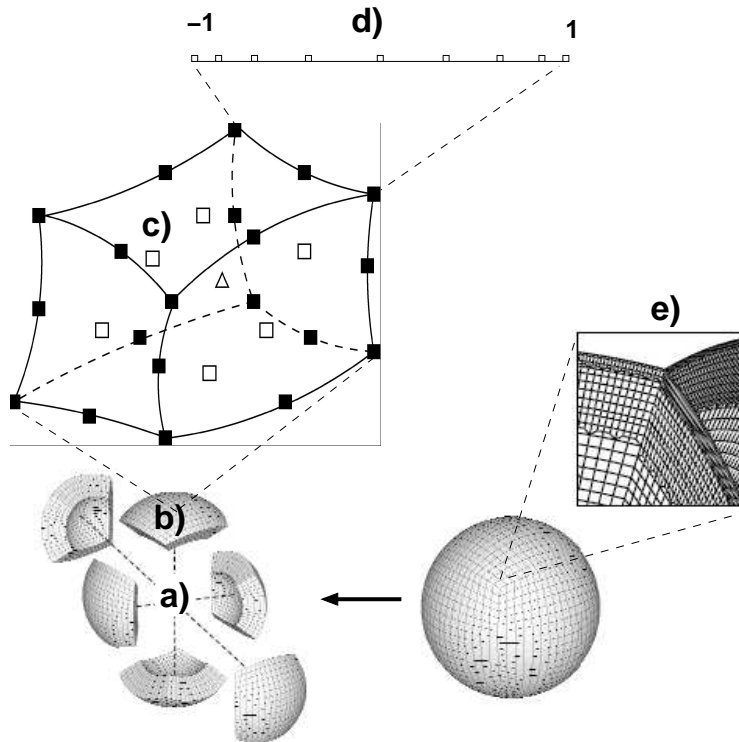


Figure 3.1: Overview of the meshing and mapping of the spectral element method as implemented in SPEC-FEM3D. **a)** The globe is split up into six “chunks” **(b)** of  $90^\circ$  (cubed sphere approach) and a central cube not shown here. The six chunks are subdivided into elements **(c)** which honor heterogeneities and discontinuities in the material properties. The sides of each element are then sampled by “anchor points” (black squares and triangle) which are mapped to a standard interval  $[-1, 1]$  **(d)**. A chunk triple-junction is shown in **(e)**. The mesh doubling below the Moho and the 660-discontinuity can be seen. It takes place at different depth for the three chunks in order to retain a conforming mesh.

It avoids singularities by decomposing the sphere into six  $90 \times 90^\circ$  sections, called “chunks”

and a central cube in the inner core. Each of the global geographical coordinates of the chunks are then mapped by projection of an equi-angular grid on the sphere to an equidistant cartesian grid on a cube that is inscribed into the sphere (see, e.g., DANECEK [2004]).

Since the seismic velocities in the Earth increase with depth, the mesh size has to be changed in the vertical direction in order to keep an approximately equal number of grid points per wavelength. This is done by doubling the mesh size at depth coinciding with the major seismic discontinuities, i.e. below the Moho, below the 670 discontinuity, and just above the inner core boundary. The mesh doubling is done by first increasing the mesh size in one lateral direction, and subsequently, at a greater depth, doubling its size in the other lateral dimension. This has to be done in slightly different depth for the different chunks, in order to obtain elements, that exactly share their faces at the chunk boundaries ("conforming mesh"). Using different depths, however, does not always honor the discontinuities and leads to an oversampling in some regions. Moreover, then the chunks are not all the same, but there are three different chunk types, with the mesh doubling taking place at different depth.

In the setup used for this work,  $240 \times 240$  elements for the surface of each chunk are used. Due to the mesh doubling, we obtain  $30 \times 30$  elements per chunk at the inner core boundary. With this resolution, the simulated seismograms are accurate down to a period of about 20s. By using five processors for each lateral direction per chunk  $6 \times 5 \times 5 = 150$  processors are needed. On the supercomputer Hitachi SR8000 of the Leibniz-Rechenzentrum several job partitions with different numbers of nodes exist. Each node has a shared memory of about 8 GB and consists of 8 processors. Using 19 nodes of the 32-node partition is the optimal configuration for using SPEC-FEM3D under these hardware requirements. Note that the auto-parallelization inside the nodes has to be explicitly switched off, because of the indirect addressing of grid nodes that would otherwise lead to a very bad performance. Moreover, the original version of the code created a lot of small files, e.g., it wrote every component of every seismogram separately. This was changed because it significantly decreased performance due to the file system of the Hitachi.

Sources are implemented using a file with one or more Centroid Moment Tensor (CMT) solutions (DZIEWONSKI *et al.* [1981]), given in the standard Harvard CMT solution format (see [www.seismology.harvard.edu/projects/CMT/](http://www.seismology.harvard.edu/projects/CMT/)). The source is specified as one or more points with a location and depth, an origin time, and a moment tensor. By plastering the desired fault plane with point sources and using appropriate time delays between the origin times of the individual sources one can mimic an extended source process. For recent large earthquakes, kinematic rupture source models are generated in the CMT solution format by CHEN JI and are offered for download on a website (<http://www.gps.caltech.edu/~jichen/Earthquake/>)

### 3.1.3 Seismogram format and data processing

Processing of synthesized seismograms was mostly carried out using the Seismic Analysis Code (SAC). Since SPEC-FEM3D in its official distribution outputs only ASCII time-series the `write_seismograms`-subroutine was altered so that it outputs seismograms in alphanumeric SAC format. The less disc space consuming way of saving the seismograms in the binary SAC format was not possible to implement, because the necessary libraries are only offered in two precompiled versions, neither of which works with the Hitachi operating system. All relevant variables of the simulation, the station, and the event are defined in the subroutine and written to SAC header variables, so that standard processing steps such as rotation of components can easily be carried out since the necessary meta information is known. For

example, rotating the horizontal components to transverse and radial direction only requires one single command (`rgp`) in SAC. The basic processing steps are described briefly in the following. After retrieving the seismogram file of each processor, the files are chopped to obtain one file per component and station. After conversion to binary SAC format for saving disc space, the seismogram files are distributed in different directories, according to the virtual network they belong to. There, the horizontal components are rotated to radial and transverse direction to the epicenter.

The subsequent processing steps are described when applied, unless otherwise stated a low-pass filter with a corner frequency of 0.05 Hz has been applied to the SEM data.

### Seismograms for the PREM model

The next three figures (3.2-3.4) show seismograms in  $10^\circ$  steps for the transverse, radial and vertical component of the PREM model, respectively. The source depth used in the simulation is 37.4 km, the moment tensor of the modeled earthquake is given in Table 3.2. The theoretical travel times of some phases are marked by colored lines, as annotated. No filtering has been applied in order to preserve the sharpness of phase onsets, therefore, numerical noise is visible on some traces. Some parts of the seismograms are clipped in order not to interfere with neighboring traces while still keeping weak phases visible.

#### 3.1.4 Plume models in SPEC3D

For implementing appropriate 3D plume models in the spectral element code a subroutine (`plume_model.f90`) was written that is called after the execution of the 1D (PREM or IASPEI) or 3D Earth model subroutine and that perturbs the velocities and density set by these routines according to a plume model.

The subroutine is called for every gridpoint by the SPEC3D-subroutine `get_model`. It allows the implementation of a variety of plume features and a broad range of model parameters by adding a negative velocity perturbation to the used velocity model. The plume properties that can be modelled with the plume-subroutine are described briefly in the following.

#### Position of the plume

The position of the plume is specified by the geographical coordinates of the plume axis. In case the option of a tilted plume is chosen, another set of coordinates for the plume origin at the CMB has to be given.

#### Plume head

For the plume head, two geometries can be modeled. One is simply just disc-shaped, with the horizontal top and bottom depths and the radius as parameters. However, independent of the depth of the given head top, it will be cut at the Moho depth. Thus, the head in that case would have a rounded top. The other head geometry is one that consists of two Gaussian functions in the vertical direction. Here again, the top is cut when intersecting with the Moho. The bottom of the head approaches the radius of the conduit. An example for this head model can be seen in Fig. 3.5.

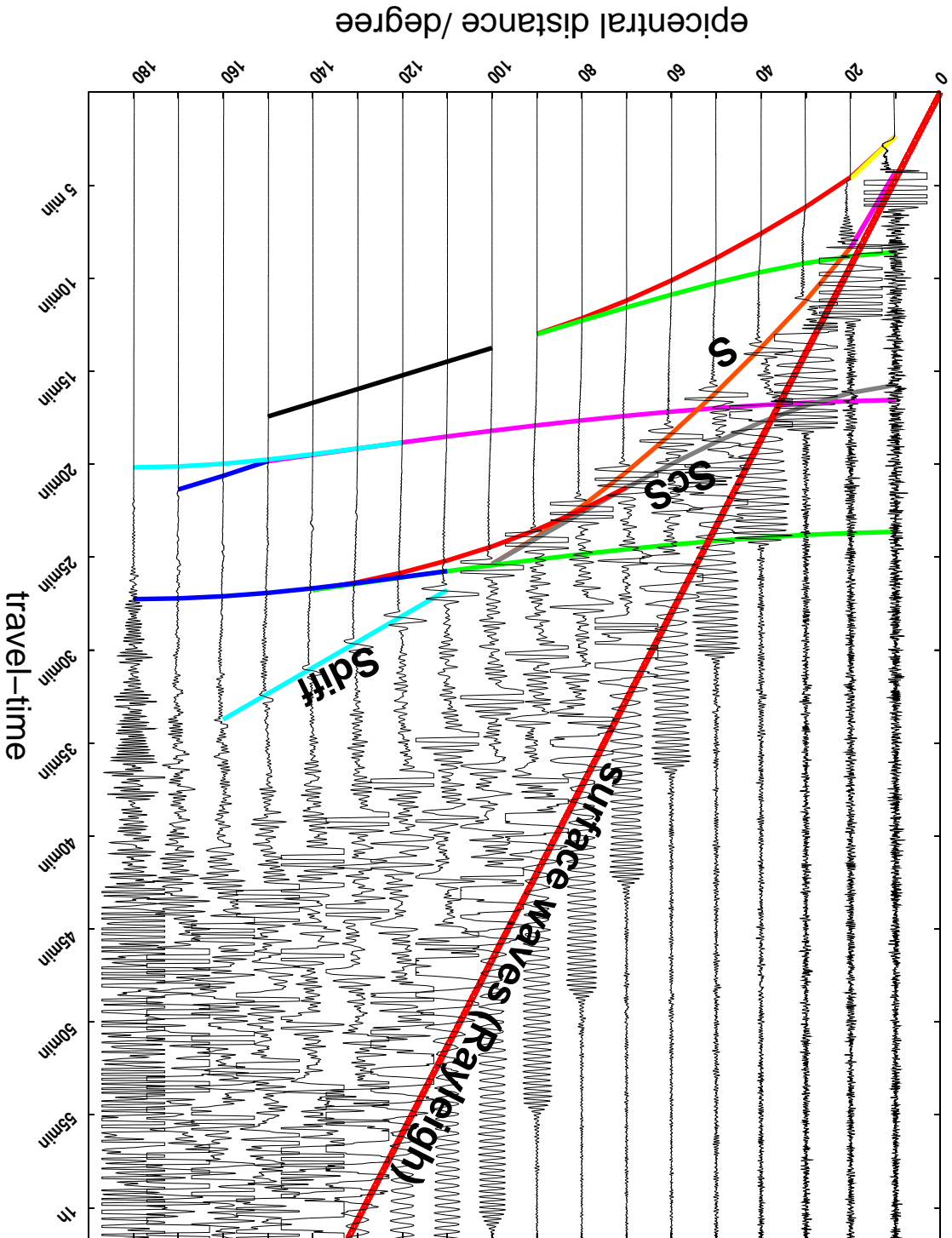


Figure 3.2: Seismograms simulated with the spectral element method code SPECSEM3D. The transverse component (SH-waves) is shown for the PREM model. Ray-theoretical travel-times are given as lines with different colors for the ease of distinction.

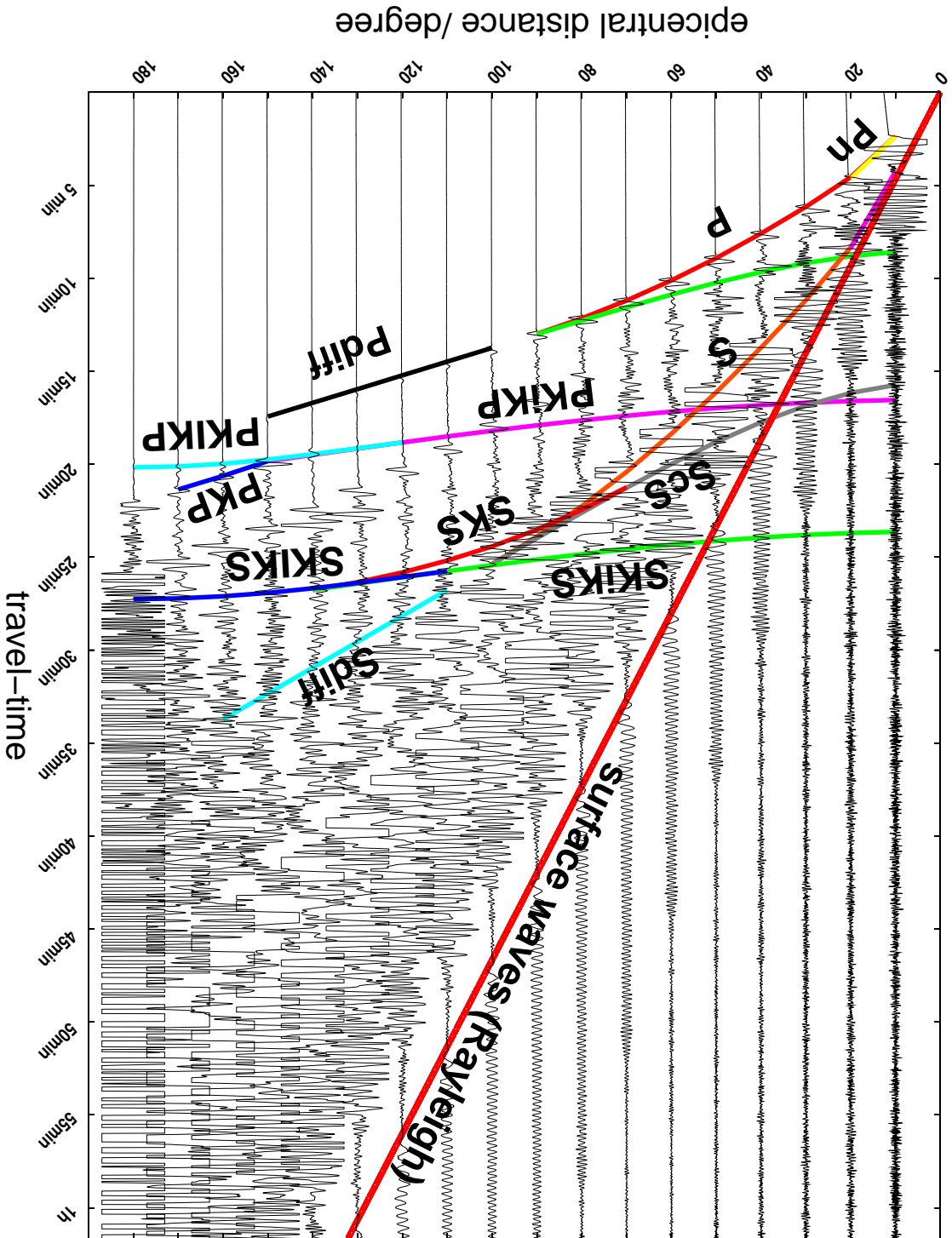
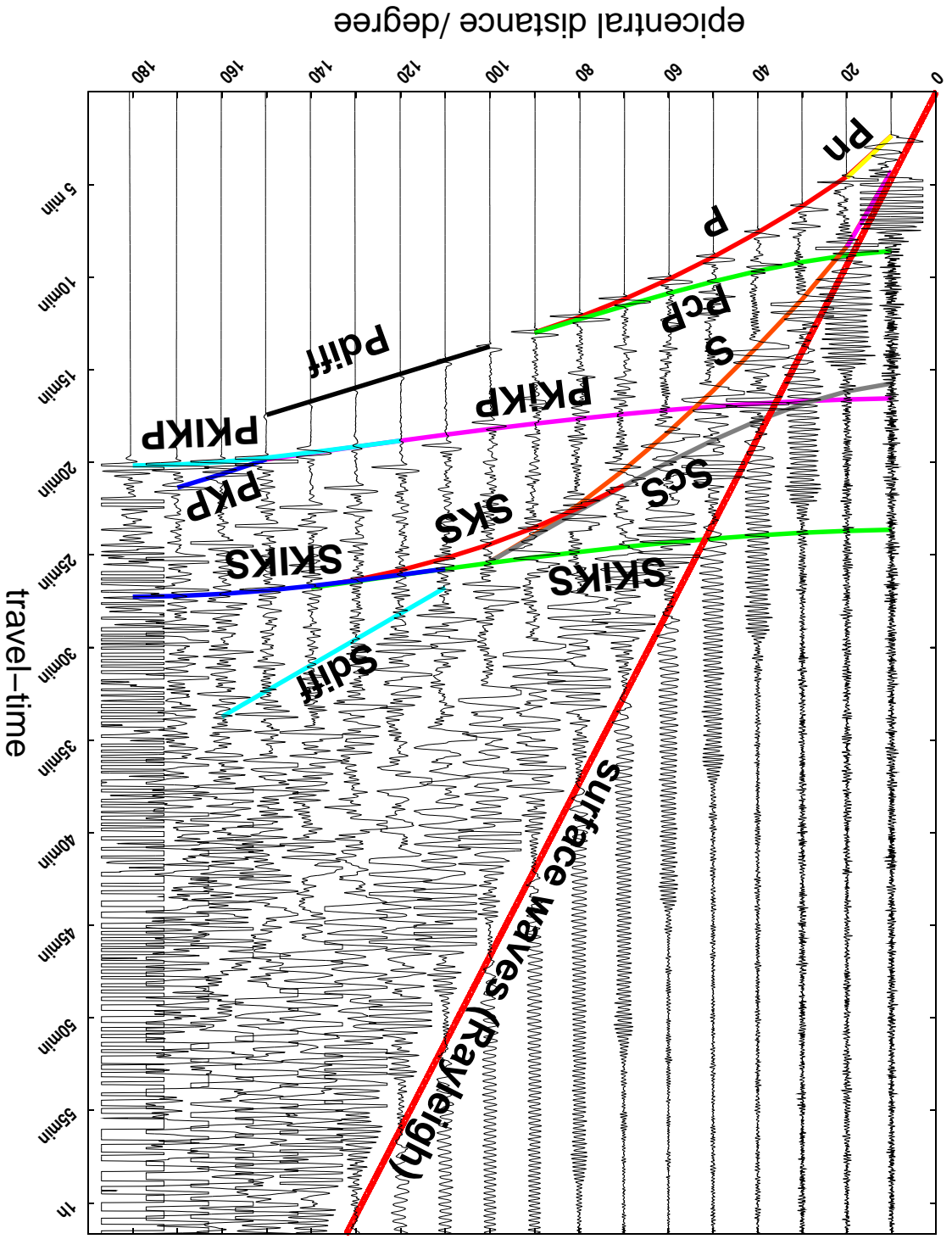


Figure 3.3: Seismograms simulated with the spectral element method code SPEC-FEM3D. The radial component (PSV-waves) is shown for the PREM model. Ray-theoretical travel-times are given as colored lines.

Figure 3.4: Seismograms simulated with the spectral element method code SPEC-FEM3D. The vertical component (PS-waves) is shown for the PREM model. Ray-theoretical travel-times are given as colored lines.



## Plume tail

The plume tail consists of four parts. The upper part starts at a prescribed depth and extends down to the base of the upper mantle with a radius  $R_{\text{tail\_um}}$ . In the transition zone the tail radius increases linearly down to the lower mantle, where it has the radius  $R_{\text{tail\_lm}}$ . With this radius the tail extends further to where it originates or where another, optional zone starts. There, the tail fades out to a prescribed percentage of the given perturbation. In case the radius for the upper and lower mantle is identical the plume will have a constant tail radius over its entire length. However, two more options for modulating the plume tail radius exist. One is to model a bulge around the 660-discontinuity (with vertical and horizontal extent as parameters) and another one is a broadening of the tail at its base in the D'' layer. In the latter case the maximal horizontal extent and the starting depth of broadening have to be defined.

In summary a complete, multi-parameter plume (Fig. 3.5) can be modeled that originates in the D'' layer with a broad foot with increasing perturbation, then extends upward with

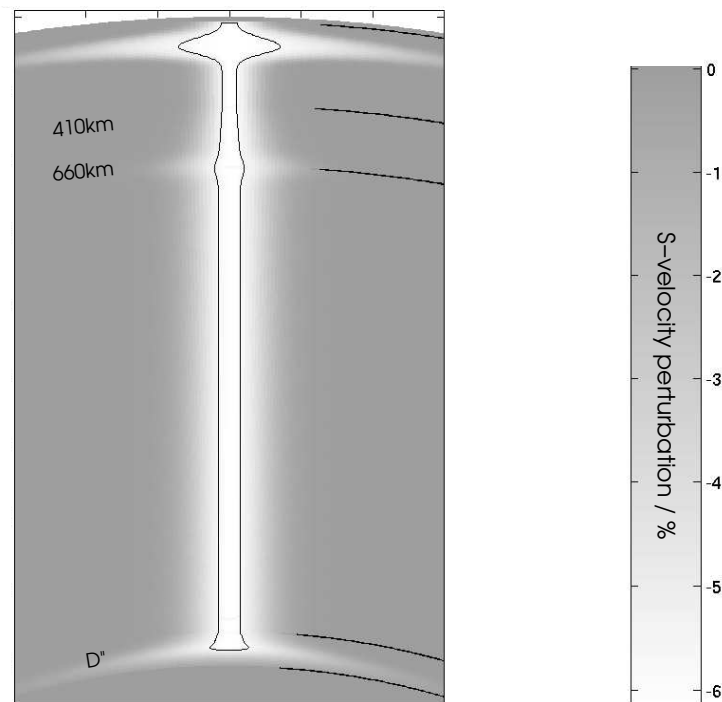


*Figure 3.5: A plume model created with the plume model subroutine written for SPEC3D. It is designed to represent the basic features of the plume model resulting from numerical simulations from DAVIES [1999]. The figure has the same layout as in Davie's book for ease of comparison. However, in contrast to Davie's figures the S-velocity perturbation is grey coded rather than the temperature. A 5% contour line and the 410- and 660-discontinuity is shown.*

a conduit that broadens below the transition zone due to the inhibiting effect of the phase transition at 660 km depth. Once the plume conduit surpasses this phase transition it thins down to a smaller diameter because of the contrary effect of the phase transition at 410 km depth. From there it continues with constant diameter into a head that ends below the crust.

model ID	$\delta v_P$	$\delta v_S$	radius	$\delta v(r)$	origin depth	other
1	3.5%	6.2%	100	sharp	CMB	
2	3.5%	6.2%	100	sharp	670 km	
3	7.0%	12.4%	100	sharp	CMB	
4	3.5%	6.2%	100	Gauss	CMB	
5	3.5%	6.2%	300	sharp	CMB	
6	3.5%	6.2%	60	sharp	CMB	
7	3.5%	6.2%	$\approx 100$	thermal	CMB	
8	3.5%	6.2%	100	sharp	CMB	with Head
13	9.72%	17.2%	60	Gauss	CMB	
30	0.39%	0.69%	300	Gauss	CMB	

Table 3.1: Parameters of the plume models whose results are discussed in this chapter

However, this was only one scenario using a lot of implemented options. One is free to switch off many of them and to let the plume originate at any arbitrary depth. Due to limited computing time and long waiting times on the supercomputer used for this work it was not feasible to explore all the possibilities just presented. Therefore, plume models were selected in order to sample the parameter space of suggested plume properties (reviewed in Chapter 1). The focus was on the values obtained for the Iceland plume, since it is very well studied with all available seismological methods (see Chapter 4).

The models the results of which are discussed in this chapter are summarized in Table 3.1. The “**default model**” consists of a plume with a sharp onset of the seismic velocity perturbation (3.5% for P-, and 6.2% for S-waves) within a radius of 100 km around the plume center. The plume originates at the core-mantle boundary. This default model is chosen for several reasons. The perturbations are those of a regional finite-frequency tomography study by HUNG *et al.* [2004] for Iceland. Since ray-tomography studies tend to underestimate the perturbation due to the ignorance of wavefront healing, we took the only available finite-frequency results from a regional experiment. The radius is a typical value for many high resolution plume studies, e.g. for Iceland (ALLEN *et al.* [1999]). The step perturbation function was used to obtain a clear effect of the plume boundaries; a previous study by STRASSER [2001] has shown that smoother perturbation functions leave a less pronounced signature in the wavefield. The origin depth at the CMB corresponds to the original plume hypothesis of MORGAN [1971].

From this model five parameters are varied to sample the model space. The **perturbation magnitude** is doubled, which leads to an S-wave perturbation of 12.4%. This is probably unrealistically high considering that its not the maximum value of a gradational perturbation function but the value for a sharp plume model. However, the expectation is that the observed effects scale linearly with the perturbation, and that weak effects that might not be detectable with the default perturbation may be highlighted and become observable with this strong plume model (P3). Two other models (P13 and P30) have higher ( $\delta v_P=17.2\%$ ) and lower (0.69%) perturbations in order to keep the same integral total perturbation because they have a smaller (60 km) and larger (300 km) **radius**. These radii were chosen because they represent end-members in the range of suggested plume perturbation dimensions (note that due to thermal interaction of the plume with the surrounding mantle the perturbation of the plume on the seismic velocities covers a larger region than the plume conduit itself. The thermal



“halo” of a plume with 300 K temperature contrast is 70 km (SLEEP [2004]), whereas conduit radii may be as small as 10 km (LOPER AND STACEY [1983]). The radius of 60 km (P6 and P13) is the lowest value suggested for Iceland (ITO *et al.* [1996]), whereas 300 km (models P5 and P30) is the largest value for this plume (RIBE *et al.* [1995]), meanwhile ruled out by tomography studies, see ALLEN AND TROMP [2005].

Models P1 and P4, P6 and P13, P5 and P30, and P7 differ in the **perturbation functions** used. Apart from the actual geometry the spatial distribution of the perturbation of seismic velocities as a function of distance from the plume axis might be a crucial parameter for detection of plumes. It is obvious that a sudden, sharp onset of the perturbation (following a Heavyside function) has the highest reflection coefficient whereas a more smooth onset seems to be more realistic, especially for older plumes, where we expect a thermal halo caused by heat conduction.

The related questions thus are a) how does the form of the perturbation function influence the waveform and thus the plume diameter derived by seismology, b) can differences in the perturbation function be resolved in the frequency range modeled or distinguished from the resulting waveforms c) what is the physical constraint on likely perturbation functions.

In order to study these issues, different plume models were set up and the resulting waveforms are compared. An important demand on the models is that the integral over the perturbation is equal for all the models in order to make the waveforms comparable. Otherwise differences in delay times are only due to the increased total perturbation rather than to the effect of the boundary.

We propose the following perturbation functions (Fig. 3.6):

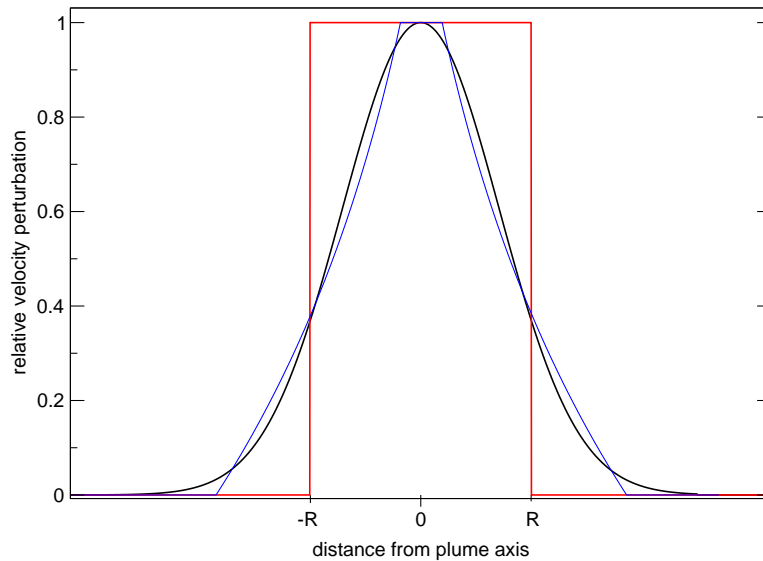


Figure 3.6: Spatial velocity perturbation functions: boxcar function (red line) for a “sharp” plume, Gaussian function (black) and a “thermal” model with a slim conduit and a decaying perturbation outwards due to heat conduction (blue). Note the similarity between the thermal model and the Gaussian function.

- **Sharp boundary.** The most simple model, physically assuming no (thermal) interaction between plume conduit and the surrounding mantle (heat conduction or entrainment) and no lateral temperature variation in the conduit. The resulting total pertur-

bation is  $P_{tot} = 2\pi r \cdot \delta P_0$ . This value is the target value of all other plume models and is used for their normalization.

- **Gaussian boundary.** The most simple analytical form of a smooth function:  $e^{-\frac{\ln(b)}{R^2} \cdot (x-x_P)^2}$  with  $x$  being the distance from the plume center  $x_P$ . The value  $b$  decides on the definition of the Radius  $R$ . For example, if  $b = 0.5$  then two times  $R$  is equal to the half-width. In our models  $b$  is set to  $1/e$ . In that case the Gaussian and the sharp boxcar function have the same height which is favorable for comparison. The radius then refers to where the Gaussian drops down to  $1/e=36.8\%$  of its maximum. Where the plume perturbation is below  $1/1000$ th of its peak values the perturbation is considered negligible and thus defined to be zero from there on.
- **Thermal boundary.** From a physical point of view, heat conduction leads to a logarithmic decay of temperature and thus of seismic velocity perturbation. Therefore, another model is set up that combines a constant perturbation plume stem out to the plume radius  $r_P$  together with a logarithmic decay out to where the unperturbed mantle values are reached ( $r_M$ ):

$$P(r) = \begin{cases} P_0 & , \text{ if } r < r_P \\ \frac{P_0}{\ln(r_P/r_M)} \cdot \ln(r/r_M) & , \text{ if } r \geq r_P \end{cases}$$

Concerning the **origin depth** only two different values are used, 660 km (model P2) and 2890 km (all other models), i.e. the bottom of the transition zone and the bottom of the mantle, respectively. These two depths are the only obvious candidates for a thermal boundary layer, the CMB because of the large temperature contrast between the mantle and the core and the 660 discontinuity in the cases of layered convection with the presence of a “second asthenosphere” as suggested by CSEREPES AND YUEN [2000] or of secondary plume upwellings from the superplumes that pond beneath the transition zone. Plume origin locations in the mid-mantle have been suggested (e.g., recently by DAVIES [2005]), however, there is no specific depth from which such mid-mantle plumes could rise. It is also difficult to set up any model for “Andersonian” types of anomalies, since their shapes are unknown as well. Therefore, we restrict ourselves to only two plume origin locations or depth extents.

## 3.2 Experiment configuration and data processing

Three experiment configurations were set up in order to systematically study the wavefield effects of plumes in general, and of the Iceland study case in particular. The aim is obtain a seismometer configuration that spans over the entire area of expected plume-perturbed arrivals with a density such that small scale features of the pertubed wavefield are not missed. On the other hand, it does not make sense to work with seismometer network that can never be realized in real experiments. Finally, the amount of data resulting from the network should still be processable with a reasonable effort.

### Array of receiver lines

For the general study two different kinds of receiver configurations are used. One, that consists of 19 lines of receivers with constant epicentral distances around 90 degrees. The largest extension of these lines are two times the biggest plume model diameter, i.e. 600 km. One

reason for choosing this extension was the statement of TILMANN *et al.* [1998] that the focal length of a plume is twice its diameter. For the default diameter of our model (200 km) this would be 400 km, however, in case of a 100 km-radius Gaussian perturbation function, the actual extension of the perturbed zone is wider, maybe about 150 km. To take that into account, we chose an extent of 600 km for the array. Moreover, an aperture of 600 km was claimed to be optimal in the proposal for the European Ocean Plume Project (HOFMANN *et al.* [2000]), the dense part of the PLUME project for Hawaii has also about this extension, and the Eifel plume project used an array of 500×500 km. These examples show that such an effort is feasible and realistic for future experiments. The geometry of our array is shown in Fig. 3.7. This geometry, originally set up for a 90° distant plume, is also used for the other plume locations in order to compare the results. The numbering of the receivers that is used throughout the rest of the text consists of four digits, where the first two represent the line number (1–20) and the last two the receiver number (1–19) on the line. If one takes all receivers with the same receiver number one obtains a receiver string with constant azimuth. Receiver line 10XX and receiver string XX10 runs through the plume center, receiver 1010 is thus right at the plume center. Note that the array is set up to be denser at the center and is not symmetric around the plume, because the region behind the plume will be more influenced by the effects of the plume. The station spacing of 50/100 km is also realistic; such inter-station distances have been realized in past experiment, e.g. in Iceland (Chapter 4). On the other hand, the station density is sufficient to resolve the wavelengths relevant for our simulations since the inter-station distance is smaller than the shortest wavelength.

### Receiver Rings

The second receiver configuration consists of concentric rings of receivers around the plume center (Fig. 3.8). The receivers are placed at steps of 10 degrees leading to 36 receiver per ring. There are nine rings (R1-R9), with diameters from 50 km up to again two times the biggest plume model diameter, i.e. 600 km. These rings are set up to capture potential effects at or around the plume rim, boundary effects etc. Moreover, the constant number of receivers per ring leads to a higher station density in the direct vicinity of the plume. The receiver IDs also consist of 4 digits, beginning with R (for ring), followed by the ring number (1-9) and the number of the receiver on the ring (1-36). The numbering is such that the receivers on the great circle through epicenter and plume center are number 18 (closest to the source) and 36 (farthest), number 9 is to the right as seen from the source, consequently number 27 is to the left, since the numbering is clockwise.

### Great-circle stations

For studying the long-distance behavior of the wavefield virtual receivers were “installed” on the great-circle through the epicenter and the plume (hereafter mostly referred to as great-circle). They have an inter-station spacing of 1° (~111 km). These stations were used for the global set of the seismograms shown in Chapter 2, Figs. 3.2–3.4.

### Existing stations

For the specific study of the Iceland plume an additional set of receivers is used. It consists of both temporary and permanent stations installed on Iceland. Apart from the permanent SIL network and the deployments for the HOTSPOT and ICEMELT experiments ocean bottom

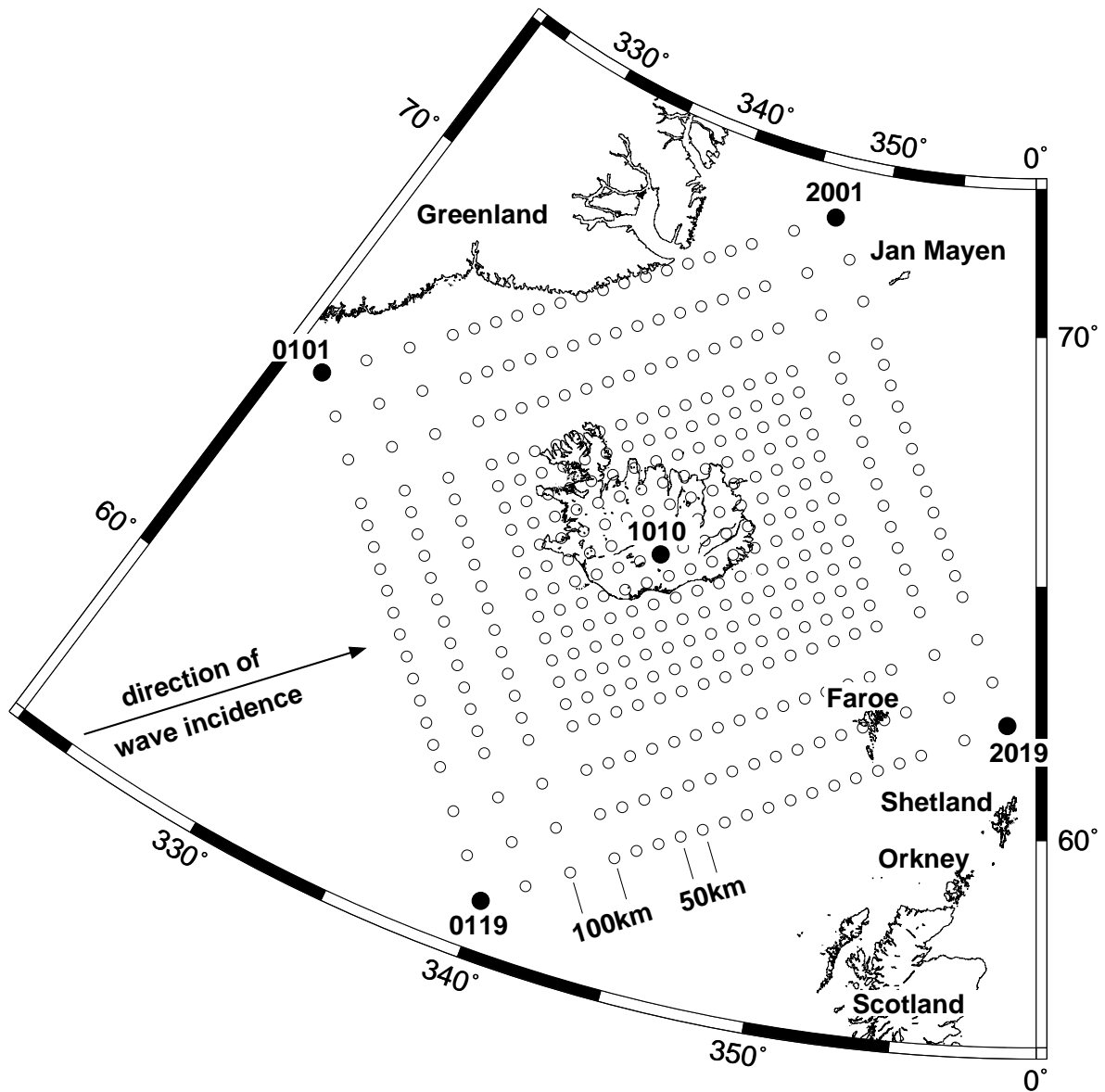


*Figure 3.7: Array of virtual seismometers used for this study. The stations at the edges and the center station are annotated with their numbers for illustrating the nomenclature: the first two digits increase with distance (01-20) the third and fourth digit represent the offset with respect to the great circle (01-19, with 10 being the great circle position). Note that the station density decreases from 50 km to 100 km towards the edges. Moreover, the array is not symmetric in the direction of wave propagation.*

*The background map shows the Iceland region, with landmasses and islands annotated for later reference.*

seismometers of the University of Hamburg and the GEOMAR research center were deployed around Iceland. Their locations were provided by T. DAHM (personal communication) and were included into the pool of virtual receivers. A map showing all stations on Iceland used for this study can be found in Chapter 4, Fig. 4.11.

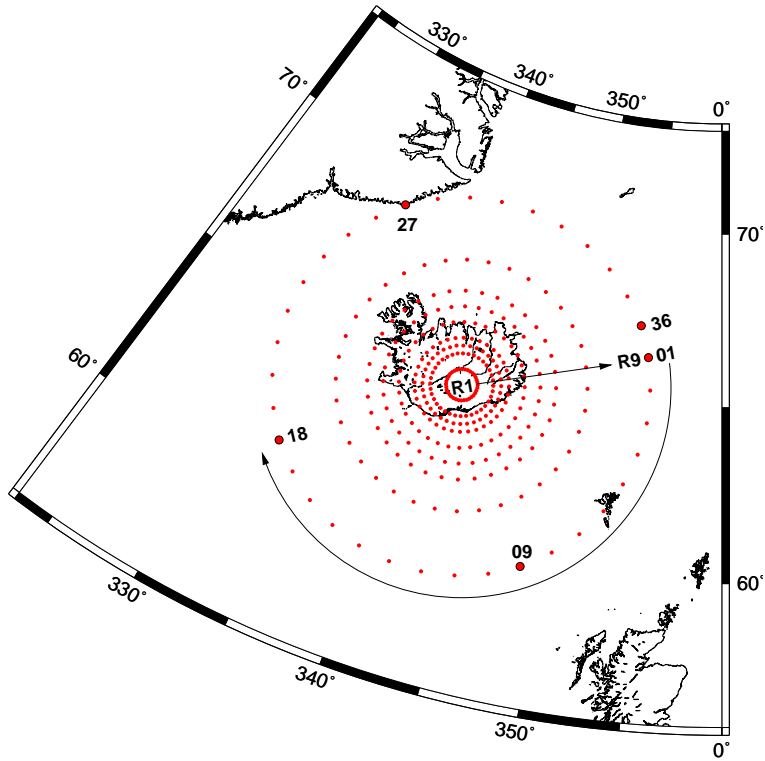


Figure 3.8: Rings of 36 receivers at radii of 50, 100, 150, 200, 250, 300, 400, 500, and 600 km (R1, . . . , R9, respectively) around the plume center. The station code is composed of the letter ‘R’ plus the ring number followed by the receiver number of the rings. Receiver numbering is carried out clock-wise starting at 10° off the great circle. For example, R509 is the receiver in ring 5 (250 km from the plume center) with the largest distance to the right of the great circle.

### 3.2.1 Modeled earthquake and epicentral distances

The parameters of the modeled earthquakes only change in epicentral distance and depth. The moment tensor and the (back-) azimuth are kept the same for the different simulations in order to isolate the influence in epicentral distance and depth when comparing the different scenarios. Table 3.2 gives the earthquake parameters for the scenarios, Fig. 3.9 illustrates the location of the earthquakes with respect to the Iceland plume.

$\Delta=90^\circ$

The default setup for this study is the one where the plume is at an epicentral distance of around 90 degrees. The exact value is  $\Delta=90.57^\circ$  which corresponds to the epicentral distance of the November 12, 1996  $M_W=7.7$  Peru earthquake with respect to the Iceland plume. Both, the earthquake and the plume are described in Chapter 4 in more detail and this setup will be used for a Iceland specific study. Therefore, the depth and the moment tensor is set to the values of this event. For the 1D models this means no loss of generality except the decision for a moment tensor and thus for a radiation pattern of the source.

The distance of 90 degrees has also some geometrical advantages. When using the hybrid codes, as originally planned, the 3D-section of the code has the best geometrical properties,

<b>Location:</b>	Earthquake 1	Earthquake 2	Earthquake 3
Country	–	Peru	–
latitude	26.8969° N	15.04° S	55.0213° S
longitude	58.5666° W	75.37° W	102.0962° W
depth	600 km	37.4 km	500 m
distance	45°	90.57°	135°
<b>Moment tensor:</b>	( $M_w=7.7$ )		
$M_{rr}$	$3.387 \times 10^{20}$ Nm		
$M_{tt}$	$-4.560 \times 10^{19}$ Nm		
$M_{pp}$	$-2.931 \times 10^{20}$ Nm		
$M_{rt}$	$-2.890 \times 10^{19}$ Nm		
$M_{rp}$	$-2.687 \times 10^{20}$ Nm		
$M_{tp}$	$1.857 \times 10^{20}$ Nm		

Table 3.2: parameters of the modeled earthquakes

i.e., the ratio of the grid in  $\varphi$  and  $\theta$  direction is about one (see Chapter 2). Moreover, when setting up chains of receivers with constant epicentral distance these form a rectangular grid (see Fig. 3.7). Another reason for studying this epicentral distance is the fact that the plume at this position is right before the S-wave shadow, i.e., direct P- and S-waves are still present.

### $\Delta=45^\circ$

The second earthquake modeled is a deep one at  $\Delta=45^\circ$  epicentral distance in a depth of 600 km. The epicentral distance has been chosen for two reasons. First, at a close distance the core-reflected phases, such as ScS and PcP have a very steep incidence and thus spend a long time in the plume. As a consequence they should be strongly influenced by the plume and from ray-theoretical point of view they should acquire a large travel-time delay. Second, 45 degrees were chosen to sample a distance at the lower bound of the epicentral distance range. At  $30^\circ$  some phases are in the time range of the surface waves (see Figs. 3.2–3.4), especially the ScS-phase which is of interest. At  $45^\circ$  the ScS-phase comes earlier than the surface wave and is also separated from other phases.

The depth of 600 km has been chosen in order to further eliminate surface waves and thus to enable a full study the entire set of body-wave phases, for example higher-order core reflections such as ScS<sub>2</sub> which have an even steeper incidence angle and may thus be also interesting for plume studies. Due to the decreasing grid size with depth in the SPEC-FEM3D mesh the spatial resolution at a depth of 600 km is reduced as compared to crustal hypocenters. As a consequence when using a delta source-time function numerical artefacts appear at frequencies higher with respect to shallow sources. This presents no problem since a higher-order (4 poles) Butterworth filter is sufficient to remove the artefact from the seismograms.

By keeping the (back-) azimuth the same as for the Peru earthquake the event would occur in the Atlantic Ocean, south-east of the Bermudas, if the modeled plume would be the Iceland plume (see Fig. 3.9). Again, using a 1D background model, this does not affect the generality.

$\Delta=135^\circ$

The third modeled earthquake is at an epicentral distance of  $\Delta=135^\circ$  with respect to the plume, at a focal depth of only 500 meters. The depth was chosen to be the other end-member in the range of hypocenter depths. At such a large distance, the surface waves take so long to travel that most of the body wave phases come before the surface waves. With respect to the Iceland plume this event would be located in the south Pacific, West of Cap Horn (Fig. 3.9).

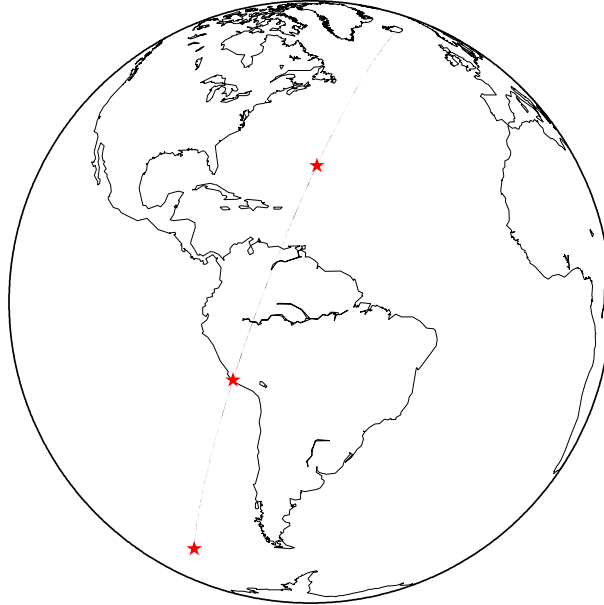


*Figure 3.9: Location of epicenters of modeled earthquakes (red stars) at  $\Delta = 45^\circ$ ,  $90^\circ$ , and  $135^\circ$  with respect to Iceland. Note that due to the used 1D background model the modeling results are not restricted to the configuration shown.*

### 3.2.2 Computation of the wavefield and processing of results

For the plume models described, full 3D wavefield simulations were carried out. The computational effort is quite high, therefore the highest frequency that can be modeled correctly is limited. With the use of 240 elements in each horizontal direction we obtain a setup that uses the resources of the Hitachi SR-8000 supercomputer at the Leibniz-Rechenzentrum (LRZ) in Munich in the best way of all the possible setups. Waveforms are considered reliable down to about 16 seconds (TROMP, personal communication). However, if one applies high demands concerning misfit with respect to analytical solutions this period might be higher, say 20–25 s. To discuss the role of this mid- to long-period range for seismological plume studies we take a look at the seismic conditions of potential plume sites.

For ocean islands that are the surface expression of many of the plumes in the world (e.g., Iceland, the Azores), oceanic seismic noise plays an important role, especially in the period band around 10 seconds. A low-noise window from 1–5 s is mostly available. Unfortunately, these high frequencies can be modeled numerically only with a prohibitive computational effort. However, with increasing frequency, waves become more and more reliably predictable using ray-theory.

The next frequency window that is not affected too much by seismic noise is from 20–50 seconds. In this frequency band, finite-frequency effects that became more and more of interest in recent years, especially for plume studies (e.g. MONTELLI *et al.* [2004b]) can already be modeled reasonably with the full-3D Spectral Element Method. To demonstrate the importance of finite-frequency effects in the frequency range studied in this thesis we take a look at the ratio between wavelength  $\lambda$  as a function of depth and the size  $L$  of our default plume model for both P- and S-waves (Fig. 3.10). This ratio is considered indicative

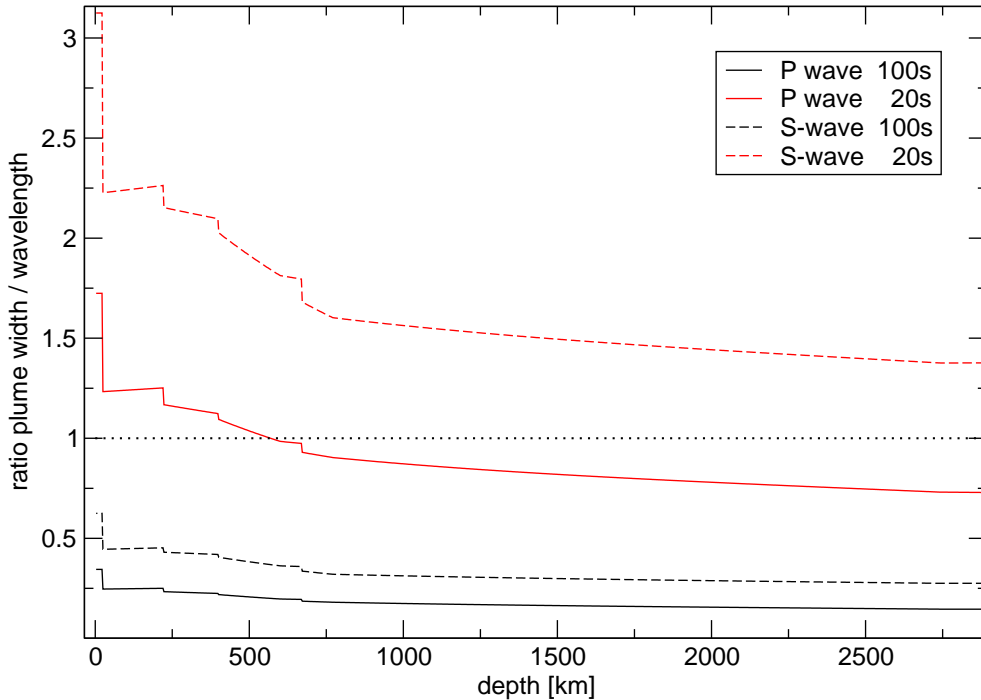


*Figure 3.10: Ratio plume width / wavelength as a function of depth for 20 and 100s using the PREM model and a plume with a radius of 100 km. The black dotted line indicates the limit below which finite-frequency effects become significant (NOLET AND DAHLEN [2000]; ALLEN AND TROMP [2005]). Motions with a period of 20 s are a border case: the S-wave is still above the threshold, while the P-wave in the lower mantle has a ratio of less than one. Ratios for a 1 Hz P-wave range between 14 and 35 and are therefore clearly in the range where ray theory holds.*

for the importance of finite-frequency effects (e.g. NOLET AND DAHLEN [2000]) which become significant when the  $L/\lambda$  is equal to or below one (ALLEN AND TROMP [2005]). We see that for a period of 100 s the ratio is clearly below one, whereas for 20 s P-waves it is below one only in the lower mantle and for S-waves with this period it reaches up to 2.25 below the Moho.

We decided to consider 20 s to be the default corner frequency used for low-pass filtering the synthetic seismograms before any further processing. However, since we are interested in relative effects of plumes or differences between different plume models, sometimes we filter only at 10 s. Nevertheless, it is not assumed that the waveform at this frequency is still correct in an absolute sense but rather that they reflect the trend of plume effects relative to longer periods.

Fig. 3.11 shows an example seismogram for the P-phase for several plume models (default



low-pass filtering with a 2-pole Butterworth filter with a corner frequency of 20 s is applied). The seismograms for the different plume models differ between each other and with respect

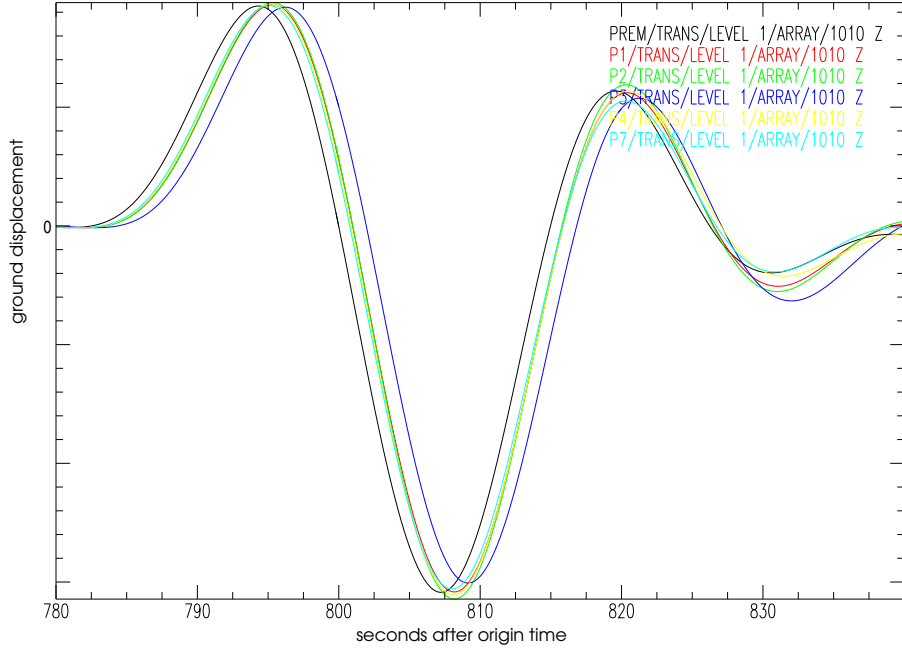


Figure 3.11: Seismograms for the P-wave at  $90^\circ$  distance for all plume models with radius=100 km. The waveforms differ in amplitude and phase. The black line is for the unperturbed PREM model, the blue one for the model with the highest perturbation. The other seismograms are from models with the same perturbation but differing in other parameters (origin depth and perturbation function, values see table 3.1).

to the PREM model in amplitude and phase. The phase shift (delay caused by the plume) is small compared to the period. Waveform effects are rare which is reflected by generally high correlation coefficients when cross-correlating PREM with the plume-perturbed PREM seismograms. An example is given in Fig. 3.12. It shows the spatial distribution of cross-correlation values of the P phase for the sharp 60 km plume. Right behind the plume (given as black circle) the value is smallest, i.e., the waveform effect is highest. However, the coefficient is still 99.558%. Correlation coefficients of above 98% are typical, in cases where they are lower there is interference with another phase in the specific time windows and therefore the coefficient does not compare the same phases.

Thus, the cross-correlation coefficients quantitatively confirm the observation that for the phases under study (Table 3.3) there are no obvious waveform effects such as pulse splitting or broadening. Waveforms are only modified if a phase is delayed by the plume such that it falls in the time window of another arrival (less affected by the plume) and interferes with it. Since these are interference effects with no systematics rather than waveform effects of a specific phase we focus on the main phenomena – travel-time delay and amplitude changes – for which we developed routines that extract these quantities from the several hundred synthetic seismograms. These tools are presented in the next subsection.

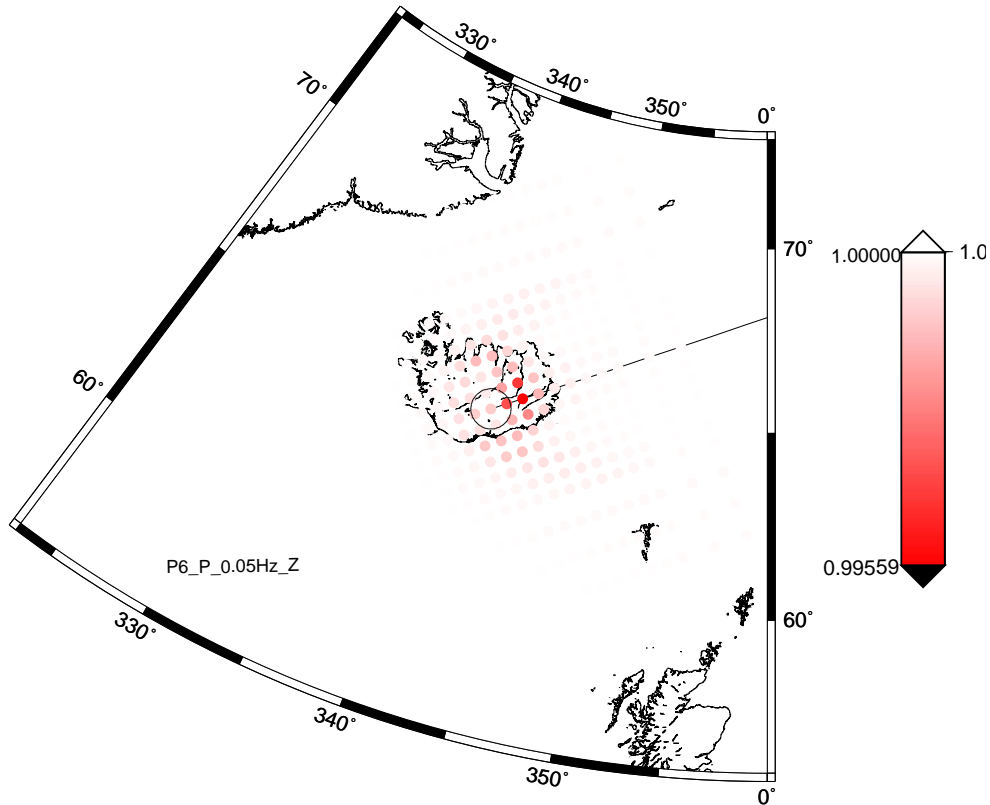
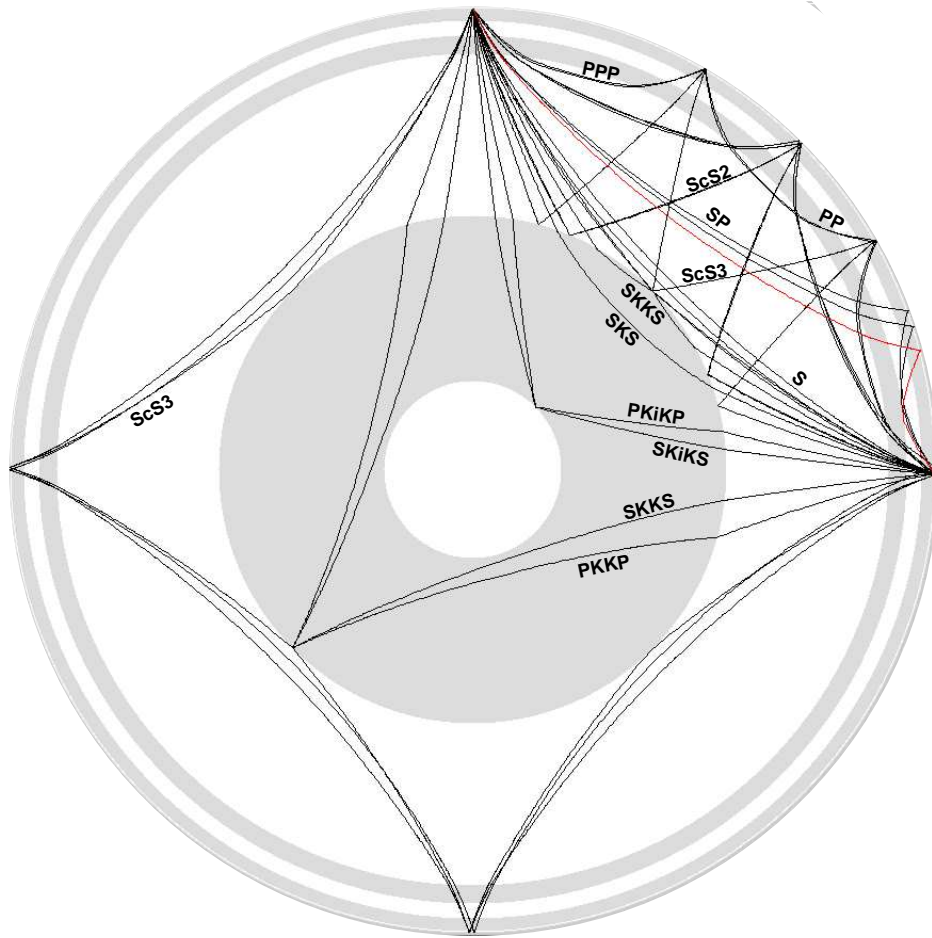


Figure 3.12: Maximum cross-correlation coefficients of the P-phase between a PREM and a plume perturbed PREM model. A sharp 60 km plume was used along with earthquake model 2 (90 degrees epicentral distance, 37 km depth). The wave incidence direction is to the upper right, as given in Fig. 3.7. The correlation coefficients are very high, reflecting almost no waveform effect of the plume.

### 3.2.3 Tools for seismogram analysis

For determining the travel-time delay of a specific phase due to the velocity perturbation of the plume a processing script was written in form of a SAC-macro. Prior to its execution phases must be marked in the SAC seismograms. Therefore, phases that can be identified in the seismograms (for an illustration of their ray-paths see Fig. 3.13) were marked in the distance range of the stations around the plume center ( $\pm 600$  km). This is done using the travel-time information from the TAUP-toolkit (CROTWELL *et al.* [1999]). The nine most prominent phases for each component (radial, transverse, and vertical) were written to a list (see Table 3.3). From this list, a script writes the phase names and travel times to the SAC header variables `kt0-kt9` and `t0-t9`, respectively.

The phase-delay script then cuts a window around the theoretical travel time of the given phase out of both, the PREM and the PREM+plume seismograms. An example for the P-phase of several plume models was given in Figure 3.11. The window width depends on the longest period in the seismograms, for a period of 20s the window would be  $-5$ s to  $+35$ s before and after the theoretical travel-time. Subsequently, the resulting time series are resampled to a sampling rate of 0.05 s (oversampling by interpolation) in order to obtain a higher time resolution for the subsequent cross-correlation of the two signals. The cross-correlation itself is



*Figure 3.13: Ray-path of some phases used for deriving travel-time delays. The epicentral distance of about 90 degrees corresponds to the default distance of this study. Some phases are annotated with names according to the seismological nomenclature. Ray-paths of P and S waves are sometimes similar, in that case, only one of the names is given (e.g. PP and PPP). Note the different incidence angles and therefore the different path length the ray would spent in a plume at 90° distance. (Figure made using the TAUP toolkit).*

done by first calculating the auto- and the cross-covariance of the signals and then normalizing the cross-covariance signal with the maximum of the PREM auto-covariance. Then, the maximum value (i.e., the cross-correlation coefficient) of the resulting cross-correlation signal, and the position of its maximum in time is determined. The latter is the time delay between the two phases. By plotting the delays color-coded for all the stations of the array described in the previous section a travel-time delay map is obtained, that shows the travel-time “shadow” caused by the plume.

The time window (of 40 s for 20 s data) was chosen such that it contains the entire PREM phase (periods of roughly 20 s for P, and 30 s for S-waves) and the delayed plume phase. Since the delays for our study plume models are expected not to be larger than 10 s a time window of 40 s (maximal 30 s for the phase and 10 s for the delay) seems appropriate. Using a bigger time window results in possibly including also other phases that might be affected by the plume in

Component	phases stored in SAC-header kt...								
	1	2	3	4	5	6	7	8	9
$\Delta=45^\circ$									
Z	PcP	P	sP	S					
R	P	PP	ScS <sub>2</sub>	sPP	sP	S	sScS <sub>2</sub>	sS	SS
T	ScS	ScS <sub>2</sub>	S	sScS <sub>2</sub>	sScS	sS	sSS	SSS	SSSS
$\Delta=90^\circ$									
Z	PcP	PcP <sub>2</sub>	PKiKP	P	PP	P <sub>3</sub>	P <sub>5</sub>	SP	SSP
R	PKKS	P <sub>5</sub>	ScS <sub>2</sub>	SKiKS	SKKS	SKS	SP	SSP	SS
T	ScS	ScS <sub>2</sub>	ScS <sub>3</sub>	S	SS	S <sub>3</sub>	S <sub>4</sub>		
$\Delta=135^\circ$									
Z	PcP <sub>2</sub>	Pdiff	PKiKP	PP	PPP	P <sub>4</sub>	P <sub>5</sub>	SP	SSP
R	P <sub>diff</sub>	PKS	PP	PPP	PPS	SKKKS	SS	SSS	S <sub>5</sub>
T	ScS <sub>2</sub>	ScS <sub>3</sub>	S <sub>diff</sub>	SS	SSS	S <sub>4</sub>	S <sub>5</sub>		

Table 3.3: phases picked for the three components and the different epicentral distances

a different way (e.g., different delay due to different slowness), thus biasing the result for the phase of interest. On the other hand, a smaller window would not capture the entire (delayed) phase and can lead to an unstable result.

However, for some phases, the travel-time curves cross each other in the distance range of interest. In this case there is interference of phases within the time window for some distances. This leads to a characteristic pattern in the travel-time delays and, as previously stated, to low cross-correlation values. This effect is particularly important for plume models with a strong perturbation and/or a large extension such as the 300 km radius plume, the one with head and the one with the doubled perturbation. Obviously, in these cases, the delay accumulated due to the strong and/or broad perturbation shifts a neighboring phase into the time window of the phase under study, which experiences a weaker/stronger delay because of a different slowness. As an example the delay-times for the SKS-phase of the plume with doubled perturbation is shown in Figure 3.14. Note that the SKS-phase is useable for all other plume models, as will be shown later. Apart from the characteristic pattern of this interference effect observed in the map, and the strong amplitudes, it can be easily detected by observing the time windows during execution of the script. Thus, even if automatized in a script, a visual check of the time windows and of the corresponding cross-correlation coefficients is imperative.

In order to visualize the effect of wavefront healing (WIELANDT [1987]) at finite frequencies the same way of measuring the travel-time delay caused by the plume is applied to the stations on the great-circle. The resulting delay curves are functions of distance from the plume center and are cross sections through the travel-time delay map on the great circle through epicenter and the plume center, but extend to farther distances. For this type of study only the P-phase can be used, any other phase would interfere with others over the large epicentral distance range.

Apart from travel-time delays also amplitude effects of plumes are expected, e.g., by focussing effects (TILMANN *et al.* [1998]), because the plume acts like an optical lens. In order to measure these amplitude effects in terms of the amplitude ratio between PREM and

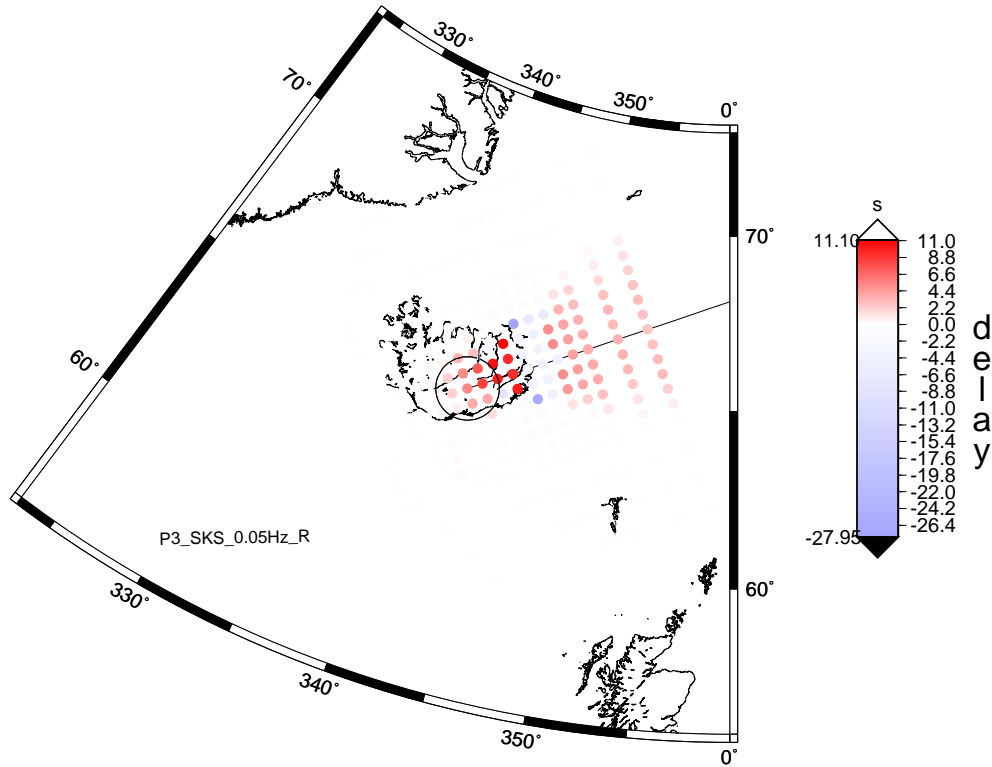


Figure 3.14: Travel-time delay of the SKS-phase (radial component) caused by plume model with a strong ( $\delta v_P=7\%$  and  $\delta v_S=12.4\%$ ) velocity perturbation (twice that of the default values). The delay shadow shows an alternating pattern with much too strong amplitudes, probably hiding weaker delays. What we see is not the actual delay of the phase due to the plume, but rather an effect of the interference of this phase with the delayed S- and ScS-phases in this distance range. The resulting image and the delay values for this phase are not useable.

PREM+plume seismograms we use an adapted version of the method of SIGLOCH AND NOLET [2005] for measuring finite-frequency amplitudes. It consists of first determining the delay between a specific phase in the PREM and the plume model seismograms (by means of the cross-correlation described above) and then systematically varying the amplitude of one of the two signals and calculating the root mean square (RMS) of the difference of the signals. The amplitude factor that minimizes the RMS is the amplification or attenuation factor due to the plume.

### 3.3 Results

In the following section the results for the different plume effects obtained with the processing tools just described are presented and discussed for the different plume models. The goal is to examine the influence of the individual plume parameters that vary between the models as well as their combined effect. The focus lies in the crucial questions of the plume debate, i.e., the depth extent and width of the plume and their resolution. Moreover, we are looking for a diagnostic signature of the plume and we want to answer the question of which phase is best suited for the detection of plumes. A candidate – as already mentioned – are core-reflected phases since they spend a long way in the plume due to their steep incidence. We first look at the spatial distribution of travel-time delays caused by plumes, then study their evolution along the great-circle over a long epicentral distance range and finally turn to amplitude effects.

#### 3.3.1 Travel-time delay shadows

Travel time delays are so far the main data source used for imaging plumes. Usually they are the input data for tomography algorithms, but their spatial distribution is rarely studied. Exceptions are the papers by ALLEN AND TROMP [2005] and KEYSER *et al.* [2002] the latter showing average delay patterns for the Eifel plume experiment. Here, we want to examine the delay patterns for different phases and epicentral distances as a function of plume parameters in order to reveal the signature of the plume in the travel-time.

First, the main characteristics of a typical spatial travel-time delay distribution are discussed with a sharp plume model of radius 100 km (Fig. 3.15). It shows the delays of the P-phase when using a PREM model that is perturbed by a plume with respect to a PREM model alone. The delays are measured by cross-correlation of seismograms that are low-pass filtered with a corner frequency of 20 s.

Strong delays are concentrated on a region the size of the plume, but slightly shifted behind the plume center. The maximum delay is 1.15 s, as given on the left side of the colorscale bar. Behind the plume the delay is decaying again, mainly, as an effect of wavefront healing. Towards the sides of the plume there is also a delay, confined to a cone shaped region. There are clear deviations from the delay distribution one would expect from ray-theory: for a sharp plume there is no ray-theoretical delay to the sides of the plume, and the decay behind the plume (in the ray-theoretical case only diminished by geometric effects discussed later) would be much weaker.

However, the most striking feature of the delay map are the negative delay values. At their location the waves arrive earlier in the presence of a plume than without. The early arrivals are at the first sight counter-intuitive, since one would expect a low-velocity anomaly to slow down the seismic wave rather than accelerating it, the latter leading to earlier arrivals. However, the observed earlier arrivals are fully consistent with finite-frequency theory, the arrivals can be explained by the second Fresnel zone in the sensitivity kernels (see Fig. 1.7). The frequency and band-width dependence shown later in this chapter further confirms this explanation.

It should be kept in mind, that the magnitude of the negative delay is quite small and it was necessary to use a different scaling for the positive and negative side of the colorscale to make it visible. In Fig. 3.15 the maximum negative delay is only 0.1 s, barely measurable using real data in the presence of noise and a heterogeneous background medium. Moreover, regional tomography studies mostly derive relative delays between the stations using a special

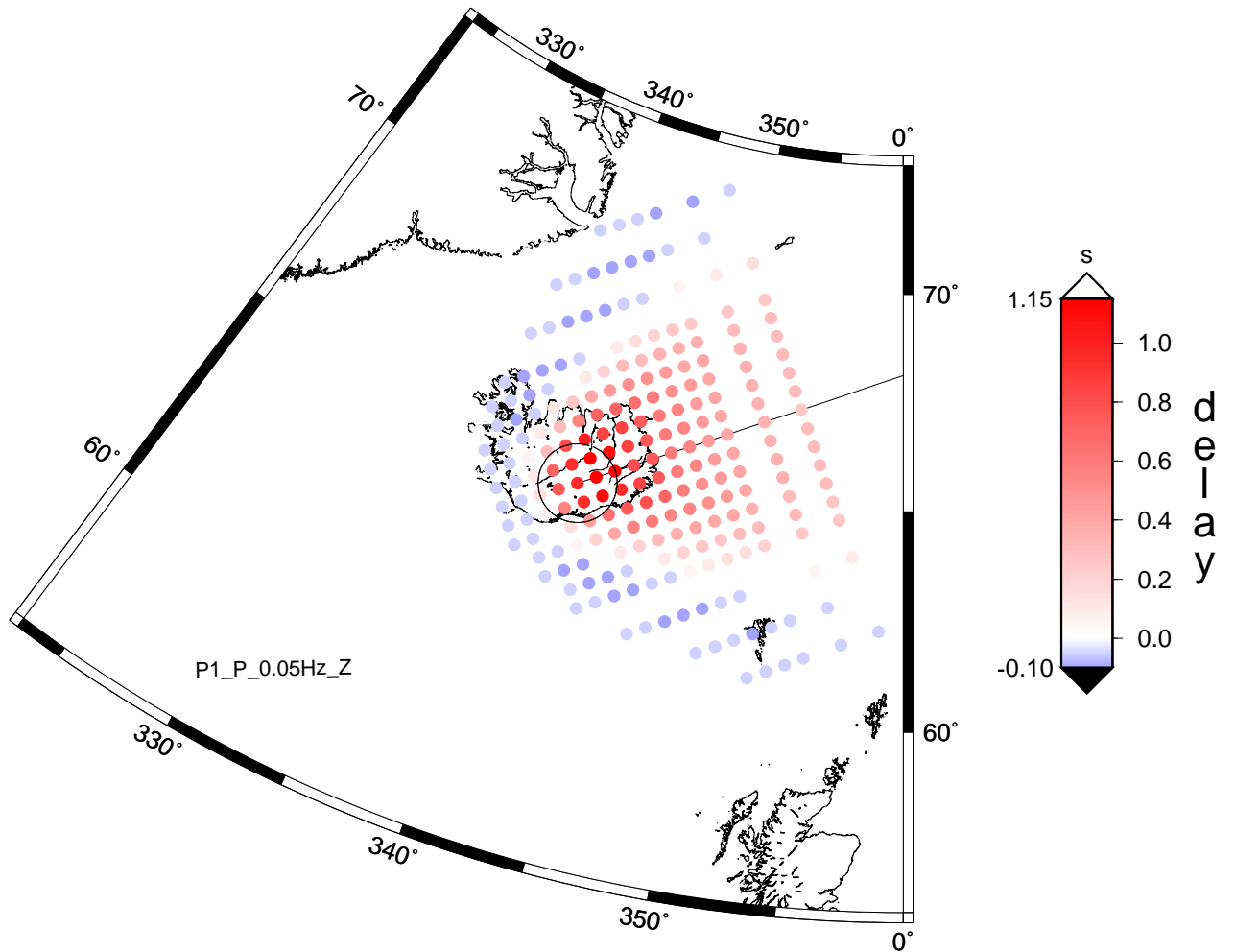


Figure 3.15: P-phase travel-time delay for a plume at  $90^\circ$  epicentral distance with radius of 100 km and a sharp perturbation function. Note that the asymmetric colorscale used overemphasizes negative values. The background map is centered on the assumed position of the Iceland plume, however, because a 1D background model (PREM) is used, the values obtained are independent of Iceland. The circle shows the position of the plume conduit. The line represents a segment of the great circle through the epicenter and the plume center. Small asymmetries in the delay pattern stem from rounding errors during computations, e.g., of the locations of the station array. In general, they do not exceed one resolution unit (0.05 s). In this and the following figures of this kind a legend in the lower-left part of the map summarizes information about the plume model (P1, see Table 3.1), the phase (P), the maximum frequency (0.05 Hz) or frequency range and the component (Z=vertical) used to derive the delays shown.

cross-correlation technique (VANDECAR AND CROSSON [1990]). With this method, absolute amplitudes get lost and therefore negative delays are not recognized due to a missing absolute zero level. Thus, the importance of the observation of early arrivals lies in the evidence of the existence of finite-frequency effects of the plume models in our simulations rather than in any applicability for real data plume studies.

In the following, examples of delay maps for pairs of plume models differing only in one plume parameter will be shown. Since we can not present the delay distributions of all the phases, we select one phase per parameter combination for discussion. A synopsis of more models is shown in Fig. 3.20 for the SKS-phase.

### Perturbation function: Sharp vs. Gaussian

Fig. 3.16 shows delay maps for the direct P-wave of a plume with a sudden perturbation onset and of one with a Gaussian perturbation function. Both plume models originate at the CMB, and are located at an epicentral distance of  $\Delta=90.57^\circ$  from the epicenter. The sharp

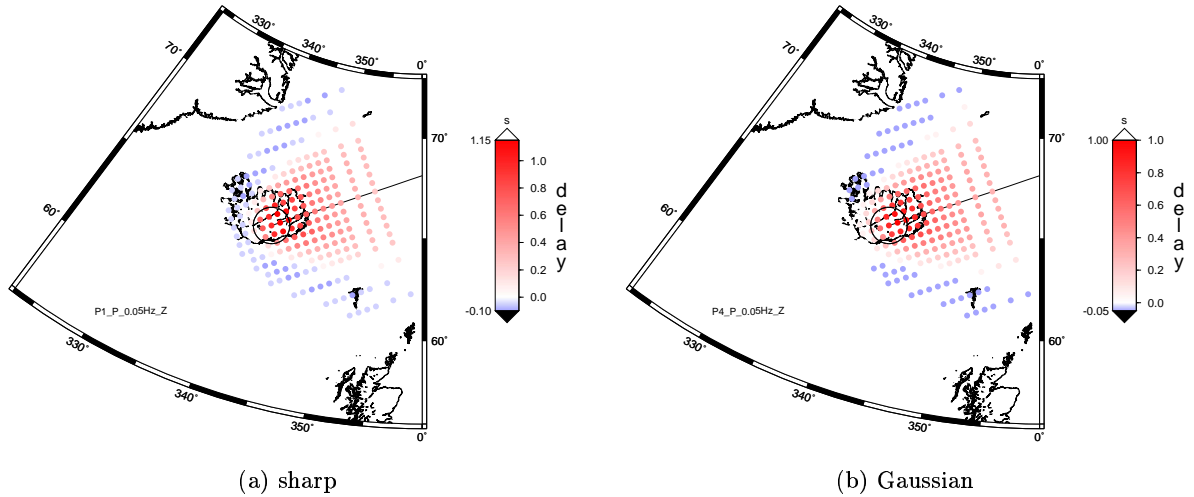


Figure 3.16: Delay maps for the P-phase,  $\Delta=90^\circ$ : comparison of the perturbation function.

plume causes a slightly higher maximum delay (1.15s with respect to 1s) over a broader region, whereas the plume with gradational boundaries has a slightly broader “shadow” of positive delays, but weaker. The explanation for this is that the sharp plume has its maximum perturbation over the entire radius, and is thus capable of causing a higher delay over an area comparable to its cross-section. The Gaussian plume reaches the maximum perturbation only at its center, therefore the delays are concentrated just behind the plume axis and fall off with the perturbation function. On the other hand, the Gaussian plume still perturbs the seismic velocities outside the defined radius, where the sharp plume perturbation is already down at zero. Therefore, the Gaussian plume delays extend further outwards. The differences seem small, however, one should keep in mind the dimensions of the plume models with respect to the station spacings of 50 km and 100 km: the Gaussian plume is broader than the sharp one by about 90 km, where it drops down to only 1% of its maximum perturbation.

Concerning the earlier arrivals the sharp plume leads to larger effects. The Gaussian plume arrival-time pattern is missing any earlier arrivals right in front of it. Both effects are clearly due to the perturbation function. For the sharp plume the velocity perturbation has well defined boundaries, thus the second Fresnel zone causing the weak early arrivals does not overlap with the first Fresnel zones of arrivals reaching the surface at larger distances. This



is the case for the Gaussian plume. That is why the influence of the second Fresnel zone is partly cancelled out in front of the plume. There, no early arrivals can be observed.

### Magnitude of perturbation: weak vs. strong plume

We next compare the delays of the shear wave that is reflected at the Earth's surface before reaching the plume (SS-phase). On the right side of Fig. 3.17 again delays of the sharp  $r=100$  km plume model is shown and compared to an identical plume model, with twice the perturbation of the first one (Fig. 3.17b). The general pattern of both delay shadows is quite

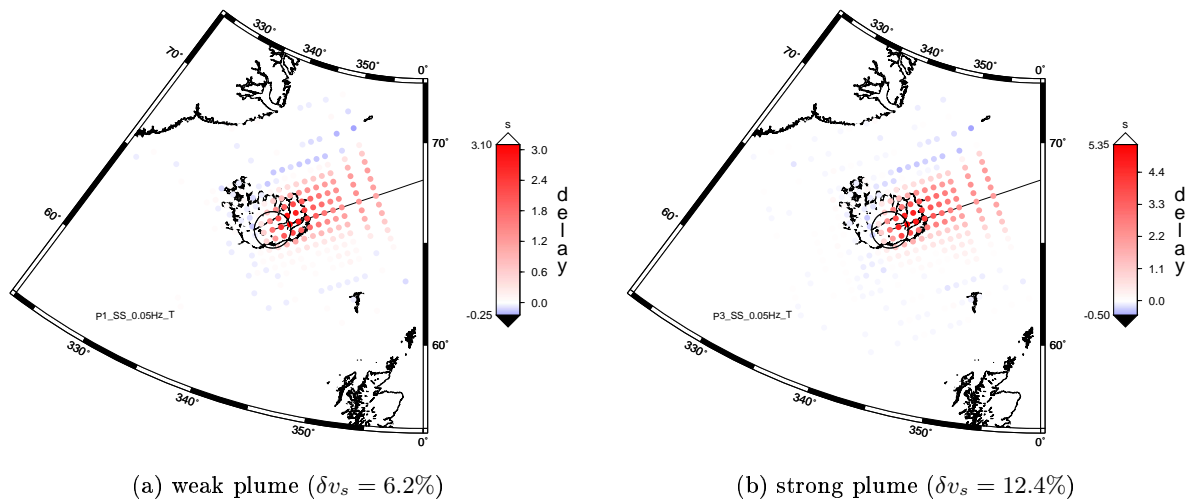


Figure 3.17: Delay maps for the SS-phase,  $\Delta=90^\circ$ : effect of the plume perturbation.

different from that of the P-phase. It is much narrower in its main part and shows some weak signals partly far away from the plume anomaly. This is a stable feature for all the SS-phase shadows, not only for the ones shown here. Also the PP-shows this behavior with respect to the direct P-phase. It might be explained by the finite-frequency kernel of these phases which is complicated by the surface reflection. On the other hand, the SS-phase (PP-phase) has a shallower incidence than the direct P- or S-phase, also influencing the sensitivity kernel. It is not believed that the weak signals further outside are caused by interference with other phases when cross-correlating since the typical pattern observed in such cases is missing. Another general feature is a pronounced asymmetry. Possibly, in the case of shallow incidence the already mentioned round-off errors causing the asymmetry have a stronger effect.

Comparing the delay patterns of the two plume models one sees that they are similar within one or two discretization units. Concerning the amplitudes of the delays one would expect a doubling of values when doubling the velocity anomaly. This is only true for the early arrivals, whereas the maximum delay of the strong plume only reaches 86.3% of twice the maximum delay of the weak plume. The reason for this remains elusive, for the P-wave, however, we obtain exactly twice the delays.

### Plume origin depth: CMB vs. 660 km

One of the most important questions in the plume debate concerns the depth from which they originate. This is relevant for the question whether hotspots (or, a particular hotspot under study) are caused by deep seated “Morganian” plumes or whether the underlying upwelling comes from the transition zone or might even be a shallow asthenospheric plate-tectonic related feature.

We compare delay shadows of plume models with two different origin depths, one coming from the CMB and the other one originating at the bottom of the transition zone. The delay maps for the S-phase of the two models is shown in Fig. 3.18. The difference between the two

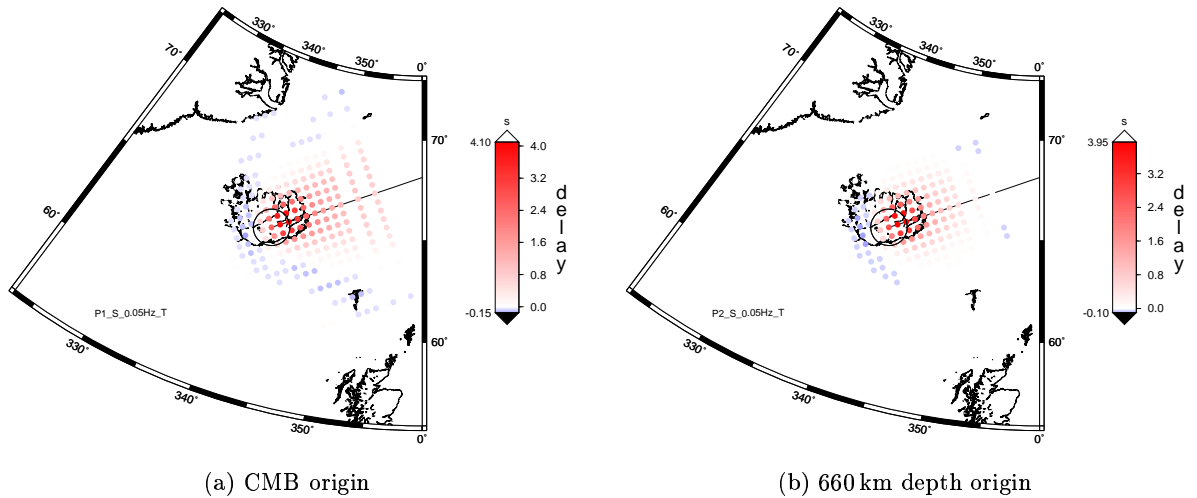


Figure 3.18: Delay maps for the S-phase,  $\Delta=90^\circ$ : comparison of origin depths.

shadows is striking. The minimum and maximum values differ only insignificantly whereas there is a marked difference in the width of the shadows. While the delay pattern of the CMB plume is similar to that of the P-phase – owing to their similar paths – the delay shadow of the transition zone plume is limited in extension in both the radial and transverse direction. At the receivers 600 km behind the plume there is no observable delay any more, on the contrary, we see early arrivals at some stations where the CMB plumes has delays of the same values or even larger. Towards the sides, however, the early arrivals of the CMB plume are missing for the plume from the 660 km discontinuity. In summary, from this difference in delay patterns the two origin depths can be distinguished. Nevertheless, in real data studies, the differences might be hard to detect, since they occur only quite far away from the plume center and concern mostly small values.

### Incidence angle: steep vs. shallow incidence

The incidence angle of the phase under investigation is another important parameter since it determines the length of the path that the wave spent in the plume and over which a delay can be acquired. Moreover, the shallower the incidence, the longer the path behind the plume over which healing takes place. In order to examine the plume effect on the incidence angle,

we take two phases that represent endmembers with respect to slowness. In Fig. 3.19 the delay maps of the SP- and the SKKS-phase (for their paths, see Fig. 3.13) are shown for comparison. As one would expect, the delay patterns differ. The SKKS shadow is much

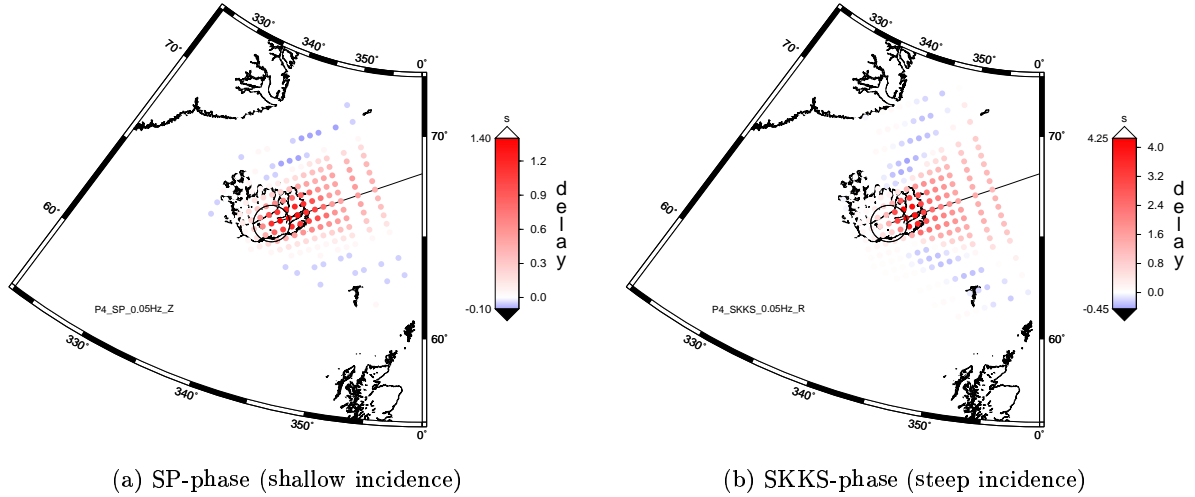


Figure 3.19: Delay maps for a Gaussian plume at  $\Delta=90^\circ$ : comparison of the shallow incident SP-phase with the steep SKKS-phase.

broader (the positions of zero-crossing of the delay is shifted by about 200 km with respect to the SP-delay) owing to sampling of the plume conduit at larger depths where the Fresnel zone is larger. Moreover, it has a much higher maximum delay. This is due to the steep incidence that lets the wave propagate a longer way in the plume. The SP-delays are smaller because this phase samples the plume as a P-wave and the P-perturbations of a plume are smaller than the one for S waves. The regions of strong delays have an elliptical shape for the shallow incident phase whereas for the steep incident phase this ellipse seems to be squeezed to a circular area, a clear consequence of the difference in incidence angle. However, note that the reduction of the problem to a simple comparison of the incidence angles is only justified from a ray-theoretical point of view.

In the (finite-frequency) wave world not only the incidence between the two phases are different, but also the sensitivity kernels. This influence may be significant, but can not be quantified here since no sensitivity kernel for these two phases at this epicentral distance are available.

Here, the need for a **catalogue of kernels** for a variety of phases and epicentral distances becomes obvious. Comprehensive plots for rays covering the entire range of epicentral distances and a broad diversity of phases have been published several times (e.g. STORCHAK AND BORMANN [2003]). In contrast, finite-frequency kernels require much more effort as it is difficult to show more than one kernel per plot (which is easy for rays due to their zero extension, e.g. Fig. 3.25). Moreover, several kernels for one phase might be needed since kernels are frequency dependent. Finally, the computational effort for computing kernels is very high, particularly for 3D models. Computing kernels using the adjoint method (TROMP *et al.* [2005]) which can deal with 3D models goes to the limits of today's computation power when

	r=60 km	r=100 km	r=300 km
thermal	n/a	3.55 s	n/a
Gauss	6.2 s	3.95 s	1 s
sharp	2.65 s	5 s	12.55 s
Gauss	2.23 s	3.95 s	8.99 s

*Table 3.4: Maximum delay times of the SKS phase for the different radii and perturbation functions. For the sharp plume models the maximum delay values are increasing with radius, whereas the for Gaussian models they are decreasing. After normalizing the values for the Gaussian plume delays such that they have the peak perturbation of the other plumes the same tendency as for the sharp plume is observed, though weaker.*

attempting to reach higher frequencies. This is why tomography studies (e.g. MONTELLI *et al.* [2004b]) use approximated ray-based Born sensitivity kernels computed for 1D Earth models. Due to the use of ray theory, the resulting kernels can not exactly reproduce the sensitivity where wave phenomena occur, e.g., diffraction at the core-mantle boundary. However, currently TARJE NISSEN-MEYER, a former member of the seismology group in Munich is working on a method that allows the creation of exact Fréchet kernels for any phase and any epicentral distance (NISSEN-MEYER *et al.* [2005]). Even though this method is limited to spherically symmetric Earth models it has a major advantage since it can deliver any kind of sensitivity kernel (travel-time, amplitude, waveform) and still is computationally quite cheap. This is achieved by computing six independent 2D solutions of the wavefield from which the full 3D kernel can then be composed. Moreover, once the 2D calculations are done they can be stored in a library and do not have to be recomputed every time.

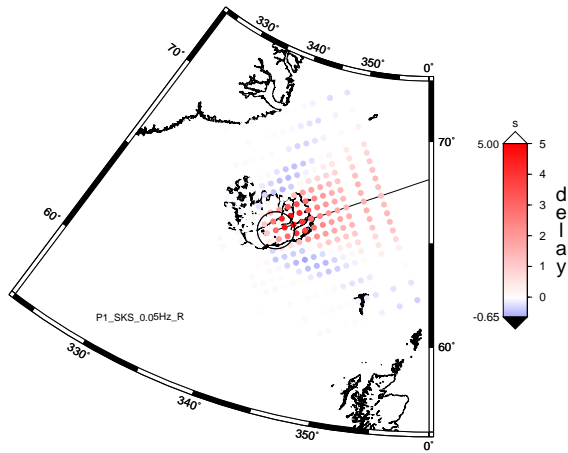
In summary, a kernel catalogue or a possibility to compute sensitivity kernels with a low effort considerably helps interpreting the results of forward-modeling studies such as the present one. It is also useful for identifying phases with a sensitivity distribution that is concentrated at the position of a desired structure, such as a plume, at a given distance.

We will come back to the issue of incidence angle and the influence of the kernel when studying the ScS-phase at an epicentral distance of  $45^\circ$ .

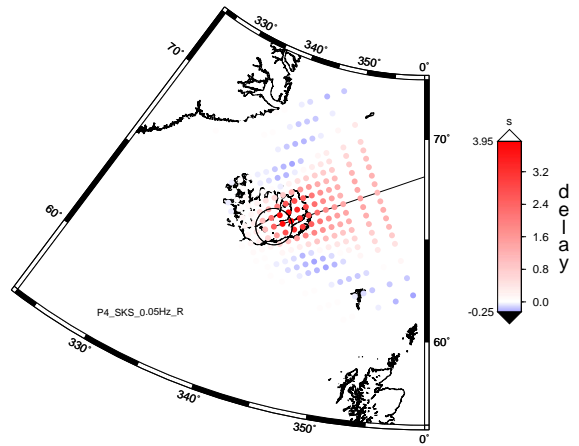
## The SKS-phase

Considering the SKS-phase as an example we compare the delay maps of various plume models. Among the phases we use for this study the SKS-phase experiences one of the strongest delays that we can measure without being disturbed by interferences with other delayed phases (an exception – as already discussed and shown in Figure 3.14 – is the delay pattern of the strong plume with doubled velocity perturbation). This is why we discuss the plume models together with the example of the SKS-phase. Fig. 3.20 shows a compilation of the delay shadows of the SKS phase.

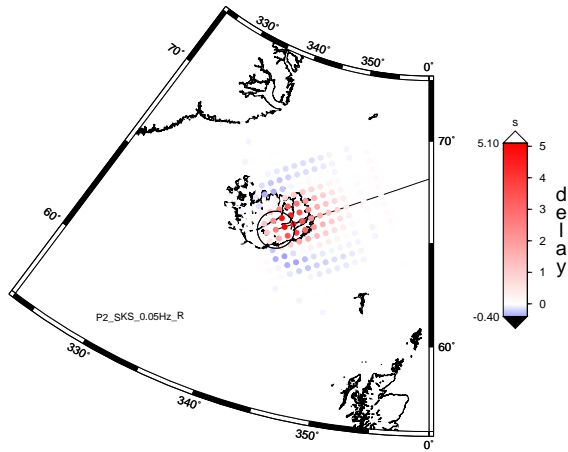
The delay magnitudes of the SKS-phase are quite sensitive to the perturbation function (Figs. 3.20a,b,d and Table 3.4), however the spatial distribution of the delay for a 100 km plume is not. The sharp plume model causes the highest maximum delay with 5 seconds and the thermal model the lowest with 3.55 seconds. This was already observed and explained when we studied the influence of the perturbation function. With the example of the SKS-phase we want to examine this effect together with the radius of the plume. Figs. 3.20e+f show the delays of a sharp 60 km plume and a Gaussian 300 km plume, respectively. The



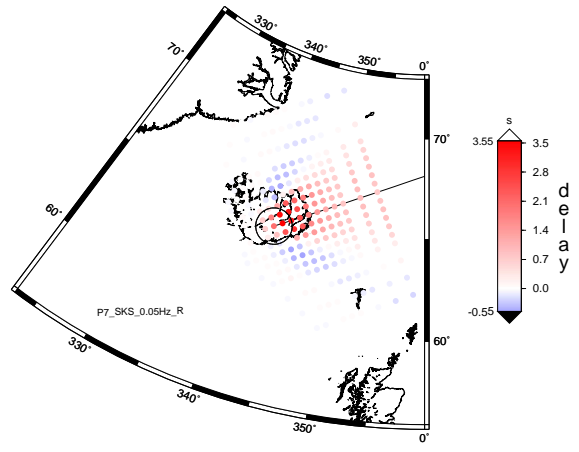
(a) sharp,  $r=100$  km



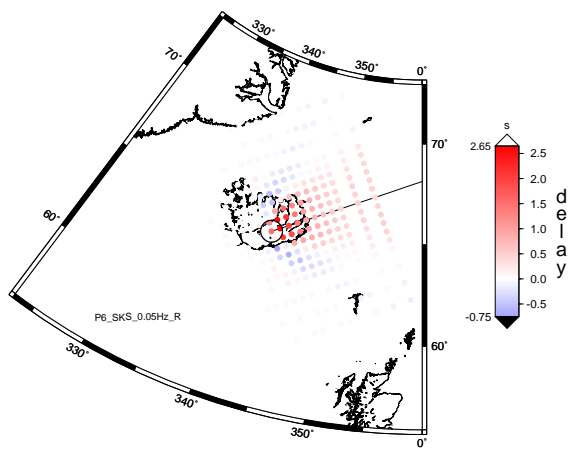
(b) Gaussian,  $r=100$  km



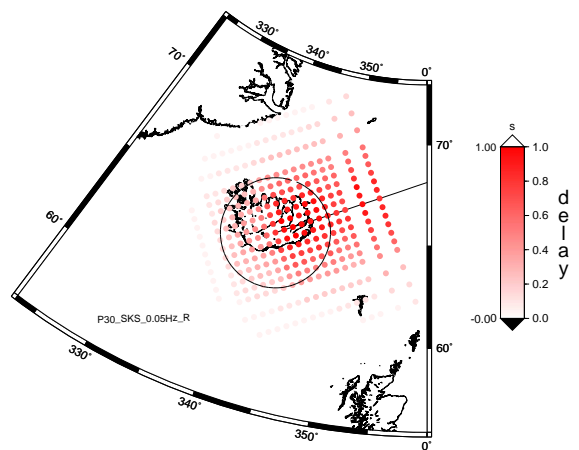
(c) sharp,  $r=100$  km, 660 km origin



(d) thermal perturbation,  $r \approx 100$  km



(e) sharp,  $r=60$  km



(f) Gaussian,  $r=300$  km

Figure 3.20: Delay maps for the SKS-phase for different plume models at  $\Delta=90^\circ$ . Origin depth of the plumes is the CMB, unless otherwise stated.

perturbed area of the Gaussian 300 km plume exceeds the aperture of the array, thus almost all the stations record a delayed SKS-phase. Table 3.4 lists the maximum delays of all the CMB-plume models with the same perturbation.

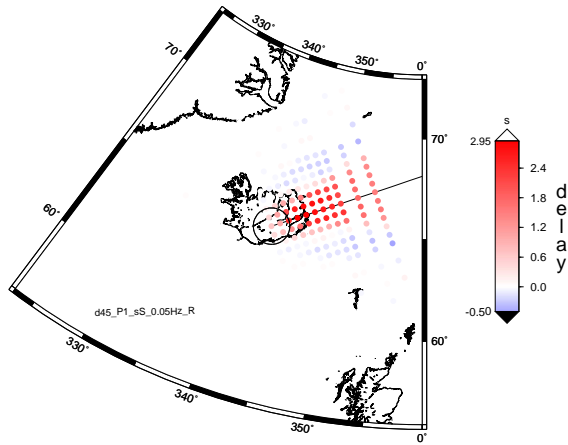
We see that for the sharp models the delay is increasing with the plume radius, a logical consequence of the longer path on that the wave passes the full perturbation of the plume. For the Gaussian plume models instead we observe the opposite effect: the delays decrease with the plume diameter. This is due to the peak perturbation that differs between the Gaussian model in order to keep the integral perturbation constant. If we normalize the delays of the small and broad plumes to be effectively caused by the same perturbation as the one of the 100 km radius plume the delay values (last line in Table 3.4) are also increasing with radius. However, the delays are generally weaker compared to the ones of the sharp plume models, as already observed and explained with the example of the P-wave.

Note also the high values of early arrivals for the SKS-phase which reach up to 0.75 s and which would be clearly detectable. On the one hand, using ray-theory, they are interpreted as being caused by fast anomalies (e.g., in global tomography), on the other hand using differential travel-times as usual for regional tomography experiments they would map into the delay amplitudes, thus enhancing them even more.

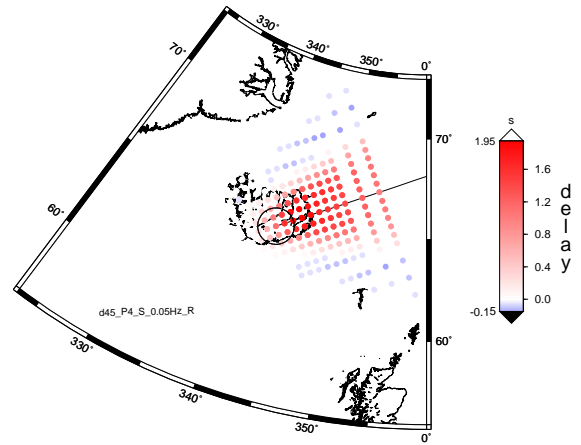
In summary, the SKS-phase at  $90^\circ$  epicentral distance has two advantageous properties: First, it has a steep incidence angle and thus samples a large portion of the plume in depth. This leads to strong delays (several seconds) observable close to the plume. Second, it seems to have a narrow sensitivity kernel in the depth range where it samples the plume, probably due to the transmission through the Earth's core. However, this is speculation and the actual kernel is needed to fully explain the delay distribution. However, the kernel leads to a relatively sharp focused zone of delays that – due to the steep incidence angle – lies very close to the plume and that is similar in diameter to the plume itself. All this makes SKS very well suited for plume studies around  $90^\circ$  epicentral distance.

### Other epicentral distances

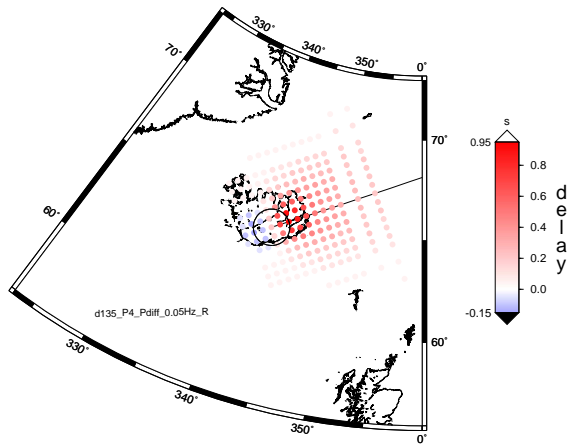
Using other epicentral distances allows for examination of additional phases. Some examples partly showing unusual patterns are summarized in Fig. 3.21. The sS-phase at  $45^\circ$  shown in Fig. 3.21a has a very small shadow with a concentration of strong delays on a confined, elongated, elliptical area. The elongation is a consequence of the relatively shallow incidence at this short epicentral distance. Right at its boundaries the negative delays, partly with high amplitudes as well, ensue. They are also confined to a small region, leading to a very concentrated zone of influence of the plume. The delays for the S-phase running through a Gaussian plume model at the same epicentral distance (Fig. 3.21b) are broader, but also elongated and remain strong up to 600 km behind the plume. The incidence angles of S and sS at this distance and this focal depth are almost identical, explaining this similarity in the two patterns. The broader pattern of the Gaussian plume is due to the wider extension of this perturbation function. In the following we come back to the question raised at the end of Chapter 1 as to whether the ScS-phase at close distances can help identifying the presence and nature of plumes. From a ray-theoretical point of view there is a strong point for the ScS-phase carrying a strong signature of the plume that is spatially confined since the ray of the ScS-phase has a steep path and thus spends a long way in the plume thereby acquiring a strong delay. In order to examine what happens to the finite-frequency ScS-phase in the presence of a plume we compare the travel-time delay plots of the shallow sS-phase



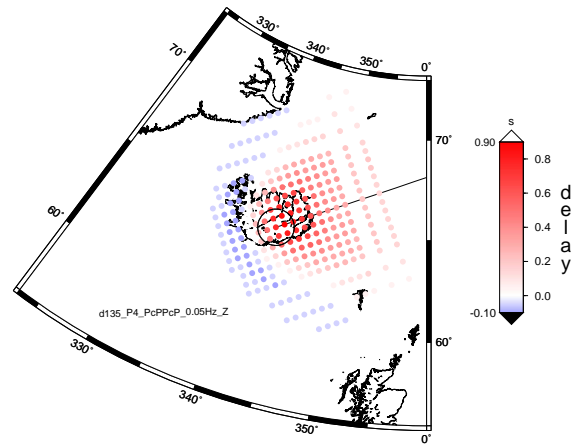
(a) sharp plume,  $\Delta=45^\circ$ , sS-phase



(b) Gaussian plume,  $\Delta=45^\circ$ , S-phase



(c) Gaussian plume,  $\Delta=135^\circ$ ,  $P_{diff}$  phase



(d) Gaussian plume,  $\Delta=135^\circ$ ,  $PcP_2$  phase

Figure 3.21: Delay maps for  $\Delta=45^\circ$  and  $135^\circ$ . Plume origin depth is the CMB for all cases.

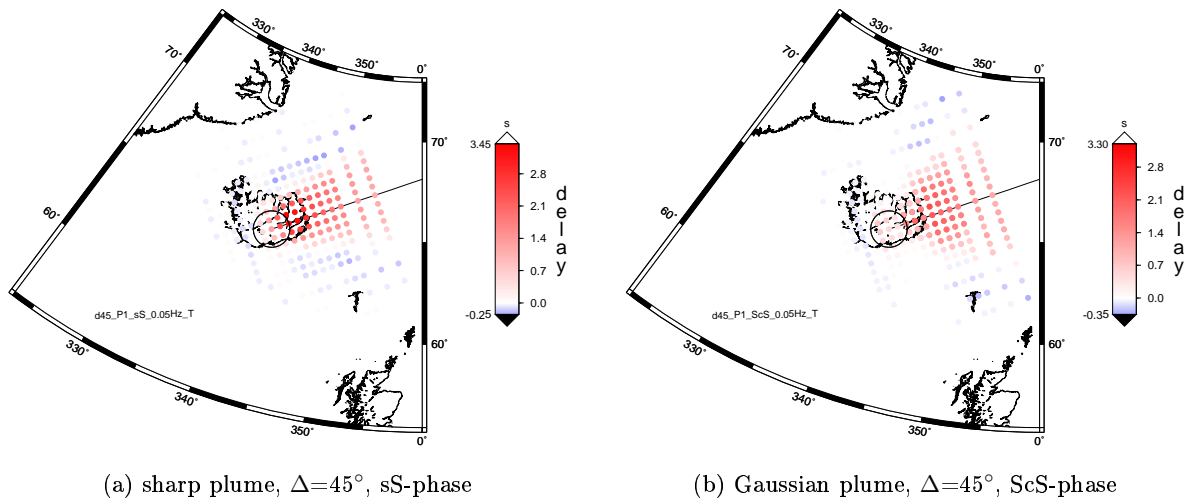


Figure 3.22: Delay maps for  $\Delta = 45^\circ$ : comparison of the shallow sS and the steep ScS-phase. From a ray-theoretical point of view the latter should be ideally suited to detect plumes at close epicentral distances. However, subfigure (b) shows that the delay distribution of the ScS-phase is smeared over a large region and thus not suited for regional tomography experiments. Plume origin depth is the CMB for all cases.



and the steep ScS-phase (transverse components, Fig. 3.22). For the ScS-phase ray-theory predicts a localized area of strong delay close to the plume axis. Using finite-frequency waves we observe this characteristic of the delay distribution for the sS-phase but not for ScS. The latter acquires strong delays (peak value of 3.3 s), however distributed over a broad region without a localized peak. In contrast to that the sS-phase has a focused peak close to the rim of the plume stem with a peak-delay of 3.45 s, thus even higher than the one of the ScS-phase. The sS-delay footprint is also much smaller than that of the ScS-phase. This is almost the opposite characteristic of what one would expect from ray-theory. The reason lies in the influence of the sensitivity kernels of the two phases. The ScS-kernel seems to smear the spatial delay distribution over a large region, probably due to its complicated geometry resulting from the core reflection. Again, a more precise discussion of the kernel's influence can not be given since no kernels for the ScS-phase at this distance are available in the literature.

For regional tomography experiments the shown delay-shadows demonstrate that within a confined station network close to the plume relative travel-time differences resolve a sharp footprint of the plume using the sS-phase which reflects the plume position and its width. In contrast, the ScS-phase which was supposed to have this property leads to relative travel-time differences of about the same magnitude but with a smooth spatial distribution and a larger spatial extension. The region of maximum delay lies about 150 km away from the plume edge, which can in the case of Iceland and Hawaii be off-shore, depending on the back-azimuth of the earthquake. In that case it can not be captured with land-based seismometers, whereas the sS-delay maximum lies so close to the plume edge that it is likely be captured on land in most cases.

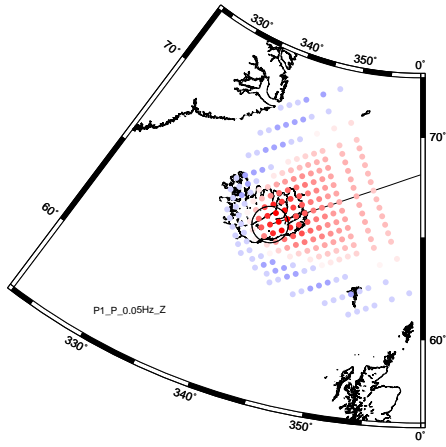
This confirms the objection by NATAF [2000] concerning the ScS-phase as a well-suited phase for plume studies, at least for regional tomography experiments. However, an emphasized healing effect as expected by NATAF could not be observed at this epicentral distance with this study.

In general, the ScS-phase example clearly shows that the application of ray-theory on plume problems can lead to wrong conclusions when dealing with finite-frequency waves. Thus, for seismometer-network design of regional experiments finite-frequency forward-modeling studies such as this one are necessary in order to know, where the travel-time effects of certain phases are to be expected.

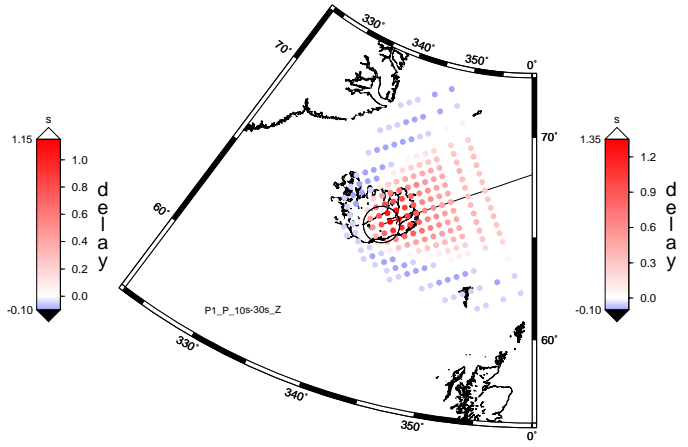
Going to higher epicentral distances, we look at the delay maps of the phases  $P_{diff}$  and  $PcP_2$  for a Gaussian plume at an epicentral distance of  $135^\circ$  shown in Fig. 3.21c+d. The delay patterns look very different, but the minimum and maximum delay amplitudes are similar. The two phases have very different paths, however, in the region where they are affected by the plume their paths are coinciding. This leads to similar amplitudes for the delays. The pattern of the delays differ (concentration of high values in a small circular region for the  $P_{diff}$  phase) probably due to a complication of the second Fresnel zones as a consequence of their totally different geometries. For the negative delays the effect is the same, but looks more dramatic since a large part of the early arrivals are below the resolution threshold.

## Frequency-dependent analysis of delay shadows

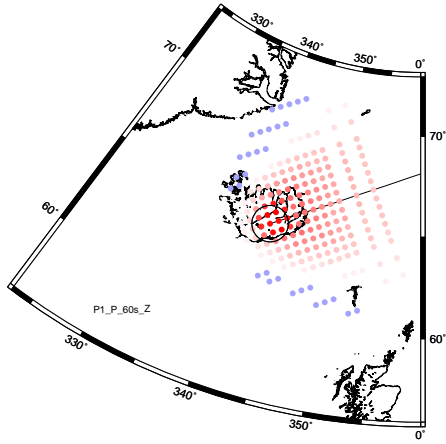
We now look at the frequency-dependence of the spatial delay distribution. Fig. 3.23 shows delay maps obtained by cross-correlation of seismograms that are low-pass filtered with corner



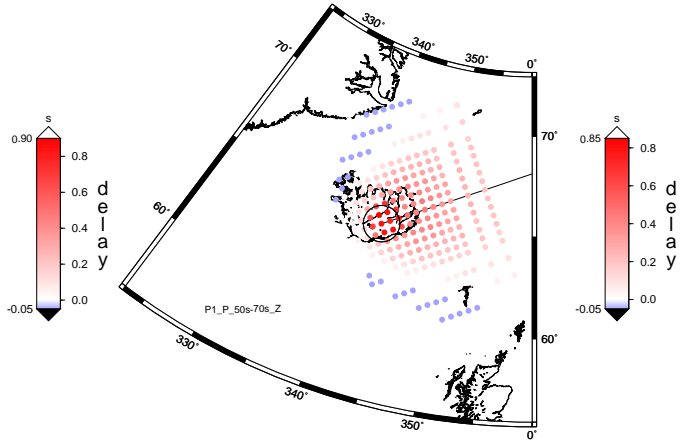
(a) low-passed,  $f_{corner}=20$  s



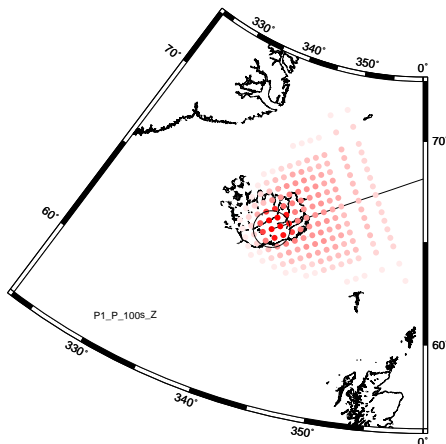
(b) band-passed,  $f_{center}=20$  s



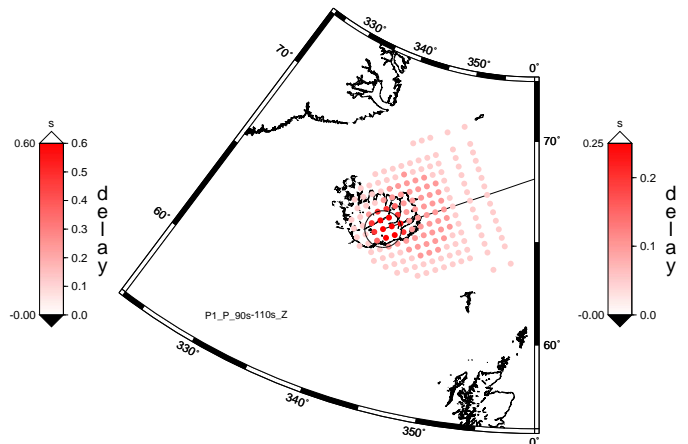
(c) low-passed,  $f_{corner}=60$  s



(d) band-passed,  $f_{center}=60$  s



(e) low-passed,  $f_{corner}=100$  s



(f) band-passed,  $f_{center}=100$  s

Figure 3.23: Frequency-dependent delay shadows for a sharp CMB plume at  $\Delta=90^\circ$ .

frequencies of 20, 60 and 100 s (left column). With decreasing frequency the delay footprints get broader and decrease in amplitude, which pushes the negative delays under the threshold of resolution. This is an effect of broadening of the sensitivity kernel with decreasing frequency. The right column of the figure shows delay maps from seismograms that are *band-pass* filtered instead, with the same frequencies as for the right columns of the figure but being *center-frequency* of a 20 s wide frequency window. The decrease in amplitudes with decreasing frequency is present, too, but more pronounced since the lower frequencies in the low-pass filtered seismograms do not contribute.

### 3.3.2 Evolution of travel-time delay along the great circle

After looking at the spatial distribution of travel-time perturbations caused by a plume we study the travel-time effect as a function of distance. Since the extension of virtual seismometer array is limited to about 600 km behind the plume center, we use the virtual receivers along the great circle through epicenter and plume to follow the evolution of travel-time perturbations with distance. The procedure for deriving the travel-time delays is basically identical with the one used for the travel-time delay maps, except that we use only the direct  $\mathbf{P}/\mathbf{P}_{diff}$ -wave. Any other phase would interfere with others over the large range of epicentral distances (here:  $75^\circ \leq \Delta \leq 150^\circ$ ) and lead to a distortion of the resulting curve. Moreover, some phases do not exist over the entire epicentral distance range. As for the delay maps, resampling of the seismograms again leads to a 0.05 s resolution in time, while the resolution in space is lower (111 km compared to 50 km for the maps) due to the use of the great-circle stations. These resolution limitations lead to a staircase-like shape of the derived travel-time perturbation curves.

We first discuss some characteristics of the evolution of delay time with distance from the plume axis using Fig. 3.24. It shows the travel-time delay curve for a sharp vertical cylindrical low-velocity anomaly (plume) with CMB origin and a radius of 100 km. Until about 300 km

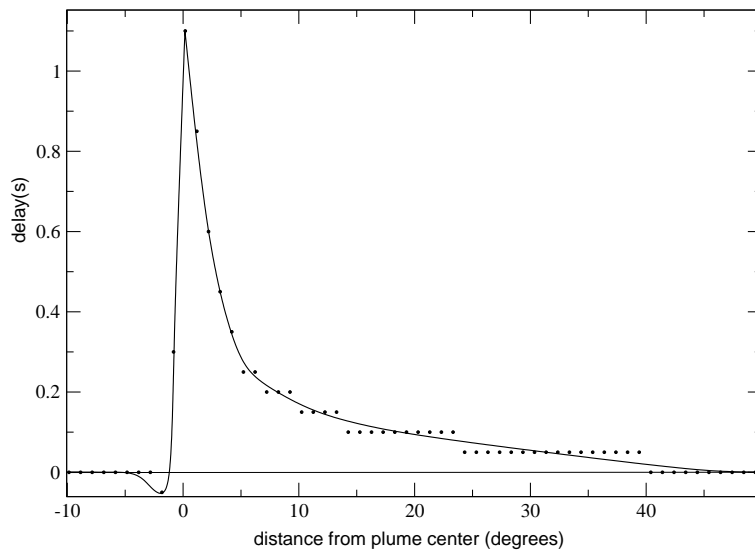


*Figure 3.24: Travel-time delay of the  $P/P_{diff}$ -phase as a function of epicentral distance: sharp  $r=100$  km radius plume. The black points are the values resulting from the cross-correlation procedure, the line represents what the actual delay curve could look like. It can not be exactly reproduced because of limitations in the spatial and temporal resolution. In the following figures the data points will be connected by straight lines for the sake of simplicity.*

in front of the plume center (200 km from its front edge) travel times are not affected by the low-velocity anomaly. Then, close to the edge of the plume one station samples the zone where the P-wave is coming earlier (0.05 s – one resolution unit) in the presence of the plume compared to PREM.

Travel-time delay is increasing steeply to reach its maximum directly behind the plume center. The curve is falling off again, primarily due to healing effects. At about  $7^\circ$  behind the plume, where the receiver array for deriving the travel-time delay maps ends, the curve

flattens. At this point already more than 75% of the delay is lost. About 4500 km ( $40^\circ$ ) behind the plume, no delay for the P-wave can be detected anymore. Note that for real data the delay will probably not be observable anymore already closer to the plume due to picking inaccuracy, noise, crustal effects and so on. This would also be true for S-waves, even though their signature is stronger (recall that for this plume model the maximum delay is 5.4s for SKKS, 5s for SKS, and 4.1s for S).

The total disappearance of any travel-time delay far behind the plume observed here is a combination of the following influences:

- the actual wavefront-healing effect, certainly dominating, responsible for the main loss of travel-time delay and its rapid decay.
- a geometrical effect: the further the seismometer location from the plume, the more horizontal are the paths of the waves at the position of the plume and thus the shorter the paths through the plume stem. This effect is not associated with wavefront healing and can also be explained by ray-theory (see Figs. 3.25 and 3.26).
- another consequence of a higher epicentral distance is that the wave is perturbed by the plume at greater depth which increases the path length behind the plume. This leads to a longer way for healing to occur (Fig. 3.26), and thus enhances the direct healing effect.
- the fact that the  $P/P_{diff}$  phase dies out at larger epicentral distances. In our noise-free simulated seismograms, however, the  $P_{diff}$  phase can be observed up to an epicentral distance of at least  $\Delta=150^\circ$ , which is  $60^\circ$  behind the plume. Thus, the effect on the results presented here (epicentral distance of  $90^\circ$ ) should be minimal, but could play a role for plumes farther away. Certain phases (such as PKP) cover only a limited range of distances which may make studies of the evolution of travel time over a long distance range difficult. For  $P_{diff}$  the more important effect is that from  $140^\circ$  on the raypath of the  $P_{diff}$  phase does no longer sample the plume, but rather diffracts on the core side (see Fig. 3.25).

Since wave effects, such as wavefront healing, are frequency dependent, we look how the delay curves change with frequency content of the seismograms. Fig. 3.27a shows the evolution of travel-time delays behind the plume as derived from seismograms filtered with a 10, 20, 40, 60, 80, and 100 s corner frequency Butterworth low-pass filter. The decay of the back flank of the delay curve for the different corner frequencies shows that the healing effect gets more pronounced the smaller the ratio between plume diameter and wavelength. In Fig. 3.27b we take a different approach: the seismograms are *band-pass* filtered before deriving the travel-time delay using cross-correlation. Instead of using information above a certain frequency, we now consider a band *around* the frequency. This enables us to distinguish the influence of the respective frequency bands and thus to examine the interaction of waves of a limited range of wavelengths with an object of a certain size. The resulting delay curves are somewhat surprising. Each curve for the frequency bands is larger in amplitude than the curves for the low-pass filtered seismograms. At first sight this is counter-intuitive. However, it is plausible that partial destructive interference of waves of different frequency bands having first and second Fresnel zones that differ in size leads to smaller delay when using a broad frequency band as compared to a smaller one.

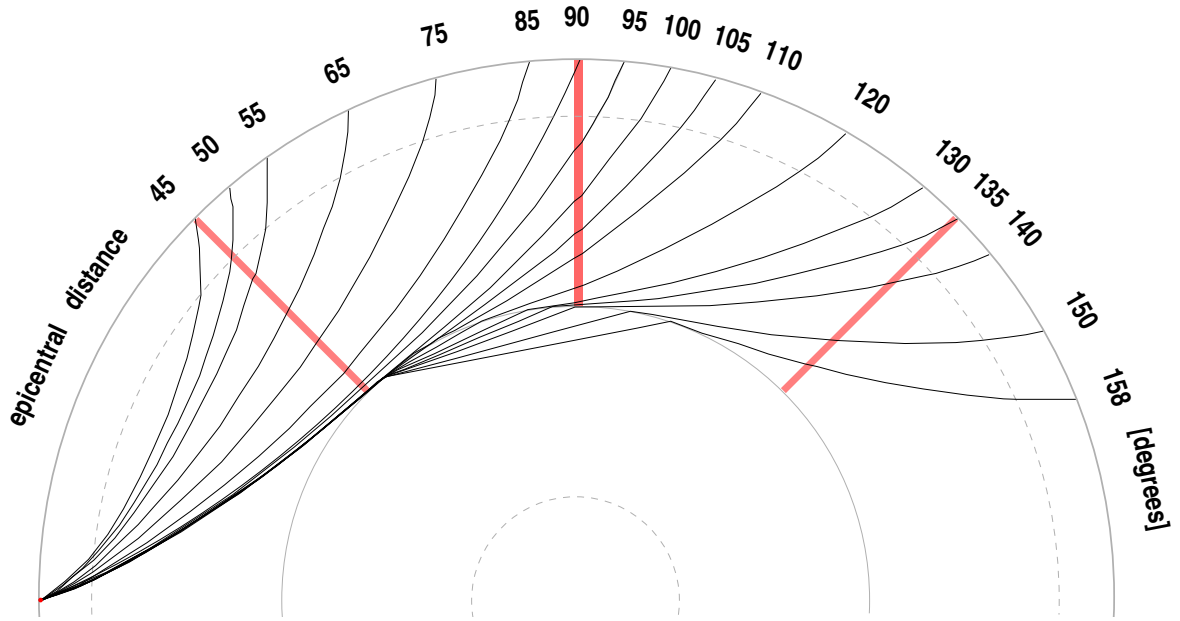


Figure 3.25: Ray paths of the  $P/P_{diff}$ -phases for several epicentral distances. Plumes at  $\Delta=45$ ,  $90$ , and  $135^\circ$ , as modeled in this study are symbolized by red areas in order to illustrate where they are sampled by the rays. For example the  $\Delta=90^\circ$ -plume is only hit by rays that are recorded up to about  $\Delta=140^\circ$  epicentral distance. Seismic waves with finite-frequencies instead sample a region around the ray, whose width is path length dependent (see Table 3.5) and further complicated by refraction. Moreover, the path length over which healing of the wavefront by diffraction can occur is increasing with increasing epicentral distance (see Fig. 3.26).

To further examine the relative contributions of the different frequencies we *low-pass* the seismograms before calculating the delays. The result is shown in Fig. 3.27c. It turns out that if we take away low frequencies nothing changes. This is true down to about 50 s period. That again demonstrates that the delays curves are dominated by high frequencies. However, as can be seen for the 20 s curve in Fig. 3.27c when we approach the highest frequencies the results starts becoming unstable as the relative importance of numerical noise expected at high frequencies becomes dominating.

In the following we will compare pairs of plume models which differ in one model parameter to study the effect on travel-time with distance.

### Perturbation magnitude: weak vs. strong plume

Fig. 3.28 shows the travel-time delay evolution of a sharp 100 km plume model for two P-wave speed perturbations: 3.5% and 7%. The delay caused by the plume with two times the perturbation of the other one is twice as high, as one would expect. For better comparison the delay values of the strong plume is divided by two and plotted as a dotted red line in Fig. 3.28. The similarity between the scaled strong and the weak-plume delay breaks down about  $20^\circ$

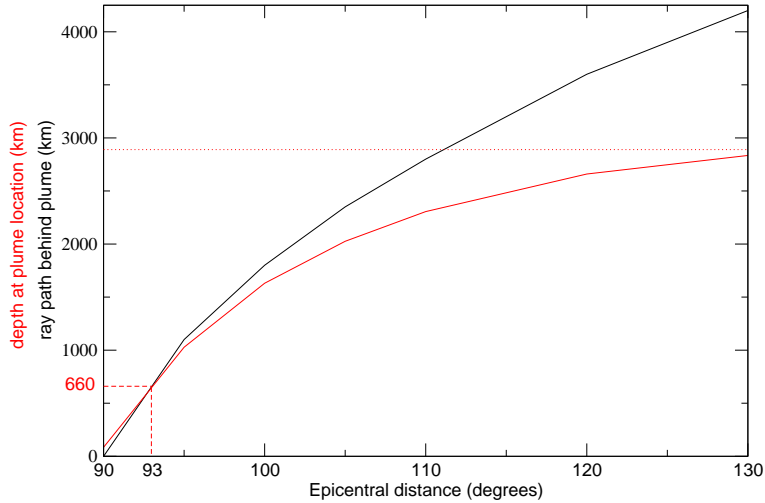


Figure 3.26: Approximate length of the  $P/P_{diff}$ -phase path (black line) after passing a plume at  $90^\circ$  epicentral distance. The depth of the ray at the plume location is represented by the red line, the dotted red line is the depth of the core-mantle boundary. The dashed lines indicate the distance behind the plume where the  $P$ -wave is to be expected that samples the plume right at the bottom of the transition zone. The rays to which the shown values refer are shown in the previous figure (3.25).

behind the plume center, where we observe an increase of the delay of the stronger plume. In contrast to the delay of the weak plume, which reaches zero at  $40^\circ$  behind the plume center due to healing, the strong plume keeps its delay at least until  $50^\circ$  behind the plume center.

One might think that the explanation for this phenomenon is that for a strong plume the wavefront running through the plume is so much delayed that it does not contribute to the healing effect, as observed for stronger anomalies (Fig. 1.6). In that case, instead, it interferes destructively with the wavefront that diffracted around the plume, thus reducing its healing effect. However, for this effect the delay would have to be half the period of the wave (10 s in our case). This is only possible with a much stronger perturbation and therefore can be ruled out.

Another explanation is that the strong plume considerably affects the path of the wave, i.e., that the assumption frequently used that perturbations are small and smooth and thus only cause a delay but do not affect the path is not valid here. For the strong plume this could mean that the sensitivity kernel – that anyway interacts with the core in a complicated manner – is significantly influenced by the plume. As a consequence, more sensitive parts of the kernel may now sample the area where the plume is and therefore the plume waves acquire more delay at this depth recorded  $40^\circ$  behind the plume. This is a very speculative explanation and it shows that simple ray-theoretical explanations have to fail in case of this complex finite-frequency interaction between the strong plume-anomaly and the core. However, since the  $D''$  layer is suspected to have large ultra-low velocity zones as well, it is worth calculating the actual 3D kernels taking into account all the complexity and to examine this effect in detail. However, this goes far beyond the scope and the possibilities of this work.

In Figure 3.29 the  $P$ -phase delay function of the sharp,  $r=100$  km plume with CMB-origin of Figure 3.24 is shown together with the one for a plume having the same geometry but coming from the 660-discontinuity. The delays are identical up to the plume center but dif-

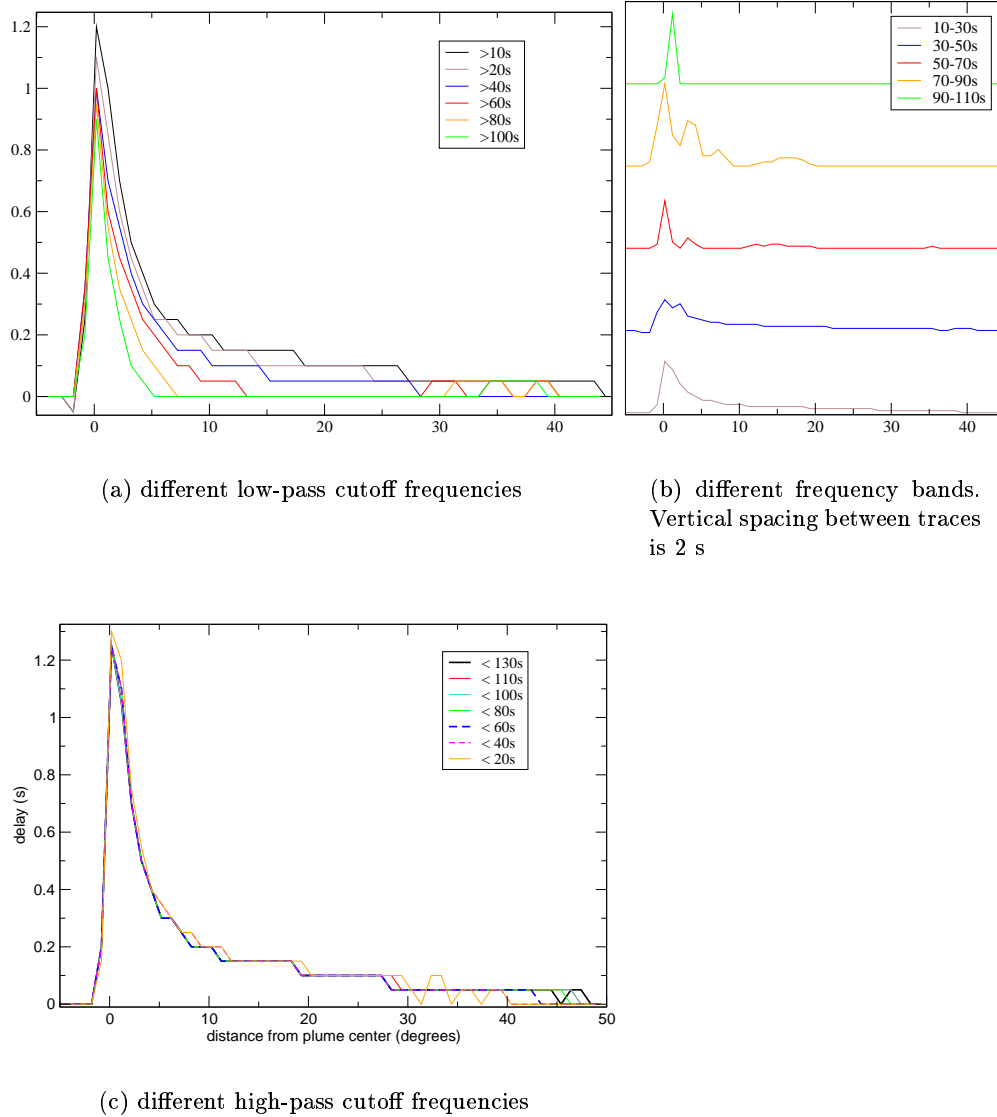


Figure 3.27: Frequency-dependent analysis of the P-phase delay time evolution with distance from the plume center (sharp CMB plume at  $\Delta=90^\circ$ ).

fer significantly from there on. The delay caused by the plume from the 660-discontinuity decreases much faster compared to the other one and is vanishing already about 700 km behind the plume center. The reason for this behavior is that from this distance on the Fresnel zone of the P-phase is lying beneath the plume and is not affected by the short conduit that terminates at the bottom of the transition zone (see Fig. 3.26). This enhances the wavefront healing effect since there is another direction from which waves can diffract around the plume and close the wavefront behind it. On the other hand, the difference between the delays of the two models can tell something about the relative importance of the influence of the four effects listed above. The decay in form of the long tail in the delay curve of the CMB origin plume may indeed reflect the geometrical effect of shorter ray path through the plume at deeper



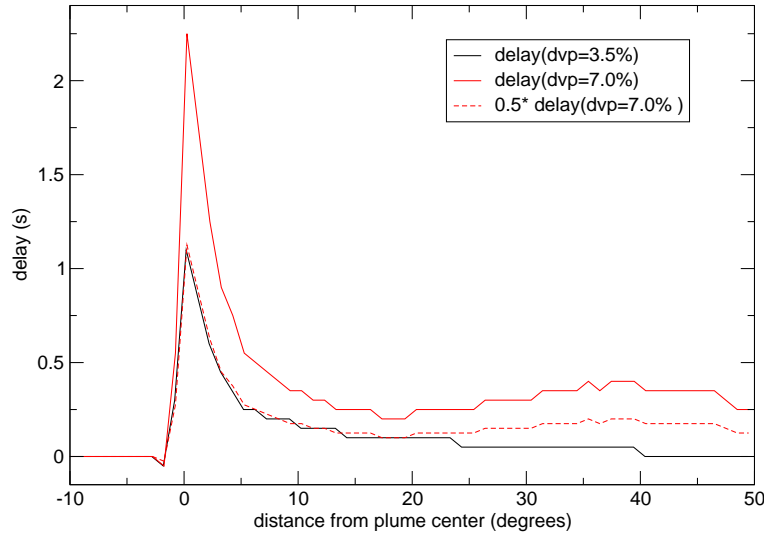


Figure 3.28: P-phase travel-time delay as a function of epicentral distance and perturbation magnitude: sharp  $r=100$  km-radius CMB-plume.

depth, since this part of the curve is missing for the plume with 660 km depth origin. While the shallow plume has only 23% of the total integrated perturbation with respect to the deep plume, the integral over its delay curve reaches 43% of the value obtained for the CMB plume. This emphasizes that perturbations close to the surface have a larger effect than deeper ones since they have a longer path behind the plume for healing to occur. However, the effects of the shallow and deep parts are clearly separated concerning the location where they can be measured, which provides a means for discrimination of plume origin depth if stations at large distances to the plume are available.

### **Perturbation function and plume radius: sharp vs. gradational, for $r=60, 100, 300$ km**

In the following the influence of the lateral perturbation function will be examined. Starting again with the 200 km wide plume from the CMB, we compare its delay curve with that of a low-velocity anomaly whose perturbation function follows a Gaussian (Fig. 3.30). The Gaussian plume model delay curve is missing the negative delay in front of the plume, as already observed in the delay shadows. The stronger positive delay caused by weaker and spatially wider perturbations cancels out the weak effect of the second Fresnel zone due to stronger perturbations closer to the axis. Note, however, that this observation is only based on one data point which has one increment difference in both delay time (0.05 s) and distance from the plume axis. Concerning the positive values the curves are fairly similar, the major difference lies in the amplitude of the peaks, which is slightly larger for the sharp plume (1.1 s vs. 0.95 s). This difference can be explained by the fact that the maximum velocity perturbation is only reached in the middle of the Gaussian plume whereas for the sharp plume it extends out to the defined radius. Therefore, waves can accumulate larger delays due to the full perturbation over a wider region. The other differences are again one increment in time and space and are thus not significant. There is almost no difference in the integral over the two curves, the

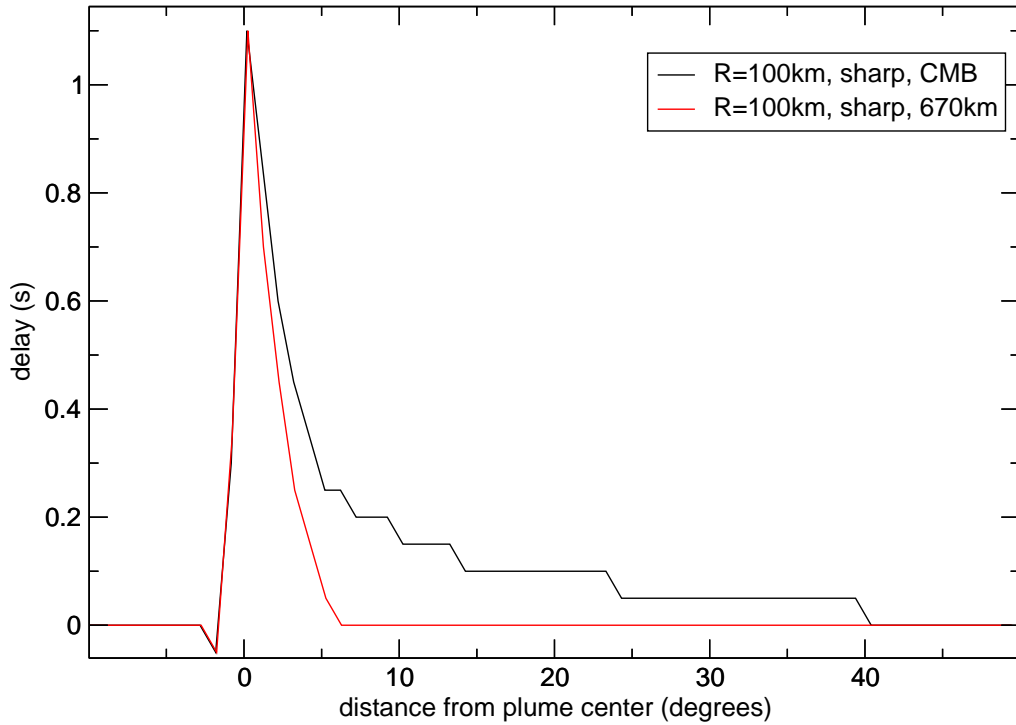


Figure 3.29: P-phase travel-time delay as a function of distance from the plume center: comparison of two origin depths, one at the CMB, one at a depth of 660 km.

Gaussian plume reaches 99.2% of the integrated perturbation of the sharp plume. Clearly, from such distance-dependent travel-time delay curves the perturbation function of a 100 km radius plume is not distinguishable with 20 s data.

Figures 3.31a+b show the delay curves for Gaussian and sharp boundaries of plume models with radii of 300 km and 60 km, respectively. Note that due to the different integral total perturbation values of models 6/13 and 5/30 one of the curves is scaled down by a factor that is equal to the perturbation ratio in order to obtain comparable values. For the 300 km plume this was the sharp model, for the 60 km plume the Gaussian model. Again – within the limits of the different resolution – the sharp and Gaussian plume delays do not differ significantly, with the one exception that the sharp 60 km plume has an increase of travel-time delay at higher distances from the plume. This is somewhat irritating, since one would expect the increase for the Gaussian plume whose high peak perturbation of 17.2% for the P-wave speed even exceeds that of the strong plume with 12.4% which also shows such an increase (Fig. 3.28).

To examine the increase we look at frequency-dependent delay curves for the Gaussian models (Figs. 3.31c+d) obtained by low-pass filtering the seismograms with different cutoff-frequencies before measuring the delays. Again, we resolve an increase at larger distances for the  $r=60$  km plume (subfigure d), but only for periods of 40 s or less, i.e., high frequencies. The inverse is true for the 300 km plume, where we observe an increase for periods of 60 s or more, which are not observed in the 20 s data of subfigure a. This demonstrates that the high-frequencies are dominating (see Figs. 3.27a+c) and that they can mask long-periods effects

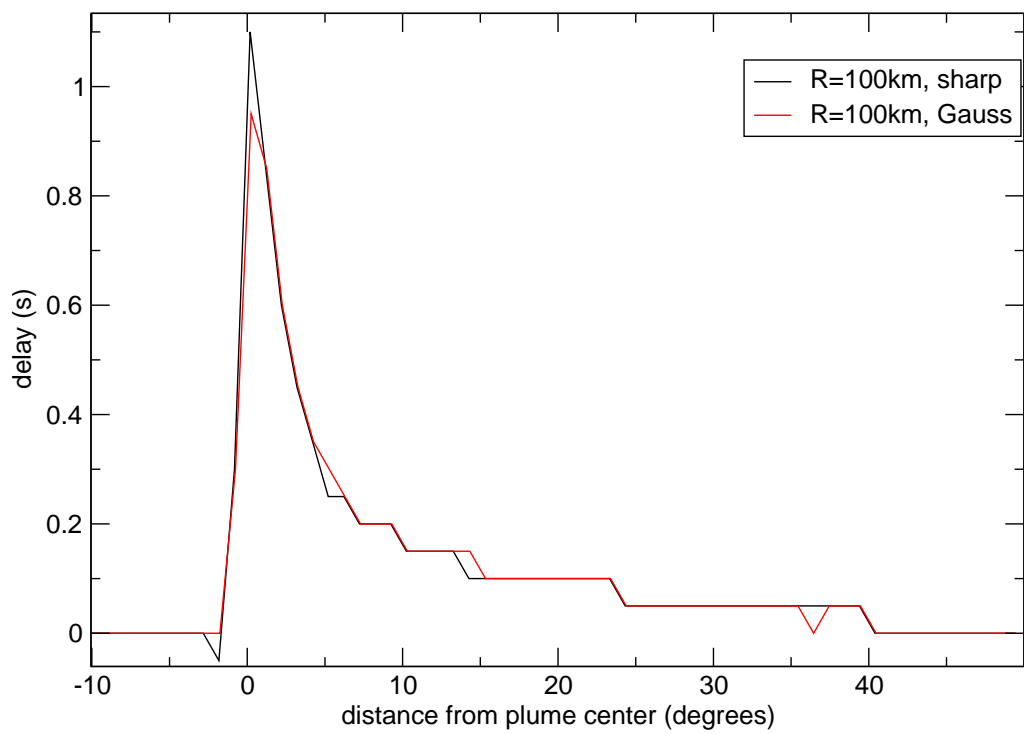
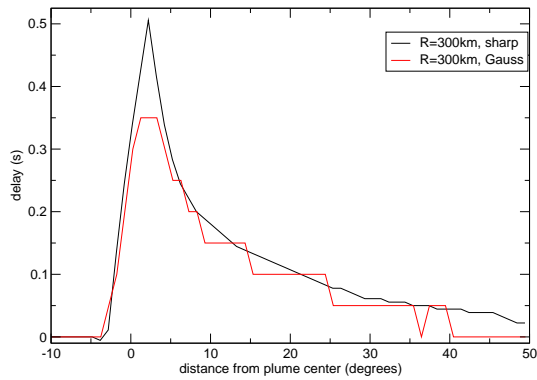
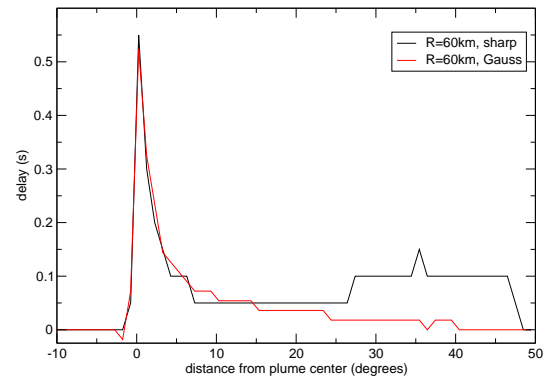


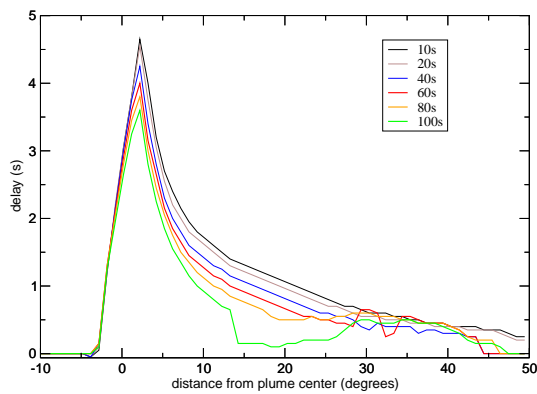
Figure 3.30: P-phase travel-time delay as a function of epicentral distance: sharp vs. Gaussian  $r=100$  km-radius plume.



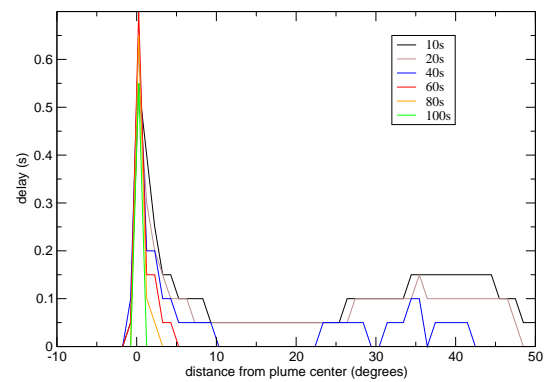
(a)  $r=300$  km



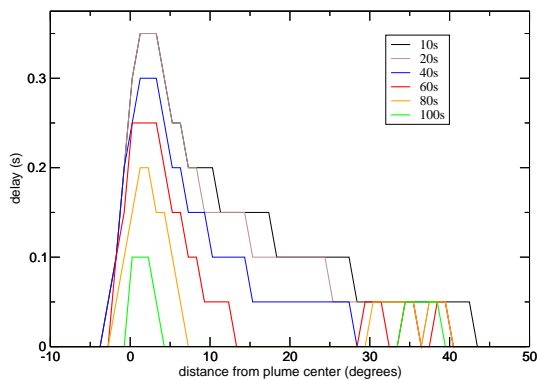
(b)  $r=60$  km



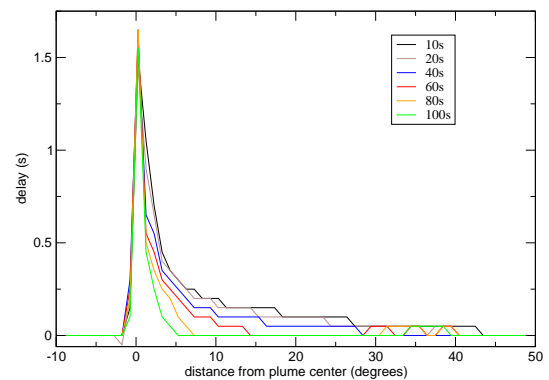
(c)  $r=300$  km, sharp plume



(d)  $r=60$  km, sharp plume



(e)  $r=300$  km, Gaussian plume



(f)  $r=60$  km, Gaussian plume

Figure 3.31: P-phase travel-time delay as function of epicentral distance: a)+b) comparison between sharp and Gaussian perturbation function for two plume radii (the curve for the plume with the higher perturbation is scaled down in order to ease comparison), c)-f): each of the delay curves separately, with frequency as parameter. Butterworth low-pass filter corner frequencies are given in the legend.

which are weaker in amplitude.

The reason for this opposed behavior (increase of delays at large distances at long periods for the large plume and at low periods for the small plume) lies in the ratio wavelength to plume width (Fig. 3.32). We consider depths in the lowermost mantle, since the raypaths of

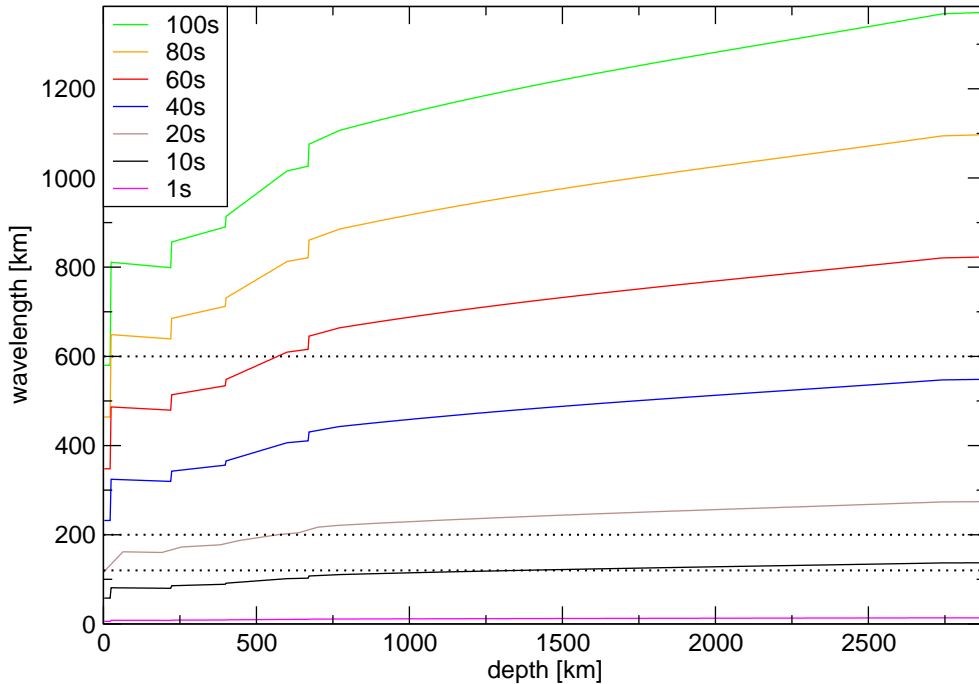


Figure 3.32: Wavelengths of compressional waves as a function of depth for several periods using the PREM model. The black dotted lines indicate the width (diameter) of the plume models with radii of 60, 100, and 300 km.

arrivals recorded  $20\text{--}50^\circ$  behind the plume sample the plume in this depth range (see Fig. 3.25). For the 300 km radius plume the periods where the increase of the delay is observed all have wavelength larger than the width of the plume (600 km). All periods where no increase is observed have wavelength below the plume size. For the 60 km plume as well the periods that show an increase of the delay have wavelength larger than the plume diameter (120 km), but here this is true for all periods, but not all of them show the increase. When looking at the amplitudes of the increased delays in Fig. 3.31d it turns out that these decrease with increasing periods. For 40 s the delays at large distances behind the plume are only two resolution increments in time, it is thus likely that also the longer periods experience an increase, however, already for 60 s it cannot be resolved anymore.

In summary, there is an increase (or recovery) of delay times around  $35^\circ$  behind the plume center for periods that correspond to wavelength equal to or larger than the plume width. It is most pronounced when the wavelength at the depth where the plume is sampled by the wave is equal to the plume diameter and becomes smaller with increasing wavelength. An explanation of this effect can not be given, we speculate that it is related to a frequency-dependent distortion of the sensitivity kernel by the core.

The effect is also visible for the Gaussian plume models (Fig. 3.31e+f), but less clear. The 300 km Gaussian plume has a very low perturbation (0.39%) therefore the increase is only re-

solved with one delay unit (0.05 s), nevertheless undoubtedly present. As already mentioned, the 60 km Gaussian plume has a very high perturbation and is thus well resolved. Note, that its effective width is even smaller than 120 km because the strong perturbation is concentrated very close to the plume axis. Therefore, the ratio of plume width to wavelength is even smaller than for the sharp plume, leading to decreased amplitudes of the recovered delays. However, we observe an increase of low frequencies instead of higher ones. The reason for that remains elusive, probably the influence of the very strong anomaly – as observed for model 3 – distorts the systematic behavior observed for the weaker anomalies.

We now compare delays of Gaussian plumes having the same integral perturbation but differ in radii ( $r=60, 100,$  and  $300$  km, Models 13, 4 and 30, Fig. 3.33). With the common

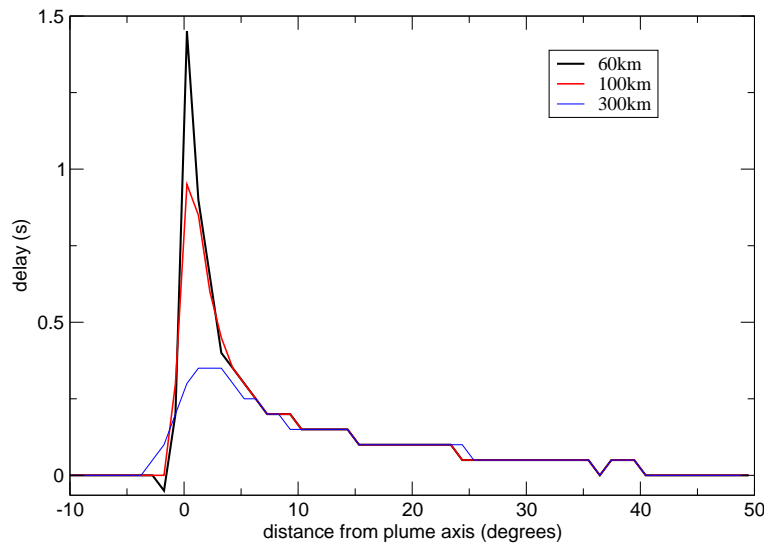


*Figure 3.33: P-phase travel-time delay as a function of epicentral distance: comparison of CMB-plume models with  $r=60, 100$  and  $300$  km radius, but the same integral perturbation.*

assumption that the ray-path does not change significantly due to the heterogeneity (here: the plume) the resulting travel-time delays should be similar, since the effective causing velocity perturbation is the same. However, from the curves it is obvious that this is only true for stations more than 650 km behind the plume centers. This distance is not coincidental, it is about the width of the zone that is perturbed by the largest plume model (radius of 300 km). This means that only arrivals that are affected by the entire perturbation of the three plumes gather the same delay. In case of the smallest ( $r=60$  km) plume the high perturbations are concentrated in a very small region around the plume axis. Therefore, arrivals right behind the plume center are affected by most of the perturbation of the plume but had no travel-path behind the perturbed zone to experience wavefront healing. This is why the maximum delay of the smallest plume is that much higher than for the larger ones. From a certain distance on, the wavefronts of all models have gathered the same integral perturbation and had the same pathlength for healing, resulting in the same delay for the different models.

## Other epicentral distances

Let us look at the two other epicentral distances. Starting with a  $r=100$  km plume at  $45^\circ$  epicentral distance (Fig. 3.34) we see the same effect as for  $90^\circ$  epicentral distance: the delays of the sharp and the Gaussian plume (left panel of the figure) are similar, with the sharp plume again causing a slightly higher peak. The frequency-dependent delays of the two plume

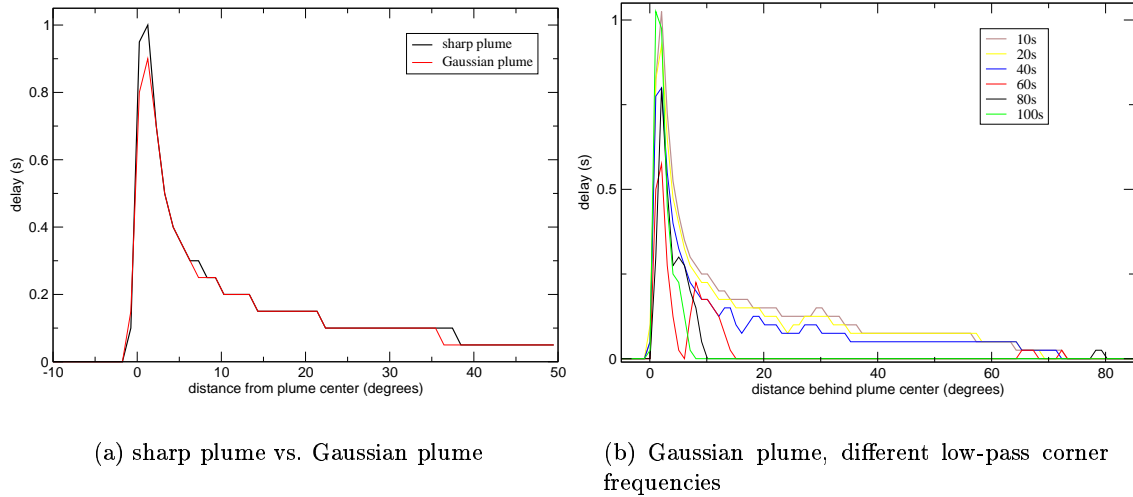


Figure 3.34:  $P$ -phase travel-time delay as a function of distance for a plume from the CMB at  $45^\circ$  epicentral distance.

models are similar as well, as an example the one for the Gaussian plume is shown on the right panel of Fig. 3.34.

The delay times for a sharp CMB-origin plume at  $135^\circ$  epicentral distance is shown in Figure 3.35 together with the ones for the sharp CMB-origin plumes at the two other distances. For interpreting and comparing the curves it is useful to recall the ray-paths and their interaction with the plume for the different plume locations given in Fig. 3.25. Nevertheless, it should be kept in mind that the ray approximation used for creating this plot is not valid for our case, and that the sensitivity of the waves is concentrated in the Fresnel zones around the ray paths shown.

The delays of the plume at  $45^\circ$  epicentral distance are not perturbed by interaction of the  $P_{diff}$ -phase with the core since in the distance range under study the plume is only sampled by  $P$ -waves. In this case the simple relationship holds that arrivals at larger distances behind the plume center carry the delay caused by a deeper part of the plume, where the Fresnel zone is larger. This is quantified in Table 3.5. Note that from about  $\Delta=80^\circ$  ( $35^\circ$  behind the plume center) the Fresnel zone does no longer fit in the mantle and starts interacting with the core. This may be the explanation for the local minimum in delays around  $42^\circ$  behind the plume center.

Another way to look at it is that the remaining path length after passing the plume becomes larger and thus provides a longer way for healing to occur. Note that in the distance range examined here there is no total healing for the  $45^\circ$ -plume, a delay of 0.1 s remains.

The plume at  $\Delta=90^\circ$  has a similar delay curve, but deviates from the one of the  $45^\circ$ -plume where it is sampled by the  $P_{diff}$ -phase. The delay drops off faster and finally vanishes

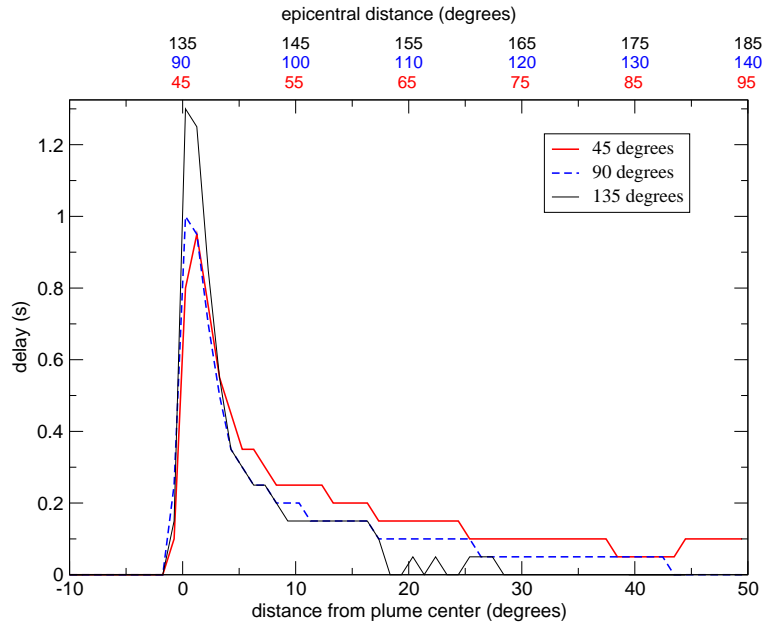


Figure 3.35:  $P$ -phase travel-time delay as a function of distance behind the plume center: sharp  $r=100$  km radius CMB-origin plume at three epicentral distances ( $45^\circ$ ,  $90^\circ$ , and  $135^\circ$ ). In order to ease association with ray paths for the different distances and plume positions in Fig. 3.25, the corresponding epicentral distances are given in the respective color for the three plume locations.

completely. This difference may be explained by the complexity of the  $P_{diff}$ -sensitivity kernel, as compared to the simple “banana”-kernel of the direct  $P$ -wave. The integral over the delay reaches only 78% of that of the  $45^\circ$ -plume.

The plume at  $\Delta=135^\circ$  is more different in the evolution of the delay than the two other ones. It has a higher maximum delay which might be due to the steeper incidence of the waves directly around the plume axis. Already two degrees behind the plume its delay curve becomes similar to the one of the  $90^\circ$ -plume, owing to the kernels that are similarly affected by interaction of the  $P_{diff}$  phase with the core. About 20 degrees behind the plume the delay drops down and has vanished 28 degrees behind the plume center. The reason for this is that the  $P_{diff}$  phase at these epicentral distances dies out. The integrated delay only reaches 70% of the value for the  $45^\circ$ -plume.



$\Delta$ [°]	depth [km]	L [km]	$\lambda$ [km]	$d_{Fresnel}$ [km]
50	626.5	5621	204	1070
55	984.2	6120	229	1183
60	1285.9	6606	238	1254
65	1557.7	7081	246	1318
70	1810.2	7543	252	1378
75	2048.7	7991	258	1434
80	2283.8	8425	263	1488
85	2515.9	8846	268	1540
90	2742.4	9269	274	1591
95	2802.2	9579	294	1677

Table 3.5: Parameters of the P-phase hitting a plume at 45° from the epicenter for several recording distances. In the columns the epicentral distance at which the ray reaches the surface, the depth at which it hits the plume, the path-length, the wavelength for a period of 20 seconds and the diameter of the Fresnel zone for this period are given.

### 3.3.3 Evolution of amplitudes behind the plume

As we have seen, in the parameter intervals studied, travel-time delay patterns are not very sensitive to the shape of the perturbation function. However, it should be kept in mind that the variation of the perturbation functions takes place in a range of about 300 km that we sample only with seven stations. We turn to the influence of a plume on the amplitudes of seismograms.

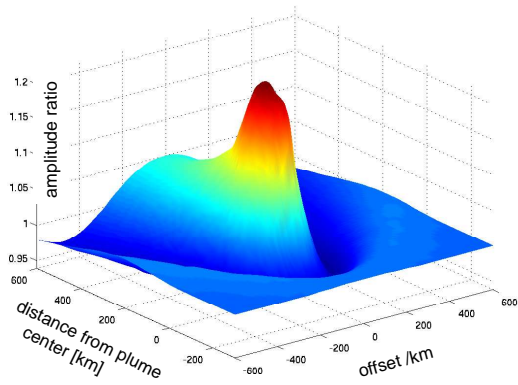
From analogy with optics, we expect an effect of a low-velocity zone on the amplitudes, since in optics low-velocity objects act as lenses, focussing energy. TILMANN *et al.* [1998] confirmed focussing effects of plume-like structures for teleseismic plane waves.

Ray theory predicts that the amplitudes behind a low-velocity anomaly are proportional to the second derivative of the perturbation function (e.g. DAHLEN AND BAIG [2002]). Since we use finite frequencies we expect deviations from this behavior, that are investigated in the following.

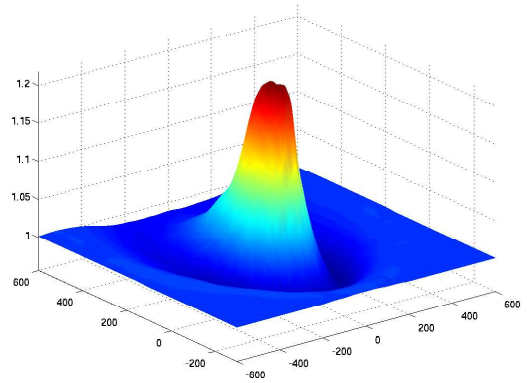
Fig. 3.36 shows the spatial distribution of the amplitude ratio of a plume-perturbed PREM P-phase with respect to a PREM P-phase alone. The plume models of the subfigures are all at an epicentral distance of 90 degrees. The amplitude ratios are derived using the method of SIGLOCH AND NOLET [2005] for measuring finite-frequency amplitudes, as described on page 75.

The focussing effect of the plumes is clearly visible, however, as for the delay shadow maps, the region where amplification is observed is surrounded by a zone of slightly decreased amplitudes. The explanation for this similar behavior of travel-time delays and amplitude focussing lies in the similarity between travel-time and amplitude sensitivity kernels. DAHLEN AND BAIG [2002] calculate amplitude kernels for several finite-frequency S-phases and compare them to travel-time kernels. The main difference between the two types of sensitivity kernels is that the amplitude kernel is missing the zero-sensitivity zone along the position of the classical ray and instead have their maximum sensitivity directly on the ray.

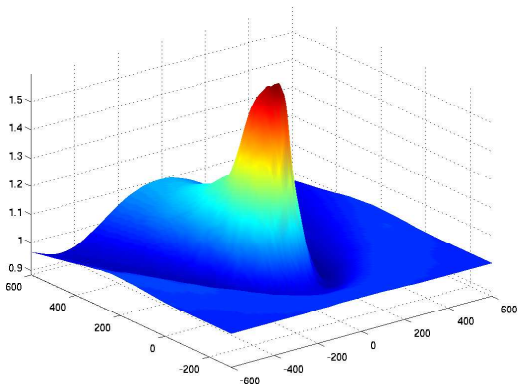
Two portions of amplitude increase can be identified. First, the stronger, roughly Gaussian-shaped center region positioned slightly behind the back-edge of the plume models. It is followed by a weaker elongated “hump” that decays slower. Comparing the amplitude distri-



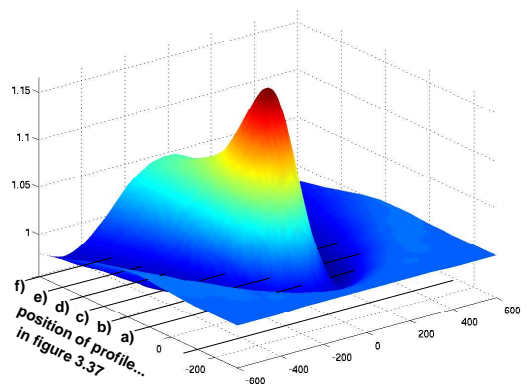
(a) sharp 100 km radius CMB plume



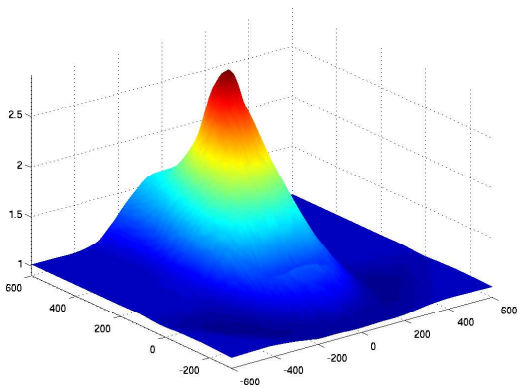
(b) sharp 100 km radius plume with 660 km origin depth



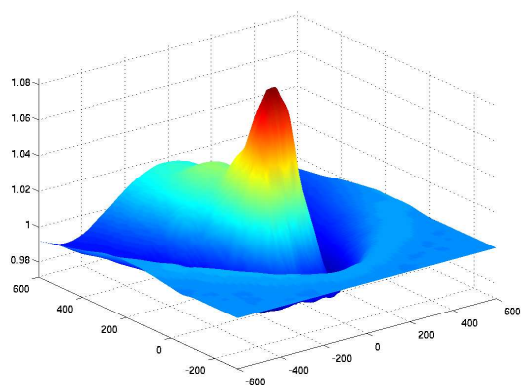
(c) same as (a) but doubled perturbation



(d) Gaussian 100 km radius CMB plume



(e) sharp 300 km radius CMB plume



(f) sharp 60 km radius CMB plume

Figure 3.36: Spatial distribution of P-phase amplitude ratios  $(PREM+Plume)/PREM$  for different plume models at  $90^\circ$  epicentral distance.

butions of the plume models differing in origin depth (CMB and 660 km, subfigures a) and b), respectively), we can distinguish where each of the two portions come from: the plume originating at the bottom of the lower mantle is exactly missing the hump, indicating that it results from focussing effects of the lower-mantle part of the plume. It is weaker because the way for healing to occur is longer, whereas the peak amplitude recorded right at the back-side of the plume are not yet affected by healing.

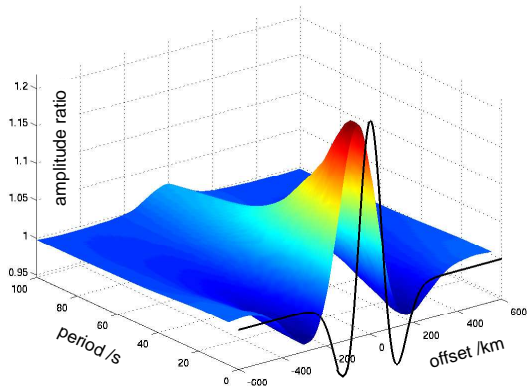
The amplitude effects of the sharp and the Gaussian plumes (subfigures a) and c)) with a radius of 100 km are similar in their spatial distribution but differ in amplitude – the sharp plume causes a stronger amplification, similar to what we observed for the travel-time delays.

Considering the plume models with differing radius (60, 100, and 300 km; subfigures a), e) and f), respectively) we see a difference between the small plumes and the 300 km-plume. Apart from the fact that the hump in the amplitude distribution for the large plume is falls outside the seismometer array due to its extension, we observe almost no amplitude decrease. This probably results from the size of the plume with respect to the wavelength and thus to the size of the second Fresnel zone. The small plumes instead cause amplitude decreases and increases that mainly differ in their magnitude. The width of the affected zones differs only insignificantly between the small models. We will later come back to this observation.

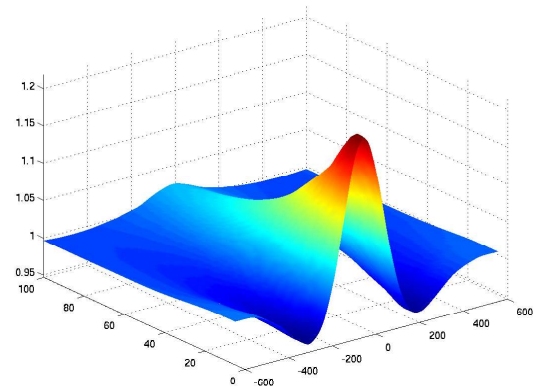
In Figure 3.37 we take a closer look at the plume model with the Gaussian perturbation function. In the subfigures the amplitude ratios for profiles perpendicular to the great circle through plume and epicenter are shown for different distances behind the plume axis, depending on the period used for low-pass filtering the seismograms. Going from 100 s period to lower periods / higher frequencies the same tendencies can be observed as when approaching the plume from far distances to closer ones (Fig. 3.36). The closer to the plume or the higher the frequency the higher the minima and maxima and the broader the function, i.e., the farther away from the plume center are the values equal to one. Both effects (the dependence on frequency and the one on the plume distance) can be explained with the amplitude sensitivity kernels. The higher the frequency the smaller the kernel and the larger its values. The farther the station the larger the cross-sectional area of the kernel at the position of the plume and the lower its amplitudes there. (The part of the plume sampled by a wave that reaches the receiver farther behind the plume is deeper compared to a closer receiver (see Fig. 3.25 and Table 3.5).

In conclusion, the amplitude ratios of the profile the nearest to the plume derived with the highest frequency is the closest to the infinite-frequency (ray theory) case for which an analytical solution exists (the second derivative of the perturbation function). It is plotted at the period=0 s position of Fig. 3.37a. The trend of the finite-frequency profiles towards the infinite-frequency solution is evident, however, the gap is significant and as will be shown below, the missing piece of information is required to distinguish different perturbation functions.

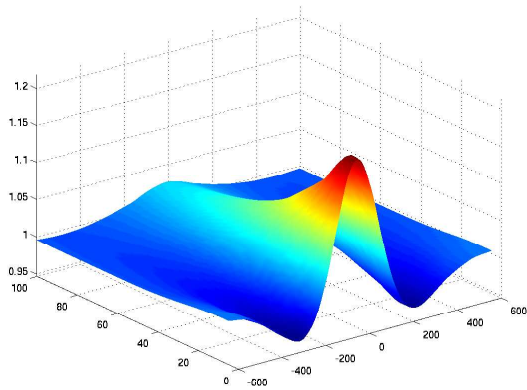
In order to examine why the different perturbation functions are not distinguishable with any of our methods, we take a look at the amplitude ratios of the models sharing an equivalent radius of 100 km (Fig. 3.38). Apart from differences in amplitude, the curves have the same width, the same position of maxima and minima and of the “one-crossings”. Thus, the difference in perturbation function does not map into a difference of amplitude ratio functions, probably due to the low-pass filtering effect of the frequencies used. We plot the theoretical infinite-frequency curve for the Gaussian plume model for comparison (black line with higher amplitude). It is the second derivative of a Gaussian (the “Mexican hat” function) with a  $1/e$ -radius of 100 km. It is obvious that the curve does not fit the Gaussian plume curve,



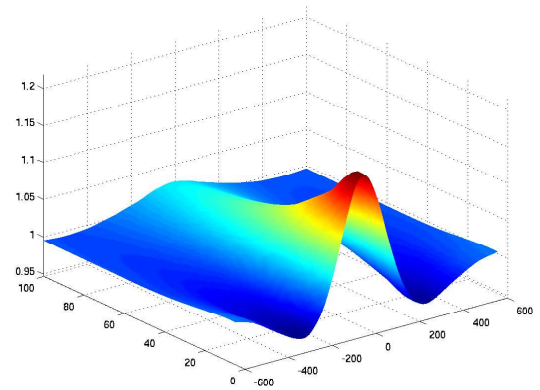
(a) 100 km behind plume



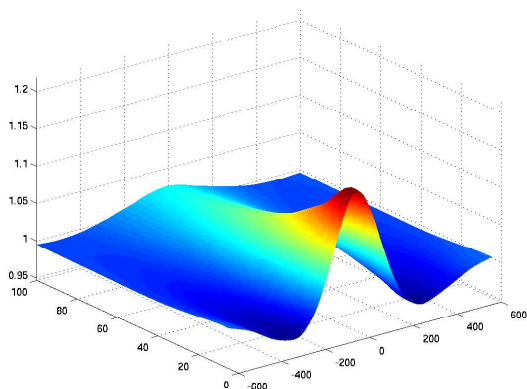
(b) 200 km behind plume



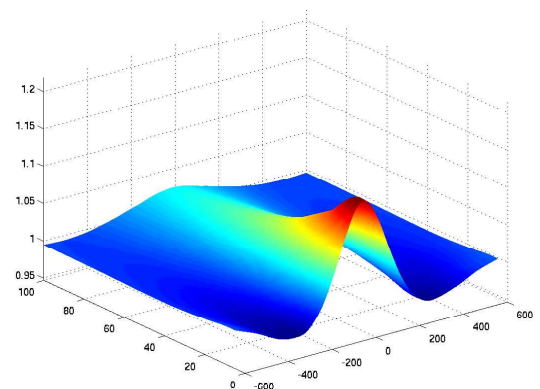
(c) 300 km behind plume



(d) 400 km behind plume



(e) 500 km behind plume



(f) 600 km behind plume

Figure 3.37: Frequency-dependent  $P$ -phase amplitude ratios  $(PREM+plume)/PREM$  as a function of offset from the great circle through plume and epicenter. The subfigures are for different distances behind the plume center, as marked in Fig. 3.36d. A plume model with  $r=100$  km and a Gaussian perturbation function is used. For discussion see text.

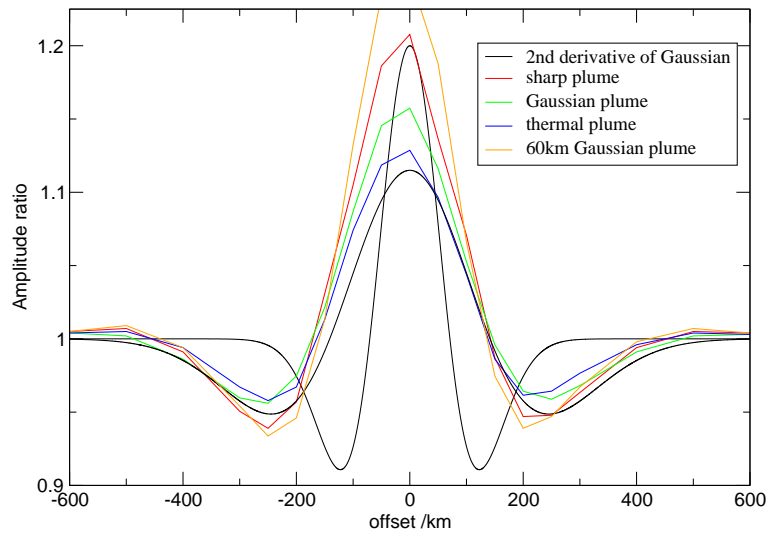


Figure 3.38:  $P$ -phase amplitude ratios of  $(PREM+plume)/PREM$  for three plume models with radii equivalent to 100 km and one with 60 km for 100 km behind the plume center (colored lines). The black lines are second derivatives of Gaussian (“Mexican hat” function) with 36.8%-width of 100 and 200 km (arbitrary amplitudes). For discussion see text.

meaning that the Gaussian perturbation function cannot be resolved. The other perturbation functions lead also to a curve which is the one of minimum resolution, including the one for the 60 km-radius plume – demonstrating that the smaller variations can not be resolved. For the sharp perturbation plume this means significant low-pass-filtering, however, the high amplitudes of the derivative of the sharp boxcar function, map into higher amplitudes of the amplitude ratios, as compared to the other, smoother functions. In order to constrain the minimum diameter that can be resolved for a Gaussian perturbation function, a Mexican hat curve is fitted to the amplitude ratio curves of the three models (Fig. 3.38 broad black curve). Its corresponding radius is 200 km, which we conclude is the smallest Gaussian perturbation function that can be resolved from 20 s data. For the 100 s data an equivalent procedure was carried out and revealed a radius of about 250–350 km.

The sensitivity kernels for amplitudes and travel times have the same shapes and widths and mainly differ in the fact that the amplitude kernels miss the “doughnut”-hole in the middle. This explains why the delay study (delay maps and great-circle delays) does not show any signature of the difference in perturbation function in the direction perpendicular to the great circle either.

In conclusion, the shape of the perturbation function is not resolvable or does not play any role if one uses long-period data ( $\geq 10$  s) keeping in mind that actual plume perturbations diameters are probably even less than 200 km. In other words, for constraining the perturbation function to separate the plume conduit from its halo, the use of high-frequency data is imperative. From our data we can not say if this is possible at all.

### 3.4 Discussion and conclusions

Full 3D waveform modeling through a variety of seismic plume models has been carried out in the long-period range of seismic frequencies in order to examine the wavefield effects of mantle plumes and their dependence on plume parameters. We did not observe significant waveform effects caused by plumes; the seismograms from the background reference model and the plume models among each other differ mainly in travel-time (delay) and amplitude. However, note that attenuation and anisotropy both of which are expected to cause waveform effects and to play an important role for plumes were not taken into account.

Routines have been developed for extracting and analyzing travel-time delay and amplitude effects. Delays measured with a  $600 \times 600$  km array consisting of 380 virtual stations are plotted in a map view to show their spatial distribution.

The delays are clearly affected by 3D wavefield (finite-frequency) effects such as wavefront healing and associated rapid decrease of delay values behind the plume. Further deviation from ray-theory is manifested in the observation of arrivals around the plume that come earlier as compared to the unperturbed background model. This somewhat counter-intuitive phenomenon is a wave effect and results from destructive interference occurring in the second Fresnel zone. Generally, the time shifts of these early arrivals are very small, but for some geometries and steeply incident phases they can reach up to 0.75 seconds and might thus be observable in real data. However, regional tomography studies often use only delays measured relative between the stations. This technique can not retrieve negative delays but might map them into positive delays, thus enhancing the latter. This issue has never been addressed before. It could mean that the underestimation of plume perturbation expected from ray-theoretical methods is not as high, since the negative values partly compensate the delay

reduction of the healing effect. The way how this affects or distorts the spatial distribution and magnitude of the resolved plume model is worth being investigated in a future synthetic tomographic study.

The perturbation function, i.e., the spatial distribution of the velocity and density anomaly, has little influence on the data in our frequency band. The smooth onset of the Gaussian function destroys the negative delays in front of the plume due to mixing of the effects of the first and the second Fresnel zone, whereas the sharp boundary of the boxcar function leads to a separated spatial concentration of the travel-time perturbations resulting from the first and second Fresnel zones towards the plume.

The delay scales with the magnitude of the plume velocity perturbation unless the perturbation is so high that it affects the travel path of the wave and thus possibly the shape of the kernel. The incidence angle of a phase is a property that depends on epicentral distance (especially for direct phases) – very steep incidences occur only for phases that have interacted with the core, again distorting the wave’s sensitivity kernel in a complex and not intuitive way. The origin depth of the plume is a parameter that maps in delay patterns only at long distances from the plume. There (the exact location depending on the source depth and the incidence angle), arrivals are recorded from waves that run beneath the plume and carry no delay. In the region around the plume, where waves sample the uppermost part of the plume no differences are observable. Even if this observation is conform with ray theory the “delay shadow” extends further than ray-theoretically predicted. This is a consequence of the extended sensitivity of a wave rather than being confined to a line as for rays. The diameter of the anomaly directly scales to the size of the area at the surface where delays are observable. Apart from this trivial effect, understandable also from a ray-theoretical point of view, the ratio of wavelength to width of the anomaly changes and thus the importance of finite-frequency effects. If plumes of different diameters but the same integral perturbation are considered, they differ in their delays wherever the wave did not travel the entire perturbed zone.

Low-velocity anomalies have an additional effect on amplitudes – they act as lenses, focussing energy. This effect has been observed in our study as well. The influence of the spatial distribution of the strength of the anomaly, however can not be resolved with the frequencies used for this study.

So what are the implications of these findings for future plume studies? Concerning the experimental configuration, a station spacing of 50–100 km as used for most plume experiments is sufficient. However, in the direct proximity of the plume (say, within two plume radii), where the gradients in delay and amplitude is highest, a higher density is recommended in order not to miss the maxima of the delay. Around the maximum, the variations in the delay pattern at least for simple plume models is smooth. For resolving the crucial question about the origin depth it is necessary to extent the aperture of the array to about 600 km or more from the expected plume axis. At such high distances wavefront healing eliminates already a large portion of the delay, therefore, phases which cause strong delays and whose incidence angles are steep such that they sample a large portion of the plume have to be used.

For epicentral distances around  $90^\circ$  and the frequency band from 0.01-0.05 Hz (periods from 20–100 s) the SKS-phase fullfills these requirements, while for an epicentral distance of  $45^\circ$  the shallow sS-phase is suited. For other epicentral distances and frequencies it is helpful to calculate the actual sensitivity kernels for a variety of phases in order to select the appropriate phase for resolving a specific plume parameter of interest. We have shown that ray-theoretical considerations, especially those based on ray-paths, can be totally misleading for the mid- to

long-period range.

Therefore, the extra-effort to compute the sensitivity kernels is indispensable. With the technique by NISSEN-MEYER *et al.* [2005] for spherically symmetric models this is possible with a moderate computational effort that is much lower than what is necessary for modeling the entire wavefield in 3D as done in this work. However, for strong plumes it might be necessary to include the plume in the model for the sensitivity kernels since there were indications that they affect the kernels significantly. This would require a costly full 3D calculation of the kernel.

It was also observed that delays calculated from band-limited seismograms can be higher with respect to delays derived by broadband-seismograms. This wavefield effect resulting from destructive interference of waves with different frequencies can help identifying delays and the frequency dependency can put further constraints on the plume size.

“Plume waves”, i.e., waves trapped in the plume conduit as suggested by JULIAN AND FOULGER [2003] could not be observed in the frequency range modeled. One reason could be that they are too weak in amplitude and are overprinted by the teleseismic wavefield where one phase comes after the other in a fast sequence. The same obviously happens to the weak reflections off the plume, that were not observed either. In order to study the question as to whether plume waves exist at all or not, it would be helpful to use a homogeneous Earth model where only few phases exist which allows for a detection of weak signals such as reflections and possibly plume waves. However, we decided not to carry out such a study since it would have little relevance for real data studies. Moreover, due to the expected high attenuation in the plume conduits it is even less likely that plume-trapped waves are observable in the real data. This could be the explanation why they have never been observed, which would in turn undermine the argument against plumes that such waves have never been observed.

The method for obtaining delay values applied in this chapter consisted of a comparison of PREM travel-times with those from modeling of a plume-perturbed PREM model. In the real world, however, these optimal conditions are not met, i.e., a (3D) model of the region without the plume that could serve as “ground truth” solution for comparison is not available. PREM or other standard Earth models are often not very helpful for this purpose, since they do not include 3D structure around the plume. Especially lateral variations in the crust, often due to the plume/hotspot activity itself, can affect travel times significantly, and have to be taken into account. This is mostly done using a crustal model for correction of the travel times. However, such models are not perfect. Uncertainties in the model then map into the travel-time delays that are assumed to be caused by the plume. Moreover, the presence of noise in real data often makes it difficult to measure exact travel times, especially when picking arrivals from seismograms by hand. Therefore, it is useful to discuss the results of this chapter also in the light of the uncertainties and the detection threshold of real Earth conditions. If we define 0.5s as the detection threshold for delays we get an idea of the region in which plume delays can realistically be detected. The farthest points at which delays still exceed 0.5s are 50, 325, and 3500 km from the plume center for the sharp  $r=60$ , 100, and 300 km plumes, respectively. There is almost no dependency of this distance on the plume perturbation function. The sharp models with the two different origin depth differ: the CMB-plume delay exceeds the one of the 660 km-plume by about 100 km. For plume experiments this means that it is very difficult to capture the delay of weak and/or small plumes.



## Chapter 4

# Application to Iceland

Following the general study, in this chapter, the modeling results of the previous chapter will be applied to Iceland. After a review of the current state of research which brings up relevant issues concerning the Icelandic plume we take a look at the real data of the modeled Peru earthquake. The goal is not to compare the available real data to the synthetic data, although an example will be shown in order to demonstrate that such an attempt is not very promising since the global model can not take into account the crustal structure.

We rather want to take advantage of the possibility to study questions raised for the Iceland plume with results not being biased or complicated by the complex Icelandic crust.

### 4.1 Iceland – the best studied plume on Earth

From geoscientific point of view, Iceland is one of the most interesting (hot) spots on Earth. A variety of geologic, tectonic, seismic, and volcanologic features are concentrated on an island the size of Southern Germany (States of Bavaria and Baden-Württemberg). Iceland is the world's largest sub-aerially exposed part of the mid-ocean ridge system. Moreover, it is a hotspot that is probably underlain by a plume, making it an example for plume-ridge interaction. As a result, major tectonic features can be found on Iceland, e.g., a spreading ridge, transform faults, and a propagating rift (Fig. 4.1). High seismicity, partly in swarm activity, and the occurrence of strong earthquakes as well as several active volcanoes (partly subglacial) make Iceland also interesting from a natural hazard point of view. The interaction of volcanic and seismic activity can be studied here as well.

There is a variety of reasons why we decided to use the Iceland hot spot as a study case for this thesis. First, this thesis is embedded in the German Iceland research program (DFG-Island-Bündel), second it is the best studied hotspot in the world. Iceland, especially in recent years, has been the target of numerous studies and experiments (e.g., ICEMELT, HOTSPOT). The HOTSPOT data are accessible e.g., using the FARM web interface of IRIS. Moreover, a permanent seismic network has been in operation on Iceland since 1989 and delivers together with the GSN station BORG data through FARM for comparison with modeling results.

Compared to other hotspots, Iceland has the advantage that the island itself is comparable or larger in size to the estimated plume perturbation diameter (100–600 km, most likely 120–200 km, compared to  $\approx 350$ –500 km of diameter of the island) so that a land based seismometer configuration can provide a good ray coverage of the upper part of the plume. However, because of the limited array aperture, resolution is limited to the upper mantle. Therefore,

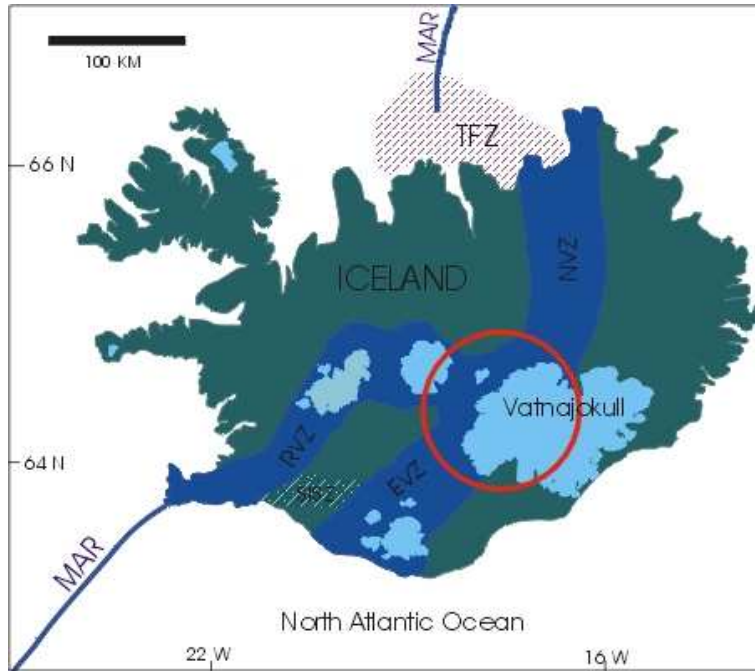


Figure 4.1: Iceland and its surrounding with main geotectonic features. The Mid-Atlantic Ridge (MAR) consists of the Reykjanes ridge to the south and the Kolbeinsey ridge to the North. Between them the plate boundary in Iceland is displaced several 100 km to the East by a set of transform faults or fracture zones, the Tjörnes Fracture Zone (TFZ) in the N, and in the S by the Reykjanes Transform Fault and S Iceland Seismic Zone (SISZ). Several areas of intensive volcanism were created through geologic times: EVZ: Eastern volcanic zone, RVZ: Ridge volcanic Zone, NVZ: Northern Volcanic Zone. The red circle indicates roughly the current plume position beneath Iceland.

deployment of Ocean bottom seismometers (OBS) is desirable to extend the array.

Moreover, the location of Iceland with respect to the global seismicity is advantageous, as compared to Hawaii, leading to a good resolution of the mantle beneath Iceland (e.g., MONTELLI *et al.* [2004b], suppl. online mat.). Furthermore, there seems to be some agreement in the seismic community about Iceland. Even plume opponents agree that there is a cylindrical slow anomaly at least in the upper mantle. The finite-frequency tomography results for P waves by MONTELLI *et al.* [2004b] confirm the confinement of the strong anomaly to the upper mantle, while in the S-wave tomography the same authors see a plume in the lower mantle whose radius varies strongly with depth.

However, questions such as the magnitude of the anomaly, its horizontal width, its depth extent and whether it is produced by a (whole mantle) plume or not are open, even if the latest finite-frequency tomographic studies MONTELLI *et al.* [2004b]; HUNG *et al.* [2004] seem to point a direction. The presence of frequency-dependent wavefield effects (a focus of this thesis) in the case of Iceland is out of question. Already ALLEN *et al.* [1999] derived the existence of diffraction and wavefront healing for Iceland, which is confirmed by finite-frequency tomography studies (HUNG *et al.* [2004]) that reveal a much higher anomaly (3.5% for  $v_P$ , 6.2% for  $v_S$ ) than previously assumed. Another advantageous feature of the Icelandic anomaly is its shape. The current tomography images all reveal a nearly vertical cylindrical

anomaly for the conduit that is easy to model with only a few parameters, as intended in our systematic parameter study.

In addition to constraints for geometric plume models, in a collaboration (framework of the German Iceland Research Group) with the geodynamics group in Frankfurt (Prof. H. Schmeling) dynamically consistent test models of the Iceland plume are to be expected in the future. These are derived by T. Ruedas and consist of 3D  $v_P$  and  $v_S$  models, with and without dehydration by water (RUEDAS [2004]).

In summary, all the plume related questions (and especially the finite frequency aspect) are debated for the Iceland hotspot, supported by a large number of studies and experiments, leading to constrained model parameters. This makes Iceland a favorable location for this study.

## 4.2 The Iceland hotspot – state of the art

### 4.2.1 General information, evolution, Geology

During the opening phase of the NE Atlantic 60–55 Ma ago, central Greenland was positioned above the assumed conduit of the Iceland plume (LAWVER AND MÜLLER [1994], Fig. 4.2). The Mid-Atlantic ridge (MAR) developed as a 3000 km long crack from south England to north Norway with strong volcanic lava eruptions. When the plume position coincided with the MAR about 20 Ma ago extensive volcanism created the island of Iceland.

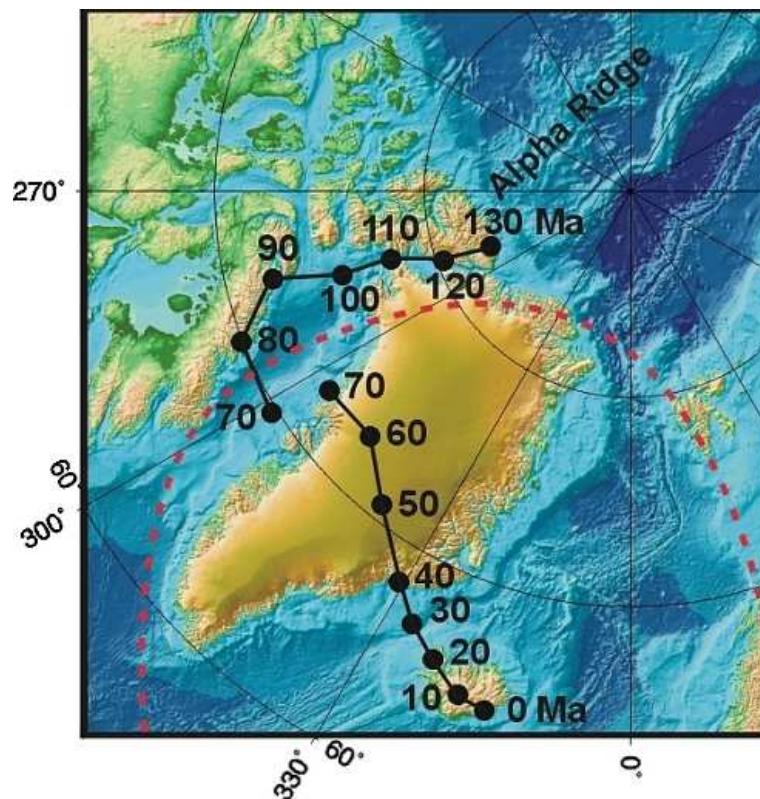


Figure 4.2: Position of the Iceland plume with time (from LAWVER AND MÜLLER [1994]).

Meanwhile, the Reykjanes-Kobeinsey plate boundary passed over the plume stem about 20 Ma ago and has since drifted to a position 150–200 km northwest of the plume axis under Vatnajökull. The Icelandic rift segments of 300–400 km length have jumped repeatedly south-eastwards to maintain their position near the plume (LAWVER AND MÜLLER [1994]). These rift jumps at about 24, 15, 7 and 3 Ma before present time occur by rift propagation within older crust. Rift jumps are only possible for strong plumes (i.e., those with high buoyancy fluxes). For example, this did not happen for the Azores, Galapos, Tristan, Juan de Fuca and Bowie plumes since they are too weak (CONDIE [2001])

The Iceland hotspot track is the Greenland-Faroe Ridge. Currently the plume stem center is under the Vatnajökull glacier, about 200 km southeast of the plate boundary defined by the Reykjanes and Kolbeinsey Ridges.

#### 4.2.2 Seismological and geophysical studies, plume parameters

This section gives an overview about the evolution of knowledge about the Icelandic anomaly and reviews the most important studies for this work and their results. The focus of this review is on the geometry of the anomaly, its dimensions, its depth extent and the magnitude of perturbations.

##### Evolution of knowledge

After the first tomography study of TRYGGVASON *et al.* [1983], a seismic network for the South Iceland Lowlands (“SIL project”) was installed. From 1993-1996, ICEMELT, the first tomography experiment with broadband stations was carried out, immediately followed by HOTSPOT, a competitive experiment using more stations. This triggered a fast series of papers. A rough overview about the dynamic research process with sometimes contradicting results is given in Table 1.

As can be seen from the compilation, most of the data from the study directly or indirectly depend on the two large experiments and on the SIL network. Therefore, a review of the experiments and tomographic studies for Iceland is given, leading to open questions or controversially discussed issues for Iceland, that will be addressed at the end of this chapter with the results of our modeling study. We start with a description of the seismic conditions and the available stations in Iceland in order to show the necessity of using the mid- to long-period range of seismic frequencies which are affected by finite-frequency effects.

##### Seismic Conditions

The general seismic conditions on Iceland, being an ocean island, are not very advantageous. Microseismic noise is high throughout Iceland, and the signal-to-noise ratio is significantly poorer during winter time due to storms (BJARNASON *et al.* [1996]). The noise has a strong peak at 4 s; apart from that noise levels are significant from 0.2-0.8 Hz (1.25 s–5 s, ALLEN *et al.* [1999]). These peaks dominate over all non-local signals in this frequency range. Generally, there is high seismic attenuation beneath Iceland and therefore little energy for teleseismic P waves above 1 Hz, and above 0.2 Hz (below 5 seconds) for S waves (BJARNASON *et al.* [1996]). Thus, the typical useful range for seismic studies is about 6–33 s (ALLEN *et al.* [1999]). As we have discussed in Chapter 3 (see Fig. 3.32), for small plumes, such as the 60 km-radius model suggested for Iceland, the ratio of plume width to wavelength drops below one, indicating the existence of significant finite-frequency effects. Two studies dealing with this issue

study	year	data	method/result
Tryggvasson et al.	1983		first tomography study
Zhang & Tanimoto	1993		low-resolution surface wave tomography
Bjarnason et al.	1993		tomographic image of plate boundary SW og Iceland
Shen et al.	1996		receiver function study: hot TZ beneath Iceland
Wolfe et al.	1997	I	ICEMELT-tomography experiment
Shen et al.	1998		receiver-function approach: TZ thinning
Helmberger et al.	1998		plume comes from ULV patch at CMB
Ritsema et al.	1999	G	plume only resolvable in upper mantle
Allen et al.	1999		thin, strong, ( $dv_S=12\%$ !) hot plume
Bijward & Spakman	1999	G	whole mantle plume
Breddam et al.	2000		mapping the Iceland plume conduit with He isotopes
Pritchard et al.	2000	O	plume in mid mantle from array data
Keller et al.	2000		questioning of ICEMELT results
Foulger et al.	2000	H	anomaly up to 400 km, but no deeper than 700 km
Foulger et al.	2001	H	plume confined to upper mantle
Zhao	2001	G	whole mantle plume from CMB
Wolfe et al.	2002	I	justification of ICEMELT results (response to Keller)
Allen et al.	2002	H	first image of plume head
Allen et al.	2002	H	model of the crust
Bjarnason et al.	2002	I	ICEMELT shear-wave splitting study
Shen et al.	2002	S,I	tilted mantle plume through transition zone
Foulger	2002		no plume at all under Iceland
Montelli et al.	2003	G	global FF tomography: upper mantle plume
Stein & Stein	2003	O	evidence against a hotspot from heat flow data
Shen et al.	2003	S,I,H	mid-mantle-discontinuity: mid-mantle origin?
Hung et al	2004	S,I,H	regional FF-tomography
Allen & Tromp	2005	Si,H,I	“Squeezing tests” to constrain parameter range

*Table 4.1: Evolution of statements concerning the origin of the Icelandic anomaly triggered by the major tomographic experiments. The third column gives the data source (S=SIL network, I=ICEMELT, H= HOSTPOT, G=global dataset, O=other). Abbreviations used: FF: finite-frequency, ULV: ultra low-velocity, TZ: transition zone.*

will be presented later in this chapter.

The direction and distance from which earthquakes come decide about the position of the travel-time and amplitude effects of the plume, and, for ocean islands, about whether they can be recorded with land-based stations or not. Iceland's position with respect to global seismicity is illustrated in figure 4.3. As can be seen, it is quite favorable, leading to a good azimuthal

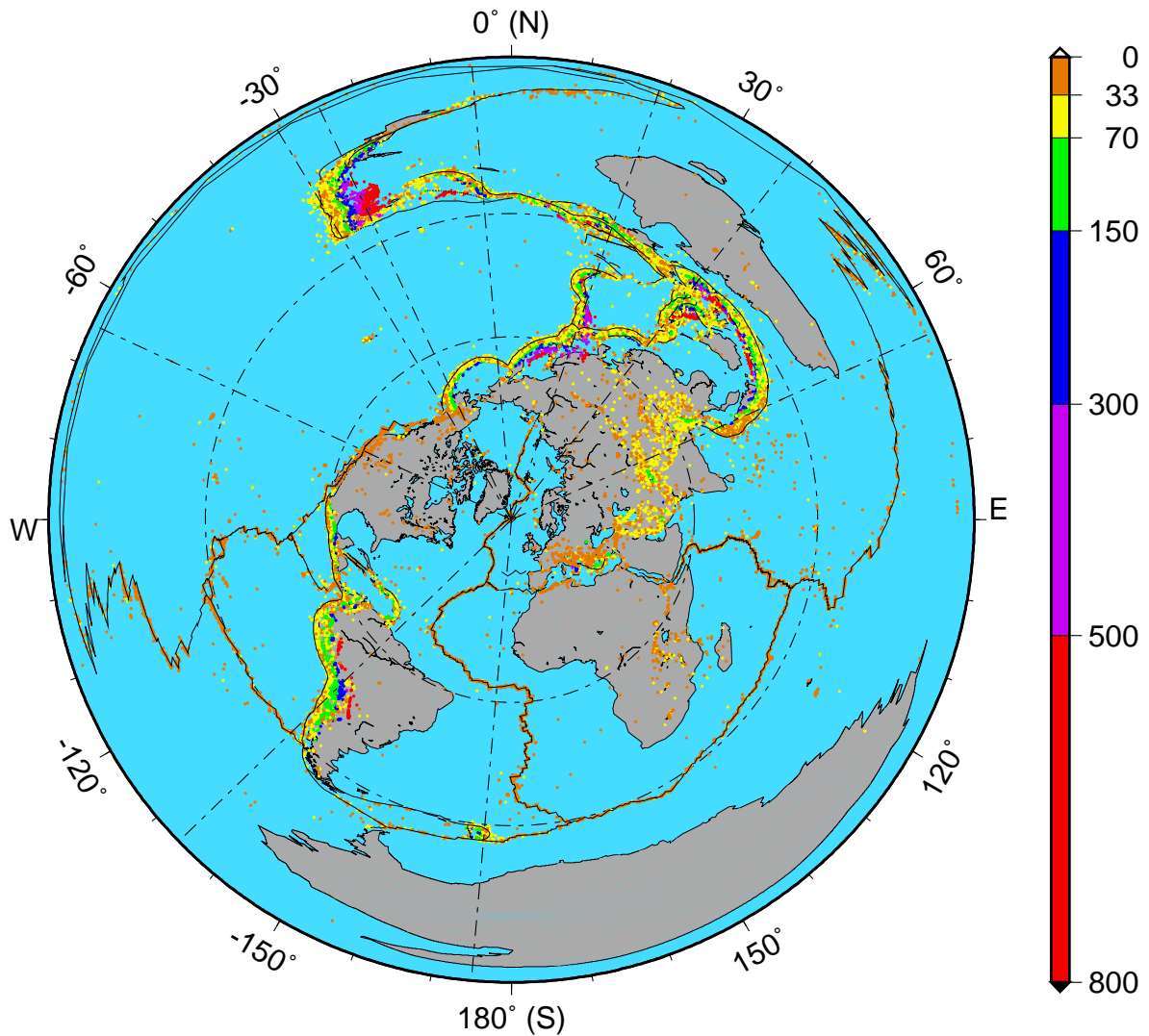


*Figure 4.3: An azimuthal equidistant map of global seismicity centered on Iceland. Epicenters of events in the PDE catalog with magnitude larger than 5 are plotted with a depth-dependent color coding as given in the scalebar on the right hand side. Plate boundaries are plotted as thin lines on top. Moreover, the back-azimuths and epicentral distances with the most frequent occurrences are indicated by the dash-dotted lines and circles, respectively. For discussion see text.*

coverage of teleseismic body waves from earthquakes stronger than  $m_B 5.7$  (BJARNASON *et al.* [1996]). In detail, several clusters in terms of back-azimuth and epicentral distance to Iceland can be clearly identified, the Tonga region being the most prominent one, covering a broad

range in azimuth, distance and as well in source depth. For a more detailed analysis the histograms for the frequency distribution with respect to the distance and the backazimuth to the Iceland plume are given in Figures 4.4 and 4.5, respectively.

The **distribution of epicentral distances** ( $\Delta$ ) of earthquakes that can be recorded on Iceland shows two distinct peaks. The first one around  $\Delta=71^\circ$  comes from the earthquake belt at the eastern end of the subducting Cocos Plate and from the Japan Trench. The second broader peak around  $\Delta=120^\circ$  is due to earthquakes at the Java Trench, the Salomon earthquake region, the Chile Ridge, and the south west Indian Ocean Ridge. Apart from these peaks there is generally one earthquake per year on average in the range  $53\text{-}144^\circ$  distance and a general trend to higher seismicity at larger distances.

The directions of the earthquakes as seen from Iceland (**backazimuth**,  $\Theta$ ) cluster around the back-azimuths of the zones of major seismic activity (e.g., Tonga, Japan, Chile/Peru), the only sparsely covered direction is the one to the South-East.

With these directions in mind the travel-time delay patterns in the last part of this chapter that are obtained using the backazimuth of the Peru event ( $\Theta=126^\circ$  West) can be notionally rotated to obtain the patterns that would be expected for the earthquakes likely recorded on Iceland. This is done later in this chapter for four directions. In general, compared to other plumes, Iceland has a fairly good azimuthal coverage for teleseismic distances and quite a few earthquakes can be expected for a typical experiment lifetime of 1-2 years.

It is obvious that for all other plumes of interest the global seismicity pattern remains the same but is seen from a different position. Thus, clustering in distance and backazimuth will occur at different places and distances. Nevertheless, directions of high likelihood (once per three month or more) for wave incidence will exist and can serve as a guideline for station position planning and array design. We have seen in Chapter 3 that the main effects of a plume on travel time and amplitude occur close to or behind the plume. Thus, the station density can be increased behind the plume as seen from directions of high seismicity.

## Permanent stations

In 1988, the SIL (South-Iceland-Lowland) project (STEFÁNSSON *et al.* [1993]) was set up for earthquake prediction studies and research of crustal dynamics at the South-Iceland Seismic zone (SISZ). A seismometer network was installed and extended in 1994 to the north-eastern part of Iceland as well and has gradually been covering larger parts of Iceland since 1996 (GUDMUNDSSON *et al.* [2003]). It concentrates on high-risk or high-activity areas of Iceland, i.e., the North and the South-West. This, so-called “SIL network”, has been used for almost all studies, partly together with stations of temporary experiments.

Another data source that is used for almost all seismic studies on Iceland is the permanent GSN station Borganes (station code BORG).

Apart from the stations on Iceland itself, there are other stations in the region, that might capture effects of the plume. The University of Bergen (Norway) is operating stations on the Jan Mayen Island (JNW, JNE), as well as NORSAR (JMIC, JMIC). The British Geological Survey (BGS) has stations on the Faroe Islands (FHV, FSD, FSV, FTO and FVA) and on the Shetland Islands (SANU, SEJ). On Greenland the KMG (Royal Danish Institute) is running several stations, moreover there is a station of the Canadian Seismic Network. If we compare the location of these stations with the map of the station array used in Chapter 3 (Fig. 3.7), we see that some of these stations are lying within our network aperture, and others are only

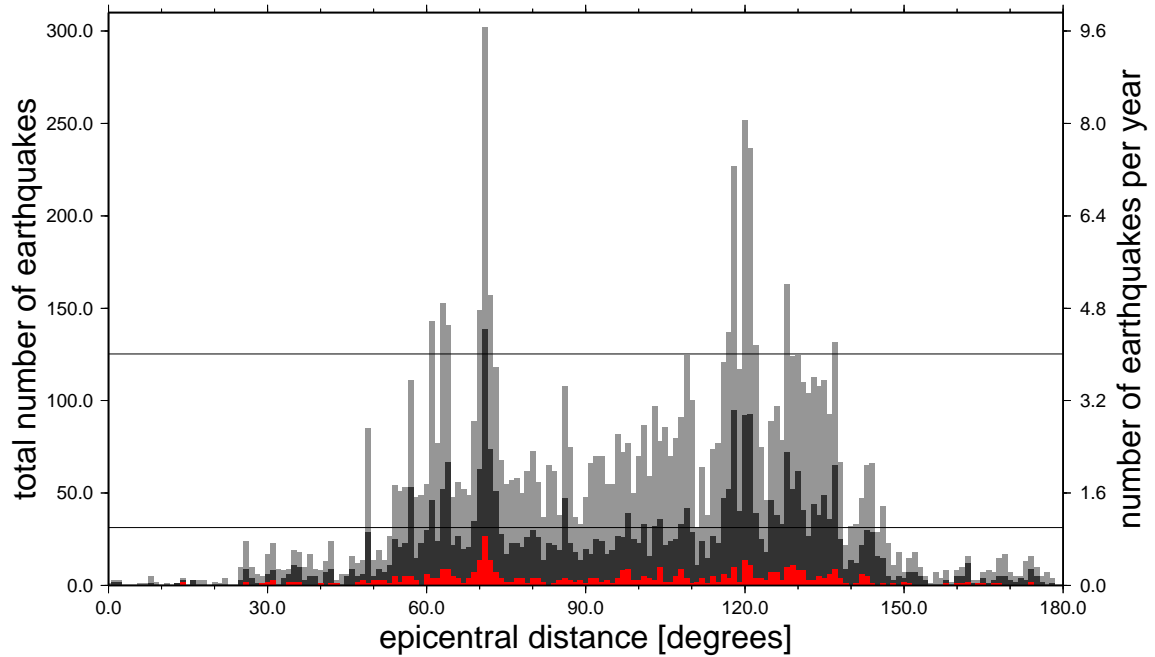


Figure 4.4: Histogram of number of earthquakes per epicentral distance (bins of one degree) to the Iceland plume. Events of magnitude of 5.7 and larger of the PDE catalog from 1973-today are plotted (grey). Events larger than magnitude 6 are plotted in dark grey, and events of magnitude 7 and larger in red. The absolute numbers of events are given on the left side, the average number of events per year on the right side. Horizontal lines indicate the level equivalent to one event per three months (top) and one event per year (bottom). For discussion see text.

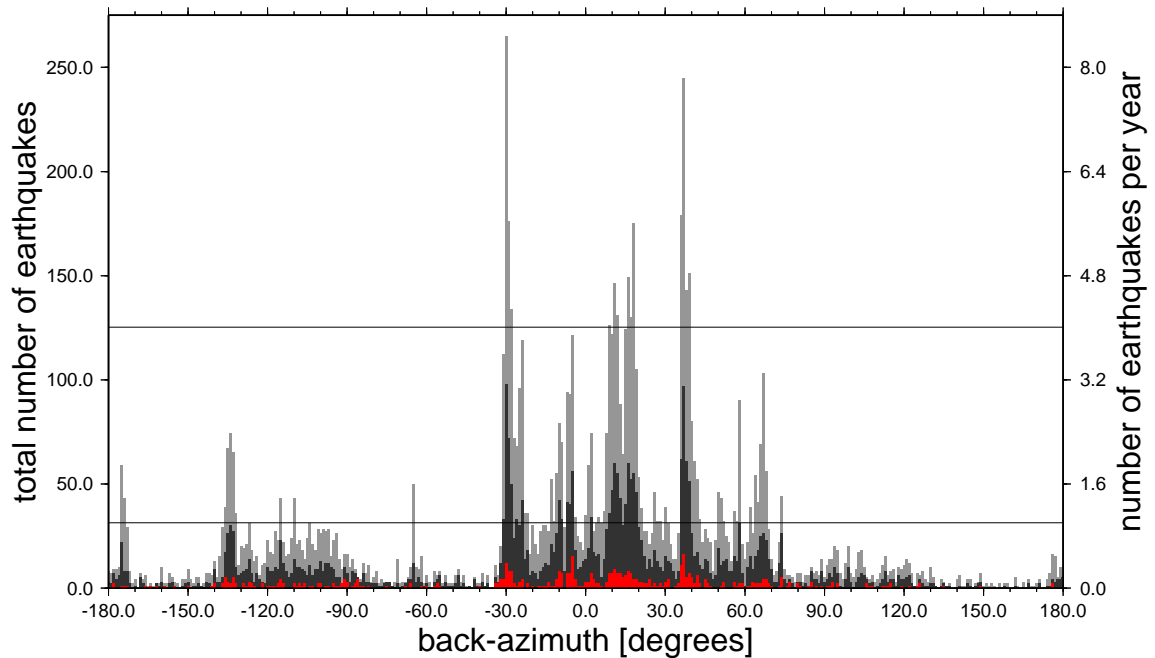


Figure 4.5: Histogram of number of earthquakes per back-azimuth (bins of one degree) from the Iceland plume. For explanation see Figure 4.4, for discussion see text.



200 km or less away from it. This shows that for the case of Iceland, the delays at the edges of our array can not solely be captured by Ocean bottom seismometers, but – depending on the backazimuth of the earthquake – also on nearby permanent land stations.

## Regional tomography studies

The first tomography study on Iceland was carried out by TRYGGVASON *et al.* [1983]. They used P-wave travel-time data from 61 events that were recorded by the SIL network that consisted of 39 stations at that time. They subdivide the regions beneath Iceland in four depth levels. From the surface down to 75 km they find a low-velocity zone that nearly coincides with the Iceland rift zone showing high values for the Krafla volcanic area. From 75-175 km the low-velocity zone is shifted southeastward with the strongest anomalies in the Surtsey-Hekla area. In the depth range from 175-275 km, low velocities are found south of the Kolbeinsey Ridge and the central part, whereas the Iceland rift zone still has a negative perturbation. In the lowest level down to a depth of 375 km the P wave velocity has a pronounced low of up to 4% beneath central Iceland.

### The ICEMELT experiment (1993-1996)

ICEMELT was a regional broadband experiment aiming at the determination of the 3D velocity structure of the upper mantle by classical ray tomography using relative travel times from body waves of teleseismic events (WOLFE *et al.* [1997]). For this purpose, a network was installed during 1993-95 which was in operation until fall 1996. It consisted of 15 portable broadband seismometers, with an interstation spacing of about 100 km (BJARNASON *et al.* [1996]). The GSN station BORG was used to complement the ICEMELT network.

WOLFE *et al.* [1996] present results from the tomography study of the ICEMELT project. They use a travel-time inversion scheme along with relative arrival times of 601 P-phases from 86 earthquakes (including 12 with core phases), and 560 S-phases from 78 events (13 core phases). The dominant wavelengths were about 10 km for P, and 50–75 km for S. The travel-time differences are measured relative between the stations, and the IASP91 model is used to correct for differences in epicentral distance. Due to the minimal station spacing of about 75 km, there are no crossing ray paths and thus no information above  $\sim 100$  km. From this depth, results show a low-velocity anomaly down to at least 400 km (Fig. 4.6). At 300 km depth the anomaly is approximately circular in shape and is 150–200 km in radius (using the  $1/e$  radius-definition). Shallower, at 125 km depth the anomaly coincides with the zone of highest  $^3\text{He}/^4\text{He}$ -ratio concentrations within the neovolcanic zone, is vertically continuous and shows no significant lateral shifts. The amplitudes of the velocity perturbations are 2%, and 4%, for P and S, respectively, and are derived by separate inversions. These values translate into a temperature perturbation of  $\Delta T=300^\circ$  for the P-, and  $600^\circ$  for the S model. However, for 100–400 km depth, resolution tests suggest that the results are likely to underestimate the perturbation. The authors think that this is due to the ray-tomography method, that neglects healing. Moreover, they speculate that seismic anisotropy could play a role. The minimum values for shear wave splitting is around of 1–2 seconds, that could explain the differences between the P- and the S-model. The reason for anisotropy could be an assumed narrow zone of upwelling flow (plume) that would tend to induce vertical alignment of the crystallographic a-axis of mantle olivine crystals. This would lead to a vertically oriented fast

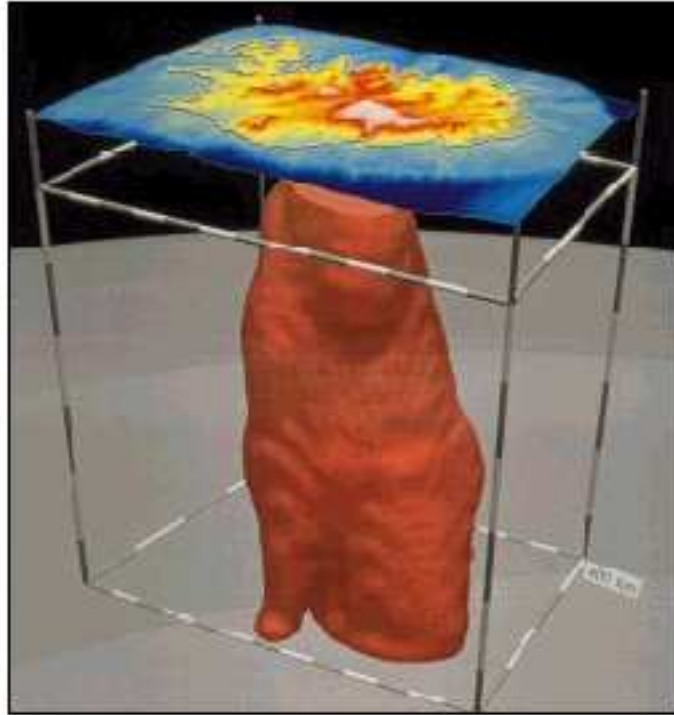


Figure 4.6: Tomographic image by WOLFE *et al.* [1996].

direction of anisotropy for P- but not for S-waves. Apart from anisotropy, the authors suggest other reasons for the differences between the P- and the S-wave model, e.g., the presence of melt, and anelasticity.

In 2000, KELLER *et al.* (plume opponents) questioned these results, arguing that the conic shaped structure results from a parallax effect of the cone of incoming rays. The lack of crossing rays, that have almost vertical incidence, leads to smearing and since the cone that is formed by the used rays is similar in shape with a plume like anomaly one tends to interpret the results in this way.

In response to the paper by KELLER *et al.*, WOLFE *et al.* [2002] show results of additional resolution tests to demonstrate that the ICEMELT dataset and the tomography method they used can distinguish between a wide and shallow anomaly, a narrow and deep anomaly, and a narrow and shallow anomaly. With these results, the authors defend their earlier results of a plume-like upper mantle anomaly against a shallow asthenospheric (“Andersonian”) anomaly that is suggested by KELLER *et al.*.

For completeness, it is mentioned that ALLEN *et al.* [1999], measured a Gaussian radius of 175 km with  $dV_S=4.2\%$  at a depth of 300 km for the data of WOLFE *et al.* In their Iceland study ALLEN *et al.* [1999] were using a method that takes into account finite-frequency effects and the healing effect they observed is as much as to 3 seconds, which explains WOLFE *et al.*'s comparably low-velocity perturbation. However, there is no difference in width between the model of WOLFE *et al.* and ALLEN, what the authors think might be due to tomographic smoothing effects. This is one of the key points in the recent discussions about the future of tomography – some tomographers claim that the improvements due to the finite-frequency technique are small against the effect of tomographic smoothing (see TRAMPERT AND SPET-

ZLER [2006] for surface-wave tomography). ALLEN's method is described in Section 4.4.3.

### The HOTSPOT experiment (1996–1998)

A subsequent project, called HOTSPOT, was carried out using three arrays in Iceland. The HOTSPOT array itself, the SIL network, and instruments operated by Raunvisindastofnun Haskolans (the University Science Institute, Iceland). The actual HOTSPOT network, an IRIS/PASSCAL array of mobile stations, was deployed between May 28 and July 31, 1996 and was in operation from June 1996 to August 1998. It consisted of 30 broadband instruments and another five broadband sensors that complemented existing short period SIL stations. One of the goals was the maximization of the aperture for extending the depth resolution of the experiment (see Fig. 4.11). This was done by coast to coast deployment including Grimsey island north of Iceland. The locations were chosen to be spaced evenly over the island while being near a connection to the power grid where possible. The final aperture of the network was 500 km in EW-, and 300 km in NS-direction (FOULGER *et al.* [2000]). The data quality of the HOTSPOT stations was very high and comparable to the borehole GSN station BORG (Allen *et al.*, see <http://www.geology.wisc.edu/~rallen/ICELAND/HOTvsBORG/>). Despite the partly difficult conditions of the large network the stations had an uptime rate of 86% (FOULGER *et al.* [2001]). The combined networks had a total of 62 stations evenly distributed throughout Iceland (compared to 380 in this study), with a station spacing of approximately 50 km.

FOULGER *et al.* [2000, 2001] used the data of the HOTSPOT experiment to improve the tomographic image of Iceland. During the runtime of the experiment the HOTSPOT network recorded seismograms of more than 120 teleseismic earthquakes. Foulger *et al.* used 3159 P arrivals from 160 phases from 113 well distributed earthquakes and 1338 S arrivals from 73 phases and 66 events recorded at 42 stations. Arrival times were hand picked for P, pP, PP, PcP, PKIKP, pPKIKP, S, S, SS and SKS phases from seismograms that were rotated to the great circle path, and band pass filtered from 0.5-2 Hz for P-, and 0.05-0.1 Hz for S-waves. The 2001 paper additionally included the phases sP, SP, Sdiff. The picking accuracy was given as  $\approx 0.05$  s for P and  $\approx 0.5$  s for S. These values are very interesting since they provide constraints on the relevance of the travel-time delays of the present study. For carrying out tomography they use the ACH method with IASP91 as reference model and NEIC final locations for the earthquakes. The peak magnitudes of mean-arrival time anomalies were 1 s for P, and 3 s for S, and thus similar to those of the modeling results in Chapter 3. They use a model parameterization with blocks of  $75 \times 75$  km horizontally (which is about the station separation) that are 50 km thick. They claim to have good and highly symmetric resolution down to 400 km. However, the model cannot extend deeper than the turning point of the shallowest incoming ray which leads to a very low resolution below 450 km and a strong tendency to smearing below that depth. Geometrically, the study volume of the experiment that the authors consider well conditioned is a truncated cone that broadens downwards. The results show that  $\delta v_P$  is strongest in the top layer (10–58 km) and reaches up to 2.7%. Beneath 58 km the largest  $\delta v_P$  is 2.1%. Anomalies in the S-wave speed are up to 4.9%, these high values are observed in the upper 300 km. The anomaly forms a coherent nearly vertical cylindrical low-wavespeed body underlying the north-eastern MVZ and centered easterly within the MVZ between the glaciers Vatnajökull and Hofsjökull. The diameter of the anomaly (defined as area where  $\delta v_P$  1%) is 200–250 km. The anomaly is truncated sharply at the TFZ. This is

verified by special resolution tests that show no tendency for any artificial termination of the TFZ. Another small anomaly is seen under the Western Fjords area. At a depth of about 250 km the morphology of the anomaly changes systematically. It begins to be elongated in north-south direction and underlies the spreading plate boundary on Iceland. The observed elongation runs counter any smearing direction and is thus considered a reliable feature. In the depth range resolved by the experiment the data do not image the base of anomaly.

Nevertheless, the authors conclude from these results that the anomaly originates at the transition zone, due to the tabular form of the imaged lower part of the anomaly that is interpreted as its root.

However, I remark, this tabular shape could also be due to the a bulge of the plume tail under the 660 and subsequent thinning of the tail, as described in chapter 1. This property could make a CMB origin plume seem to come from the 660-discontinuity. The authors do not exclude that the upper-mantle anomaly might be related to a lower-mantle upwelling. If so, they claim this would argue for layered convection. The positive  $\delta v_P/\delta v_S$  ratio of the anomaly suggests the presence of partial melt beneath the MVZ in a depth range of about  $\approx 100$ – $200$  km.

### **Regional finite-frequency tomography**

HUNG *et al.* [2004] took P- and S-wave data from both the HOTSPOT and the ICEMELT experiment together with the GSN station BORG to carry out a regional finite-frequency tomography study.

After applying a crustal correction to the data they use both ray tomography and finite-frequency tomography and compare the results. Both agree in showing a quasi-cylindrical zone of low P- and S-velocity anomaly centered in Iceland with a diameter of about 250–300 km that extends from 150 km to at least 400 km depth. They differ significantly in the magnitudes of the resolved anomaly and in the resolution power, especially in the deeper mantle.

The maximum velocity perturbations of the ray-theory inversion are  $-1.5\%$  and  $-3.5\%$  for P and S, respectively. Due to the used damping and regularization schemes used in ray methods they give an upper limit of  $-2\%$  for P, and  $-4\%$  for S, translating into a temperature anomaly of  $200$ – $300^\circ$ . In contrast, the finite-frequency tomography method gives  $-3.5\%$  and  $-6.2\%$  for P and S, respectively. These are the values used as default perturbations for the present study, as motivated in Chapter 1. They correspond to an excess temperature of the anomaly of  $350$ – $500^\circ\text{C}$ , assuming a purely thermal effect as a reason for the anomaly.

### **Ambiguity of tomography results**

As already mentioned in Chapter 1, seismic tomography problems are generally ill-posed and require regularization (smoothing and damping) in order to choose one of the possible solutions (TRAMPERT [1998]). Once a regularization is chosen, the tomographic results seem unique, at least when results of the study are presented. Nevertheless, tomographic studies remain ambiguous – several models and not only the minimum-norm solution that is usually shown, might be able to explain a given dataset. This problem is addressed by ALLEN AND TROMP [2005] who explore the range of possible models for the Iceland plume concerning the parameters origin depth and horizontal extent of the anomaly.

They use data of former tomographic studies and carry out synthetic resolution tests to find out if the velocity structure recovered by former studies can be resolved with a given dataset. Moreover, they use squeezing tests to check if a hypothetical smaller structure is

compatible with the dataset as well. Using this method the authors find that the low-velocity anomaly has to reach down to at least 375 km depth.

For constraining the bounds on the horizontal extent of the anomaly ALLEN AND TROMP carry out a study partly very similar to the present work. By comparison of a travel-time delay shadow of a 100 km-radius plume obtained by ray theory with one of a 50 km-radius plume derived with finite-frequency simulations they can show that a 100 km-radius plume imaged by ray-theory inversion could be the product of an actual 50 km-radius plume model. However, this only applies to the width of the travel-time shadow, but not the magnitude of the delays. These would have to be much larger for a real 50 km-radius plume and such large perturbations (on the order of 10% and 20% for P and S, respectively) are unrealistic without large amounts of melt. ALLEN AND TROMP thus give 50 km as a lower, but not realistic bound for the radius. Since the 100 km-radius plume is not compatible with the low-frequency shear wave delays this radius value is the upper bound.

In summary, this very careful and comprehensive work on the Iceland anomaly helps to test tomographic models against what *can* be constrained by seismic data. The termination of the Icelandic anomaly with depth, as claimed by FOULGER *et al.* [2000], in any case is certainly *not* resolvable with regional seismic tomography data.

In order to answer the question about the origin of the Icelandic anomaly, global tomographic studies are required, which are reviewed in the following.

### Full-mantle global tomography Iceland

BIJWAARD AND SPAKMAN [1999], using the global mantle tomography model by BIJWAARD *et al.* [1998], took a closer look on Iceland and claim to have found the first image of a whole mantle plume. Their figure shows an optically continuous feature of reduced (with respect to AK135) wave speeds throughout the mantle, that is deflected to the east in the mid-mantle. However, one has to note that their colorscale saturates at very low anomaly values of  $\pm 0.5\%$ , which makes any value higher than that to appear strong and thus makes the feature look continuous. The additional contour line they give in the figure 'for clarity' represents only 0.15% anomaly, a value that is for usual tomography studies considered to be insignificant 'noise'. Misleadingly, the reader tends to interpret this line as the boundary of the imaged plume. In this respect, it also remains unclear what radius definition is used when the authors give a rather high radius value. Moreover, the paper does not state explicitly if the model is for P- or for S-waves.

With a irregular-cell parameterization of laterally 65-200 km in the upper mantle, and 150-400 km in the lower mantle and vertically 35 km (lithosphere) to 200 km (lower mantle) they get only a resolution of 300-500 km laterally through the entire mantle and 120-200 km vertically.

In another global tomographic study RITSEMA *et al.* [1999] use the 3D, 20 degree shear-wave velocity model (S20RTS) by RITSEMA AND VAN HEIJST [2000]. This model was derived using the entire spectrum of seismic frequencies, incorporating phase velocities, body wave travel-times, and free-oscillation splitting measurements. Its perturbations are given with respect to PREM.

Concerning Iceland, the authors state that the 660 km phase transition marks the lower boundary of the low-velocity anomaly (defined as 2.5% difference to PREM). A connection

to the CMB by a narrow plume conduit is not modeled by S20RTS. The authors demonstrate several cross-sections of the model through Iceland using a linear colorscale with a range of  $\pm 1.4\%$ . The basic features of the model are similar to the later model of ZHAO, but since RITSEMA *et al.* do not saturate their color scale at a low level they probably give the most reliable image. They conclude that the anomaly beneath Iceland is confined to the upper mantle.

ZHAO [2001] developed a global P-velocity model for the mantle. The peculiarity of this method is that it takes into account the Moho, the 410- and 660 discontinuities, what leads to a considerable change in amplitude and pattern of the derived anomalies.

Moreover a grid approach is used (versus block parameterization or spherical harmonics), thus avoiding artificial velocity boundaries. Another feature is the 3D ray-tracing technique. Zhao applies this method to the ISC-dataset (1964-1998) containing 7128 events with around one million arrival times. With this dataset, resolution test show that a 300 km diameter plume beneath Iceland could be resolved.

Due to use of the same double-saturated color scale with range  $\pm 0.5\%$  his results are similar to the ones of BIJWAARD AND SPAKMAN. In addition to their work ZHAO also shows a S-N profile. He also concludes that his model “shows that the Iceland plume extends down to the CMB”. Again, taking into account the results of RITSEMA *et al.* [1999], this is probably a false conclusion and is likely only an effect of the early saturation of the color-scale used. However, concerning the general features, both models (the S-wave model by RITSEMA *et al.*, and the P-wave model by ZHAO) agree.

Finally, MONTELLI *et al.* [2004b] carried out a global finite-frequency tomography study for P-wave speeds in the mantle. To test this new approach they focused on plumes, especially on their depth extent.

They used long-period P-wave data, re-analyzed the original seismograms and corrected previously undetected clock errors. By cross-correlation with a synthetic pulse they measured travel times of 66 210 P-waves and differential travel times of 20 147 PP-P and 2 382 pP-P waves, with a dominant period of 20 s. The standard deviations of the long-period times were assigned to three accuracy classes and range from 0.5 to 1.15 s. These travel times were inverted using three-dimensional finite-frequency sensitivity kernels.

This inversion is combined with 1 427 114 short-period P and 68 911 short-period pP travel times from the ISC bulletin using conventional ray tomography.

With this dataset they simultaneously inverted for the fractional perturbation in the compressional velocity,  $\delta v_P/v_P$ , and the perturbations in the earthquake hypocentral parameters (origin time, longitude, latitude, and depth).

In the resulting images (Fig. 4.7), there is a very strong upper-mantle anomaly beneath Iceland that almost disappears at 1000 km depth. The authors speculate that the weak lower-mantle anomaly of 0.3% is due to vertical leakage down and below this depth. They suspect that such leakage also appeared in the earlier global tomographic studies and could have led to BIJWAARD AND SPAKMAN [1999] suggesting a deep plume.

A possible explanation for a weak root of a strong upper mantle plume might be a large drop in the temperature dependence of  $v_P$  in the transition zone (as suggested by KARATO [1993]) that could make plumes a much weaker velocity anomaly in the lower mantle and therefore more difficult to image, leading to apparent source regions near 670 km. However, the fact that they observe numerous plumes extending to the deep mantle weakens this argument, at least as a phenomenon affecting the stronger upper-mantle plumes.

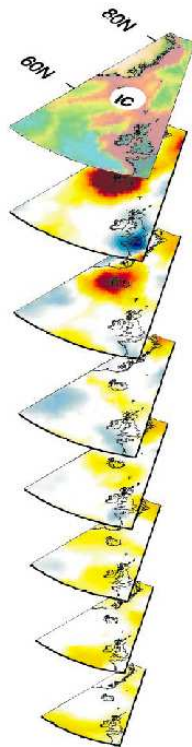


Figure 4.7: Horizontal slices through the finite-frequency tomography model of Iceland. Dark red colors represent a negative velocity perturbation of 1.5%. Taken from MONTELLI *et al.* [2004b].

Thus, they conclude that the upper mantle anomaly beneath Iceland is not generated by a large upwelling from the lower mantle and that a deep origin for an Iceland plume can be ruled out.

In summary, global tomography studies indicate that there is no CMB origin of the Iceland plume. The two papers claiming that there is one, suffer from methodological deficiencies, at least in the presentation (saturated color-scales) and interpretation of their results. The results of the conventional tomography study by RITSEMA *et al.* [1999] is affirmed by the finite-frequency tomography study by MONTELLI *et al.* [2004b] in that there is no downward continuation of the Icelandic anomaly below 1000 km.

To complement the statements of global seismology on the origin of the Iceland anomaly we review the contradicting observation of a **Ultra-Low-Velocity Zone beneath Iceland** presented by HELMBERGER *et al.* [1998]. They use the phase SKS along with the associated diffraction phases SPdKS and SKPdS for a study of the base of the mantle. These phases have an almost identical ray path in the upper and middle mantle, while they differ in two small segments at its base (being P-waves there). Through complex interaction of these phases they are highly sensitive to P- and S-velocity structure at their core-entry and core-exit points. Using these phases from South-American events the authors find stations in northern Scandinavia that record anomalous (with respect to PREM) waveform interferences that can not be

explained by complex source-time functions of the events. The corresponding SKS and SKKS are undisturbed and their core-entry and exit points, that mark the region sampled by the diffraction phases, lie to the east-south-east of Iceland. For one station in the North-Atlantic observes the same anomaly, sampling a small part beneath Greenland, west of Iceland. From these sparse observations the authors deduce the existence of an anomalous region beneath Iceland, that they explain with an Ultra-Low-Velocity-Zone. To constrain this ULVZ further they model wave propagation through 2D ULV-structures at the CMB using a WKB-type code and end up with a favored model that consists of a 250 km wide, 40 km high dome-shaped structure with velocity perturbations of 10, and 30% for P, and S-wave-speed, respectively. Through the local coincidence with the Iceland thermal anomaly and a more general global relationship between ULVZ and hotspots positions (recently confirmed by THORNE *et al.* [2004]) they suggest ULVZs as being the origins of hotspots.

The next section treats the different geophysical and partly geochemical anomalies, that may put further constraints on the nature and origin of the Icelandic anomaly.

### Gravity anomaly

A Bouguer gravity anomaly map is provided by DARBYSHIRE *et al.* [2000] using data from Orkustofnun Islands. The map shows a roughly elliptical zero-mgal isoline centered in central Iceland. Within this isoline values are decreasing monotonously towards a minimum which is in eastern central Iceland, the currently assumed center of the Iceland plume (RICHARD ALLEN, personal communication)

### Heat flow anomaly

To date, the only publication that focuses on anomalous heat flow on Iceland is the one by STEIN AND STEIN [2003]. They claim that there is no heat flow anomaly beneath Iceland. Remarkably, to date there has not been any further paper on that topic. This indicates little evidence for a heat flow anomaly.

### Crust

A lot of work has been done on the crustal structure, partly with large-scale dedicated experiments (e.g., RRISP, FIRE), also by workers of the University of Munich, e.g. ANGENHEISTER *et al.* [1980], GEBRANDE *et al.* [1980] or with receiver function techniques (mainly Du and coworkers, e.g. DU AND FOULGER [2001]).

Since the fine-scale crustal structure cannot be modeled with the global wavefield approach used in this thesis, and since a review of these studies would go beyond the scope of this chapter we restrict ourselves to a brief summary of main crustal features, giving constraints of the mantle plume. A good review of relevant crustal studies is given in DARBYSHIRE *et al.* [2000]. Since these (mainly wide-angle refraction) studies do not cover the entire island, they close the gaps in the coverage of Iceland using gravity modeling, with the seismic data and the Bouguer map of Iceland as constraints. This results in two maps, one for the base of the upper crust, and one for the Moho depth. The upper crustal thickness is on average  $\sim 5$  km, but varies in the range of  $\sim 2$ -11 km.

In the Moho-depth map (Fig. 4.9) the most prominent feature is the thickening of crust under eastern central Iceland with a maximum of  $\sim 40$  km under the Vatnajökull icecap that



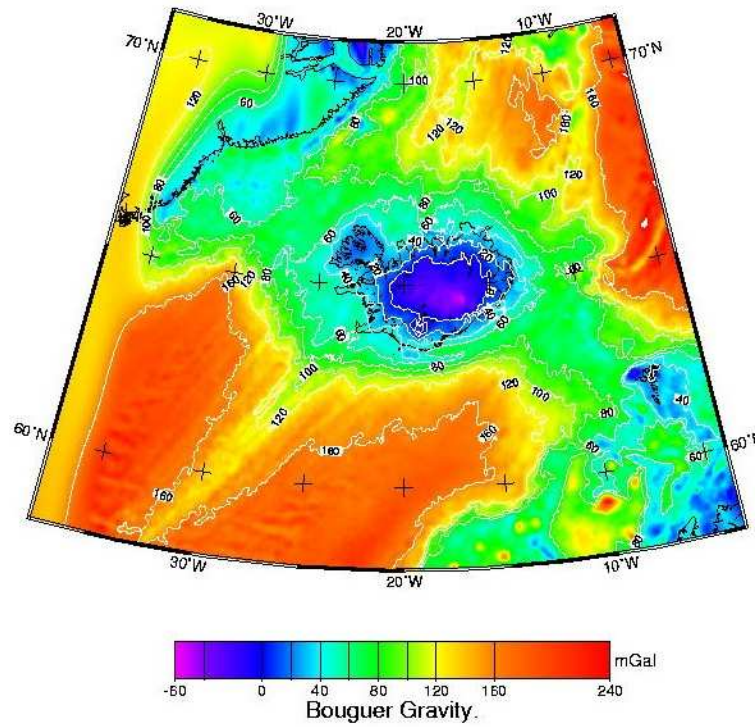


Figure 4.8: Bouguer anomaly map of Iceland from DARBYSHIRE *et al.* [2000]. Note that the zero-mGal isoline that separates negative from positive values runs within Iceland. The lowest anomaly value coincides with the assumed current position of the plume center, as used in this study.

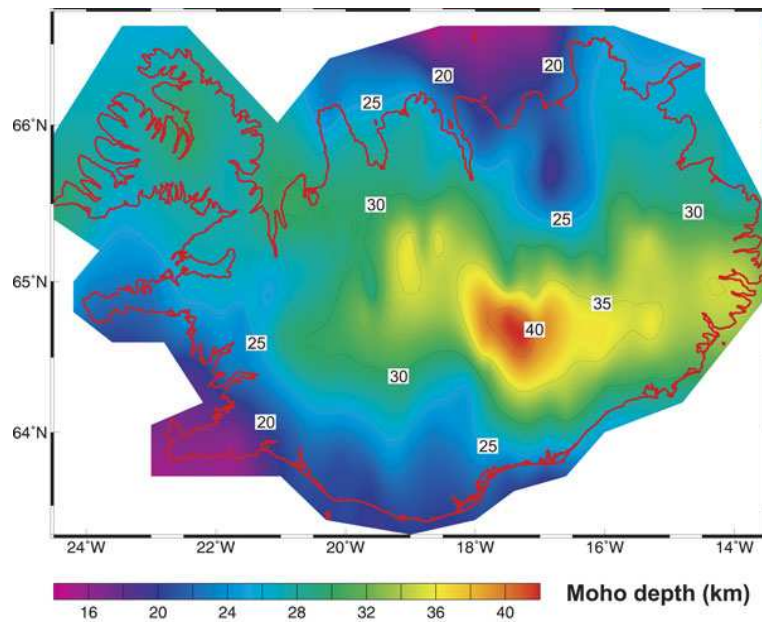


Figure 4.9: Map of Moho depth by DARBYSHIRE *et al.* [2000].

the authors designate as the plume center. East of it a band of thick crust ( $\sim 35\text{-}36$  km) extends to the westernmost end of the Faroe-Iceland ridge. The authors speculate that this may be the track of the plume center. However, a general west-east elongation of thicker crust is evident from the map, which is the signature of the plume motion with respect to the MAR.

### Transition zone effects, receiver function studies

In a series of papers (SHEN *et al.* [1996, 1998, 2002, 2003]) Yang Shen with changing co-workers examine the depth of discontinuities beneath Iceland (Receiver function studies on shallower depths, i.e., on the crustal-structure was carried out by DU *et al.* [2002] and DU AND FOULGER [1999]).

In the first paper SHEN *et al.* [1996] use data of the first phase of the ICEMELT experiment (August 1993 – December 1994) and of the GSN station BORG to examine particle motions and receiver functions. By comparison of the receiver functions with predictions from the IASPEI model they obtain average differential time of  $2.3\pm 0.9$  s, which is equivalent to a transition zone thinning of  $23\pm 9$  km. This translates to  $180\pm 70^\circ\text{K}$  excess temperature. They finally conclude that the mantle upwelling beneath Iceland extends at least to a depth of 400–700 km.

In a subsequent paper, SHEN *et al.* [1998] extend the receiver-function approach to the entire ICEMELT dataset after completion of the experiment. They bin their data in overlapping patches of  $200\times 200$  km, which reflects roughly the Fresnel zone of phase P660s at 0.1–0.3 Hz. In central and southern Iceland they observe differential travel times that are smaller than that predicted by IASP91 by 2.2 s ( $\sim 20$  km thinner transition zone), while surrounding areas are normal with respect to the reference model. Thus confirming and specifying the previous results they call into question the model that the Icelandic anomaly originates in the upper mantle due to regional heating of the lower mantle because the heating zone would be much larger than the plume conduit.

SHEN *et al.* [2002] extend the earlier studies by using a new arrival time picking method and a larger data set by including the data of the HOTSPOT experiment, thus increasing the amount of data by a factor of four. They map a P660s–P410s anomaly beneath central and southern Iceland with a reduction of this differential travel time of up to 1.6 s with respect to what is predicted by the IASP91 model. This translates to a thinning of the transition zone of 19 kilometers with respect to the surrounding areas, that in turn corresponds to an excess temperature of  $140^\circ\text{K}$ . The authors note that this is probably a lower bound due to smoothing of the method by the finiteness of the Fresnel zone and the patches they used for stacking. Since an excess temperature of  $>140^\circ\text{K}$  is consistent with the temperature of the Iceland plume, they interpret this anomaly as being associated with the Iceland mantle plume. The offset between the mapped transition zone anomaly and data constraining the shallow upper mantle location of the plume enable the authors to suggest that the Iceland plume conduit is tilted by 9 degrees or more from the vertical.

In the last paper, SHEN *et al.* [2003] use stacked radial receiver functions and find an arrival  $110\pm 1$  s after P. They attribute this arrival to a discontinuity in the mid-mantle at approximately 1050 km depth. This discontinuity is resolvable only beneath southern Iceland where the transition zone has been shown to be thin. This spatial correlation strengthens the idea that both are caused by the same plume. The derived velocity transition occurs over a depth interval of only  $\sim 50$  km, which is only half the wavelength of the converted phases (having  $\sim 15$  s dominant period) and can thus be considered sharp. An elevated temperature

study	year	model	$\delta v_P$	$\delta v_S$	radius	def.	depth extent	TZ thinning	excess temp.	remarks
Tryggvasson et al.	1983		4%		100km		$\geq 375$ km			
Ribe et al.	1995				$\geq 300$ km				$\leq 100^\circ\text{C}$	No. 1
Ito et al.	1996				300km				$75^\circ\text{C}$	No. 2
Ito et al.	1996				60km				$170^\circ\text{C}$	
Shen et al.	1996	IASP91+						$23\pm 9$ km	$180\pm 70$ K	
Wolfe et al.	1997	IASP91	$>2\%$	$>4\%$	150-200km	1/e	$\geq 400$ km			
Shen et al.	1998	IASP91			$\leq 200$ km		( $\geq 660$ km)	20km	$\geq 150$ K	
Helmberger et al.	1998	PREM					2900km			
Ito et al.	1999				100km				$180^\circ\text{C}$	
Ritsema et al.	1999	PREM	-	1.4%		$>2.5\%$	660km			
Allen et al.	1999	IASP91		12%	100km	1/e				
Bijward & Spakman	1999	AK135			$\leq 250$ km		2900km		200-300K	
Pritchard et al.	2000		$<1.5\%$		$\leq 125$ km	1/e	1500km			He study
Foulger et al.	2000	IASP91	2.1%	4.9%	100-130km	$>1\%$	$\leq 660$ km			
Foulger et al.	2001	IASP91	2.1%	4.9%	100-125km	$>1\%$	$\leq 660$ km			
Zhao	2001				$\geq 150$ km		2900km			
Allen et al.	2002	"ICAV"	2.1%	3.8%	60-100km	2/3	$\geq 400$ km			surface waves
Shen et al.	2002	IASP91						19km	$\geq 140$ K	tilt $\geq 9^\circ$
Montelli et al.	2003		$\geq 1.5\%$		100km		$\leq 1000$ km			
Shen et al.	2003						1050km			
Du & Foulger	2004	IASP91		5%			$\geq 200$ km			
Hung et al.	2004	IASP91	3.5%	6.2%	125-150km		$\geq 400$ km			
Allen & Tromp.	2005	PREM+	$>2\%$	$>4\%$	$>100$ km	1/e	$\geq 350$ km		350-500K	
		Icemelt		$<10\%$	$\leq 200$ km	1/e				
range:			1.5-4%	3.8-12%	60- $\geq 300$ km		$\geq 350$ -2900km	19-23km	70-500°	

Table 4.2: Summary of plume parameters as derived by different studies. In case of seismic studies the underlying background model to which the perturbations refer is given. If available, the radius definition used is given in the column left of the radius.

alone cannot explain such a sharp boundary, thus, such a mid-mantle discontinuity is more consistent with compositionally distinct reservoirs in lower mantle, as claimed by geochemists.

### 4.2.3 Iceland plume properties: summary and appraisalment

Table 4.2 shows a summary of results of different studies concerning the geometrical, and, if available, additional parameters of the Iceland Plume.

A final appraisalment of the results, however, is quite difficult, due to their partial contrariness. From a seismological point of view, one tends to trust most the finite-frequency tomography results by MONTELLI *et al.* [2004b] for the whole mantle picture since it is the most careful study concerning data inspection and selection and HUNG *et al.* [2004] for the upper mantle image since they use data of all the experiments. Moreover, both approaches are based on finite-frequency theory. Following MONTELLI *et al.* [2004b] the Iceland mantle plume is confined to the upper mantle, which, in turn contradicts the results of Shen and co-workers, indicating the transection of a plume through the transition zone. A solution to this could be the postulation of a weak and broad, and maybe pulsing plume in the lower mantle as suggested by MONTELLI *et al.* [2004a]. Concerning the diameter of the plume, the suggested values range from 100–600 km. However, the recent paper by ALLEN AND TROMP [2005] reduces the range to 120–200 km, which is in agreement with seismic studies, especially those taking into account finite-frequency effects. For the magnitude of the Icelandic anomaly, the finite-frequency study of HUNG *et al.* [2004] probably gives the the most reliable values. They exceed the perturbations obtained with ray tomography (which is expected to underestimate the actual perturbation), but still does not imply unrealistically high excess temperatures.

## 4.3 The 1995 Peru earthquake and its records on Iceland

In the following the 1996 Peru earthquake and its source process is described since real and synthetic data from this earthquake is used in the next section.

### 4.3.1 The earthquake

A strong earthquake occurred on November 12, 1996 off the coast beneath southern Peru. It was a thrust earthquake caused by subduction of the Nazca ridge beneath the American Plate (USGS NEIS-earthquake catalogue of 1996) and re-ruptured parts of the previous event in 1942 (SWENSON AND BECK [1999]) with a rupture length of about 200 km and an average slip of about 1.4 m (SPENCE *et al.* [1999]). A tsunami with a maximum recorded amplitude of 35 cm was generated (USGS NEIS report). The earthquake killed at least 14 people, injured more than 560 and damaged or destroyed more than 4 000, buildings reaching intensities up to VIII. Moment estimates range from  $3\text{--}5 \times 10^{20}$  Nm (SWENSON AND BECK [1999]) to  $2 \times 10^{21}$  Nm (SPENCE *et al.* [1999]), corresponding to moment magnitudes of  $M_W=7.6\text{--}8.0$ .

The temporal evolution of moment release consisted of three pulses with a total duration of about 45–50 seconds as resolved by finite fault inversion of teleseismically recorded broadband body waves (SWENSON AND BECK [1999], SPENCE *et al.* [1999]). Concerning the spatial distribution of moment release three asperities could be identified, with the largest moment release (70% of the seismic moment) occurring  $\sim 90$  km southeast of the hypocenter, approximately 35–40 seconds after rupture initiation.

Based on the studies of SWENSON AND BECK [1999], SPENCE *et al.* [1999] and WINSLOW *et al.* we developed a source-time function (STF) for this event. It consists of three pulses that are represented by Gauss functions and in their sum closely follow the STF from the catalogue by WINSLOW *et al.* (Fig. 4.10). Moreover, the Gaussian sub-STF are set up in a way such that when each of them is associated with a sub-event placed at the corresponding asperity locations of the Peru event (identified by SPENCE *et al.* [1999]) and has an appropriate origin time they add up to the temporal evolution of moment release.

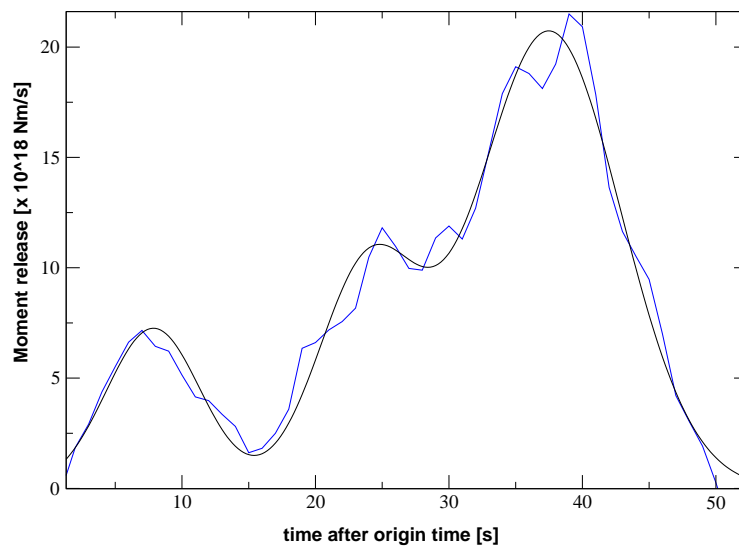


*Figure 4.10: The source-time function of the November 12, 1996 Peru earthquake. The moment release can be grouped into three subevents, that may be due to asperities on the rupture surface. The blue line is the data from WINSLOW *et al.*, University of Michigan. The black line is the STF model used for this study which is composed of three Gaussian functions representing the individual asperities.*

For the following comparison with real data this source-time function is convolved with the seismograms used in Chapter 3 that were calculated with a delta-pulse function excitation.

### 4.3.2 Data at Icelandic stations

The 1996, Peru Earthquake was recorded by the GSN station BORG, by the permanent seismic network SIL and by the temporary broadband stations of the ICEMELT and the HOTSPOT experiments. A reason for selecting this earthquake was the fact, that this earthquake occurred in a year where both experiments ICEMELT and HOTSPOT were running. Unfortunately, the ICEMELT stations were already dismantled at the time the earthquake occurred.

## 4.4 Synthetic data for the Peru earthquake

In order to obtain synthetic seismograms of the Peru earthquake for Icelandic sites, numerous seismic stations that were temporarily installed on or around Iceland were included in the receiver pool (see Fig. 4.11). In detail, these were stations of the SIL network, of the ICEMELT

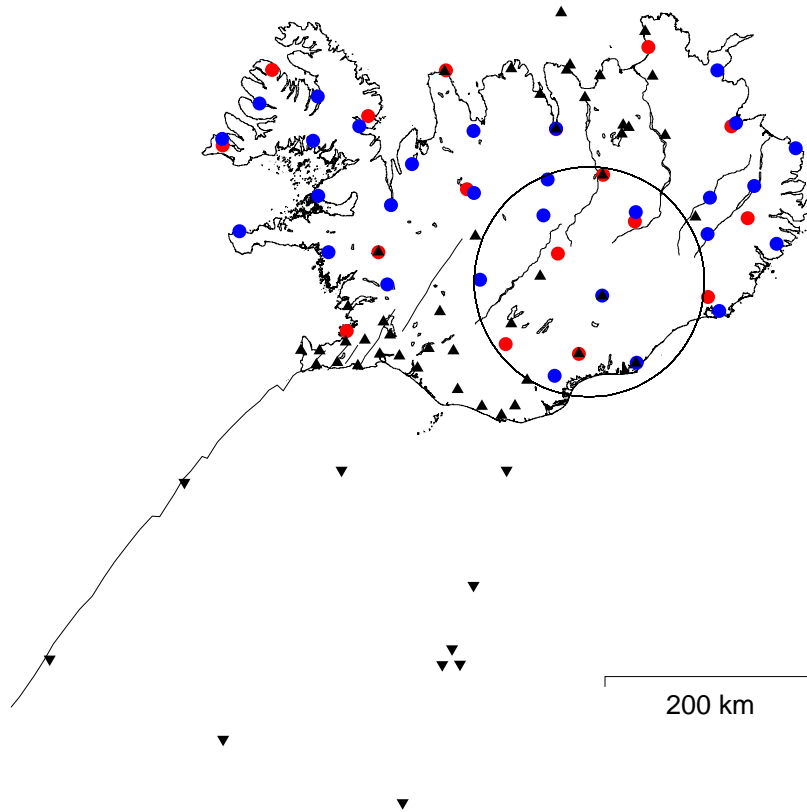


*Figure 4.11: Map of stations installed in and around Iceland. Stations of the ICEMELT and HOTSPOT experiment are plotted in red and blue, respectively, the permanent stations of the SIL network are represented by black triangles, and temporary OBS deployments by German research institutes are plotted as inverted triangles. A circle with a diameter of 200 km indicates the approximate position and size of the plume conduit.*

and the HOTSPOT experiment, and hydrophones and seismometers of a temporary Ocean Bottom Seismometer (OBS) deployment of the University of Hamburg and the GEOMAR research center (Kiel). Stations of the NEAT-project (2000–2002; PILIDOU *et al.* [2004]) and those at the Tarfajökull volcano (deployed between June and November 2002; LIPPITSCH *et al.* [2005]) were not included in the simulations because their existence was unknown at the time when the setup was designed.

### 4.4.1 Processing and comparison of seismograms

After convolving the synthetic seismograms with the source-time function of the Peru event and filtering of both synthetic and real data such that they cover the same frequency range

(10 s–100 s) both sets of seismograms were compared. As expected, there were large differences in amplitude but as well in timing, the latter changing from station to station, indicating that there are significant crustal effects (cf. ALLEN *et al.* [2002b]) that the global Earth model with its resolution does not take into account. They are influencing the travel time more than the plume does. Therefore, a direct comparison of synthetics and data does not provide useful information about the plume.

In Figure 4.12 an example is shown for the GSN station BORG and the sharp 100 km-radius CMB plume embedded in PREM. The time axis of the synthetic event has been shifted such that the main body phases match, also the amplitude was scaled. Amplitude differences mainly come from not including attenuation in the simulation.

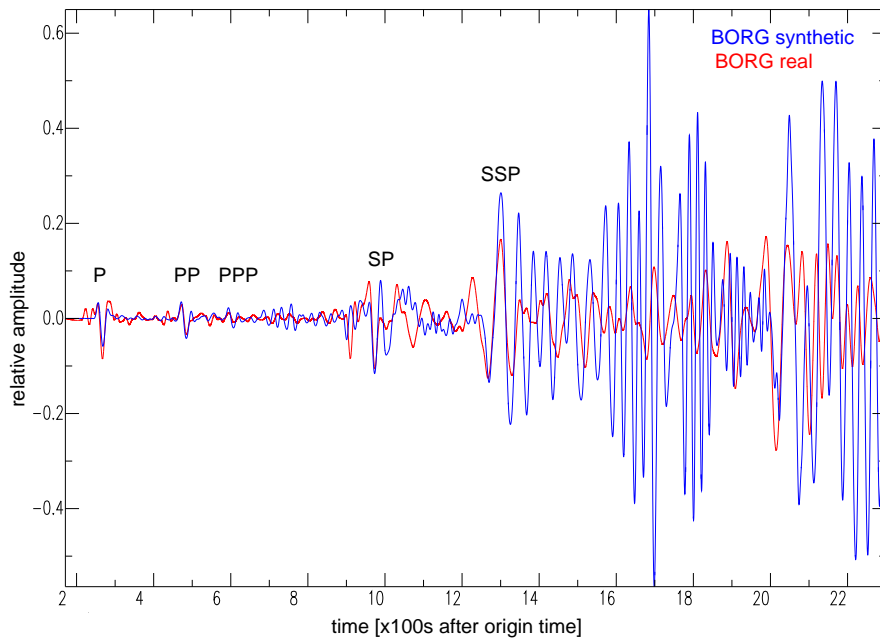


*Figure 4.12: Comparison of synthetic with real data for station BORG (vertical component). A 100 km-radius CMB-plume with a sharp perturbation onset in PREM is used. Due to the large influence of the thick crust in Iceland the synthetic data had to be time shifted since the crustal effects are not included in the synthetic model. Moreover, the synthetic amplitude is scaled to roughly fit the first body wave arrivals because no attenuation is included in the synthetic model. This leads to the large differences for the S-waves from 1500 seconds on.*

#### 4.4.2 Fk analysis

Therefore we go a different way and try to apply a method that is suited also for real data in the presence of noise and exploits another effect of plumes. Lateral low-velocity perturbations are not only expected to cause travel time delays and changes in amplitude but also the slowness of particular phases. The slowness vector of a phase at a station is a combination of the incidence angle and the direction of the ray (i.e., the back-azimuth) (JAHNKE [1998], ROST AND THOMAS [2002]). A means for measuring the slowness vector from seismograms is the frequency wavenumber analysis (“fk-analysis”). It has been used extensively in global seismology and is summarized in a comprehensive review paper by ROST AND THOMAS [2002].

The method basically makes use of the travel-time differences of a wave when running across an array to derive the direction of the wave and its incidence angle. At teleseismic distances, a plane wave approximation for a given phase under an array can be assumed. A plane wave can be uniquely described with an incidence angle and a back-azimuth angle for all the stations (see Fig. 4.13a,b). The range of vertical slowness (0 to 32.7 s/°) and back azimuths ( $\Theta=0$  to 180°) is discretized and all discrete combinations of the two angles that form the slowness vector are used to derive time delays for the stations of the array that would result from an incoming plane wave with this slowness vector. The actual seismograms of the array are then shifted with these time delays and stacked. The maximal amplitude of the stacked phase is plotted as a function of azimuth (Fig. 4.13d), explanation see Figure 4.13c. If the slowness vector used to derive the time shifts is the same as the actual slowness vector of the phase the signal obtained by stacking of the shifted seismograms is maximal with respect to other time shift combinations. Thus, the “measured” slowness and back-azimuth can be identified in the azimuth plot as the maximum. The ratio of the amplitude of the maximum and the adjacent local maximum is a measure for the quality of the analysis and depends on the array configuration. The grid search through slowness and backazimuth combinations of the fk-analysis is carried out in the spectral (frequency-wavenumber; fk) domain in order to save computation time.

For real seismograms this method has the advantage that it sums the coherent signal while the non-coherent noise is reduced by destructive interference. This way, phases can be identified that could not be seen in individual seismograms.

Some general characteristics of the fk-analysis method and array methods in general with respect to the array parameters (SCHWEIZER *et al.* [2002], S. ROST, personal comm.) are briefly described here:

- The resolution for small slowness values is determined by and increases with the aperture of the array.
- The limit of wavelength  $\lambda$  that can be analyzed is the aperture of the array ( $\lambda \leq a$ ), that is, in our case 600 km. If  $\lambda \gg a$  the array acts like a single receiver
- The total number of stations determines the filter quality of the array against noise (this point does not play any role for synthetic data)
- The station interspacing determines the smallest resolvable wavelength: the smaller the distance between the seismometers, the smaller the wavelength.
- The array geometry, i.e., the position of the receivers, determines the azimuth dependence of the resolution. This becomes clear if we consider extremal geometries: an array that consists of stations in a linear arrangement at constant backazimuth will not be able to resolve variations in backazimuth but has very high resolution for the slowness. Another array perpendicular to the last one will have the opposite characteristic. Therefore, several concentric rings of seismometers seem useful, however, strong symmetry should also be avoided.

To our knowledge, array methods such as fk-analysis using stations on top of the plume have not been applied to study plumes under an array. However, due to the use of dense networks for regional plume tomography experiments the idea of applying array techniques is obvious.



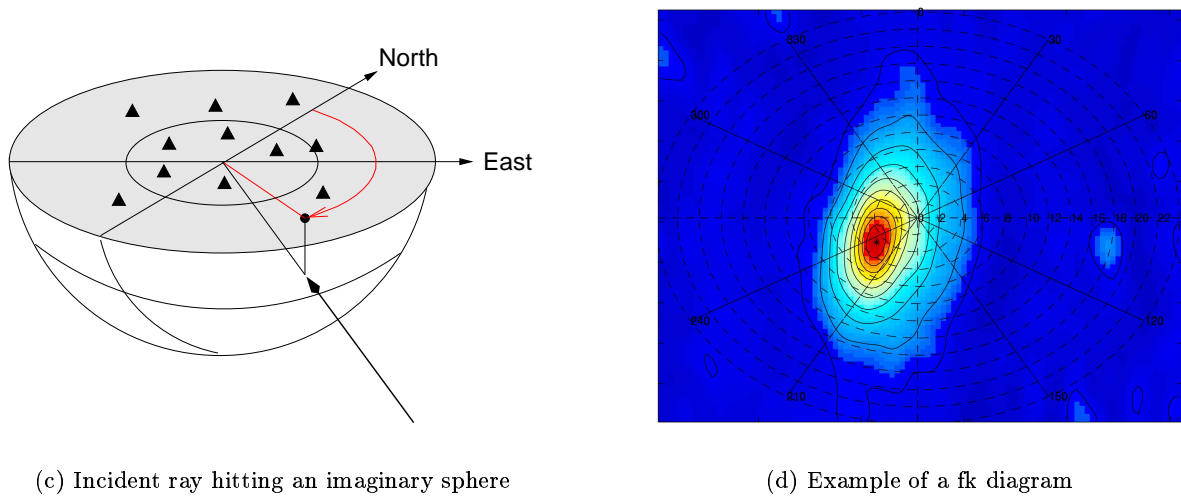
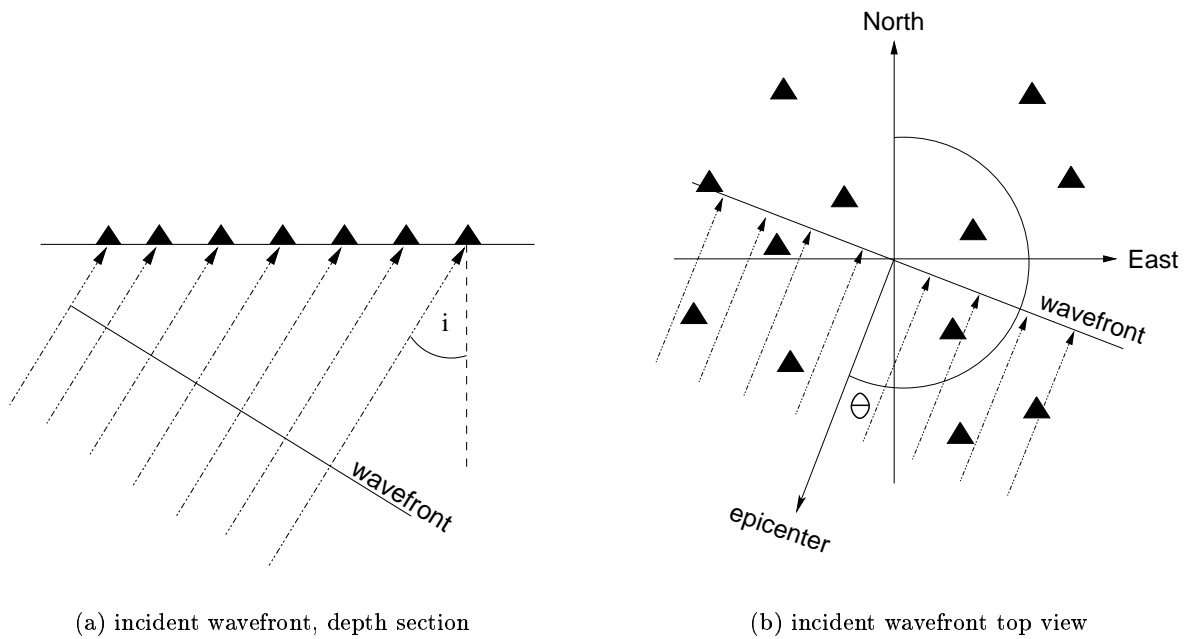


Figure 4.13: Illustration of the *fk*-analysis: **a)** an incoming plane wave in the vertical plane is described by the incidence angle  $i$ . The stations (triangles) record the wave with a time shift that is proportional to their horizontal distance  $d$ . **b)** an incoming plane wave in the horizontal plane is described by the angle  $\theta$  i.e., the angle between the incident ray and the north direction.  $\theta$  is known as the back azimuth. **c)** An incoming ray hits an imaginary hemisphere under the array. The projection of the pierce point onto the surface yields the *fk* diagram. The radial distance of the point from the center is proportional to the vertical slowness (incidence angle), the angle from north gives the back azimuth. (all figures after JAHNKE [1998]; ROST AND THOMAS [2002]). **d)** An actual *fk*-diagram as obtained for the data used in this study. The energy at the slowness-backazimuth combinations is color-coded, the highest value, marked with an asterisk, is the “measured” slowness-backazimuth.

We decided to use a variant of the *fk*-analysis, first used by ROST AND WEBER [2001]. They developed a method for continuously measuring the slowness vector of the incoming wavefield by moving a time window over the seismogram and applying the *fk*-analysis for all the time windows (“sliding window *fk*-analysis”, SWFK).

Two parameters have to be set for carrying out the SWFK, the window width and its step width. The window width has to be chosen such that the phases lie in it for all stations. A rule of thumb gives a value of three times the period of the phase, but actually the window width is also a function of the vertical slowness and the maximal size of the array. After a careful analysis the window width for this study is chosen to be 90 seconds. The step width, with which the window is shifted over the seismogram determines the time resolution (i.e., the “sampling rate”) of the derived slowness trace. It can be theoretically set to as low as the sampling rate of the seismogram but this increases the computation time of the *fk*-analysis. We decided to take five seconds, which is twenty-five times the sampling rate of the seismogram. In the resulting time series for the derived slowness the slowness values are assigned to the time of the middle of the time window.

As a preliminary step, we compare the slowness values obtained by using the moving window *fk*-analysis for the synthetic seismograms with the ray-theoretical values given by the TAUP-toolkit. This is not a test for the *fk*-method, since we measure the slowness from long-period ( $\leq 20$  s) seismograms and it is not a priori evident that this slowness fits the values derived using ray-theory. The comparison of the measured and theoretical values rather tells us if a specific phase can be detected in the seismograms. We generally observe that phases running through the core do not leave a strong signature in the measured slowness.

The results of an *fk*-analysis using the stations of the HOTSPOT experiment presented in Fig. 4.14 look promising. The slowness curves of the PREM seismograms closely fits the ray-theoretical values calculated with the TAUP toolkit (note that the curve is based on datapoints every five seconds). The curve for the real data (red line) shows higher than PREM slowness values in the time windows containing the first P-arrivals. Since the incidence angle of a wave is proportional to its slowness the waves under Iceland have shallower incidence. This is what we expect from a low-velocity anomaly. The same applies to the two curves for the sharp and the gradational plume. The increase of slowness for the sharp plume is higher and its slowness curve is very close to the real-data curve. From these results one would say that the sharp  $r=100$  km plume fits the data. However, the high perturbation values of the Gaussian plume concentrate close to the plume axis – the only station there delivered no seismograms for this event. Therefore, due to the station configuration used we can not compare real data slowness values with models for a sharp and a gradational plume.

Moreover, recalling the assumptions of the *fk*-analysis method we realize that the plane-wave assumption is obviously violated here since the array we use for the *fk*-analysis is much larger than the anomaly, which leads to a distortion of the teleseismic wavefront, an effect we explore in Chapter 3. Here, this distortion leads to a curved wavefront within the array and therefore we see only an averaged effect of velocity perturbed areas and unperturbed background model. It is thus likely that the actual slowness effect of the plume is higher than measured with this array.

It is therefore desirable to further reduce the extent of the array and to use moving subsets that sit at different epicentral distances on one side of the plume. However, comparing the size of the plume with the station spacing it becomes clear that we do not have enough virtual receivers (and no real stations anyway) for carrying out such a high resolution study (see list of general characteristics).

P-phase window, Peru 1996, HOTSPOT stations  
 sliding window fk analysis: slowness (s/deg)

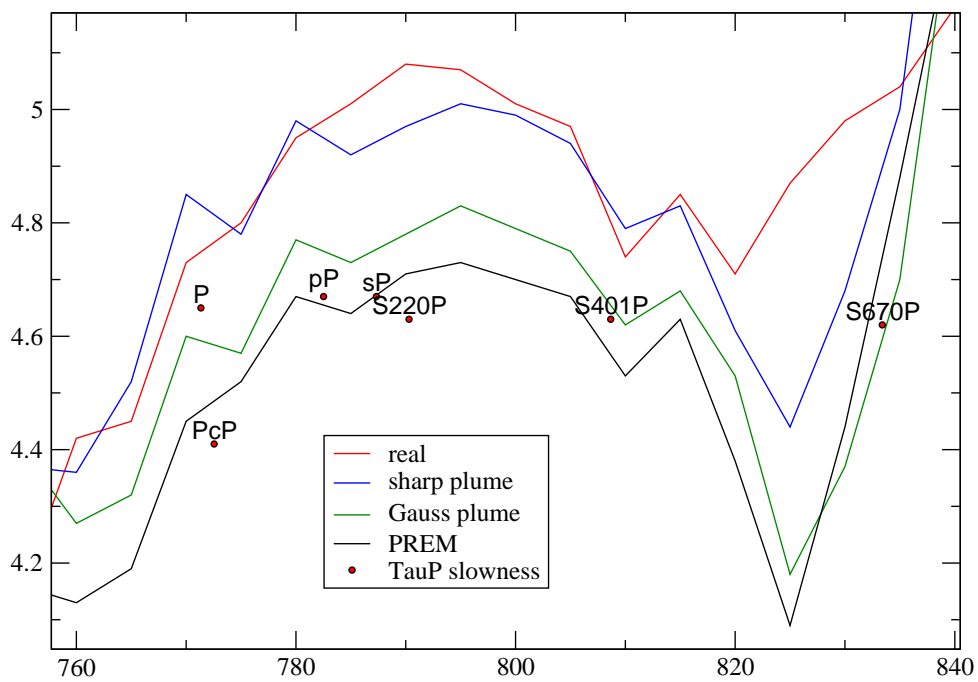


Figure 4.14: *fk*-analysis of the P phase window of the 1996 Peru event using HOTSPOT stations. Real data results are shown as a red line, other lines represent synthetic slowness values for plume model 1 (“sharp” perturbation function) and 4 (Gaussian perturbation function). For comparison, ray-theoretical slowness values are given by red filled circles at the expected arrival times.

### 4.4.3 Interpretation of synthetic results with respect to Iceland

What follows is a discussion of the results from the previous chapter in terms of their consequences for seismological imaging the Iceland plume with low frequencies. The maps of section 3.31 with Iceland as background will be helpful for developing a notion of the size of the plume effect with respect to the extension of the landmass of Iceland and possible (OBS-) locations for recording long distance effects. Due to the 1D background model used to create the travel-time delay maps we can rotate them around the plume axis to any desired backazimuthal direction.

When doing so, the minimum and maximum distances from the coast to the plume axis in the direction of the great circle through plume axis and epicenter changes, and thus the range of potential locations of land-based seismometers in the corresponding directions. The two endmembers in these distances are the minimum and the maximum distance of the plume axis to the coastline of Iceland. The point the farthest away from the plume axis lies in the Western Fjords and is about 350 km from the assumed plume center. The closest point lies to the south of the plume axis at the Skeidarársandur coast about 70 km away. Note that at both places real stations were installed.

#### Width and magnitude of the anomaly finite-frequency inversion

A general problem plume studies face is the trade-off between plume-diameter and temperature. To resolve this, ALLEN *et al.* [1999] take an alternative approach by extending the  $t^*$  methodology usually used to derive anelastic attenuation (Q value). They show that in case of Iceland the diffraction effects of a cylindrical plume structure (TILMANN *et al.* [1998]) has the dominating effect on amplitude variations in Iceland. Even if effects by attenuation ( $t^*$ ) and diffraction (Allen's notation  $d^*$ ) mix up and only the sum ( $s^*=t^*+d^*$ ) is observable, the patterns of these effects are so different that they allow a distinction. The effect of attenuation results in a simple pattern of high positive  $t^*$ -values (after subtracting the mean  $t^*$ -value) for stations receiving waves that passed the (attenuating) plume. The diffraction effect instead – as shown in Chapter 3 – is much more complex and consists of positive and negative values. Moreover, it is frequency dependent, which can be used for distinction.

ALLEN *et al.* [1999] applied this approach to S- and SS-arrivals with a typical useful frequency range of 0.03-0.175 Hz (5.7-33 s). The modeling was carried out with a 2D FD code and a 2D cylindrical plume with a Gaussian plume perturbation against IASP91 was used (cf. 3D modelling in our study with PREM). The MAR was not modeled, since the data shows not much variation with azimuth. The source-time function was a Berlage wavelet with a characteristic frequency of 0.07 Hz (14.3 s). The best ray coverage is obtained at a depth of  $\sim 300$  km. No plume head can be seen. The result of this study is a best fitting model with a S-wave-perturbation of  $dv_{Smax}=12\%$ , and a plume radius of  $r=100$  km, thus a thin and hot plume. This has to be considered an upper bound if not even unrealistic, since it could not be confirmed by later finite-frequency tomography studies.

An important issue in the early phase of Iceland plume studies was the question as to whether the plume beneath Iceland is thin and hot or rather broad and cooler. The problem was a trade-off between magnitude of the anomaly and its width that could not be resolved seismologically. Figure 3.28 shows the travel-time delay curves for combinations of peak anomalies and plume diameters of Gaussian plumes with the same integral total perturbation. The three curves converge with distance to the same values but show large differences within

five degrees around the plume axis. Within 350 km around the plume center, where we can obtain data from land-based seismometers, the differences are highest, clearly distinguishable from seismograms.

In Fig. 4.15 we illustrate this by showing only delays that can be captured with land based seismometers. Every delay pattern is shown for four different back-azimuths: the one of the Peru earthquake ( $\Theta=239^\circ$ ), one that correspond to Tonga events ( $\Theta=324^\circ$ ), one from directions corresponding roughly to the Philippine trench ( $\Theta=54^\circ$ ) and one for events from Western Europe and northern Africa ( $\Theta=144^\circ$ ). The patterns of the different plume diameter (columns in Fig. 4.15) differ significantly, also the amplitudes and their ranges differ strongly. The highest variations in the delay is observed for the 60 km radius plume. It has the strongest delays (almost 4 seconds) and also shows significant early arrivals (0.2 s), all observable in Iceland, almost independent of where the earthquake waves come from. For the large but weak 300 km plume all the sites on Iceland record waves delayed by the plume. As a consequence it is not possible with a relative travel-time delay method to give absolute delays due to a lack of a zero reference. The 300 km plume would thus be underestimated in its travel-time effect and its (anyway only weak) perturbation, while the 60 km plume would have enhanced delays because the negative values would shift the zero line and thus add to the relative delay.

In summary, the effect of the three models with same integrated perturbation but different widths is very different and should be resolvable from land-based recordings in Iceland. Meanwhile, ALLEN AND TROMP [2005] constrained the possible range of anomaly-width combinations using finite-frequency considerations to about  $>60 \text{ km} - \leq 100 \text{ km}$ .

## Origin depth

A different situation from the thin-hot/broad-cool problem is met when we turn to the second important question in the discussion about the Icelandic anomaly, that of the origin depth. While the differences between the competing models for the thin-hot/broad-cool issue were largest close to the plume axis and thus distinguishable with data in Iceland, the inverse is true for the signature of the origin depth in the delay shadows (Fig. 4.16). Almost no difference can be seen between the delay shadows of the deep seated plume and the one with the shallow origin. This is true for both phases shown, which are representatives of shallow (PP) and steep (SKKS) incidences. This confirms that not only for rays but also for waves, owing an extended sensitivity, the origin depth is not resolvable with stations located only on the island of Iceland and that it is not legitimate to exclude a CMB origin of the Icelandic anomaly with land-based data (cf. FOULGER *et al.* [2000]).

## Amplitudes

The amplitude effects discussed in the last section of the last chapter can probably not be exploited to image the plume. First, for realistic models such as the 60 or 100 km radius plumes with 3.5/6.2% velocity perturbation the amplitude effects are weak (factors of 1.15%) even for the highest frequencies we modelled. Secondly, measuring the amplitude effect in practice will be not possible since there is no unperturbed reference case as for our synthetics. Alternative methods, such as taking relative amplitudes between the stations will be biased by Iceland's large crustal effects and will therefore not be able to deliver the necessary resolution for the relatively small effect.

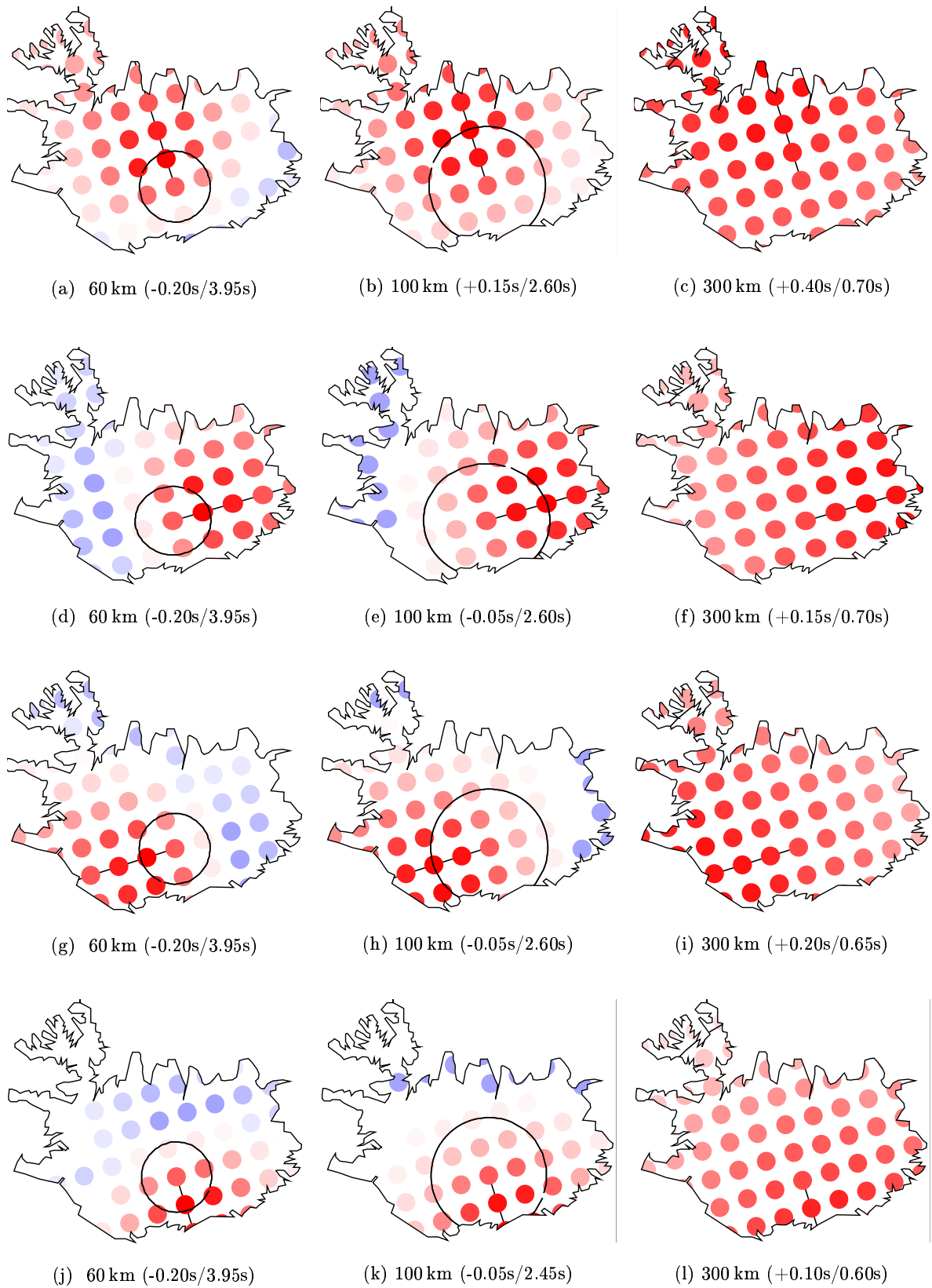


Figure 4.15: Delay distribution of the ScS phase in Iceland for different CMB-plume models (IDs 4, 13, 30) with Gaussian perturbation function at  $\Delta=90^\circ$ .

**Iceland's plume tail – hidden by the head?**

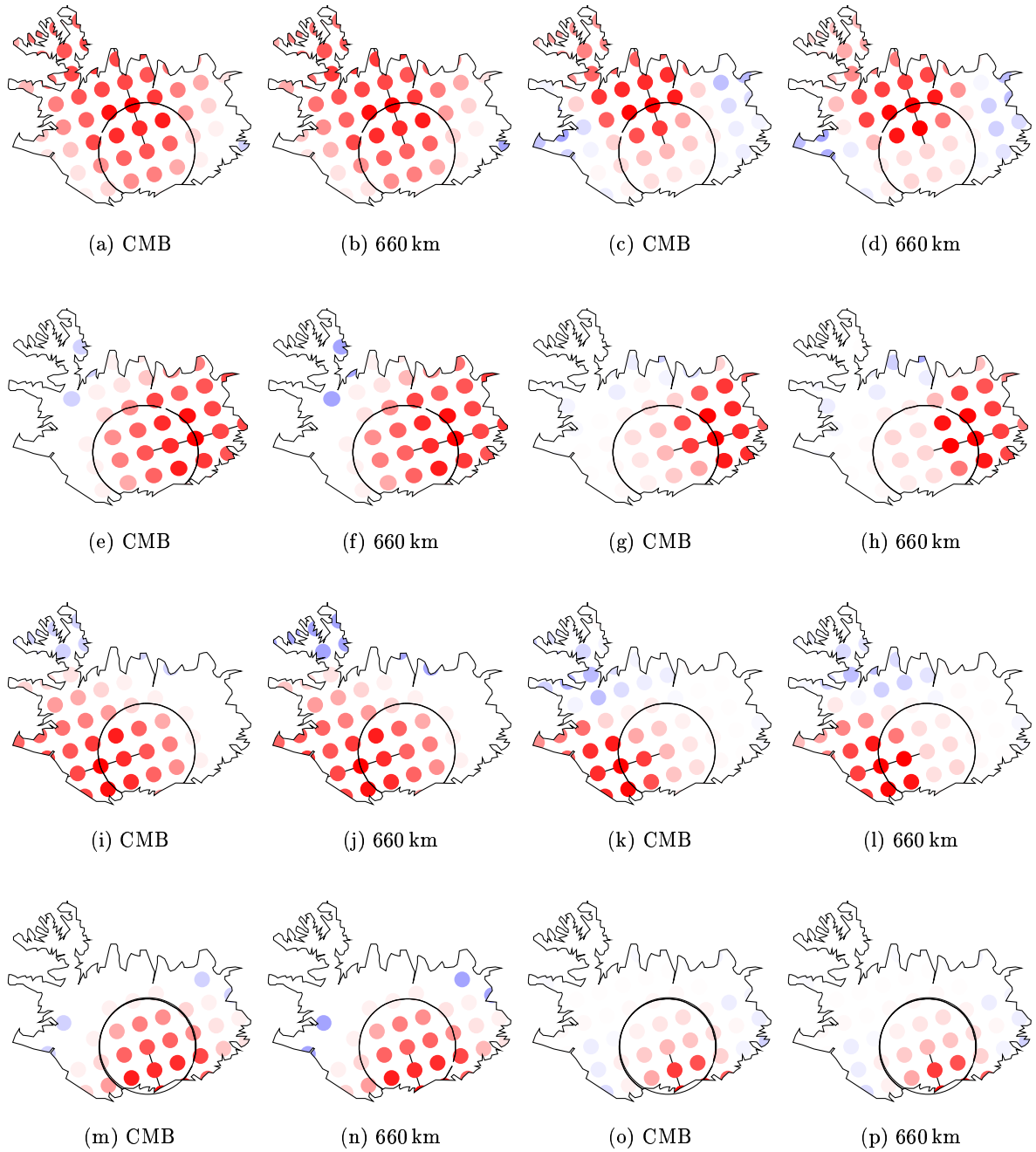


Figure 4.16: Delay distribution of the PP (left two columns) and SKKS (right columns) phase on Iceland for different origin depths at  $\Delta=90^\circ$ . Plume models P1 and P2 are used (boxcar perturbation function,  $\delta v_P=3.5\%$ ,  $\delta v_S=6.2\%$ , 100 km radius, CMB origin).

Since regional tomographic studies for Iceland have used the cross-correlation technique by VANDECAR AND CROSSON [1990] that reveals only relative travel-time perturbations a head for the Iceland plume could not be resolved since its area likely exceeds the island of Iceland and thus the aperture of the station network by far.

Therefore, ALLEN *et al.* [2002a] combined body-wave tomography with surface-wave tomography the latter being able to constrain absolute velocity perturbations. They find a head with a vertical extension of approximately 200 km. This large horizontal structure might be a voluminous lateral accumulation of plume material feeding the asthenosphere rather than a classical initial plume head. Plume tails might be difficult to detect seismologically since they are hidden in the signature of the heads (RITSEMA AND ALLEN [2003]). In Figure 4.17 we examine this effect. On the left column the travel-time delay shadow of the PP-phase is shown for a sharp CMB-plume with a 100 km-radius conduit and a 500 km-radius head and for a sharp plume with only a conduit. Visually one sees no signature of the conduit in the delay map of the plume with head. The subfigure e) is a map of the differences of delay times between the two models. Taking the difference effectively removes the conduit out of the head and should thus leave a signature of the conduits. Indeed, the maximum delay is reduced by 0.5s but the effect is not dramatic. The same three maps but for the SKKS phase is shown on the right hand side of Fig. 4.17. Here, we see a clear signature of the conduit in the delay difference - a hole in the delay pattern right behind the conduit develops where the delay values are significantly reduced. The difference between the two phases is due to the different incidence angles. This can be already observed in Fig. 4.17b where the large head leaves a concentrated zone of strong delays, whereas for the shallow PP phase (Fig. 4.17a) the delays are distributed all over the area of the head.

In summary, the head indeed masks the signature of the tail, but the effect depends on the incidence angle of the used phase. When using relative travel-time delays, as most regional tomography studies do, the effect of the tail nevertheless is observable but modified by the head. The question of how this effect changes the tomographic images of the tail can not be answered here. However, one should keep in mind that the head resolved by ALLEN *et al.* [2002a] has a perturbation of up to 8% which is about twice that of the tail. In that case a strong bias of the plume image caused by the head can not be excluded.

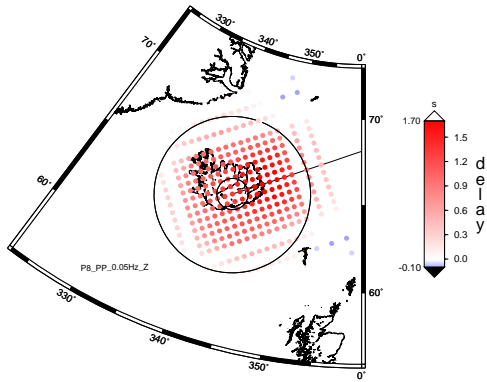
## 4.5 Summary

Iceland is the type example for a hotspot on a mid-ocean ridge. Compared to Hawaii, the textbook example of a mid-plate hotspot, Iceland can be better studied with land based seismometers due to its large landmass extension. Moreover, Iceland has been the target of several seismic studies and is probably the best studied hotspot in the world. As a result, all the plume related questions are raised about the Iceland plume, and attempts of answers have been made in a lot of studies. However, these are discordant, and thus all the questions of the plume debate are still open for Iceland. For that reason, Iceland was chosen as a study case, and the general simulations of wave propagation through plume structures of the last chapter were extended by including the majority of stations ever installed in or around Iceland.

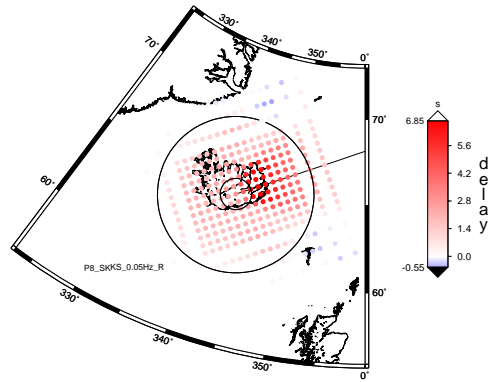
A direct comparison of synthetic with real data, however, is problematic and was not intended, since our simulations did not include the crustal structure which affects the travel times as much as the perturbation of the plume does. Moreover, attenuation that is either not included in the modeling leads to large differences in the amplitudes. Comparing real and synthetic data indirectly, using a sliding window fk-analysis turned out to be not useful due to the low station density of both, real and synthetic stations.

The examination of the three Iceland-related issues with the synthetic dataset illustrates the characteristics of effects shown in Chapter 3 and the problems for constraining the param-

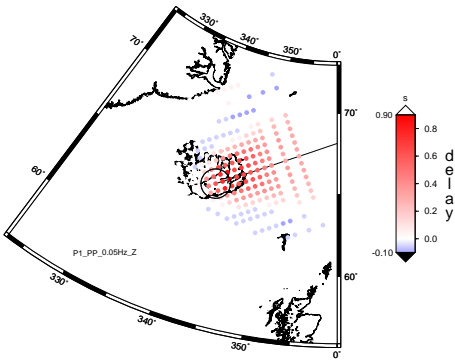




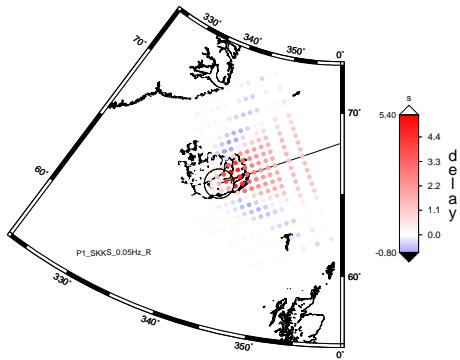
(a) plume model with head, PP-phase



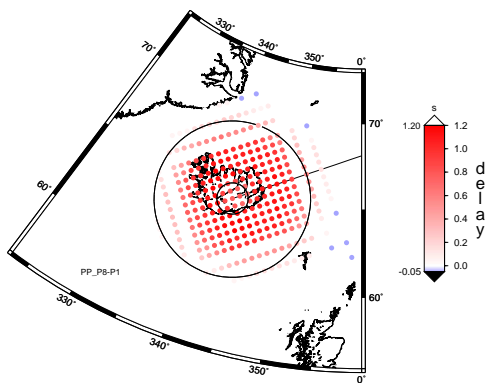
(b) plume model with head, SKKS-phase



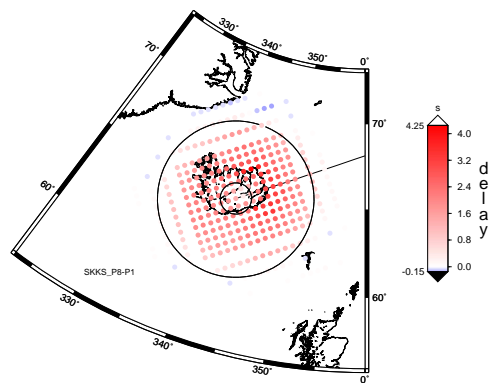
(c) plume model without head, PP-phase



(d) plume model without head, SKKS-phase



(e) difference (c)-(a)



(f) difference (b)-(d)

Figure 4.17: Delay distribution in Iceland for the SKS phase: influence of the head.

eters of the Iceland plume reviewed in this chapter. By rotation of the travel-time shadows to four different backazimuths and restricting the shown delay values to what is observable in Iceland it could be shown that the discussed thin-hot and broad-cool scenarios for the Iceland plume can be distinguished with long-period data, but that the question about the origin depth can not. As a consequence, it is necessary to carry out an experiment with ocean-bottom seismometers or – maybe as a first step – to include data of the existing stations around Iceland (e.g., in Greenland, or on the Jan Mayen, Faroer or Shetland islands) in a future study. The travel-time delays in the last chapter have shown that these stations are in the distance range that is crucial to answer the question about the depth extent of the plume.

Finally, using a model of a plume with a head and comparing it to a model with only a conduit we could show the effect of the presence of a head. Depending on the incidence angle of the phase the head can mask the characteristics of the tail. For a steep core-phase the relative travel-time differences shows the signature of the tail, whereas for a shallow phase the delay distribution is dominated by the head.

# Conclusions

This study deals with the signature that mantle plumes leave on the seismic wavefield emanated by teleseismic ( $\Delta \geq 30^\circ / \approx 3300$  km distance) earthquakes. These plumes, the concept of which was introduced by JASON MORGAN almost 35 years ago to explain ocean island volcanism, have gained wide-spread acceptance. A detailed knowledge of their properties, such as origin depth, buoyancy and heat flux and their total number could provide important constraints about the form of convection in the Earth's mantle and the thermal state of the Earth.

However, geoscience, despite a large number of plume studies especially in the last decades, was not yet able to provide an image of a plume originating from the lowermost mantle, as originally suggested by MORGAN. Therefore, in recent years some scientists put the plume hypothesis into question and argued for different mechanisms in order to explain features commonly associated with the presence of plumes.

Mantle plumes, their properties and the question of their existence – for all these issues seismology plays a major role since it is the method for imaging the Earth's interior that provides the highest resolution. Nevertheless, even with seismic methods a detailed image of a mantle plume could not yet be delivered.

In the last century, seismology used mostly ray-theory for imaging plumes, even though it has been known for centuries that the wave aspect becomes important when the object size is on the same order of magnitude as the wavelength. Only recently wavefield effects have been taken into account for inversion studies, leading to the first “finite-frequency tomography”.

With the present work it could be demonstrated in a *forward-modeling* study that wavefield- or finite-frequency effects *are* important for plumes, particularly in the mid- to long-period range (20 s–100 s) of seismograms.

The wavelengths corresponding to these periods – depending on the depth – are equal to or larger than the diameters of plume conduits (100–600 km). Thus, the assumptions of ray-theory are violated and finite-frequency effects occur, the strength of which depends on the ratio of plume diameter and the wavelength corresponding to the considered frequency. This frequency-dependency can help constraining the plume diameter.

Wavefront healing, being the most prominent wavefield effect of small-scale low-velocity anomalies, has been shown to be able to cancel the entire delay signature of a plume for frequencies below 0.05 Hz. Arrivals that come earlier in the presence of a plume and which are not predicted with ray theory may bias relative travel-time measurements by as much as three quarters of a second for steep phases. For regional tomography experiments this might be another source of error, if ignored. On the one hand, it might partly compensate the underestimation of velocity perturbation caused by wavefront healing that is typical for ray-tomographic studies. On the other hand, it could affect the geometry of the resolved

anomaly. The latter should be investigated with a synthetic tomography study.

Wavefront healing diminishes the travel-time delay of a plume so much, that it might be hard to detect already about 500 km behind the plume. For experiment design this means that a confined array with this radius (typical for recent experiments) captures most of the plume's effect. However, one can only decide about the question as to whether the plume comes from the lower mantle with seismograms from about this distance on, since there waves that run underneath an upper-mantle plume are recorded that do not carry a delay. The exact distance where this occurs is slightly larger than ray-theoretically expected, because of the extent of the wave's sensitivity (Fresnel zone).

The depth where plumes originate is one of the key questions in the recent plume debate. Therefore, also stations at larger distances from the plume are necessary for regional experiments.

We suggest seismometer networks that consist of three parts:

- a dense array of seismometers (interstation spacing  $\leq 50$  km) within about two plume radii from the expected plume axis for sampling the area where the travel-time delays and amplitude effects of the plume have their strongest gradients.
- another array of about 600 km with an interstation spacing of 50-100 km, as frequently used for plume tomography studies.
- Individual stations at larger distances in order to capture waves that sample the lower mantle at the position of the plume. Since wavefront healing diminishes the travel-time delay of the plume to a large amount at such large distances from the plume, a careful site selection is necessary. A low noise level and a good model of the crust below the seismometer would be helpful. As shown for Iceland, there may be permanent stations in the region which are likely to fulfill these requirements. Furthermore, it is useful to take into account global seismicity when planning the location of these stations. With the example of Iceland we have shown that there are concentrations of earthquake activity for some distances and directions whereas others are sparsely covered. Therefore, seismometers should be concentrated on three or four directions with a good azimuthal distribution from which the probability of recording earthquakes during the live-time of an experiment is high.

Moreover, it is important to select phases that either reveal the difference in origin depth closer to the plume, or that still have a strong delay at larger distances.

Concerning the selection of phases suited for studying plumes, ray theoretical considerations can be completely misleading for the used mid- to long period range. This was exemplified with the ScS- and SKS-phase. The ScS-phase at a close distance seemed to be an ideal candidate for delivering a strong and sharp footprint of the plume. Wavefield modeling showed that the contrary is true and that the travel-time delay of that phase resulting from a plume is smeared over a broad region.

In contrast, the sS-phase with a very shallow incidence produced a focused and strong delay effect very close to the plume (which is important in order to capture it with a confined land-based station network). This is not expected from ray-theory but results from the uneven distribution of sensitivity around the ray path. At an epicentral distance of  $90^\circ$ , the SKS-phase, also a candidate due to its steep incidence, fulfills the expectations that the ray-path raises. It provides a strong and localized delay footprint which shows that there is no general

coherence between ray and kernel. In the case of the SKS-phase probably the interaction with the core leads to a slim zone of sensitivity around the ray.

This shows that for determining phases that are suited for sampling a plume at a certain depth finite-frequency sensitivity kernels are required and ray-paths should not be used. With the promising method suggested by NISSEN-MEYER *et al.* [2005] an efficient computation for kernels will be feasible in near future – although only for spherically symmetric models. These will be sufficient in most cases, however, there were indications in this study that a strong plume itself might influence the sensitivity kernel in a way that is not negligible. In those special cases the high effort for computing sensitivity kernels for a 3D model has to be made.

The required extra effort for calculating the kernels and the usage of a more complicated theory should not be considered an annoyance only. The uneven distribution of sensitivity of waves also provides some major advantages with respect to the simple ray model. For ray studies, it is never known where on the ray the delay was acquired. Thus, seismologists usually assumed that rays reaching a confined region under the study area are affected by receiver-side effects the same way. If this assumption is not true, heterogeneities outside the study area are mapped into it.

The finite-frequency sensitivity kernels with the known distribution of the actual sensitivity along the path partly overcome this ambiguity and help pinpointing where the recorded phase is influenced and how strong and where not. For designing experiments or for the selection of phases for a specific study, e.g., of the D" region, this can be very helpful. For example sensitivity kernels of core-reflected phases show strong local concentrations of sensitivity but are almost insensitive in other areas.

Therefore, until the break-through of full-waveform inversion methods, the effort of using finite-frequency theory instead of ray-theory still promises some progress in seismic inversion.

Apart from the computation of sensitivity kernels further *experiment-specific* 3D modeling of wave propagation preceding or while interpreting data of a plume experiment will help its planning or understanding the results. In contrast to the modeling carried out in this study such plume-specific numerical experiments should include attenuation and anisotropy. Both of them are expected to play a significant role for plumes and possibly lead to *waveform-effects* that do not appear in our results. With specific models for a plume under study the parameter space for these two effects is limited and taking them into account becomes feasible with a limited computational effort. Also the use of a suitable 3D background model is recommended for a specific study while in this thesis we restricted ourselves to 1D Earth models for the sake of generality.

With pilot studies for Ocean bottom seismometers in recent years and currently with the first large-scale deployment of such instruments to study a plume, the time has now come to go beyond the restriction of seismometer placement on land. On the one hand, this extends the depth of resolution of regional teleseismic tomography studies as shown for the example of Iceland and could provide an answer as to whether plumes, or some of them, originate at the bottom of the transition zone or indeed come from the lowermost mantle. On the other hand, this will enhance the resolution of tomographic studies, also and particularly for plumes. However, due to oceanic noise conditions the long-period range of seismograms will play an important role and thus, as demonstrated in this work, wavefield effects will be of eminent importance.

The dataset that is currently collected for the Hawaiian plume by the PLUME experiment provides an excellent opportunity to transfer these wavefield issues of mantle plumes raised in this thesis to the real world.



# Bibliography

- AKI, K. and P. RICHARDS. *Quantitative Seismology – Second Edition*. University Science Books, Sausalito, CA, **2002**.
- ALLEN, R. M., G. NOLET, W. J. MORGAN, K. VOGFJORD, B. H. BERGSSON, P. ERLENDSSON, G. R. FOULGER, S. JAKOBSDOTTIR, B. R. JULIAN, M. PRITCHARD, S. RAGNARSSON and R. STEFANSSON. *Imaging the mantle beneath Iceland using integrated seismological techniques*. Journal of Geophysical Research, B, Solid Earth and Planets, volume 107(12): 2325, **2002a**.
- ALLEN, R. M., G. NOLET, W. J. MORGAN, K. VOGFJORD, B. H. BERGSSON, P. ERLENDSSON, G. R. FOULGER, S. JAKOBSDOTTIR, B. R. JULIAN, M. J. PRITCHARD, S. RAGNARSSON and R. STEFANSSON. *The thin hot plume beneath Iceland*. Geophysical Journal International, volume 137(1): 51–63, **1999**.
- ALLEN, R. M., G. NOLET, W. J. MORGAN, K. VOGFJORD, M. NETTLES, G. EKSTROM, B. H. BERGSSON, P. ERLENDSSON, G. R. FOULGER, S. JAKOBSDOTTIR, B. R. JULIAN, M. PRITCHARD, S. RAGNARSSON and R. STEFANSSON. *Plume-driven plumbing and crustal formation in Iceland*. Journal of Geophysical Research, volume 107(B8): 1–19, **2002b**.
- ALLEN, R. M. and J. TROMP. *Resolution of regional seismic models: Squeezing the Iceland anomaly*. Geophys. J. Int., volume 161: 373–386, **2005**.
- ANDERSON, D. L. *The thermal state of the upper mantle; no role for mantle plumes*. Geophys. Res. Lett., volume 27(22): 3623–3626, **2000**.
- ANGENHEISTER, G., H. GEBRANDE, H. MILLER and RRISP WORKING GROUP. *Reykjanes Ridge Iceland Seismic Experiment (RRISP 77)*. J.Geophys., volume 47: 228–238, **1980**.
- ANTRETTTER, M. *Moving hotspots – Evidence from paleomagnetism and modeling*. Ph.D. thesis, Ludwig-Maximilians-Universität München, **2001**.
- BECKER, T. W. and L. BOSCHI. *A comparison of tomographic and geodynamic mantle models*. G cubed, volume 3: 1003, **2002**.
- BIJWAARD, H. and W. SPAKMAN. *Tomographic evidence for a narrow whole mantle plume below Iceland*. Earth and Planetary Science Letters, volume 166(3-4): 121–126, **1999**.
- BIJWAARD, H., W. SPAKMAN and E. R. ENGDAHL. *Closing the gap between regional and global travel time tomography*. Geophys. J. Int., volume 103(B12): 30 055–30 078, **1998**.

- BJARNASON, I. P., C. J. WOLFE, S. C. SOLOMON and G. GUDMUNDSSON. *Initial results from the ICEMELT experiment: Body-wave delay times and shear-wave splitting across Iceland*. Geoph. Res. Lett., volume 23(5): 459–462, **1996**. Corr. in Geoph. Res. Lett. 23, no.8, p. 903 (1996).
- BJARNASON, I. T., P. G. SILVER, G. RÜMPKER and S. C. SOLOMON. *Shear wave splitting across the Iceland hot spot; results from the ICEMELT experiment*. Journal of Geophysical Research, B, Solid Earth and Planets, volume 107(12): 12, **2002**.
- BLEIBINHAUS, F. *Entwicklung einer simultanen refraktions- und reflexionsseismischen 3D-Laufzeitomographie mit Anwendung auf tiefenseismische TRANSALP-Weitwinkeldaten aus den Ostalpen*. Ph.D. thesis, Ludwig-Maximilians-Universität München, **2003**.
- BÖHLER, R., A. CHOPELAS and A. ZERR. *Temperature and chemistry of the core-mantle boundary*. Chemical Geology, volume 120: 199–205, **1995**.
- BUDWEG, M. *Der obere Mantel in der Eifel-Region untersucht mit der Receiver Function Methode*. Ph.D. thesis, Universität Potsdam, **2002**.
- BUNGE, H.-P., M. RICHARDS and J. BAUMGARDNER. *A sensitivity study of 3D-spherical mantle convection at  $10^8$  Rayleigh number: effects of depth-dependent viscosity, heating mode and an endothermic phase change*. J. Geophys. Res., volume 102: 11 991–12 007, **1997**.
- CAPDEVILLE, Y., E. CHALJUB, J. P. VILOTTE and J. P. MONTAGNER. *Coupling the spectral element method with a modal solution for elastic wave propagation in global earth models*. Geophys. J. Int., volume 152: 34–67, **2003**.
- CAPDEVILLE, Y., C. LARMAT, J.-P. VILOTTE and J.-P. MONTAGNER. *A new coupled spectral element and modal solution method for global seismology: A first application to the scattering induced by a plume-like anomaly*. Geophys. Res. Lett., volume 29(9): 31–1 – 32–4, **2002**.
- CAPDEVILLE, Y., E. STUTZMANN and J. P. MONTAGNER. *Effect of a plume on long period surface waves computed with normal modes coupling*. Phys. Earth Planet. Inter., volume 119: 57–74, **2000**.
- CHALJUB, E. *Modélisation numérique de la propagation d'ondes sismiques en géométrie sphérique : application à la sismologie globale*. Ph.D. thesis, Université Denis Diderot, Paris VII, **2000**.
- CHALJUB, E., D. KOMATITSCH, J.-P. VILOTTE, Y. CAPDEVILLE and G. FESTA. *Spectral element analysis in seismology*. In: R.-S. WU and V. MAUPIN (editors), *Advances in Wave Propagation in Heterogeneous Media*, Advances in Geophysics. Elsevier Academic Press, **2006**.
- CHALJUB, E. and A. TARANTOLA. *Sensitivity of SS precursors to topography on the upper-mantle 660-km discontinuity*. Geophys. Res. Lett., volume 24: 2613–2616, **1997**.
- CHAPMAN, C. H. *A new method for computing synthetic seismograms*. Geophys. J. R. astr. Soc., volume 140: 81–85, **1978**.
- CONDIE, K. C. *Mantle Plumes and their Record in Earth History*. Cambridge University Press, **2001**.



- COURTILLOT, V., A. DAVAILLE, J. BESSE and J. STOCK. *Three distinct types of hotspots in the Earth's mantle*. Earth and Planetary Science Letters, volume 205: 295–308, **2003**.
- CROTWELL, H. P., T. J. OWENS and J. RITSEMA. *The TauP Toolkit: Flexible travel time and ray path utilities*. Seism. Res. Lett., volume 70(2): 154–160, **1999**.
- CSEREPES, L. and D. YUEN. *On the possibility of a second type of mantle plume*. Earth and Planetary Science Letters, volume 183: 61–71, **2000**.
- DAHLEN, F. A. *Resolution limit of travelttime tomography*. Geophys. J. Int., volume 157: 315–331, **2004**.
- DAHLEN, F. A. and A. BAIG. *Fréchet kernels for body-wave amplitudes*. Geophys. J. Int., volume 150: 440–466, **2002**.
- DAHLEN, F. A., S.-H. HUNG and G. NOLET. *Fréchet kernels for finite-frequency traveltimes — I. Theory*. GJI, volume 141(1): 157–174, **2000**.
- DANECEK, P. *Partial Differential Equations in 3-D Spherical Geometry*. Diplomarbeit, Ludwig-Maximilians-Universität München, **2004**.
- DARBYSHIRE, F. A., R. S. WHITE and K. F. PRIESTLEY. *Structure of the crust and uppermost mantle of Iceland from a combined seismic and gravity study*. Earth and Planetary Science Letters, volume 181(3): 409–428, **2000**.
- DAVAILLE, A. and J. VATTEVILLE. *On the transient nature of mantle plumes*. Geophys. Res. Lett., volume 32: L14309, **2005**.
- DAVIES, G. F. *Ocean bathymetry and mantle convection 1. Large-scale flow and hotspots*. J. Geophys. Res., volume 93: 10 467–10 480, **1988**.
- DAVIES, G. F. *Dynamic Earth: Plates, Plumes and Mantle Convection*. Cambridge University Press, **1999**.
- DAVIES, J. H. *Mantle convection: Plumes rooted in the mid-mantle*. In: *Abstracts of the AGU Chapman Conference on the Great Plume Debate*. Fort William, Scotland, **2005**.
- DEUSS, A. and J. H. WOODHOUSE. *Seismic observations of splitting of the mid-transition zone discontinuity in Earth's mantle*. Science, volume 294(354–357), **2001**.
- DOORNBOS, D. *Diffraction and seismic tomography*. Geophys. J. Int., volume 108: 256–266, **1992**.
- DU, Z. and G. R. FOULGER. *Variation in the crustal structure across central Iceland*. Geophys. J. Int., volume 145(1): 246–264, **2001**.
- DU, Z. J. and G. R. FOULGER. *The crustal structure beneath the Northwest Fjords, Iceland, from receiver functions and surface waves*. Geophysical Journal International, volume 139(2): 419–432, **1999**.
- DU, Z. J., G. R. FOULGER, B. R. JULIAN, R. M. ALLEN, G. NOLET, W. J. MORGAN, B. H. BERGSSON, P. ERLENDSSON, S. JAKOBSDÓTTIR, S. RAGNARSSON, R. STEFÁNSSON and K. VOGFJORD. *Crustal structure beneath western and eastern Iceland from surface waves and receiver functions*. Geophys. J. Int., volume 149(2): 349–363, **2002**.

- DZIEWONSKI, A. and D. ANDERSON. *Preliminary Reference Earth Model*. Phys. Earth Planet. Inter., volume 25: 297–356, **1981**.
- DZIEWONSKI, A., T.-A. CHOU and J. WOODHOUSE. *Determination of earthquake source parameters from waveform data for studies of global and regional seismicity*. J. Geophys. Res., volume 86: 2825–2852, **1981**.
- ESTABROOK, C. and R. KIND. *The nature of the 660-kilometer upper-mantle seismic discontinuity from precursors to the PP phase*. Science, volume 274: 1179–1182, **1996**.
- FARNETANI, C. G. *Excess temperature of mantle plumes: The role of chemical stratification across D''*. Geophys. Res. Lett., volume 24(13): 1583–1586, **1997**.
- FARNETANI, C. G. and H. SAMUEL. *Beyond the thermal plume paradigm*. Geophys. Res. Lett., volume 32: L07311, **2005**.
- FITTON, J. G., A. D. SAUNDERS, M. J. NORRY, B. S. HARDARSON and R. N. TAYLOR. *Thermal and chemical structure of the Iceland plume*. Earth Planet. Sci. Lett., volume 153: 197–208, **1997**.
- FLANAGAN, M. P. and P. M. SHEARER. *Global mapping of topography on transition zone velocity discontinuities by stacking SS precursors*. J. Geophys. Res., volume 103(B2): 2673–2692, **1998**.
- FOHRMANN, M., H. IGEL, G. JAHNKE and Y. BEN-ZION. *Guided waves from sources outside faults: An indication for shallow fault zone structure ?*. Pure and Appl. Geoph., volume 161: 2125–2137, **2004**.
- FOUCH, M. J., K. M. FISCHER and M. E. WYSESSION. *Lowermost mantle anisotropy beneath the Pacific; imaging the source of the Hawaiian Plume*. Earth and Planetary Science Letters, volume 190(3-4): 167–180, **2001**.
- FOULGER, G. R., M. J. PRITCHARD, J. R. JULIAN, B. R. EVANS, R. M. ALLEN, G. NOLET, W. J. MORGAN, B. H. BERGSSON, P. ERLENDSSON, S. JAKOBSDÓTTIR, S. RAGNARSSON, R. STEFÁNSSON and K. VOGFJORD. *The seismic anomaly beneath Iceland extends down to the mantle transition zone and no deeper*. Geophys. J. Int., volume 142(3): F1–F5, **2000**.
- FOULGER, G. R., M. J. PRITCHARD, J. R. JULIAN, B. R. EVANS, R. M. ALLEN, G. NOLET, W. J. MORGAN, B. H. BERGSSON, P. ERLENDSSON, S. JAKOBSDÓTTIR, S. RAGNARSSON, R. STEFÁNSSON and K. VOGFJORD. *Seismic tomography shows that upwelling beneath Iceland is confined to the upper mantle*. Geophys. J. Int., volume 146(2): 504–530, **2001**.
- FUCHS, K. and G. MÜLLER. *Computation of synthetic seismograms with the reflectivity method and comparison with observations*. Geophys. J. R. astr. Soc., volume 23: 417–433, **1971**.
- GARNERO, E. J. *A new paradigm for earth's core-mantle boundary*. Science, volume 304(5672): 834–837, **2004**.
- GARNERO, E. J. and D. V. HELMBERGER. *Shear velocity variations in D''*. Eos, Transactions, American Geophysical Union, volume 67(44): 1113, **1986**.

- GARNERO, E. J., D. V. HELMBERGER and S. P. GRAND. *Constraining outermost core velocity with SmKS waves*. Geophysical Research Letters, volume 20(22): 2463–2466, **1993**.
- GEBRANDE, H., H. MILLER and P. EINARSSON. *Seismic structure of Iceland along RRISP-Profile I*. J.Geophys., volume 47: 239–249, **1980**.
- GOLDSTEIN, P. and L. MINNER. *SAC2000: Seismic Signal Processing and Analysis Tools For the 21st Century*. Seis. Res. Lett., volume 67: 39, **1996**.
- GREEN, H. W. I. *Plate tectonics: A graveyard for buoyant slabs?*. Science, volume 292: 2445–2446, **2001**.
- GRIFFITHS, R. W. and I. H. CAMPBELL. *On the dynamics of long-lived plume conduits in the convecting mantle*. Earth and Planetary Science Letters, volume 103: 214–227, **1991**.
- GRUNEWALD, S., M. WEBER and R. KIND. *The upper mantle under Central Europe: indications for the Eifel plume*. Geophysical Journal International, volume 147: 590–601, **2001**.
- GUDMUNDSSON, G. B., K. VOGFJORD and B. PORBJARNARDOTTIR. *SIL data status report. Technical report*, Met. Agency of Iceland, **2003**.
- GUDMUNDSSON, O. *On the effect of diffraction on traveltimes measurements*. Geophys. J. Int, volume 124: 304–314, **1996**.
- HELMBERGER, D. V., L. WEN and X. DING. *Seismic evidence that the source of the Iceland hotspot lies at the core-mantle boundary*. Nature, volume 396(6708): 251–255, **1998**.
- HOFMANN, A., D. MCKENZIE, J. MONTAGNER and J. PHIPPS MORGAN. *Rationale for a European Ocean Plume Project. Proposal*, **2000**.
- HUNG, S. H., F. A. DAHLEN and G. NOLET. *Fréchet kernels for finite-frequency traveltimes – II. Examples*. Geophysical Journal International, volume 141(1): 175–203, **2000**.
- HUNG, S.-H., Y. SHEN and L.-Y. CHIAO. *Imaging seismic velocity structure beneath the Iceland Hotspot - A finite-frequency approach*. J. Geophys. Res., volume 109: B08 305, **2004**.
- IGEL, H. *Seismic Modelling and Inversion*. Ph.D. thesis, Université Paris 7, **1993**.
- IGEL, H. and O. GUDMUNDSSON. *Frequency-dependent effects on travel times and waveforms of long-period S and SS waves*. Phys. Earth Planet. Inter., volume 104: 229–246, **1997**.
- IGEL, H., T. NISSEN-MEYER and G. JAHNKE. *Wave propagation in 3D spherical sections: Effects of subduction zones*. Phys. Earth Planet. Inter., volume 132: 219–234, **2002**.
- IGEL, H., N. TAKEUCHI, R. GELLER, C. MÉGNIN, H.-P. BUNGE, E. CLÉVÉDÉ, J. DALKOLMO and B. ROMANOWICZ. *The COSY Project: verification of global seismic modeling algorithms*. Phys. Earth Planet. Inter., volume 119: 3–23, **1999**.
- IGEL, H. and M. WEBER. *SH-wave propagation in the whole mantle using high-order finite differences*. Geophys. Res. Lett., volume 22: 731–734, **1995**.

- IGEL, H. and M. WEBER. *P-SV wave propagation in the Earth's mantle using finite differences: Application to heterogeneous lowermost mantle structure*. Geophys. Res. Lett., volume 23(5): 415–418, **1996**.
- ISHIDA, M., S. MARUYAMA, D. SUETSUGU, S. MATSUZAKA and T. EGUCHI. *Superplume Project: Towards a new view of whole Earth dynamics*. Earth Planets Space, volume 51(1): i–iv, **1999**.
- ITO, G., J. LIN and C. W. GABLE. *Dynamics of mantle flow and melting at a ridge-centered hotspot; Iceland and the Mid-Atlantic Ridge*. Earth and Planetary Science Letters, volume 144(1-2): 53–74, **1996**.
- JAHNKE, G. *Analyse schwacher teleseismischer Einsätze an kleinen Arrays: Möglichkeiten und Grenzen*. Diplomarbeit, Georg-August-Universität Göttingen, **1998**.
- JAHNKE, G. *Numerical modeling of seismic wave propagation: fault zones and global earthquakes (in preparation)*. Ph.D. thesis, Ludwig-Maximilians-Universität München, **2006**.
- JAHNKE, G., T. NISSEN-MEYER, M. TREML and H. IGEL. *High Resolution Global Wave Propagation for Axi-Symmetric and additional 3D Geometries*. EGS XXVII General Assembly, Nice, 21-26 April 2002, abstract #4580, volume 27: 4580–+, **2002**.
- JEANLOZ, R. and S. MORRIS. *Temperature distribution in the crust and in the mantle*. Ann. Re. Earth Planet. Sci. Lett., volume 14: 377–415, **1986**.
- Ji, Y. and H.-C. NATAF. *Detection of mantle plumes in the lower mantle by diffraction tomography: Hawaii*. Earth and Planetary Science Letters, volume 159: 99–115, **1998a**.
- Ji, Y. and H.-C. NATAF. *Detection of mantle plumes in the lower mantle by diffraction tomography: theory*. Earth and Planetary Science Letters, volume 159: 87–98, **1998b**.
- JULIAN, B. R. and G. R. FOULGER. *What can seismology say about hot spots ?*. In: *The Hotspot Handbook, Proceedings of Penrose Conference Plume IV: Beyond the Plume Hypothesis, August 2003*. Hveragerdi, Iceland, **2003**.
- KARATO, S.-I. *Importance of anelasticity in the interpretation of seismic tomography*. Geophys. Res. Lett., volume 20: 1623–1626, **1993**.
- KATZMAN, R., L. ZHAO and T. H. JORDAN. *High-resolution, two-dimensional vertical tomography of the Central Pacific mantle using ScS reverberations and frequency-dependent travel times*. J. Geophys. Res., volume 103(B8): 17933–17971, **1998**.
- KEAREY, P. and F. J. VINE. *Global Tectonics*. Blackwell Publishing, 2nd edition, **1996**.
- VAN KEKEN, P. E., E. H. HAURI and C. J. BALLENTINE. *Mantle mixing: The generation, preservation and destruction of chemical heterogeneity*. Ann. Rev. Earth Planet. Sci. Lett., volume 30: 493–525, **2002**.
- KELLER, W. R., D. L. ANDERSON and R. W. CLAYTON. *Resolution of tomographic models of the mantle beneath Iceland*. Geophys. Res. Lett., volume 27(234): 3993–3996, **2000**.
- KENNETT, B. L. N. and E. R. ENGDAHL. *Traveltime for global earthquake location and phase identification*. Geophys. J. Int, volume 105: 429–465, **1991**.

- KENNETT, B. L. N., E. R. ENGBAHL and R. BULAND. *Constraints on seismic velocities in the Earth from travel-times*. Geophys. J. Int., volume 122(1): 108–124, **1995**.
- KERR, R. A. *Mantle plumes both tall and short?*. Science, volume 302(5651): 1643, **2003**.
- KEYSER, M., J. R. R. RITTER and M. JORDAN. *3D shear-wave velocity structure of the Eifel plume, Germany*. Earth and Planetary Science Letters, volume 203: 59–82, **2002**.
- KOMATITSCH, D., J. RITSEMA and J. TROMP. *The spectral-element method, Beowulf computing, and global seismology*. Science, volume 298: 1737–1742, **2002**.
- KOMATITSCH, D. and J. TROMP. *Introduction to the spectral-element method for 3-D seismic wave propagation*. Geophys. J. Int., volume 139: 806–822, **1999**.
- KOMATITSCH, D. and J. TROMP. *Spectral-element simulations of global seismic wave propagation — I. Validation*. Geophys. J. Int., volume 149: 390–412, **2002a**.
- KOMATITSCH, D. and J. TROMP. *Spectral-element simulations of global seismic wave propagation — II. Three-dimensional models, oceans, rotation and self-gravitation*. Geophys. J. Int., volume 150: 303–318, **2002b**.
- KOMATITSCH, D., S. TSUBOI, J. CHEN and J. TROMP. *A 14.6 billion degrees of freedom, 5 teraflop, 2.5 terabyte earthquake simulation on the Earth Simulator*. Proceedings of the ACM/IEEE Supercomputing SC'2003 conference, **2003**.
- LABROSSE, S. *Hotspots, mantle plumes and core heat loss*. Earth and Planetary Science Letters, volume 199(1): 147–156, **2002**.
- LARSEN, T. B., D. A. YUEN and M. STOREY. *Ultrafast mantle plumes and implications for flood basalt volcanism in the Northern Atlantic Region*. Tectonophysics, volume 311(1–4): 31–43, **1999**.
- LASKE, G. *A wish list for updating PREM: Lessons we learnt*. Geophys. Res. Abstracts, volume 7: 03910, **2005**.
- LASKE, G., J. ORCUTT, S. SOLOMON, E. HAURI, C. WOLFE, R. DETRICK, J. COLLINS and D. BERCOVICI. *PLUME: Imaging the Hawaiian HOTSPOT and Swell. Proposal*, Scripps Institution of Oceanography, Woods Hole Oceanographic Institution, University of Hawaii, Carnegie Institution of Washington, **1999**.
- LAWVER, L. A. and R. D. MÜLLER. *Iceland hotspot track*. Geology, volume 22: 311–314, **1994**.
- LI, A. and R. S. DETRICK. *Azimuthal anisotropy and phase velocity beneath Iceland; implication for plume-ridge interaction*. Earth and Planetary Science Letters, volume 214(1–2): 153–165, **2003**.
- LI, X., R. KIND, K. PRIESTLEY, S. V. SOBOLEV, F. TILMANN, X. YUAN and M. WEBER. *Mapping the Hawaiian plume conduit with converted seismic waves*. Nature, volume 405(6789): 938–941, **2000**.
- LI, X., R. KIND and X. YUAN. *Seismic study of upper mantle and transition zone beneath hotspots*. Phys. Earth Planet. Inter., volume 136: 79–92, **2003**.

- LIPPITSCH, R., R. S. WHITE and H. SOOSALU. *Precise hypocentre relocation of microearthquakes in a high-temperature geothermal field: the Torfajökull central volcano, Iceland*. *Geophys. J. Int.*, volume 160: 371–388, **2005**.
- LOPER, D. E. and F. D. STACEY. *The dynamical and thermal structure of deep mantle plumes*. *Phys. Earth Planet. Inter.*, volume 33: 304–317, **1983**.
- MALAMUD, B. D. and D. L. TURCOTTE. *How many plumes are there ?*. *Earth and Planetary Science Letters*, volume 174: 113–124, **1999**.
- MARCINKOVICH, C. and K. B. OLSEN. *On the implementation of Perfectly Matched Layers in a three-dimensional fourth-order velocity-stress finite-difference scheme*. *J. Geophys. Res.*, volume 108(B5): ESE18, **2003**.
- MARQUERING, H., F. A. DAHLEN and G. NOLET. *Three-dimensional sensitivity kernels for finite-frequency traveltimes; the banana-doughnut paradox*. *Geophysical Journal International*, volume 137(3): 805–815, **1999**.
- MARQUERING, H., G. NOLET and F. A. DAHLEN. *Three-dimensional waveform sensitivity kernels*. *Geophys. J. Int.*, volume 132: 521–534, **1998**.
- MOCZO, P., J. KRISTEK and L. HALADA. *The Finite-Difference Method for Seismologists. An Introduction*. Comenius University, Bratislava, **2004**. ISSN 80-223-2000-5.
- MOCZO, P., J. O. A. ROBERTSSON and L. EISNER. *The finite-difference time-domain method for modelling of seismic wave propagation*. In: R. DMOWSKA (editor), *Advances in Wave Propagation in heterogeneous Earth*, *Advances in Geophysics*. Elsevier Academic Press, **2006**.
- MONTELLI, R., G. NOLET, F. DAHLEN, G. MASTERS, R. ENGDAHL and S.-H. HUNG. *Global tomographic models with finite-frequency modeling reveal a variety of plumes in the mantle*. *Geophys. Res. Abstracts*, volume 6: 01 257, **2004a**.
- MONTELLI, R., G. NOLET, F. A. DAHLEN, G. MASTERS, E. R. ENGDAHL and S.-H. HUNG. *Finite-frequency tomography reveals a variety of plumes in the mantle*. *Science Express*, (5656), **2003a**. Published online.
- MONTELLI, R., G. NOLET, F. A. DAHLEN, G. MASTERS, E. R. ENGDAHL and S.-H. HUNG. *Finite-frequency tomography reveals a variety of plumes in the mantle*. *Science*, volume 303(5656): 338–343, **2004b**.
- MONTELLI, R., G. NOLET, G. MASTERS, F. DAHLEN and S.-H. HUNG. *Finite frequency tomography reveals a variety of plumes in the mantle*. In: *The Hotspot Handbook, Proceedings of Penrose Conference Plume IV: Beyond the Plume Hypothesis, August 2003*. Hveragerdi, Iceland, **2003b**.
- MORGAN, W. J. *Convection plumes in the lower mantle*. *Nature*, volume 230: 42–43, **1971**.
- MORGAN, W. J. *Hotspot tracks and the opening of the Atlantic and Indian Oceans*. In: C. EMILIANI (editor), *The Sea*, volume 7, chapter *The Oceanic Lithosphere*, (pp. 443–487). John Wiley, New York, **1981**.

- MURAKAMI, M., K. HIROSE, K. KAWAMURA, N. SATA and Y. OHISHI. *Post-perovskite phase transition in MgSiO<sub>3</sub>*. Science, volume 304: 855–858, **2004**.
- NATAF, H.-C. *Seismic imaging of mantle plumes*. Ann. Rev. Earth Planet. Sci., volume 28: 391–417, **2000**.
- NISSEN-MEYER, T. *Numerical Simulation of 3-D Seismic Wave Propagation through Subduction Zones*. Diplomarbeit, Ludwig-Maximilians-Universität München, **2001**.
- NISSEN-MEYER, T., F. DAHLEN and A. FOURNIER. *Spherical earth fréchet sensitivity kernels*, **2005**. Submitted to Geophys. J. Int.
- NOLET, G. and F. A. DAHLEN. *Wave front healing and the evolution of seismic delay times*. Journal of Geophysical Research, B, Solid Earth and Planets, volume 105(8): 19, **2000**.
- PATERA, A. T. *A spectral element method for fluid dynamics: laminar flow in a channel expansion*. J. Comput. Phys., volume 54: 468–488, **1984**.
- PHIPPS MORGAN, J. and W. J. MORGAN. *Two-stage melting and the geochemical evolution of the mantle; a recipe for mantle plum-pudding*. Earth and Planetary Science Letters, volume 170(3): 215–239, **1999**.
- PHIPPS MORGAN, J., W. J. MORGAN, Y.-S. ZHANG and W. H. F. SMITH. *Observational hints for a plume-fed, suboceanic asthenosphere and its role in mantle convection*. Journal of Geophysical Research, volume 100(B7): 12 753–12 768, **1995**.
- PILIDOU, S., K. PRIESTLEY, O. GUDMUNDSSON and E. DEBAYLE. *Upper mantle S-wave speed heterogeneity and anisotropy beneath the North Atlantic from regional surface wave tomography: the Iceland and Azores plumes*. Geophys. J. Int., volume 159(3): 157, **2004**.
- RÜMPKER, G., A. TOMMASI and J.-M. KENDALL. *Numerical simulations of depth-dependent anisotropy and frequency-dependent wave propagation effects*. J. Geophys. Res., volume 104: 23 141–23 154, **1999**.
- RIBE, N. M., U. R. CHRISTENSEN and J. THEISSING. *The dynamics of plume-ridge interaction, 1: Ridge-centered plumes*. Earth and Planetary Science Letters, volume 134: 155–168, **1995**.
- RICHARDS, M. A., R. A. DUNCAN and V. E. COURTILOTT. *Flood basalts and hot-spot tracks: Plume heads and tails*. Science, volume 246: 103–107, **1989**.
- RITSEMA, J. and R. M. ALLEN. *The elusive mantle plume*. Earth and Planetary Science Letters, volume 207(1-4): 1–12, **2003**.
- RITSEMA, J., H.-J. VAN HEIJST and J. H. WOODHOUSE. *Complex shear wave velocity structure imaged beneath Africa and Iceland*. Science, volume 286: 1925–1928, **1999**.
- RITSEMA, J. and H. VAN HEIJST. *Seismic imaging of structural heterogeneity in Earth's mantle: evidence for large-scale mantle flow*. Sci Prog., volume 83: 243–259, **2000**.

- RITTER, J. R. R., U. ACHAUER, U. R. CHRISTENSEN, G. BOCK, G. BOKELMANN, M. BUDWEG, T. CAMELBEECK, F. COLLIN, N. D'OREYE, I. ESCHGHI, H. GAENSICHE, K.-G. HINZEN, M. JORDAN, T. KASPAR, R. PELZING, F. SCHERBAUM, Y.-F. TEMME, K. WALKER and M. WEBER. *The teleseismic tomography experiment in the Eifel region, Central Europe; design and first results*. Seismological Research Letters, volume 71(4): 437–443, **2000**.
- RITTER, J. R. R., M. JORDAN, U. R. CHRISTENSEN and U. ACHAUER. *A mantle plume below the Eifel volcanic fields, Germany*. Earth and Planetary Science Letters, volume 186: 7–14, **2001**.
- ROMANOWICZ, B. *Global mantle tomography: progress status in the last 10 years*. Annu. Rev. Geoph. Space Phys., volume 31: 303–333, **2003**.
- RONCHI, C., R. IACONO and P. S. PAOLUCCI. *The "cubed sphere": A new method for the solution of partial differential equations in spherical geometry*. J. Comput. Phys., volume 124: 93–114, **1996**.
- ROST, S., E. J. GARNERO, Q. WILLIAMS and M. MANGA. *Seismic constraints on a possible plume root at the core-mantle boundary*. Nature, volume 435: 666–669, **2005**.
- ROST, S. and C. THOMAS. *Array seismology: Methods and applications*. Reviews of Geophysics, volume 40(3): 1008, **2002**.
- ROST, S. and M. WEBER. *A reflector at 200 km depth beneath the NW Pacific*. Geophys. J. Int., volume 147: 12–28, **2001**.
- RUEDAS, T. *Convection and melting processes in a Mantle Plume under a Spreading Ridge, with Application to Iceland*. Ph.D. thesis, Johann Wolfgang Goethe – Universität, Frankfurt am Main, **2004**.
- RÜMPKER, G. and P. G. SILVER. *Calculating splitting parameters for plume-type anisotropic structures of the upper mantle*. Geophysical Journal International, volume 143(3): 507–520, **2000**.
- RUSSELL, S. A., T. LAY and E. J. GARNERO. *Seismic evidence for small-scale dynamics in the lowermost mantle at the root of the hawaiian hotspot*. Nature (London), volume 396(6708): 255–258, **1998**.
- RYBERG, T., G. RÜMPKER, C. HABERLAND, D. STROMEYER and M. WEBER. *Simultaneous inversion of shear wave splitting observations from seismic arrays*. Journal of Geophysical Research (Solid Earth), volume 110: 3301, **2005**.
- SADOURNY, R. *Conservative finite-difference approximations of the primitive equations on quasi-uniform spherical grids*. Monthly Weather Review, volume 100: 136–144, **1972**.
- SCHLINDWEIN, V. *Azimuthal variation of the P phase in Icelandic receiver functions*. Geophys. J. Int., volume 144(1): 221–230, **2001**.
- SCHMERR, N., E. GARNERO, H. IGEL, G. JAHNKE, M. THORNE and M. TREML. *Imaging upper mantle discontinuity structure beneath Hawaii using the SS-prescursors*. In: *9th Symposium on Study of the Earth's Deep Interior (abstract)*. Garmisch-Partenkirchen, **2004**.



- SCHUBERT, G., D. L. TURCOTTE and P. OLSON. *Mantle Convection in the Earth and Planets*. Cambridge University Press, Cambridge, United Kingdom, **2001**.
- SCHUBERTH, B. *The Spectral Element Method for Seismic Wave Propagation – Theory, Implementation and Comparison to Finite Difference Methods*. Diplomarbeit, Ludwig-Maximilians-Universität München, **2003**.
- SCHWEIZER, J., J. FYEN, S. MYKKELVEIT and T. KVAERNA. *New Manual of Seismic Observatory Practice*, volume 1, chapter 9, (pp. 1–52). GeoForschungsZentrum Potsdam, **2002**.
- SERIANI, G., E. PRIOLO, J. CARCIONE and E. PADOVANI. *High-order spectral element method for elastic wave modeling*. In: *Extended Abstracts of 62. Ann. Int. Meet., Soc. Expl. Geophys.*, (pp. 1285–1288). **1992**.
- SHEN, Y., S. C. SOLOMON, I. T. BJARNASON, G. NOLET, W. J. MORGAN, R. M. ALLEN, K. VOGFJORD, S. JAKOBSDÓTTIR, R. STEFANSSON, B. R. JULIAN and G. R. FOULGER. *Seismic evidence for a tilted mantle plume and north-south mantle flow beneath Iceland*. *Earth and Planetary Science Letters*, volume 197(3-4): 261–272, **2002**.
- SHEN, Y., S. C. SOLOMON, I. T. BJARNASON and G. M. PURDY. *Hot mantle transition zone beneath Iceland and the adjacent Mid-Atlantic Ridge inferred from P-to-S conversions at the 410- and 660-km discontinuities*. *Geophysical Research Letters*, volume 23(24): 3527–3530, **1996**.
- SHEN, Y., S. C. SOLOMON, I. T. BJARNASON and C. J. WOLFE. *Seismic evidence for a lower-mantle origin of the Iceland plume*. *Nature*, volume 395: 62–65, **1998**.
- SHEN, Y., C. J. WOLFE and S. C. SOLOMON. *Seismological evidence for a mid-mantle discontinuity beneath Hawaii and Iceland*. *Earth and Planetary Science Letters*, volume 214(1-2): 143–151, **2003**.
- SIGLOCH, K. and G. NOLET. *A method to measure finite-frequency amplitudes and travel times of teleseismic body waves*. *Geophys. Res. Abstracts*, volume 7: A–02 359, **2005**.
- SLEEP, N. H. *Hotspots and mantle plumes: Some phenomenology*. *J. Geophys. Res.*, volume 95(B5): 6715–6736, **1990**.
- SLEEP, N. H. *Thermal haloes around plume tails*. *Geophysical Journal International*, volume 156(2): 359–362, **2004**.
- SPENCE, W., C. MENDOZA, E. R. ENGDahl, G. L. CHOY and E. NORABUENA. *Seismic Subduction of the Nazca Ridge as shown by the 1996–97 Peru Earthquakes*. *Pure and Applied Geophysics*, volume 154(3-4): 753–776, **1999**.
- STACEY, F. D. and D. E. LOPER. *The thermal boundary-layer interpretation of D" and its role as a plume source*. *Phys. Earth Planet. Inter.*, volume 33: 45–55, **1983**.
- STEFÁNSSON, R., P. BODVARSSON, R. SLUNGA, P. EINARSSON, S. JAKOBSDÓTTIR, H. BUNGUM, S. GREGERSEN, J. HAVSKOV, J. HJELME and H. KORHONEN. *Earthquake prediction research in the south Iceland seismic zone and the SIL project*. *Bull. Seis. Soc. Am.*, volume 83: 696–716, **1993**.

- STEIN, C. and S. STEIN. *Mantle plumes: heat flow near Iceland*. *Astronomy & Geophysics*, volume 44: 1.8–1.10, **2003**.
- STEINBERGER, B. *Plumes in a convecting mantle; models and observations for individual hotspots*. *Journal of Geophysical Research, B, Solid Earth and Planets*, volume 105(5): 11 127–11 152, **2000**.
- STEINBERGER, B. and R. J. O'CONNELL. *Advection of plumes in mantle flow; implications for hot spot motion, mantle viscosity and plume distribution*. *Geophysical Journal International*, volume 132(2): 412–434, **1998**.
- STORCHAK, D. J. S. and P. BORMANN. *The iaspei standard seismic phase list*. *Seismol. Res. Lett.*, volume 64(6): 761–772, **2003**.
- STRASSER, M. *Numerical modeling of 3D wave effects of plumes*. Diplomarbeit, Ludwig-Maximilians-Universität München, **2001**.
- SWENSON, J. L. and S. L. BECK. *Source Characteristics of the 12 November 1996 Mw 7.7 Peru Subduction Zone Earthquake*. *Pure and Applied Geophysics*, volume 154(3–4): 731 – 751, **1999**.
- TACKLEY, P. J. *Mantle convection and plate tectonics: Towards an integrated physical and chemical theory*. *Science*, volume 288: 2002–2007, **2000**.
- TAYLOR, M., J. TRIBBA and ISKANDARANI. *The spectral-element method for the shallow water equation on a sphere*. *J. Comput. Phys.*, volume 130: 92–108, **1997**.
- THOMAS, C., H. IGEL, M. WEBER and F. SCHERBAUM. *Acoustic simulation of P-wave propagation in a heterogeneous spherical Earth: numerical method and application to precursor waves to PKP<sub>df</sub>*. *Geophys. J. Int.*, volume 141: 307–320, **2000**.
- THORNE, M. S. *Broadband waveform modeling of deep mantle structure*. Ph.D. thesis, Arizona State University, Tempe, Arizona, **2005**.
- THORNE, M. S. and E. J. GARNERO. *Inferences on ultralow-velocity zone structure from global analysis of SPdKS waves*. *J. Geophys. Res.*, volume 109: B08 301, **2004**.
- THORNE, M. S., E. J. GARNERO and S. P. GRAND. *Geographic correlation between hot spots and deep mantle lateral shear-wave velocity gradients*. *Phys. Earth Planet. Inter.*, volume 146: 47–63, **2004**.
- TILMANN, F. J., D. MCKENZIE and K. F. PRIESTLEY. *P and S wave scattering from mantle plumes*. *J. Geophys. Res.*, volume 103(B9): 21, **1998**.
- TRAMPERT, J. *Global seismic tomography: the inverse problem and beyond*. *Inv. Probl.*, volume 14(3): 371–385, **1998**.
- TRAMPERT, J. and J. SPETZLER. *Surface wave tomography: finite-frequency effects lost in the null space*. *gji*, volume 164(2): 394–400, **2006**.
- TROMP, J., C. TAPE and Q. LIU. *Seismic tomography, adjoint methods, time reversal, and banana-doughnut kernels*. *Geophys. J. Int.*, **2005**.

- TRYGGVASON, K., E. HUSEBYE and R. STEFÁNSSON. *Seismic image of the hypothesized Icelandic hot spot*. Tectonophysics, volume 100: 97–118, **1983**.
- VAN DER HILST, R. D., S. WILDIYANTORO and E. R. ENGDAHL. *Evidence for deep mantle circulation from global tomography*. Nature, (pp. 578–585), **1997**.
- VAN WIJK, J. W., R. S. HUISMANS, M. TER VOORDE and S. A. P. L. CLOETINGH. *Melt generation at volcanic continental margins: No need for a mantle plume?*. Geophys. Res. Lett., volume 28: 3995–3998, **2001**.
- VANDECAR, J. C. and R. S. CROSSON. *Determination of teleseismic relative phase arrival times using multi-channel cross-correlation and least squares*. Bull. Seism. Soc. Am., volume 80(1): 150–159, **1990**.
- VIRIEUX, J. *P-SV wave propagation in heterogeneous media: Velocity-stress finite-difference method*. Geophysics, volume 51(4): 889–901, **1986**.
- WEGENER, A. *Die Entstehung der Kontinente*. Geologische Rundschau, volume 3: 276–292, **1912**.
- WEGENER, A. *Die Theorie der Kontinentalverschiebungen*. ZS. d. Ges. f. Erdkunde, (pp. 89–103), **1921**.
- WEN, L. *An SH hybrid method and shear velocity structures in the lowermost mantle beneath the central Pacific and South Atlantic Oceans*. J. Geophys. Res., volume 107(B3): ESE 4–1 – ESE 4–20, **2002**.
- WEN, L. and D. V. HELMBERGER. *A 2-D P-SV hybrid method and its application to modeling localized structures near the core-mantle boundary*. J. Geophys. Res., volume 103: 17901–17918, **1998**.
- WHITEHEAD, J. A. and D. S. LUTHER. *Dynamics of laboratory diapir and plume models*. J. Geophys. Res., volume 80: 705–717, **1975**.
- WIELANDT, E. *On the validity of the ray approximation for interpreting delay times*. In: G. NOLET (editor), *Seismic Tomography with Applications in Global Seismology and Exploration Geophysics*, (pp. 85–98). D. Reidel, Dordrecht, The Netherlands, **1987**.
- WILLIAMS, Q., J. REVENAUGH and E. GARNERO. *A Correlation between Ultra-Low Basal Velocities in the Mantle and Hot Spots*. Science, volume 281: 546–549, **1998**.
- WILSON, J. T. *A possible origin of the Hawaiian islands*. Can. J. Physics, volume 41: 863–868, **1963**.
- WILSON, J. T. *Evidence from oceanic islands suggesting movement in the Earth*. Philos. Trans. R. Soc., volume Ser. A 258: 145–167, **1965**.
- WOLFE, C. J. *Prospecting for hotspot roots*. Nature (London), volume 396(6708): 212–213, **1998**.
- WOLFE, C. J., I. P. BJARNASON, J. VANDECAR and S. SOLOMON. *Seismic structure of the Iceland mantle plume*. Nature, volume 385(5727): 245–247, **1997**.

- WOLFE, C. J., I. T. BJARNASON, S. C. SOLOMON and J. C. VANDECAR. *Three-dimensional seismic imaging of the Icelandic hot spot; results from the ICEMELT experiment*. Eos, Transactions, American Geophysical Union, Suppl., volume 77(17): 276, **1996**.
- WOLFE, C. J., I. T. BJARNASON, J. C. VANDECAR and S. C. SOLOMON. *Assessing the depth resolution of tomographic models of upper mantle structure beneath Iceland*. Geophys. Res. Lett., volume 29(1): 1–4, **2002**.
- ZHAO, D. *Seismic structure and origin of hotspots and mantle plumes*. Earth Planet. Sci. Lett., volume 192(3): 251–265, **2001**.
- ZHAO, L., T. H. JORDAN and C. H. CHAPMAN. *Three-dimensional Fréchet differential kernels for seismic delay times*. Geophys. J. Int., volume 141: 558–576, **2000**.
- ZHOU, Y., F. A. DAHLEN and G. NOLET. *Three-dimensional sensitivity kernels for surface wave observables*. Geophysical Journal International, volume 158(1): 142–168, **2004**.

# Acknowledgements

Herrn Prof. Igel danke ich, dass er es mir ermöglicht hat, nach München zu kommen und diese Arbeit durchzuführen. Seine ansteckende Begeisterung, seine dynamische Herangehensweise und die ungezwungene Atmosphäre in seiner Arbeitsgruppe haben dafür gesorgt, dass so manches Motivationsloch, das sich beim Programmieren zwangsläufig einstellt, überwunden wurde. Die von ihm geschaffenen Möglichkeiten zum Besuch internationaler Konferenzen, als auch von ihm in Bayern organisierten Tagungen sorgten regelmäßig für den Kontakt mit anderen Wissenschaftlern.

Herr Prof. Bunge hat mir wertvolle Einblicke in die Geodynamik gegeben. Dafür, und für das freundliche Interesse an meiner Arbeit danke ich ihm. Darüber hinaus hat er als Institutsleiter immer wieder andere hochrangige Forscher in unser Department gebracht, was zu einem anregenden Arbeitsumfeld beitrug.

So konnte ich durch die zahlreichen Möglichkeiten, die mir geboten wurden, in Diskussionen mit Jason Morgan, Saskia Goes, Guust Nolet, Karin Sigloch, Joachim Ritter und Frederik Tillmann meinen fachlichen Horizont erweitern.

Vielen Dank an die gesamte Arbeitsgruppe Seismologie und auch an andere Mitglieder des Instituts für die schöne Zeit und die Hilfe, die ich immer wieder erfuhr.

Max Strasser, dessen Diplomarbeit eine Vorstudie zu dieser Arbeit darstellt, möchte ich für die Überlassung des kartesischen 3D-Codes sowie für die Unterstützung zu Beginn der Arbeit herzlich danken.

Suzan Emiroglu hat einiges dazu beigetragen, dass es mich nach München verschlagen hat und hat kontinuierlich dafür gesorgt, dass ich diesen Schritt nicht bereut habe.

Tarje Nissen-Meyer und Gunnar Jahnke waren insbesondere in der ersten Zeit hier eine wertvolle Hilfe, vor allem bei allen numerischen Themen und dem hybriden Code.

Auch Michael Ewald, Gilbert Brietzke und Peter Danecek waren geduldige und kompetente Ansprechpartner, wenn es um Computerprobleme aller Art, Numerik, aber auch um die notwendigen Pausen ging.

Meinen Zimmer-Kollegen Wiwit und Toni bin ich für die angenehme und anregende Atmosphäre in unserem Büro dankbar, Toni hat mir darüber hinaus mit viel Geduld bei awk und gmt geholfen. Auch Christoph Moder half mit der Erstellung zahlreicher kleiner Skripts für die Lösung von großen Aufgaben, vielen Dank dafür.

Zu guter Letzt hat Bernard Schuberth viel zu dieser Arbeit beigetragen. Seine Vorarbeiten zur Spektralen Elemente Methode und die Einführung, die er mir gab, eröffnete eine intensive Zusammenarbeit im Bereich globale Seismologie. Die vielen Diskussionen unserer Ergebnisse waren unverzichtbar für das Verständnis der beobachteten Effekte. Vielen Dank, Bernhard, dass es dazu auch noch Spaß gemacht hat.

Dimitrii Komatisch provided us with the SPECFEM3D code and did not get tired of answering emails from Bernhard and me.

Vielen Dank an die freiwilligen als auch die Hauptamtlichen Systemadministratoren, d.h. mehr oder weniger die gesamte Seismologie-Gruppe der frühen Tage, sowie Gunnar Jahnke, Roman Leonhard, Conrad Genarro und letztendlich Jens Öser, dessen Assoziationen mit „Feringa“ vermutlich eher die eines problematischen Computers als die eines schönen Badesees sind. Auch dem LRZ sei für die Unterstützung und das zur Verfügung stellen der erforderlichen SuperComputer gedankt.

Erika Vye hat Teile des Manuskripts im Hinblick auf sprachliche Aspekte Korrektur gelesen. Darüberhinaus bin ich ihr für die Organisation der ersten „PhD Conference“ dankbar, wo ich unter anderem Nicole Jeutter kennenlernte, die in mancher Kaffeepause dafür sorgte, dass ich nicht nur in eigenen Saft der numerischen Seismologie schmorte.

Der Doktorand, insbesondere mit Familie, lebt nicht von der Mensa allein. Ich danke Heiner Igel ganz herzlich für das kreative Sicherstellen der Finanzierung meines Projekts und meiner Reisen durch die DFG-Projekte Ig 16/4-1, Ig16/2-2, Ig 16/4-2, das EU SPICE Projekt, und die Projekte CONWIHR und SISMOVALP. Auch der Deutschen Forschungsgemeinschaft und den anderen Mittelgebern an dieser Stelle ein herzlicher Dank.

For the hospitality and fun during my reseach stay in Tempe/Arizona I would like to thank Amy & Nick Schmerr, Sean Ford and Teresa Lussack, Ed Garnero & Pamela Neuthard, Abigail Bull, and Dawn & Mike Thorne. For the scientific exchange with and the input from the entire group at ASU I am very grateful, especially to Sebastian Rost who introduced me to SeismicHandler and fk-analysis.

Nicht zuletzt verdanke ich dem Rückhalt in meiner Familie und deren Unterstützung sehr viel. Meine Frau Rosemarie mit ihrer Geduld und Hanna und Martin, die immer wieder für Ablenkung sorgten, wenn ich im Kopf noch Arbeit mit nach Hause genommen hatte, haben mir immer wieder den Freiraum, aber auch den Ausgleich zu einer kopflastigen Arbeit gegeben.

# Lebenslauf

**04. September 1972** Geboren in Marburg als Kind der Eheleute Maria und Gustav Treml.

**August 1979** Einschulung in die Grundschule Marburg-Wehrshausen.

**August 1983** Übertritt in das Gymnasium Martin-Luther Schule in Marburg.

**Mai 1992** Erwerb der Allgemeinen Hochschulreife.

**August 1992** Aufnahme einer Berufsausbildung zum Radio-Fernsehtechniker in Marburg.

**Januar 1995** Erlangung des Gesellenbriefes (Innungsbester).

**April 1995** Aufnahme des Geophysikstudiums an der Universität Karlsruhe (TH).

**September 1997** Erwerb des Vordiploms.

**Juli 2000** Verleihung des Diploms in Geophysik („mit Auszeichnung bestanden“). Titel der Diplomarbeit: „Starkbebensynthese mit Empirischen Greenschen Funktionen am Beispiel der Cascadia Subduktionszone“.

**August 2000 – Juli 2001** Anstellung als wissenschaftlicher Mitarbeiter am Sonderforschungsbereich 471 „Starkbeben“, Universität Karlsruhe.

**August 2001 – September 2005** Anstellung als wissenschaftlicher Mitarbeiter an der Ludwig-Maximilians Universität München über eine Drittmittelstelle der Deutschen Forschungsgemeinschaft (DFG). Thema: „Die seismische Signatur von Plumes“.

**seit Februar 2006** Referent im Aufgabengebiet Risikomanagement für Naturgefahren bei der Allianz AG, München.